Nonlinear System Identification of Physical Parameters for Damage Prognosis and Localization in Structures

Giancarlo G. Bordonaro

Dissertation submitted to Virginia Polytechnic Institute and State University
in partial fulfillment of the requirements for the degree of

Doctor of Philosophy
in
Engineering Mechanics

Muhammad R. Hajj, Chairman
John C. Duke
Mayuresh J. Patil
Ishwar K. Puri
Saad Ragab

November 30, 2009
Blacksburg, Virginia

Keywords: Damage Prognosis, Structural Health Monitoring, Fiber Bragg Grating Sensors,
Nonlinear Identification, Higher-Order Spectra

Nonlinear System Identification of Physical Parameters for Damage Prognosis and Localization in Structures

Giancarlo G. Bordonaro

(ABSTRACT)

The understanding of how structural components endure loads, in particular variable loads, is that these components gradually, over some period of time depending on the nature of the loading and the material, develop a microcrack. After some additional time and loading, the microcrack grows to a size that might be detected. Beyond that point, the microcrack propagates in a manner that can be reliably predicted by computer analysis codes. Consequently, one can define different stages for the life of a structural component. These are: 1) the period prior to the formation of a microcrack, 2) the period of microcrack growth, and finally 3) the period of crack growth. To date, structural health monitoring approaches that seek to detect cracks offer no insight into the extent of deterioration occurring in the initial stage that is a precursor to the formation of the microcrack or its growth. However, an approach that would facilitate monitoring the extent of the deterioration that takes place during this stage promises to improve life prediction capabilities of structural components.

The challenge, thus, is to develop quantitative assessment of damage accumulation from the earliest stages of the fatigue process and to provide a structure's signature that is dependent of the damage stage. One such signature is the structure's response to forced excitation. The realization of such a goal would help in advancing structural health monitoring procedures using interrogative system identification techniques and determine sensitivities of physical parameters to damage. Additionally, vibration-based spectral quantities are related to physical properties of the structure under test.

In this thesis, nonlinear response to parametric excitation is exploited for nonlinear system identification of metallic and composite beam-mass systems before damage initiation through intermediate states of damage progression to failure. Parametric identification procedure combines linear and higher order spectral analysis of vibration measurements and perturbation techniques for the derivation of the approximate solution of the system non-

linear governing differential equation. The possibility of using optical Fiber Bragg Grating sensors technology for damage localization is also assessed. Spectral moments and quantities obtained from fiber optic strain measurements are evaluated near and away from cracks to assess the relation between these moments and cracks.

Variations in parameters representing natural frequency, damping and effective nonlinearities for different levels of progressive damage in a beam-mass system have been determined. Their percentage variations have been quantified to establish their sensitivities to damage initiation. The results show that damping and effective nonlinearity parameters are more sensitive to damage conditions than the natural frequency of the first mode. Crack localization is assessed by means of optical fiber technology for a composite beam-mass system. The results show that noise levels in fiber optic signals are high in comparison to strain gage signals. Of particular interest, however, is the observation that the nonlinear response is more pronounced near the cracks than away from them.

Acknowledgments

First and foremost, I would like to acknowledge my family, without their love and encouragement, I could have never finished this study. They have always believed in me and gave their emotional support at difficult times.

I had the privilege of working with exceptionally good people in my PhD study. Their extensive knowledge, experience, and encouragement played an important role in the success of this project. I am grateful to my advisor Dr. Muhammad Hajj, for his academic advice, support, and dedication. I would like to thank for his help and guidance.

I would like to thank the faculty members who served on my committee, Dr. Duke, Dr. Patil, Dr. Puri, and Dr. Ragab for their contribution to my academic development and for always being available for advice and questions.

Many thanks go to Dr. Mook for the time he spent with me in many enlightening and pleasant discussions on nonlinear phenomena and advanced vibrations. My thanks also go to Dr. Nayfeh who influenced my knowledge in the fields of nonlinear dynamics and perturbation techniques.

I would also like to acknowledge the other many graduate students in ESM Department who became real friends throughout the years I spent in Virginia Tech. I am thankful for their friendly and enjoyable conversations.

Photographs in this dissertation were taken by the author and with the help of Doug Harold to whom I am very grateful.

Contents

Abstract ii

Acknowledgments iv

Contents v

List of Figures viii

List of Tables xxi

1 Introduction 1

1.1 Issues, Needs and Opportunities in SHM 1

1.2 Sensor technology 2

1.2.1 Fiber optic sensors 2

1.3 Analysis procedures for structural health monitoring 3

1.3.1 Inverse methods 3

1.3.2 Vibration-based data: time-series methods 4

1.3.3 Time-frequency and time-scale analysis methods 5

1.3.4 Vibration and wave propagation data as diagnosis for SHM 6

1.4 Objective and Approach 7

2 Digital Time Series Analysis 9

2.1 Fourier Analysis Tools 9

2.1.1 Continuous and Discrete Fourier Transform 9

2.1.2 Spectral Moments 10
2.2 Phase Relationship Between Fundamental and Subharmonic 18

3 Prognosis of a Steel Beam-Mass System 22
3.1 Introduction 23
3.2 Analytical Model 24
3.3 Approximate Solution 31
3.4 Experimental Setup 36
3.5 Spectral Analysis of Excitation and Response Data 40
3.6 System Identification 58
3.6.1 Sensitivity analysis 62
3.6.2 Validation 62
3.7 Second Metallic Beam 63
3.7.1 Spectral Analysis of Excitation and Response 66
3.7.2 System Identification 68
3.7.3 Sensitivity Analysis 76
3.8 Third Metallic Beam 78

4 Prognosis of a Composite Beam-Mass System 80
4.1 Experimental Setup 81
4.2 Experimental Results on the Composite Beam-Mass System 81
4.2.1 Frequency-response 81
4.2.2 Spectral Analysis of Excitation and Response Data 83
4.3 Representative Model 87
4.4 System Identification 96
4.4.1 Sensitivity Analysis 98

5 Cracks Localization by Fiber Optics Sensors 101
5.1 Experimental Setup 101
5.2 Damage Effects on Beam's Response 106
5.2.1 Power Spectra of the Undamaged Beam Response 110

5.2.2 Power Spectra of the Damaged Beam Response 110
5.2.3 Excitation-Response Linear Coherence of the Undamaged Beam . . . 118
5.2.4 Excitation-Response Linear Coherence of the Damaged Beam 120
5.2.5 Identification of Nonlinear Response-Excitation Dynamics of the Undamaged Beam 127
5.2.6 Identification of Nonlinear Response-Excitation Dynamics of the Damaged Beam 134
5.3 Crack Localization 142

6 Conclusions **151**

Bibliography **153**

List of Figures

2.1 A $10Hz$ sine wave is shown in the top and its power spectrum is in the bottom showing its frequency component at $10Hz$. 11

2.2 Time history of a signal containing white Gaussian noise in the top and its power spectrum in the bottom showing its two frequency components at $10Hz$ and $20Hz$. 12

2.3 Time series of two signals both with added white Gaussian noise. 13

2.4 The power spectra show two frequency components at $15Hz$ and $20Hz$ of the signal $x(t)$ and one frequency component at $15Hz$ of the signal $y(t)$. 14

2.5 Time history of a signal $x(t)$ sampled at a frequency $f_s = 512Hz$. 16

2.6 Power spectrum of the signal $x(t)$ showing its frequency components at $f_1 = 20Hz$, $f_2 = 15Hz$, $f_1 + f_2 = 35Hz$, and $f_1 - f_2 = 5Hz$. 16

2.7 Auto-bicoherence of the signal $x(t)$ which detects quadratic phase coupling among the frequency triples $(15Hz, 5Hz, 20Hz)$ and $(20Hz, 15Hz, 35Hz)$. . . 17

2.8 Time series of two signals $x(t)$ and $y(t)$ sampled at $512Hz$. 19

2.9 Signal $x(t)$ has one frequency component at $f_2 = 15Hz$. Signal $y(t)$ has three frequency components at $f_1 = 20Hz$, $f_1 + f_2 = 35Hz$, and $f_2 - f_1 = 5Hz$. . . 19

2.10 Auto-bispectra of both signals indicates there is no quadratic coupling among the frequency components within the signal itself. 20

2.11 Example where the fundamental is perfectly phase-coupled with its subharmonic. 21

3.1 Variations in the response amplitude of the beam-mass system as the excitation frequency Ω is swept down (Zavodney and Nayfeh (1989)). 24

3.2 Schematic of the cantilever beam carrying a lumped mass under study. 25
3.3 Experimental setup of the first metallic beam-mass system as mounted on a shaker. 37
3.4 The first mode natural frequency is numerically checked using the finite element model of the steel beam carrying a lumped mass. 38
3.5 Photograph of the steel beam-mass system which has been used for the experiments. 39
3.6 Variation of the steady-state response amplitude of the first metallic beam-mass system while the excitation frequency was swept near twice the natural frequency. 41
3.7 Time series of beam response (plot at the top, ϵ) and the corresponding excitation (plot at the bottom, $Volts$) over a 60-seconds time duration. 42
3.8 High resolution imaging of the beam after extended excitations showed a crack that has developed over more than 60% of the width of the beam (Z axis) and accross its thickness (Y axis). 43
3.9 Time histories of excitation and response in $State_1$ for three different measurements when the excitation frequency is set equal to (a) $24.417Hz$, (b) $24.414Hz$, and (c) $24.411Hz$, respectively. 46
3.10 Time histories of excitation and response in $State_2$ for three different measurements when the excitation frequency is set equal to (a) $24.372Hz$, (b) $24.367Hz$, and (c) $24.362Hz$, respectively. 47
3.11 Time histories of excitation and response in $State_3$ for three different measurements when the excitation frequency is set equal to (a) $24.335Hz$, (b) $24.319Hz$, and (c) $24.316Hz$, respectively. 48
3.12 Time histories of excitation and response in $State_4$ for three different measurements when the excitation frequency is set equal to (a) $24.246Hz$, (b) $24.237Hz$, and (c) $24.226Hz$, respectively. 49
3.13 Time histories of excitation and response in $State_5$ for three different measurements when the excitation frequency is set equal to (a) $24.189Hz$, (b) $24.181Hz$, and (c) $24.172Hz$, respectively. 50

3.14 Power spectra of excitation and response in $State_1$ for three different measurements when the excitation frequency is set equal to (a) $24.417Hz$, (b) $24.414Hz$, and (c) $24.411Hz$, respectively. 51
3.15 Power spectra of excitation and response in $State_2$ for three different measurements when the excitation frequency is set equal to (a) $24.372Hz$, (b) $24.367Hz$, and (c) $24.362Hz$, respectively. 52
3.16 Power spectra of excitation and response in $State_3$ for three different measurements when the excitation frequency is set equal to (a) $24.335Hz$, (b) $24.319Hz$, and (c) $24.316Hz$, respectively. 53
3.17 Power spectra of excitation and response in $State_4$ for three different measurements when the excitation frequency is set equal to (a) $24.246Hz$, (b) $24.237Hz$, and (c) $24.226Hz$, respectively. 54
3.18 Power spectra of excitation and response in $State_5$ for three different measurements when the excitation frequency is set equal to (a) $24.189Hz$, (b) $24.181Hz$, and (c) $24.172Hz$, respectively. 55
3.19 Cross-bicoherence $State_1$ for three different measurements when the excitation frequency is set equal to (a) $24.417Hz$, (b) $24.414Hz$, and (c) $24.411Hz$, respectively. 56
3.20 Cross-bicoherence $State_2$ for three different measurements when the excitation frequency is set equal to (a) $24.372Hz$, (b) $24.367Hz$, and (c) $24.362Hz$, respectively. 56
3.21 Cross-bicoherence $State_3$ for three different measurements when the excitation frequency is set equal to (a) $24.335Hz$, (b) $24.319Hz$, and (c) $24.316Hz$, respectively. 57
3.22 Cross-bicoherence $State_4$ for three different measurements when the excitation frequency is set equal to (a) $24.246Hz$, (b) $24.237Hz$, and (c) $24.226Hz$, respectively. 58
3.23 Cross-bicoherence $State_5$ for three different measurements when the excitation frequency is set equal to (a) $24.189Hz$, (b) $24.181Hz$, and (c) $24.172Hz$, respectively. 59

3.24 Variations of $f \cos 2\beta$ vs. a^2 used for identification of the effective nonlinearity coefficient α_e. 61
3.25 Variation of $f \sin 2\beta$ vs. a used for identification of linear and quadratic damping coefficients. 61
3.26 Variations of the third harmonic a_3 vs. the first harmonic a. 62
3.27 Validation of predicted response through comparison with the measured response for three different measurements of $State_1$ when the excitation frequency is set equal to (a) $24.417Hz$, (b) $24.414Hz$, and (c) $24.411Hz$, respectively. 63
3.28 Validation of predicted response through comparison with the measured response for three different measurements of $State_2$ for three different measurements when the excitation frequency is set equal to (a) $24.372Hz$, (b) $24.367Hz$, and (c) $24.362Hz$, respectively. 64
3.29 Validation of predicted response through comparison with the measured response for three different measurements of $State_3$ for three different measurements when the excitation frequency is set equal to (a) $24.335Hz$, (b) $24.319Hz$, and (c) $24.316Hz$, respectively. 64
3.30 Validation of predicted response through comparison with the measured response for three different measurements of $State_4$ for three different measurements when the excitation frequency is set equal to (a) $24.246Hz$, (b) $24.237Hz$, and (c) $24.226Hz$, respectively. 65
3.31 Validation of predicted response through comparison with the measured response for three different measurements of $State_5$ for three different measurements when the excitation frequency is set equal to (a) $24.189Hz$, (b) $24.181Hz$, and (c) $24.172Hz$, respectively. 65
3.32 Frequency-response plot of the second metallic beam. 66
3.33 Photograph of the crack in the second metallic beam. 67
3.34 Time histories of excitation and response in $State_1$ for three different measurements when the excitation frequency is set equal to (a) $24.091Hz$, (b) $24.074Hz$, and (c) $24.061Hz$, respectively. 69

3.35 Time histories of excitation and response in $State_2$ for three different measurements when the excitation frequency is set equal to (a) $23.961Hz$, (b) $23.955Hz$, and (c) $23.949Hz$, respectively. 70
3.36 Power spectra of excitation and response in $State_1$ for three different measurements when the excitation frequency is set equal to (a) $24.091Hz$, (b) $24.074Hz$, and (c) $24.061Hz$, respectively. 71
3.37 Power spectra of excitation and response in $State_2$ for three different measurements when the excitation frequency is set equal to (a) $23.961Hz$, (b) $23.955Hz$, and (c) $23.949Hz$, respectively. 72
3.38 Cross-bicoherence $State_1$ for three different measurements when the excitation frequency is set equal to (a) $24.091Hz$, (b) $24.074Hz$, and (c) $24.061Hz$, respectively. 73
3.39 Cross-bicoherence $State_2$ for three different measurements when the excitation frequency is set equal to (a) $23.961Hz$, (b) $23.955Hz$, and (c) $23.949Hz$, respectively. 73
3.40 Variations of $fcos2\beta$ vs. a^2 used for identification of the effective nonlinearity coefficient α_e for the second metallic beam. 74
3.41 Variations of $fsin2\beta$ vs. a used for identification of linear and quadratic damping coefficients for the second metallic beam. 75
3.42 Variation of the third harmonic a_3 vs. first harmonic a for the second metallic beam. 76
3.43 Validation of three measurements in $State_1$ for three different measurements when the excitation frequency is set equal to (a) $24.091Hz$, (b) $24.074Hz$, and (c) $24.061Hz$, respectively. 77
3.44 Validation of three measurements in $State_2$ for three different measurements when the excitation frequency is set equal to (a) $23.961Hz$, (b) $23.955Hz$, and (c) $23.949Hz$, respectively. 77
3.45 These frequency response curves were obtained in order to check whether or not the beam-mass system starts its damaging process before the very first jump occurs. 79

4.1 Photograph of the experimental setup representing the composite beam carrying a steel lumped mass as mounted on a shaker. 82
4.2 Frequency response curves quantify the change in the natural frequency due to damage initiation and further propagation. 84
4.3 Top: Time series of the composite beam response variation when the excitation frequency Ω is set equal to 23.9943 Hz, exactly twice the system's natural frequency. Bottom: Time series of the constant amplitude excitation. 85
4.4 Photograph of the crack which has clearly propagated across the whole thickness and width, even without reaching the permanent failure of the structure. 86
4.5 Time histories of excitation and response in $State_1$ for three different measurements when the excitation frequency is set equal to (a) $24.069Hz$, (b) $24.047Hz$, and (c) $24.017Hz$, respectively. 88
4.6 Time histories of excitation and response in $State_2$ for three different measurements when the excitation frequency is set equal to (a) $23.985Hz$, (b) $23.967Hz$, and (c) $23.952Hz$, respectively. 89
4.7 Time histories of excitation and response in $State_3$ for three different measurements when the excitation frequency is set equal to (a) $23.935Hz$, (b) $23.924Hz$, and (c) $23.918Hz$, respectively. 90
4.8 Power spectrum of excitation and response in $State_1$ for three different measurements when the excitation frequency is set equal to (a) $24.069Hz$, (b) $24.047Hz$, and (c) $24.017Hz$, respectively. 91
4.9 Power spectrum of excitation and response in $State_2$ for three different measurements when the excitation frequency is set equal to (a) $23.985Hz$, (b) $23.967Hz$, and (c) $23.952Hz$, respectively. 92
4.10 Power spectrum of excitation and response in $State_3$ for three different measurements when the excitation frequency is set equal to (a) $23.935Hz$, (b) $23.924Hz$, and (c) $23.918Hz$, respectively. 93
4.11 Cross-bicoherence $State_1$ for three different measurements when the excitation frequency is set equal to (a) $24.069Hz$, (b) $24.047Hz$, and (c) $24.017Hz$, respectively. Contour levels are set to [0.98 0.99]. 94

4.12 Cross-bicoherence $State_2$ for three different measurements when the excitation frequency is set equal to (a) $23.985Hz$, (b) $23.967Hz$, and (c) $23.952Hz$, respectively. Contour levels are set to [0.98 0.99]. 94
4.13 Cross-bicoherence $State_3$ for three different measurements when the excitation frequency is set equal to (a) $23.935Hz$, (b) $23.924Hz$, and (c) $23.918Hz$, respectively. Contour levels are set to [0.98 0.99]. 95
4.14 Variation of $fcos2\beta$ vs. a^2 used for identification of the effective nonlinearity coefficient α_e. 99
4.15 Variation of $fsin2\beta$ vs. a used for identification of linear and quadratic damping coefficients, ζ_1 and ζ_2. 99
4.16 Variations of third harmonic a_3 vs. first harmonic a. 100

5.1 Photograph of the experimental setup representing the beam-mass system as mounted on a shaker. 103
5.2 Schematic of the experimental setup, including composite beam geometry and locations of the strain gage and gratings of the fiber optic. 104
5.3 Locations, away from the mounting plate, of the seven cracks produced through the tensile force. 106
5.4 Photograph of the crack located *42.746 mm* away from the mounting plate. . 107
5.5 Time series showing the jump in the response of the undamaged composite beam when the excitation frequency is set to 16.545 Hz, which is near twice the natural frequency, 8.273 Hz. 107
5.6 Time series showing jump and variations in the response of the damaged composite beam when the excitation frequency is set to 15.945 Hz, which is twice the natural frequency of the first-mode, 7.974 Hz. 108
5.7 Frequency response curves for the *Undamaged* and *Damaged* beam-mass systems. 109
5.8 Power spectra of the strain measurements before damage as captured by (a) the lowest end, (b) the centerline, and (c) the highest end of fiber grating 2. . 111

5.9 Power spectra of the strain measurements before damage as captured by (a) the lowest end, (b) the centerline, and (c) the highest end of fiber grating 3. . 111
5.10 Power spectra of the strain measurements before damage as captured by (a) the lowest end, (b) the centerline, and (c) the highest end of fiber grating 4. . 111
5.11 Power spectra of the strain measurements before damage as captured by (a) the lowest end, (b) the centerline, and (c) the highest end of fiber grating 5. . 112
5.12 Power spectra of the strain measurements before damage as captured by (a) the lowest end, (b) the centerline, and (c) the highest end of fiber grating 6. . 112
5.13 Power spectra of the strain measurements before damage as captured by (a) the lowest end, (b) the centerline, and (c) the highest end of fiber grating 7. . 112
5.14 Power spectra of the strain measurements before damage as captured by (a) the lowest end, (b) the centerline, and (c) the highest end of fiber grating 8. . 113
5.15 Power spectra of the strain measurements before damage as captured by (a) the lowest end, (b) the centerline, and (c) the highest end of fiber grating 9. . 113
5.16 Power spectra of the strain measurements before damage as captured by (a) the lowest end, (b) the centerline, and (c) the highest end of fiber grating 10. 113
5.17 Power spectrum of the strain measurements captured before damage by the strain gage which is co-located on the opposite side of the beam with the sixth grating. 114
5.18 Power spectra of the strain measurements after damage as captured by (a) the lowest end, (b) the centerline, and (c) the highest end of fiber grating 2. . . . 115
5.19 Power spectra of the strain measurements after damage as captured by (a) the lowest end, (b) the centerline, and (c) the highest end of fiber grating 3. . . . 116
5.20 Power spectra of the strain measurements after damage as captured by (a) the lowest end, (b) the centerline, and (c) the highest end of fiber grating 4. . . . 116
5.21 Power spectra of the strain measurements after damage as captured by (a) the lowest end, (b) the centerline, and (c) the highest end of fiber grating 5. . . . 116
5.22 Power spectra of the strain measurements after damage as captured by (a) the lowest end, (b) the centerline, and (c) the highest end of fiber grating 6. . . . 117

5.23 Power spectra of the strain measurements after damage as captured by (a) the lowest end, (b) the centerline, and (c) the highest end of fiber grating 7. . . . 117
5.24 Power spectra of the strain measurements after damage as captured by (a) the lowest end, (b) the centerline, and (c) the highest end of fiber grating 8. . . . 118
5.25 Power spectra of the strain measurements after damage as captured by (a) the lowest end, (b) the centerline, and (c) the highest end of fiber grating 9. . . . 118
5.26 Power spectra of the strain measurements after damage as captured by (a) the lowest end, (b) the centerline, and (c) the highest end of fiber grating 10. . . 119
5.27 Power spectrum of the strain measurements captured after damage by the strain gage which is co-located on the opposite side of the beam with the sixth grating. 119
5.28 Linear coherence of the strain measurements before damage as captured by (a) the lowest end, (b) the centerline, and (c) the highest end of fiber grating 2. . 120
5.29 Linear coherence of the strain measurements before damage as captured by (a) the lowest end, (b) the centerline, and (c) the highest end of fiber grating 3. . 121
5.30 Linear coherence of the strain measurements before damage as captured by (a) the lowest end, (b) the centerline, and (c) the highest end of fiber grating 4. . 121
5.31 Linear coherence of the strain measurements before damage as captured by (a) the lowest end, (b) the centerline, and (c) the highest end of fiber grating 5. . 121
5.32 Linear coherence of the strain measurements before damage as captured by (a) the lowest end, (b) the centerline, and (c) the highest end of fiber grating 6. . 122
5.33 Linear coherence of the strain measurements before damage as captured by (a) the lowest end, (b) the centerline, and (c) the highest end of fiber grating 7. . 122
5.34 Linear coherence of the strain measurements before damage as captured by (a) the lowest end, (b) the centerline, and (c) the highest end of fiber grating 8. . 122
5.35 Linear coherence of the strain measurements before damage as captured by (a) the lowest end, (b) the centerline, and (c) the highest end of fiber grating 9. . 123
5.36 Linear coherence of the strain measurements before damage as captured by (a) the lowest end, (b) the centerline, and (c) the highest end of fiber grating 10. 123

5.37 Linear coherence of the strain measurements captured before damage by the strain gage which is co-located on the opposite side of the beam with the sixth grating. 124
5.38 Linear coherence of the strain measurements after damage as captured by (a) the lowest end, (b) the centerline, and (c) the highest end of fiber grating 2. . 125
5.39 Linear coherence of the strain measurements after damage as captured by (a) the lowest end, (b) the centerline, and (c) the highest end of fiber grating 3. . 125
5.40 Linear coherence of the strain measurements after damage as captured by (a) the lowest end, (b) the centerline, and (c) the highest end of fiber grating 4. . 125
5.41 Linear coherence of the strain measurements after damage as captured by (a) the lowest end, (b) the centerline, and (c) the highest end of fiber grating 5. . 126
5.42 Linear coherence of the strain measurements after damage as captured by (a) the lowest end, (b) the centerline, and (c) the highest end of fiber grating 6. . 126
5.43 Linear coherence of the strain measurements after damage as captured by (a) the lowest end, (b) the centerline, and (c) the highest end of fiber grating 7. . 127
5.44 Linear coherence of the strain measurements after damage as captured by (a) the lowest end, (b) the centerline, and (c) the highest end of fiber grating 8. . 127
5.45 Linear coherence of the strain measurements after damage as captured by (a) the lowest end, (b) the centerline, and (c) the highest end of fiber grating 9. . 128
5.46 Linear coherence of the strain measurements after damage as captured by (a) the lowest end, (b) the centerline, and (c) the highest end of fiber grating 10. 128
5.47 Linear coherence of the strain measurements captured after damage by the strain gage which is co-located on the opposite side of the beam with the sixth grating. 129
5.48 Cross-bicoherence between excitation and response at (a) the lowest end, (b) the centerline, and (c) the highest end of the fiber grating 2 before damage. Contour levels [0.7, 0.8]. 130
5.49 Cross-bicoherence between excitation and response at (a) the lowest end, (b) the centerline, and (c) the highest end of the fiber grating 3 before damage. Contour levels [0.7, 0.8]. 131

5.50 Cross-bicoherence between excitation and response at (a) the lowest end, (b) the centerline, and (c) the highest end of the fiber grating 4 before damage. Contour levels [0.7, 0.8]. 131
5.51 Cross-bicoherence between excitation and response at (a) the lowest end, (b) the centerline, and (c) the highest end of the fiber grating 5 before damage. Contour levels [0.7, 0.8]. 132
5.52 Cross-bicoherence between excitation and response at (a) the lowest end, (b) the centerline, and (c) the highest end of the fiber grating 6 before damage. Contour levels [0.7, 0.8]. 132
5.53 Cross-bicoherence between excitation and response at (a) the lowest end, (b) the centerline, and (c) the highest end of the fiber grating 7 before damage. Contour levels [0.7, 0.8]. 133
5.54 Cross-bicoherence between excitation and response at (a) the lowest end, (b) the centerline, and (c) the highest end of the fiber grating 8 before damage. Contour levels [0.7, 0.8]. 134
5.55 Cross-bicoherence between excitation and response at (a) the lowest end, (b) the centerline, and (c) the highest end of the fiber grating 9 before damage. Contour levels [0.7, 0.8]. 135
5.56 Cross-bicoherence between excitation and response at (a) the lowest end, (b) the centerline, and (c) the highest end of the fiber grating 10 before damage. Contour levels [0.7, 0.8]. 135
5.57 Cross-bicoherence between excitation and response from strain gage measurement before damage. Contour levels [0.9, 0.99]. 136
5.58 Cross-bicoherence between excitation and response at (a) the lowest end, (b) the centerline, and (c) the highest end of the fiber grating 2 after damage. Contour levels [0.8, 0.9]. 137
5.59 Cross-bicoherence between excitation and response at (a) the lowest end, (b) the centerline, and (c) the highest end of the fiber grating 3 after damage. Contour levels [0.8, 0.9]. 137

5.60 Cross-bicoherence between excitation and response at (a) the lowest end, (b) the centerline, and (c) the highest end of the fiber grating 4 after damage. Contour levels [0.8, 0.9]. 138
5.61 Cross-bicoherence between excitation and response at (a) the lowest end, (b) the centerline, and (c) the highest end of the fiber grating 5 after damage. Contour levels [0.8, 0.9]. 138
5.62 Cross-bicoherence between excitation and response at (a) the lowest end, (b) the centerline, and (c) the highest end of the fiber grating 6 after damage. Contour levels [0.7, 0.8]. 139
5.63 Cross-bicoherence between excitation and response at (a) the lowest end, (b) the centerline, and (c) the highest end of the fiber grating 7 after damage. Contour levels [0.6, 0.7]. 139
5.64 Cross-bicoherence between excitation and response at (a) the lowest end, (b) the centerline, and (c) the highest end of the fiber grating 8 after damage. Contour levels [0.7, 0.8]. 140
5.65 Cross-bicoherence between excitation and response at (a) the lowest end, (b) the centerline, and (c) the highest end of the fiber grating 9 after damage. Contour levels [0.6, 0.7]. 140
5.66 Cross-bicoherence between excitation and response at (a) the lowest end, (b) the centerline, and (c) the highest end of the fiber grating 10 after damage. Contour levels [0.2, 0.3]. 141
5.67 Cross-bicoherence between excitation and response from strain gage measurement after damage. Contour levels [0.9, 0.99]. 141
5.68 Comparison between undamaged and damaged beam of the peaks of the power spectrum at the fundamental frequency for (a) the lowest end, (b) the centerline, and (c) the highest end of each grating. 143
5.69 Ratio of the peak of the power spectrum at the fundamental frequency for (a) the lowest end, (b) the centerline, and (c) the highest end of each grating. . . 143
5.70 Ratio of the peak of the power spectrum at the fundamental frequency averaged over (a) the lowest end, (b) the centerline, and (c) the highest end of each grating. 144

5.71 Comparison between undamaged and damaged beam of the linear coherence computed between excitation and response evaluated at the fundamental frequency for (a) the lowest end, (b) the centerline, and (c) the highest end of each grating. 145
5.72 Comparison between undamaged and damaged beam of the linear coherence computed between excitation and response evaluated at the excitation frequency for (a) the lowest end, (b) the centerline, and (c) the highest end of each grating. 146
5.73 Comparison between undamaged and damaged beam of the cross-bicoherence levels at the frequencies triple $(f_{resp}, f_{resp}, f_{exc})$ of (a) the lowest end, (b) the centerline, and (c) the highest end. 146
5.74 Comparison between undamaged and damaged beam of the cross-bicoherence levels at the frequencies triple $(f_{resp}, f_{resp}, f_{exc})$ averaged over (a) the lowest end, (b) the centerline, and (c) the highest end. 147
5.75 Comparison between undamaged and damaged beam of the cross-bicoherence levels at the frequencies triple $(3f_{resp}, f_{resp}, f_{exc})$ of (a) the lowest end, (b) the centerline, and (c) the highest end. 148
5.76 Comparison between undamaged and damaged beam of the cross-bicoherence levels at the frequencies triple $(3f_{resp}, f_{resp}, f_{exc})$ averaged over (a) the lowest end, (b) the centerline, and (c) the highest end. 149
5.77 Comparison between undamaged and damaged beam of the cross-bicoherence levels at the frequencies triple $(4f_{resp}, f_{exc}, f_{exc})$ of (a) the lowest end, (b) the centerline, and (c) the highest end. 150
5.78 Comparison between undamaged and damaged beam of the cross-bicoherence levels at the frequencies triple $(4f_{resp}, f_{exc}, f_{exc})$ averaged over (a) the lowest end, (b) the centerline, and (c) the highest end. 150

List of Tables

3.1 Phase and bicoherence for the first metallic beam. 59

3.2 Identified values of ω, f, α_e, ζ_1, and ζ_2. 60

3.3 Percentage variation of ω, α_e, ζ_1, and ζ_2. 63

3.4 Phase and bicoherence values for the second metallic beam. 68

3.5 Identified values of ω, f, α_e, ζ_1, and ζ_2 for the second metallic beam. 74

3.6 Percentage variation of ω, α_e, ζ_1, and ζ_2 for the second metallic beam. 77

4.1 Phase and bicoherence values for the composite beam. 97

4.2 Identified values of ω, f, α_e, ζ_1, and ζ_2 for the composite beam. 97

4.3 Percentage variation of ω, α_e, ζ_1, and ζ_2. 100

Chapter 1

Introduction

1.1 Issues, Needs and Opportunities in SHM

Large multi-disciplinary engineered systems (e.g., aerospace vehicles, ships, submarines, offshore structures, high-rise buildings, and long-span bridges) are usually subjected to varying loading conditions and must survive operating conditions in a wide range of environments and over extended periods. These systems are usually intricate assemblies of thousands of components and unique materials. The combination of high static, impulsive and dynamic loads across a wide range of frequencies and geometric and material disparities cause variations in the state of damage of such systems over their lifetimes. As such, continuous diagnosis of this state through structural health monitoring (SHM) and estimation of the remaining future useful life (prognosis) have developed into emerging research fields that aim at answering whether a system's performance or operation is acceptable during different stages of damage accumulation.

In the case of aerospace systems, their fatigue design includes fatigue life curves that characterize the behavior of the materials and components. Yet, the fatigue life of identical components may undergo different fatigue behaviors because of slight variations in the material properties or in the loading cycle or spectra. Currently, aircraft are monitored by visual inspection that is supported by nondestructive testing (NDT) methods including ultrasonics and eddy current (Park and Inman (2007)) and that is performed at prescribed intervals. The monitoring could also include dismantling and reassembly of the aircraft structure to

reach a specific component of interest (Boller and Buderath (2007)). Visual inspection is also the main method used in the monitoring of civil structures, especially bridges. These inspections could be labor-intensive and dependent upon the inspectors judgment. Other non-destructive evaluation (NDE) technologies including acoustic emission (Bramban et al. (2005)), ultrasonic testing (Cawley and Simonetti (2005)), and radar tomography (Davidson and Chase (1998)) have also been used to monitor civil structures.

Recent advancements in the design of low-cost sensors, wireless communications and data storage and analysis should prove to be very beneficial for the purpose of improving structural health monitoring and prognosis capabilities. Sensors such as optical fibers or piezoelectric elements can be integrated into structures. The combination of such sensors with wireless technologies would allow for placing them in hard-to-reach locations and for continuous monitoring and damage related variations in the structure's response to different excitations. This work aims at combining interrogative testing with system identification tools that are based on modern methods of nonlinear dynamics and higher-order spectral analysis to improve SHM and prognosis capabilities. As a prelude of the research presented in this dissertation, summaries of advancements made in sensing technologies and current data analysis procedures that have been proposed for use in structural health monitoring are presented next.

1.2 Sensor technology

1.2.1 Fiber optic sensors

Improvements made over the past decade in optical fiber technology have presented new opportunities for structural health monitoring. In comparison with other sensors, fiber optics sensors have a very high resolution, large bandwidth and multiplexing capability (Todd et al. (2007)). Thier weight is negligible, and they cannot be affected by electromagnetic noise (Todd et al. (2007)). Since damage initiation in structures is often at the material or geometric level and relatively small size, a small-gauge length sensing should prove to be very useful. The most used fiber optic sensors is the Fiber Bragg Grating sensor (FBG) because it meets the above requirements. Sensors based on FBG may interrogate length-scales in millimeters

range. This property allows them to be embedded in the material itself. Because damage initiation in structures happens locally over a small-length range and because FBGs can be embedded in the material, they present an opportunity to detect small length scale defects. Leng et al. (2005) have demonstrated that Fiber Bragg Grating sensors can be embedded in concrete materials in order to monitor successfully the change of strain with more sensitivity and from early stages of damage initiation to failure. Their compressive strain measurements on the surface of concrete cylinders by optical fibers sensors showed excellent agreement with measurements from conventional strain gages.

From the point of view of large-scale applications, the work by Jiang and Liu (2005) is an application of particular interest. They installed FBG load cells on the Qingchuan Bridge in Wuhan (China). The objective of using FBG load cells resides in the real-time tension monitoring during the replacement of the bridge bowstring and long-term monitoring during their lifetime. Their results showed that FBG load cells have several advantages in comparison with traditional existing technology, namely, longer-term usability and more feasibility in monitoring the status of cables tension in long-span bridges.

1.3 Analysis procedures for structural health monitoring

1.3.1 Inverse methods

Inverse methods for damage identification and location combine a model of the structure with measured data. The model is usually based on finite element analysis and measured data are usually acceleration and force data. Inverse methods can be divided into sensitivity- and direct-type methods. The first needs a parametric model of the structure and is based on the minimization of the error between measurements and model predictions of the model. Sensitivity-based methods are characterized by different types of physical parameters related to the model of the damage and of the structure. These parameters are identified by the combination of numerical models with experimental measurements. The correct set of physical parameters has to be chosen in order to guarantee feasibility of the model which is supposed to capture the dynamics of the structure. Thus, the problem with damage detection here is related to the difficulty in quantifying parameters variations due to damage or to the inad-

equacy of the numeral model. Direct-based methods change and adapt mass and stiffness matrices in order to match with measured data. These methods have several disadvantages related to the fact that forcing the model to reproduce the measured data doesn't guarantee accuracy in the measurement of mode shapes because the matrices may not be positive definite (Friswell (2007)).

Bahlous et al. (2007) applied a statistical-based inverse method for damage detection, localization and quantification of an 8-DoF beam modeled using finite elements. Vibration data were used as a signature of the structure's damage status. Physical and geometrical properties were computed from the vibration data in the reference undamaged state and compared to those estimated from the current damaged state. Sensitivity and rejection statistical tests were then performed on residual quantities computed between reference and updated finite element model to assess the presence and location of damage.

1.3.2 Vibration-based data: time-series methods

Vibration-based methods don't require physical or finite element models because they are based on the performance of the structure. The most important part of the analysis is the definition of the nominal state which corresponds to the healthy structure and a certain number of different failure modes and magnitudes. These techniques imply periodic inspections and diagnosis. Time-series methods include fault detection and fault estimation (Fassois and Sakellariou (2007)). At first the acquired data are analyzed in order to estimate a characteristic quantity related to the failure status of the system and then it is compared to the predefined failure mode through a statistical decision making technique based on hypothesis testing procedures. In this way, it is possible to distinguish whether the structure is healthy or not and determine the type of failure mode. Fault estimation defines, instead, the probabilities related to the risk of false alarm and missed fault. Time-series fault detection and identification methods can be divided in non-parametric and parametric methods. Non-parametric methods are based on power spectral density (PSD), frequency-response function (FRF), and coherence-based methods. Parametric methods are classified into parameter-based methods, residual-based methods, and functional model-based methods. The residual-based methods include residual variance, residual uncorrelatedness, and likelihood function.

Nair and Kiremidjian (2005) developed a time series damage diagnosis algorithm that is based on Gaussian mixture models whereby the dynamic properties of a vibrating structure are widely related to its integrity. Damage is then detected by comparing the vibration time series of the undamaged structure to those of the damaged structure. The developed algorithm, using appropriate sensors, starts from the measurement of vibration or strain data. This data is selected as a reference signal for the undamaged structure. The measured reference signal is then modeled using Gaussian mixture techniques and a set of feature coefficients are extracted from them. At this point, the difference between a newly measured actual signal and the predicted time series, constructed using the features computed on the reference signal through the Gaussian mixture model, is calculated and constitutes the residual error. This is also called damage-sensitive feature. If the residual error is large, it means that damage occurred in the structure. The signal, produced using the prediction model and based on the reference signal acquired from the undamaged structure, is not able to reproduce the new time series measured from the damaged structure. This method has been successfully validated on the ASCE Benchmark Structure.

1.3.3 Time-frequency and time-scale analysis methods

Most damage detection methods are based on Fourier analysis for signal processing techniques. Spectral quantities yield useful information about the frequency and modal content of a signal which is associated to the health state of the structure under consideration. Yet, this information may be subjected to variations in time because the forcing could be time-varying. From this point of view time-variant analyses need to be performed. Two different approaches are mostly used for this purpose. These are time-frequency and time-scale analysis methods.

When the spectral content of a signal changes in time, it's not possible to accurately describe its properties neither in time nor in frequency domain because the Fourier Transform (FT) fails to show how and when the frequency content of the signal changes over time. There are mainly three methods which can accomplish this task. The Short-Time Fourier Transform (STFT) is a Fourier related transform that determines the frequency and phase content of a local section (window) of the signal. The resolution is limited by the size of the window

that is used in the analysis. The Wigner-Ville Distribution (WVD) overcomes this limit increasing the resolution by considering the FT not of the signal but of its correlation function. The Pseudo-Wigner-Ville Distribution (PWVD) and the Choi-Williams Distribution (CWD) adopts different types of windowing techniques to the Wigner-Ville Distribution.

Time-scale analyses are based on the wavelet transform. The main advantage of the wavelet transform is that it captures not only information of the frequency content of the signal, by examining it at different scales, but also temporal information yielding the times at which these frequencies occur. Wavelet transform can be classified as continuous and discrete. Continuous wavelet transforms are usually used for time-frequency analysis and discrete wavelet are better applied to a discrete for data decomposition, preconditioning, and data compression (Staszewski and Robertson (2005)).

1.3.4 Vibration and wave propagation data as diagnosis for SHM

Because the presence of damage changes the dynamics of the structure, it is important to detect the location and the nature of the damage to guarantee safety requirements and to meet design specifications. Ultrasonic non destructive evaluations methods and vibration-based techniques have been used to monitor in real-time the structural integrity of structures. These methods are only capable of monitoring the global structure and the change in the modal parameters due to a small defect is too small to be detected with good reliability. Elastic waves are instead very sensitive to the presence of any kind of small local defects along their propagation path. The limit of these methods based on ultrasound technology is that they are strongly dependant on environmental variations and noise presence. A recently proposed damage identification technique(Mal et al. (2007)) combines low-frequency sensors to measure the structure global response with high-frequency ultrasonic sensors positioned in critical locations to capture local response of the structure. Vibrations and wave propagations effects are captured in damage and undamaged plates. A damage index is then defined based on damage level and the vibrational structural response for that damage level and location and set equal to zero for the undamaged case. In the same way, the damage index is defined for the same structure in response to wave propagation effects. Two types of defects are analyzed: internal delamination caused by impact loads and holes drilled across the thickness of the

plate. These two types of defects modify the elastic wave characteristics, and the differences with the respect to the undamaged structure are compared. This technique requires, however, more laboratory tests and theoretical modeling for the final implementation in a real structure and the combination with a wireless network of miniaturized embedded sensors.

Salvino et al. (2005) developed a method using time-frequency response and wave propagation data. The experimental model used in their work consists of a composite plate where damage is introduced in the form of delamination. Wave propagation properties change as they interact with delaminations. A set of sensors is used to monitor changes in the wave propagation. Time series of structural response are collected from the experimental model for both the undamaged and damaged states. Signals of waves propagating in time domain are examined using time-frequency analyses and their instantaneous phases are computed as damage detection method as they are related to the presence or not of delamination.

1.4 Objective and Approach

The ultimate goal of this effort is to provide tools that can be used to assess damage in different systems and over different stages of their lifetimes. In this work, we show the advantages of setting up interrogative experimental procedures using nonlinear system identification tools to achieve this goal. The procedure is based on exploiting physical behavior of the system. The tools make use of modern methods of nonlinear dynamics and state-of-the-art higher order spectral analysis.

The organization of this thesis is as follows. In Chapter 2, a description of nonlinear time-series analysis and higher order spectral statistics is presented. These tools are widely used in this work for identification of nonlinearities by exploiting phase couplings of frequency components. A hierarchy of spectral moments is defined and discussed in terms of estimating power and linear and nonlinear couplings distribution among frequency components in one signal or between signals. Special emphasis is given to bispectra and bicoherence since they are extremely useful to identify phase relationships among frequency components of signals as needed in the nonlinear system identification procedure used herein.

In Chapter 3, a novel damage prognosis technique is presented. This technique is based

on nonlinear system identification. It combines modern methods of nonlinear dynamics with first and higher order spectral moments. The chapter starts with the development of a parametric model for the nonlinear response of a metallic beam carrying a lumped mass under forced excitation. The governing differential equation is analitically derived and perturbation methods are used to determine an analytical approximate solution. The chapter continues with a description of the experimental setup based on the previously presented analytical model. The parametric system identification technique is then explained in detail and is applied to signals of the beam response as damage is developed. Sensitivities of physical parameters to damage initiation and progression are then established. As such, variations in parameters representing natural frequency, damping and effective nonlinearities with damage are assessed. The representative model and identified coefficients are validated through comparison of measured and predicted responses. The repeatibility of this technique has been successfully checked and validated.

In Chapter 4, the nonlinear system identification procedure for the purpose of damage prognosis is implemented on a composite beam carrying a steel lumped mass. The same experimental procedure and identification technique as described in the previous chapter, is used here. Differences in the response behavior of the metal and composite beams are discussed. Physical parameters appearing in the representative model are estimated through the whole stages of damage initiation and progression.

In Chapter 5, the possibility of using fiber optics technology for damage localization is assessed. The model used in the experiments consists of a slender composite beam carrying a steel lumped mass which is equipped with strain gage and Fiber Bragg Grating sensors. The global measurement from the strain gage are compared with the local measurements from the optical fiber. Spectral moments and quantities obtained from fiber optic strain measurements are evaluated near and away from cracks to assess the relation between these moments and cracks. The conclusions of this work are summarized in Chapter 6 and the bibliography follows.

Chapter 2

Digital Time Series Analysis

In this chapter, a summary of nonlinear digital time-series analysis and higher order spectral statistics is presented. These tools are widely used for quadratic and cubic nonlinearities detection by exploiting phase couplings of frequency components. First, Fourier analysis and first order spectral moments are presented as estimates of the power distribution among all the frequency components of a signal (Hajj et al. (1993)). Then, higher order spectral moments are defined. Their usefulness, as efficient tools for the identification of nonlinear dynamics and coupling is detailed.

2.1 Fourier Analysis Tools

2.1.1 Continuous and Discrete Fourier Transform

The Fourier transform $X(f)$ for a continuous stochatic process $x(t)$ is defined as

$$X(f) = \int_{-\infty}^{\infty} x(t) e^{-i2\pi ft} dt \tag{2.1}$$

It is used to decompose the generic signal $x(t)$ in a summation of frequency components that have different amplitudes and phases. The inverse Fourier transform is defined as

$$x(t) = \frac{1}{2\pi} \int_{-\infty}^{\infty} X(f) e^{i2\pi ft} dt \tag{2.2}$$

and is used to convert the complex-valued function $X(f)$ defined in the frequency domain back to the time domain where, $x(t)$ as a real-valued function, is defined. The discrete

Fourier transform establishes a relationship between two finite complex-valued series made of N values. Given the series

$$x_l, \text{ for } l = 0, 1, ..., \text{N-1} \tag{2.3}$$

its discrete Fourier transform is the series

$$X_k, \text{ for } k = 0, 1, ..., \text{N-1} \tag{2.4}$$

defined as

$$X_k = \mathcal{F}_d(x_l) = \sum_{l=0}^{N-1} x_j e^{-i\frac{2\pi}{N}kl}, \text{ for } k = 0, 1, ..., \text{N-1} \tag{2.5}$$

and the inverse discrete Fourier transform is

$$Y_l = \mathcal{F}_d^{-1} = (X_k) \sum_{k=0}^{N-1} X_k e^{+i\frac{2\pi}{N}kl}, \text{ for } l = 0, 1, ..., \text{N-1} \tag{2.6}$$

There exists a relationship between the discrete Fourier transform and the continuous Fourier transform which makes it possible to obtain one another.

2.1.2 Spectral Moments

Power Spectrum

Given a time series $x(t)$, the second order moment function, denoted as $m_{xx}(\tau)$, is the auto-correlation and is defined as

$$m_{xx}(\tau) = E[x(\tau)x(t+\tau)] \tag{2.7}$$

where $E[\cdot]$ is the expected value operator. The Fourier transform of the auto-correlation function results in the auto-power spectrum $P_{xx}(f)$ defined in the frequency domain. It is also known as second order moment spectrum and is defined as

$$P_{xx}(f) = \lim_{T\to\infty} \frac{1}{T} E[X_T(f)X_T^*(f)] \tag{2.8}$$

where $X_T(f)$ is the Fourier transform in the interval T and the superscript $*$ stands for complex conjugate operator. The power spectrum is used to estimate how the power content of the signal is divided among the frequency components that are contained in the signal. Its value at a certain frequency equals the square of the rms amplitude of this frequency

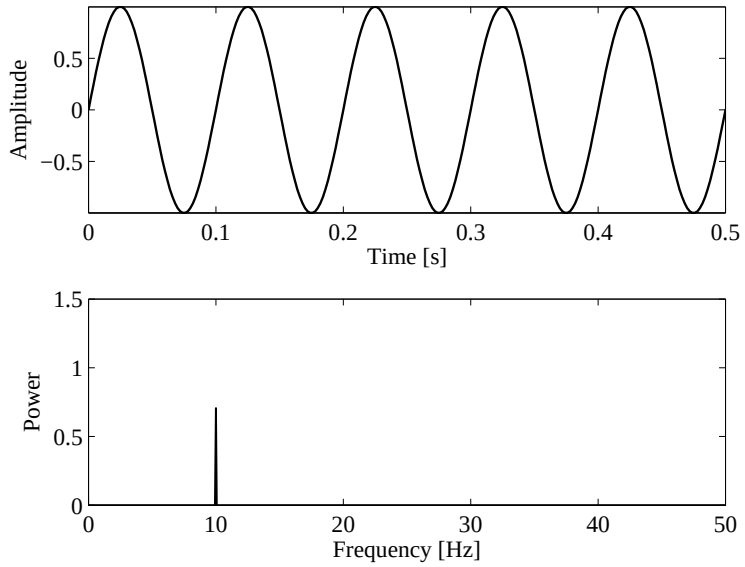

Figure 2.1: A $10Hz$ sine wave is shown in the top and its power spectrum is in the bottom showing its frequency component at $10Hz$.

component in the time-varying process. Thus, the power spectrum points out the frequency components of a signal, but because it is a real-valued function it keeps only the signal magnitude information and not the phase. For instance, a $10Hz$ sine wave is shown in the top of Figure 2.1 and its power spectrum is in the bottom. Another example is given by Figure 2.2 which shows, in the top, the time history of a signal in which white Gaussian noise is added. In the bottom of the same figure its power spectrum shows its two frequency components at $10Hz$ and $20Hz$.

Cross-Power Spectrum

In order to relate the frequency content of two different signals $x(t)$ and $y(t)$, one can define the cross-power spectrum

$$P_{yx}(f) = \lim_{T\to\infty} \frac{1}{T} E[X_T^*(f) Y_T(f)] \tag{2.9}$$

The cross-power spectrum, this is a complex-valued function and measures the phase difference between two signals $x(t)$ and $y(t)$ at the same frequency component. If this phase does

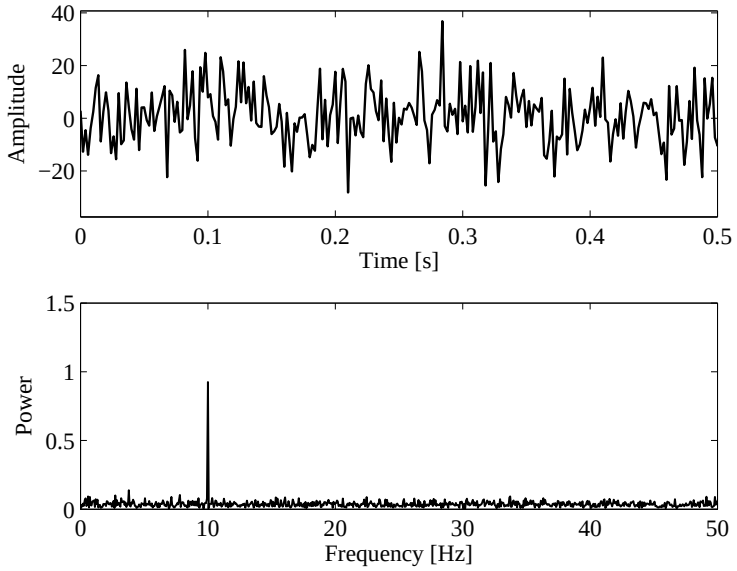

Figure 2.2: Time history of a signal containing white Gaussian noise in the top and its power spectrum in the bottom showing its two frequency components at $10Hz$ and $20Hz$.

not have a large variance over many time records, the magnitude of the cross-power spectrum is large and its phase is a good estimate of the phase difference between two signals. Conversely, if the variance is large, then the estimate is not very accurate.

Linear Coherence

The linear coherence $\gamma^2_{yx}(f)$ is a normalized value of the cross-power spectrum and is a measure of the extent of linear coupling between two signals $x(t)$ and $y(t)$. It is defined as

$$\gamma^2_{yx}(f) = \lim_{T\to\infty} \frac{1}{T} \frac{|E[X^*_T(f)Y_T(f)]|^2}{E[X_T(f)X^*_T]E[Y_T(f)Y^*_T]} \tag{2.10}$$

Based on the Schwarz's inequality, this quantity ranges between 0 and 1, which means weak or strong phase coupling respectively between two different signals $x(t)$ and $y(t)$ at the frequency f. Figure 2.3 shows the time series of two signals both with white Gaussian noise. The one in the top contains two frequency components at $20Hz$ and $15Hz$, and the one in the bottom contains one frequency at $15Hz$ and one phase coupled at $15Hz$. Figure 2.4 shows the power spectra P_{xx} and P_{yy} of both signals and the linear coherence $\gamma^2_{yx}(f)$ which points out the

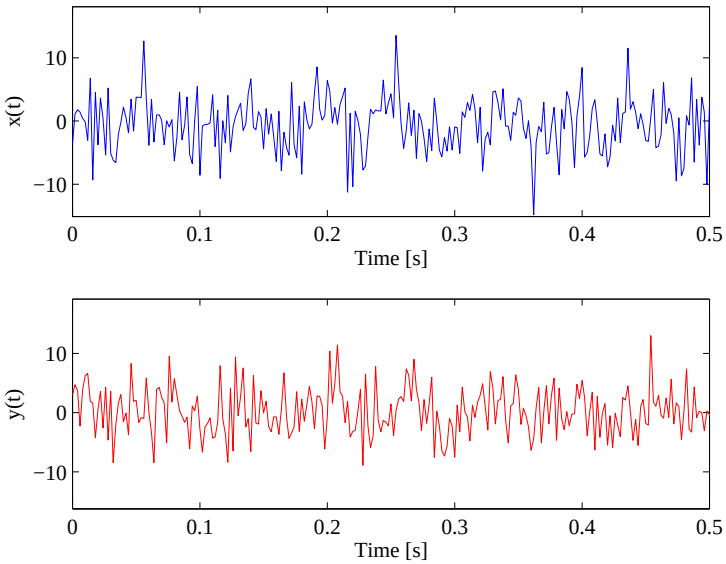

Figure 2.3: Time series of two signals both with added white Gaussian noise.

expected high linear coupling level at $15Hz$ capturing the phase relationships between $x(t)$ and $y(t)$.

Auto-Bispectrum

The auto-bispectrum is the third order moment spectrum and it is defined as

$$B_{xxx}(f_1, f_2) = \lim_{T\to\infty} \frac{1}{T} E[X_T(f_1 + f_2)X_T^*(f_1)X_T^*(f_2)] \tag{2.11}$$

It is a function of two frequency components, f_1 and f_2. The bispectrum is a complex-valued function. In general, this function has symmetry properties over the frequency domain, which allows to reduce this domain over which it needs to be calculated.

$$X^*(f) = X^*(-f) \tag{2.12}$$

$$b^2_{xxx}(f_1, f_2) = b^2_{xxx}(f_2, f_1) \tag{2.13}$$

For this reason, the computation of the bispectrum can be carried out by considering only positive values for frequency components at f_1, f_2, and $f_1 + f_2$. Because the bispectrum is a

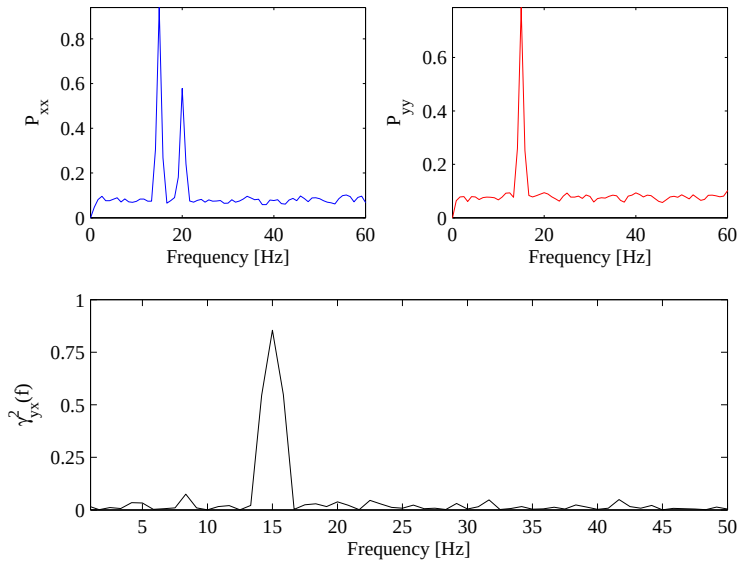

Figure 2.4: The power spectra show two frequency components at $15Hz$ and $20Hz$ of the signal $x(t)$ and one frequency component at $15Hz$ of the signal $y(t)$. The linear coherence $\gamma^2_{yx}(f)$ points out the presence of linear coupling of these two signals at $15Hz$.

complex-valued function and, by definition, requires the calculation of expected values, if the phase of $X_T(f_1+f_2)X_T^*(f_1)X_T^*(f_2)$, i.e. $\phi(f_1+f_2)-\phi(f_1)-\phi(f_2)$, has a large variance over many records, it has a small value. On the contrary, if this phase has a small variance, the bispectrum has a large value. This discussion suggests that quadratic coupling between f_1 and f_2 is indicated by the magnitude which is taken on by the bispectrum. In other words, this function is able to detect quadratic phase coupling among different frequency components of a signal because it relates two frequency components f_1 and f_2 to their sum f_1+f_2.

Auto-Bicoherence

The normalization of the auto-bispectrum yields the auto-bicoherence function which is defined as

$$b^2_{xxx}(f_1,f_2)=\lim_{T\to\infty}\frac{1}{T}\frac{|B_{xxx}(f_1,f_2)|^2}{E[|X_T(f_1+f_2)|^2]E[X_T(f_1)X_T^*(f_1)]E[X_T(f_2)X_T^*(f_2)]} \tag{2.14}$$

where $E[.]$ is used to denote the expected value. If the frequency components of a signal at f_1, f_2, and f_1+f_2 are characterized by partial quadratic phase coupling, the corresponding auto-bicoherence takes on a value which ranges between zero and one. This case is due to the presence of noise in the signal. A value of one indicates full quadratic phase coupling and a value of zero indicates no quadratic phase coupling between frequencies f_1, f_2, and f_1+f_2. Thus, the auto-bicoherence function is more useful than auto-bispectrum for assessing the degree of quadratic phase coupling. As for example, Figure 2.5 shows the time history of a signal $x(t)$ sampled at a frequency $f_s=512Hz$ which contains frequency components at $f_1=20Hz$, $f_2=15Hz$, $f_1+f_2=35Hz$, and $f_1-f_2=5Hz$. Figure 2.6 shows its power spectrum and points out these frequency components. Figure 2.7 shows the auto-bicoherence of this signal from which one can identify quadratic phase coupling among the frequency triples $(15Hz,5Hz,20Hz)$ and $(20Hz,15Hz,35Hz)$. The bicoherence is projected onto the f_1-f_2 plane and it is displayed as a contour plot where the color represents the value of the auto-bicoherence at a specific triple of frequency. The conditions on f_1 are limited by the Nyquist frequency f_N such that $0\le f_1\le f_N$, and f_2 such that $f_1\le f_1+f_2\le f_N$.

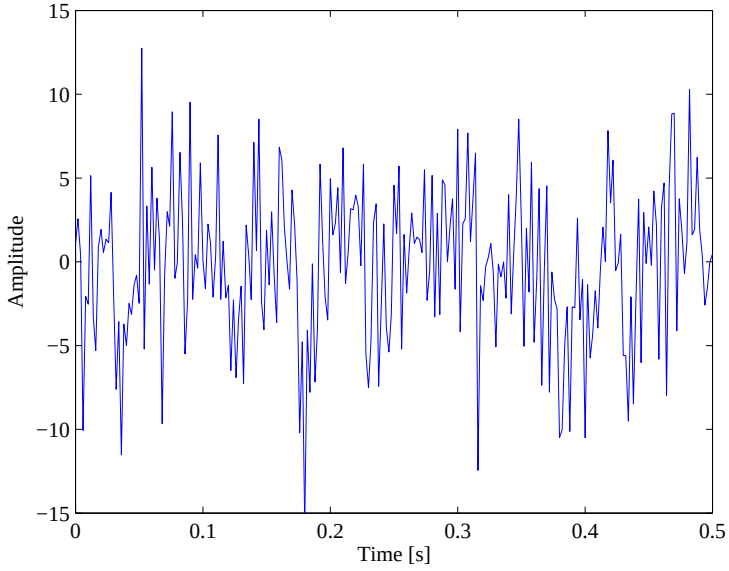

Figure 2.5: Time history of a signal $x(t)$ sampled at a frequency $f_s = 512Hz$.

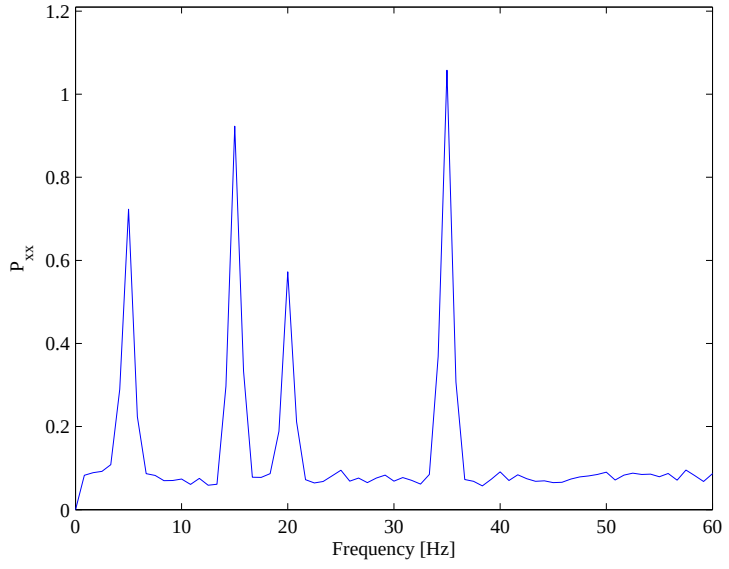

Figure 2.6: Power spectrum of the signal $x(t)$ showing its frequency components at $f_1 = 20Hz$, $f_2 = 15Hz$, $f_1 + f_2 = 35Hz$, and $f_1 - f_2 = 5Hz$.

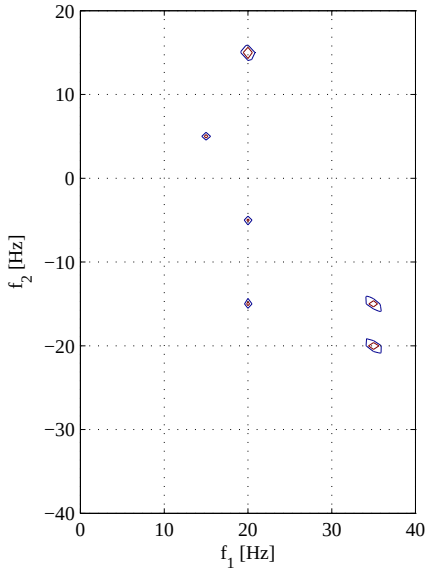

Figure 2.7: Auto-bicoherence of the signal $x(t)$ which detects quadratic phase coupling among the frequency triples $(15Hz, 5Hz, 20Hz)$ and $(20Hz, 15Hz, 35Hz)$.

Cross-Bispectrum

The cross-bispectrum is a quantity used to detect quadratic coupling between frequency components in two different signals $x(t)$ and $y(t)$. If $X(f)$ and $Y(f)$ are their Fourier transforms respectively, the cross-bispectrum is defined as

$$B_{yxx}(f_1, f_2) = \lim_{T\to\infty} \frac{1}{T} E[Y_T(f_1 + f_2) X_T^*(f_1) X_T^*(f_2)] \tag{2.15}$$

Since it is computed using three Fourier transforms, it is in general a complex-valued function. By averaging over many time records, the magnitude of the cross-bispectrum depends on how large is the level of quadratic phase coupling among triples of frequency components f_1, f_2, $f_1 + f_2$. If the phases are randomly distributed, the cross-bispectrum will average to a very small value. Otherwise a large value of the cross-bispectrum magnitude indicates high phase coupling among these frequency components between $X(f)$ and $Y(f)$.

Cross-Bicoherence

The same discussion introduced with the auto-bispectrum, applies to the cross-bispectrum in the normalization and definition of the cross-bicoherence. It is then defined as

$$b^2_{yxx}(f_1, f_2) = \lim_{T\to\infty} \frac{1}{T} \frac{|B_{yxx}(f_1, f_2)|^2}{E[|Y_T(f_1 + f_2)|^2]E[X_T(f_1)X^*_T(f_1)]E[X_T(f_2)X^*_T(f_2)]} \tag{2.16}$$

Also this quantity is boundend between zero and one, again based on the Schwarz's inequality. If we consider two signals $x(t)$ and $y(t)$ a strong quadratic phase coupling between frequency components at f_1, f_2 in $x(t)$ and the frequency component $f_1 + f_2$ in $y(t)$ yields a value equal to one, otherwise a value near zero indicates no coupling. Figure 2.8 shows the time series of two signals $x(t)$ and $y(t)$ sampled at $512Hz$. Figure 2.9 shows their power spectra and linear coherence γ^2_{xy}. Signal $x(t)$ has one frequency component at $f_2 = 15Hz$. Signal $y(t)$ has three frequency components at $f_1 = 20Hz$, $f_1+f_2 = 35Hz$, and $f_2-f_1 = 5Hz$. The linear coherence shows that these two signals are not linearly coupled. Using only power spectra and linear coherence, one is not able to detect any quadratic coupling between two independent and not correlated signals. Figure 2.10 shows that the auto-bispectra of both signals indicate no quadratic coupling among the frequency components within the signal itself. On the contrary, the cross-bicoherence computed between signals $x(t)$ and $y(t)$ indicates the frequency triples $(20Hz, -5Hz, 15Hz)$ and $(35Hz, -20Hz, 15Hz)$ are quadratically phase coupled.

2.2 Phase Relationship Between Fundamental and Subharmonic

Given the signal $x(t)$, characterized by a frequency equal to the fundamental f_0, and $y(t)$, characterised by a frequency equal to the subharmonic $\frac{f_0}{2}$, if these two signals are modeled as sine waves, then the phase difference between fundamental and subharmonic is computed by $\angle(f_0) - 2\angle(\frac{f_0}{2})$, or equivalently, the phase of the fundamental when the subharmonic is zero. This quantity is constant at any time t. Figure 2.11 shows the case of the fundamental f_0 perfectly coupled with its subharmonic $\frac{f_0}{2}$ such that their phase difference is equal to $\pi/2$ at time $t = 0$. Since the frequency of the fundamental is twice that of the subharmonic, the phase difference, $\angle(f_0) - 2\angle(\frac{f_0}{2})$, will be always equal to the value measured at time $t = 0$.

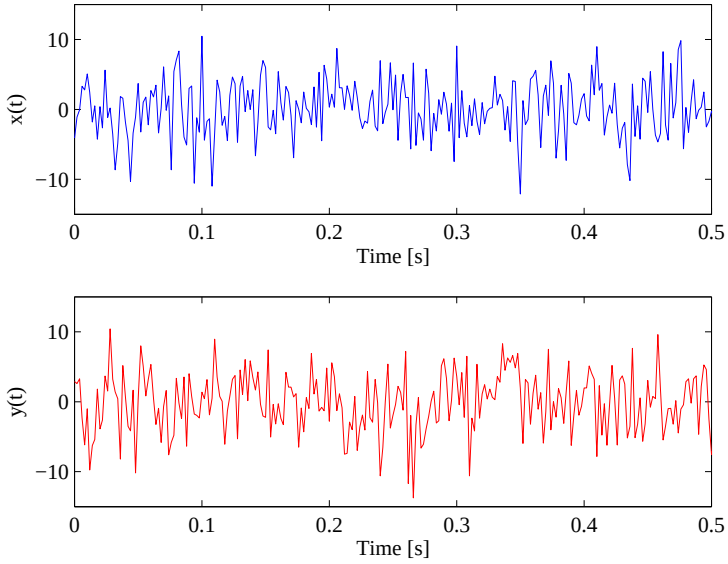

Figure 2.8: Time series of two signals $x(t)$ and $y(t)$ sampled at $512Hz$.

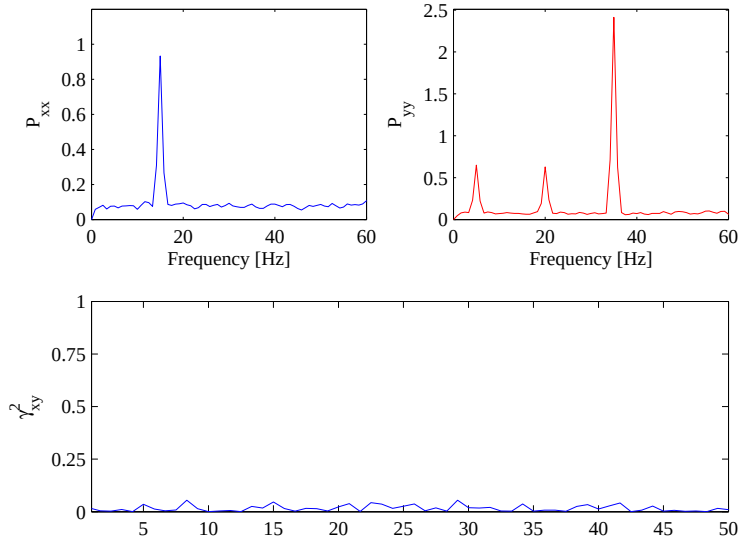

Figure 2.9: Signal $x(t)$ has one frequency component at $f_2 = 15Hz$. Signal $y(t)$ has three frequency components at $f_1 = 20Hz$, $f_1 + f_2 = 35Hz$, and $f_2 - f_1 = 5Hz$. The linear coherence γ^2_{xy} shows that these two signal are not linearly coupled.

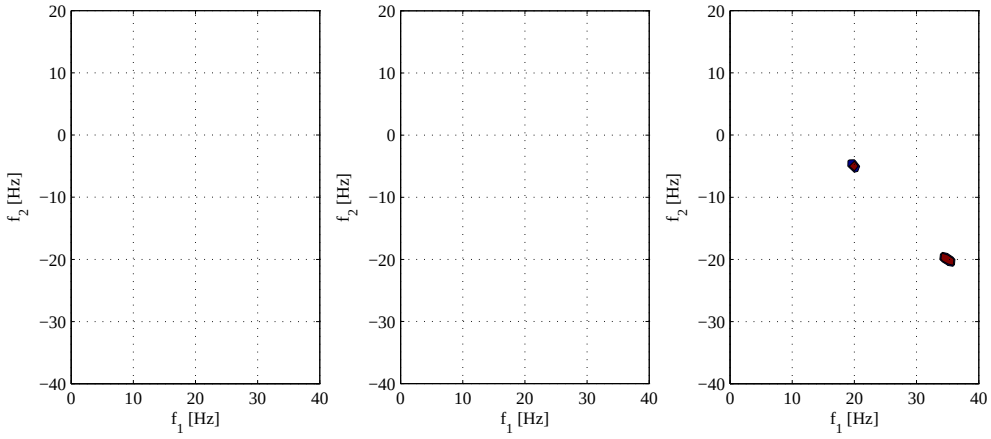

Figure 2.10: Auto-bispectra of both signals indicates there is no quadratic coupling among the frequency components within the signal itself. On the contrary, the cross-bicoherence computed between signals $x(t)$ and $y(t)$ indicates the frequency triples $(20Hz, -5Hz, 15Hz)$ and $(35Hz, -20Hz, 15Hz)$ are quadratically phase coupled.

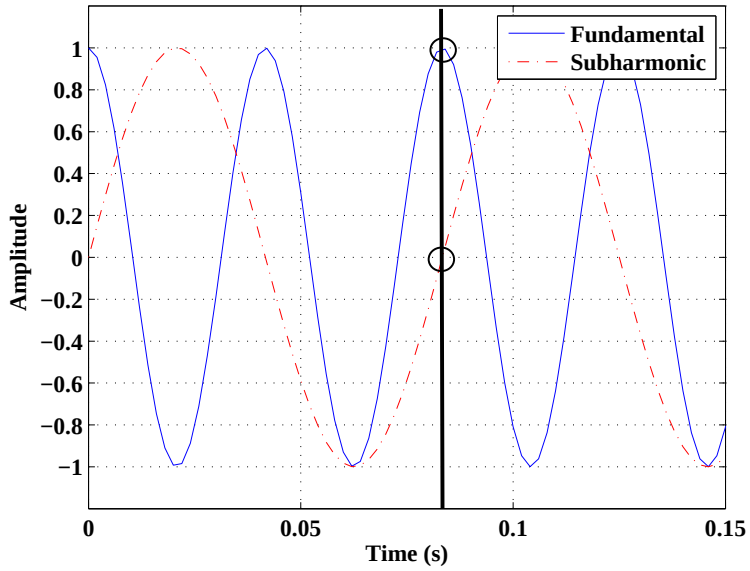

Figure 2.11: Example where the fundamental is perfectly phase-coupled with its subharmonic. Their phase difference between f_0 and $\frac{f_0}{2}$ is equal to $\frac{\pi}{2}$ at any time t.

Chapter 3

Prognosis of a Steel Beam-Mass System

In this chapter, sensitivities of physical parameters to damage initiation and progression in a structural system are established. As such, variations in parameters representing natural frequency, damping and effective nonlinearities with fatigue damage are assessed. The experimental system under consideration consists of a steel beam carrying a lumped mass. The identification of the parameters is performed by exploiting and modeling nonlinear behavior of the beam-mass system and matching an approximate solution of a representative model with quantities obtained from spectral analysis of measured vibrations. The representative model and identified coefficients are validated through comparison of measured and predicted responses. Percentage variations of the identified parameters with damage progression up to the point where cracks were observed are determined. Their sensitivities to the state of damage of the beam-mass system is also quantified. The results show that damping and effective nonlinearity parameters are more sensitive to damage progression than the natural frequency. Moreover, the sensitivity of nonlinear parameters to damage is better established using a physically-derived parameter rather than spectral parameters such as amplitudes, bispectra or bicoherence levels and/or amplitude ratios of harmonic components.

3.1 Introduction

Most of the reported damage analysis procedures of structures and their components that make use of vibration signatures relate their state of damage to a reduction in their stiffness. Consequently, the decrease in a structure's natural frequency has been proposed as a measure of its damage condition. Yet, such a reduction in the initial fatigue stages may not be large enough to be accurately quantified. This raises the issue of whether other parameters, such as damping or geometric and inertial nonlinearities, would have a higher sensitivity to damage initiation and progression in these stages. Over the past decade, there has been some interest in performing higher-order spectral analysis on measured vibrations to yield nonlinear coupling levels that are thought to be more sensitive than linear parameters to damage conditions. Rivola and White (1998) used the bispectrum as an indicator of fatigue crack in a cantilever beam. George et al. (2000) used the bicoherence as an identification tool of nonlinear effects that can be related to the damage state. Gelman et al. (2005) showed that the real and imaginary values of the complex bicoherence present a more effective approach for damage detection than an approach that is based on the bicoherence magnitude. To date, such spectral parameters have not been related to physical parameters such damping or specific nonlinearities that can be associated with the damage conditions.

In this part of the dissertation, sensitivities of different parameters including natural frequency, damping, and nonlinear effects to damage initiation and progression are identified with the goal of using representative parameters of these properties for damage identification. This objective is demonstrated through nonlinear excitations of a beam carrying a lumped mass and undergoing large amplitude motions. Vibration measurements are then used to quantify damage-induced variations in stiffness, damping and nonlinear parameters. The system identification follows the interrogative procedures proposed by Nayfeh (1985) and Hajj et al. (2000) in that it exploits a physical behavior. The parameter identification is then performed by combining spectral analysis of measured vibrations with approximate solutions of models that represent the nonlinear response of the beam-mass system.

The beam-mass configuration, used in these experiments, is similar to the one described by Zavodney and Nayfeh (1989). This choice is based on one of their observations that is

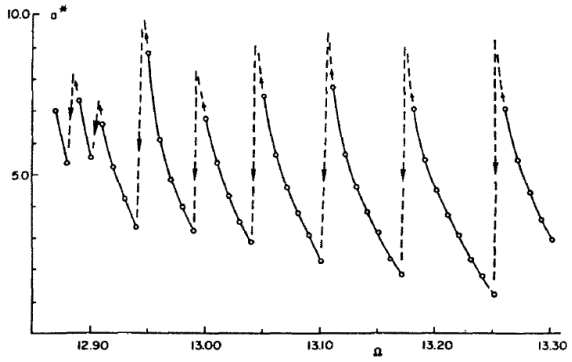

Figure 3.1: Variations in the response amplitude of the beam-mass system as the excitation frequency Ω is swept down (Zavodney and Nayfeh (1989)). Sudden jumps, in its response were encountered. These jumps were accompanied by a clicking sound. Zavodney and Nayfeh (1989) concluded that each click and subsequent jump were associated with crack initiation and development. Reprinted from International Journal of Non-Linear Mechanics, Vol. 24, L. D. Zavodney and A. H. Nayfeh, The Non-Linear Response of a Slender Beam Carrying a Lumped Mass to a Principal Parametric Excitation: Theory and Experiment, 105-125, 1989, with permission from Elsevier.

depicted in their Figure 6 and repeated here in Figure 3.1. In summary, they observed that when the excitation frequency of their beam-mass system was swept down, sudden jumps in its response were encountered. These jumps were accompanied by a clicking sound and a decrease in the natural frequency. Zavodney and Nayfeh (1989) concluded that each click and subsequent jump were associated with crack initiation and development. Here, we repeat the experiments and examine variations in relevant mechanical properties across the jumps.

3.2 Analytical Model

A schematic of the beam-mass system used in this work is presented in Figure 3.2. The system consists of a steel cantilever beam having a length L and a mass m per unit length. The beam is clamped at the base and carries a steel lumped mass M positioned at $s = d$ along the beam. Since the transverse deflection of the beam is large, a curvilinear coordinate s is used

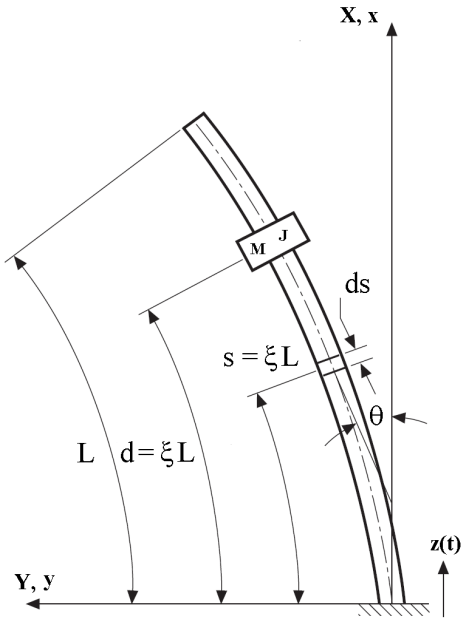

Figure 3.2: Schematic of the cantilever beam carrying a lumped mass under study.

such that the corresponding dimensionless coordinate ξ varies from 0 to 1 along the beam. The thickness of the beam is assumed to be small compared to the beam length, so that the effects of rotary inertia and shearing deformation could be neglected. Moreover, since the lumped mass M is placed symmetrically with respect to the beam length and the ratio of the beam length to width is < 30, the beam transverse motion can be considered purely planar (Zavodney and Nayfeh (1989)). Since the clamped end of the beam is given a parametrical excitation $z(t)$, a relative moving coordinate system, denoted by $x - y$, is defined in addition to the fixed coordinate system, denoted by $X - Y$. Below, the govering differential equation of the beam-mass system described above is derived from the Euer-Lagrange's equation.

In general, a beam which is subjected to an external excitation can react with a nonlinear large deflection and, depending on the boundary conditions, its motion can be defined as extensional, if both ends are rigidly clamped, or inextensional, if one of the two ends is free to move in-plane. The beam-mass system under consideration is a clamped-free beam and experiences inextensional transverse motion. Its potential energy, V, is due to the bending motion and is stored in the beam through the strain. It is given by

$$V = \frac{1}{2} EIL \int_0^1 \kappa^2 (\xi, t)\, d\xi \tag{3.1}$$

where $\xi = \frac{s}{L}$ is a nondimensional arc length, EI is the modulus of flexural rigidity and $\kappa(\xi, t)$ is the radius of curvature of the axis passing through the beam centroid, which corresponds to the neutral axis because the beam is inextensible and has no axial forces. For large amplitude free vibrations of the beam, the radius of curvature $\kappa(\xi, t)$ is given by Wagner (1965) as

$$\kappa(\xi, t) = \lambda^3 \left(x' y'' - x'' y' \right) \tag{3.2}$$

where $\lambda = 1/L$ and the prime sign $'$ stands for differentiation with respect to the nondimensional arc length $\xi = s/L$.

The kinetic energy, T, with contributions from the translational motion of the beam and both translational and rotational motions of the mass is given by

$$T = \frac{1}{2} mL \int_0^1 \left(\dot{X}^2 + \dot{Y}^2 \right) d\xi + \frac{1}{2} J \dot{\theta}^2 \mid_{\xi=d} + \frac{1}{2} M \left(\dot{X}^2 + \dot{Y}^2 \right) \mid_{\xi=d} \tag{3.3}$$

where J is the mass moment of inertia and θ is the angle of deflection of the beam at its base. The dot sign $' \cdot '$ denotes differentiation with respect to time t. To express the kinetic energy in the relative coordinate system $x - y$, the relation

$$X(\xi, t) = x(\xi, t) - z(t)\,, \; Y(\xi, t) = y(\xi, t) \tag{3.4}$$

between the fixed and the relative coordinate system is used. Substituting these relations in equation 3.3, the kinetic energy T is obtained as

$$T = \frac{1}{2} mL \int_0^1 \left[(\dot{x} - \dot{z})^2 + \dot{y}^2 \right] d\xi + \frac{1}{2} J \dot{\theta}^2 \mid_{\xi=d} + \frac{1}{2} M \left[(\dot{x} - \dot{z})^2 + \dot{y}^2 \right] \mid_{\xi=d} \tag{3.5}$$

Noting that the two relative coordinates x and y are not independent, the potential and kinetic energy are expressed as a function of the common transverse deflection coordinate y. This substitution yields

$$x'^2 + y'^2 = L^2 \Rightarrow \left(\lambda x' \right)^2 + \left(\lambda y' \right)^2 = 1 \tag{3.6}$$

which entails the physical aspect that for an inextensible beam the length of the beam neutral axis remains constant during the motion (Silva and Glynn (1978)). Substituting equations 3.6 and 3.2 into equation 3.1 and eliminating x' and y' from equation 3.2, one obtains a new expression for the potential energy as

$$V = \frac{1}{2}EI\lambda^3 \int_0^1 \left(1-\lambda^2 y'^2\right)^{-1} \left[\left(1-\lambda^2 y'^2\right) y'' + \lambda^2 y'^2 y''\right]^2 d\xi \tag{3.7}$$

Noting that $\lambda^2 y'^2 < 1$, the term $\left(1-\lambda^2 y'^2\right)^{-1}$ in equation 3.7 is expanded into a power series in order to derive its polynomial form. Keeping only the first two terms of the expansion, one obtains the final form of the potential energy as

$$V = \frac{1}{2}EI\lambda^3 \int_0^1 \left[y''^2 + \left(\lambda y' y''\right)^2\right] d\xi \tag{3.8}$$

Next, the kinetic energy, given by equation 3.5, is expressed in terms only of the relative coordinate y. Implementing the polynomial expansion in equation 3.6 yields

$$\lambda x' = \left(1-\lambda^2 y'^2\right)^{1/2} \approx 1 - \frac{1}{2}\lambda^2 y'^2 \tag{3.9}$$

Integrating this equation first with respect to the nondimensional arc length ξ and differentiating the resulting expression with respect to time t, a relation between $\dot{x}$ and y is obtained as

$$\dot{x}^2 = \frac{1}{4}\left[\frac{d}{dt}\left(\int_0^\xi \lambda y'^2 d\xi\right)\right]^2 \tag{3.10}$$

The relation between $\dot{\theta}$ and y is given by Hamdan and Dado (1997)

$$\sin\theta = \frac{dy}{ds} = \lambda y' \tag{3.11}$$

Moreover, plugging the identity $\cos^2\theta = 1 - \sin^2\theta$ into equation 3.11 and differentiating the resulting expression with respect to time t, yields

$$\dot{\theta}^2 = \frac{\left(\lambda \dot{y'}\right)^2}{1-\left(\lambda y'\right)^2} \tag{3.12}$$

Expanding the denominator in Taylor series yields

$$\dot{\theta}^2 \approx \left(\lambda \dot{y'}\right)^2 + \left(\lambda^2 \dot{y'} y'\right)^2 \tag{3.13}$$

The final form of the kinetic energy T in terms of the relative coordinate y is then obtained by substituting equations 3.10 and 3.13 into equation 3.3 which yields,

$$\begin{aligned} T &= \frac{1}{2}mL\int_0^1 \left\{ \dot{y}^2 + \left(\frac{1}{2}\left[\frac{d}{dt}\left(\int_0^\xi \lambda y'^2 d\xi \right) \right] - \dot{z} \right)^2 \right\} d\xi + \\ &+ \frac{1}{2}M\left[\dot{y}^2 + \left(\frac{1}{2}\left[\frac{d}{dt}\left(\int_0^\xi \lambda y'^2 d\xi \right) \right] - \dot{z} \right)^2 \right]_{\xi=d} + \\ &+ \frac{1}{2}\lambda^2 J\left[\dot{y'}^2 + \left(\lambda \dot{y'} y' \right)^2 \right]_{\xi=d} \end{aligned} \tag{3.14}$$

The dissipation energy within the beam is accounted for by relating the time-variation of the curvature to the internal viscous damping of the beam. This is written as

$$D = \frac{1}{2}EIL\int_0^1 \dot{\kappa}^2(\xi,t)\, d\xi \tag{3.15}$$

Using the time-derivative of the curvature in equation 3.2 and the approximation 3.9, equation 3.15 is re-written as

$$\begin{aligned} D &= \frac{1}{2}EIL\int_0^1 \left[\lambda^3 \left(\dot{x}'y'' + x'\dot{y}'' - \dot{x}''y' - x''\dot{y}' \right) \right]^2 d\xi = \\ &= \frac{1}{2}EIL\int_0^1 \left[\lambda^2 \dot{y}'' + \frac{\lambda^4}{2} y'^2 \dot{y}'' + \lambda^4 \dot{y}'^2 y'' \right]^2 d\xi \end{aligned} \tag{3.16}$$

The Lagrangian $L = T - V$ is given by

$$\begin{aligned} L = T - V &= \frac{1}{2}mL\int_0^1 \left\{ \dot{y}^2 + \left(\frac{1}{2}\left[\frac{d}{dt}\left(\int_0^\xi \lambda y'^2 d\xi \right) \right] - \dot{z} \right)^2 \right\} d\xi + \\ &+ \frac{1}{2}mLa_2\left[\dot{y}^2 + \left(\frac{1}{2}\left[\frac{d}{dt}\left(\int_0^\xi \lambda y'^2 d\xi \right) \right] - \dot{z} \right)^2 \right]_{\xi=d} + \\ &+ \frac{1}{2}mLa_1\left[\dot{y'}^2 + \left(\lambda \dot{y'} y' \right)^2 \right]_{\xi=d} - \frac{1}{2}mL\beta^2\int_0^1 \left[y''^2 + \left(\lambda y' y'' \right)^2 \right] d\xi \end{aligned} \tag{3.17}$$

where the coefficients $a_1 = J\lambda^3/m$ and $a_2 = M\lambda/m$ are nondimensional constants related to the rotary inertia ratio between the lumped mass M and the mass of the beam, and $\beta^2 = EI\lambda^4/m$ is a nondimensional constant related to the vibration frequencies of the beam. The Lagrangian L of equation 3.17 can be discretized using any of variational methods like Rayleigh-Ritz or Galerkin's procedure and then apply the Euler-Lagrange equation to obtain the discrete temporal problem. An approximate single-mode solution is then assumed to be

of the form:

$$y(\xi,t)=\sum_{n} r\psi_n(\xi)q_n(t) \tag{3.18}$$

where r is a scaling factor, $\psi_n(\xi)$ is the shape function of the n_{th} linear mode which is assumed to remain independent of motion amplitude during the beam motion, and $q_n(t)$ is an unknown modal coordinate which represents the time modulation of the n_{th} mode. By considering only the first mode, $n=1$, and substituing equation 3.18 into equation 3.17, one obtains the Lagrangian of the beam in modal coordinates $q(t)$ as

$$L=\frac{1}{2}mL\left[\alpha_1\dot{q}^2-2\alpha_5\dot{z}\dot{q}+\lambda^2\alpha_3q^2\dot{q}^2-\beta^2\alpha_2q^2-\beta^2\alpha_4\lambda^2q^4+(a_2+1)\,\dot{z}^2\right] \tag{3.19}$$

where the new constants appearing in this equation for the Lagrangian are defined as follows

$$\begin{aligned}
\alpha_1 &= \int_0^1\psi^2d\xi+a_1\psi'^2(d)+a_2\psi^2(d),\quad \alpha_2=\int_0^1\psi''^2d\xi \\
\alpha_3 &= \int_0^1\left(\int_0^\xi\psi'^2d\xi\right)^2d\xi+a_1\psi'^4(d)+a_2\left(\int_0^\xi\psi'^2d\xi\right)^2|_{\xi=d} \\
\alpha_4 &= \int_0^1\psi'^2\psi''^2d\xi,\quad \alpha_5=\int_0^1\psi d\xi+a_2\psi(d)
\end{aligned} \tag{3.20}$$

Considering the first mode only, the dissipation energy, given by equation 3.16, is re-written as

$$D=\frac{1}{2}mL\beta^2\left(\gamma_1\dot{q}+\gamma_2\frac{\lambda^4}{4}\dot{q}^2q^2+\gamma_3\lambda^4\dot{q}^4q^4+\lambda^2\gamma_4\dot{q}^2q+2\lambda^2\gamma_5\dot{q}^3q^2+\lambda^4\gamma_6\dot{q}^3q^3\right) \tag{3.21}$$

where the set of constants appearing in the equation 3.21 are defined as follows

$$\begin{aligned}
\gamma_1=\int_0^1\psi''^2d\xi\ \ \gamma_2=\int_0^1\psi''^2\psi'^4d\xi\ \ \gamma_3=\int_0^1\psi'^4\psi''^2d\xi \\
\gamma_4=\int_0^1\psi''^2\psi'^2d\xi\ \ \gamma_5=\int_0^1\psi'^2\psi''^2d\xi\ \ \gamma_6=\int_0^1\psi''^2\psi'^4d\xi
\end{aligned} \tag{3.22}$$

Applying the Euler-Lagrangian equation:

$$\frac{d}{dt}\frac{\partial L}{\partial\dot{q}}-\frac{\partial L}{\partial q}+\frac{\partial D}{\partial\dot{q}}=0 \tag{3.23}$$

and substituting equation 3.19 for L in equation 3.23 one obtains the discrete single-mode equation of motion of the beam in modal coordinates as

$$\alpha_1\ddot{q}+2\beta^2\gamma_1\dot{q}+2\beta^2\gamma_4\dot{q}|\dot{q}|+\beta^2\alpha_2q+\alpha_3\lambda^2q^2\ddot{q}+\alpha_3\lambda^2q\dot{q}^2+2\beta^2\alpha_4\lambda^2q^3=\alpha_5\ddot{z} \tag{3.24}$$

Dividing by α_1 yields

$$\ddot{q} + 2\zeta_1\dot{q} + 2\zeta_2\dot{q}|\dot{q}| + \omega^2 q + \epsilon_1 q^2\ddot{q} + \epsilon_1 q\dot{q}^2 + \epsilon_2 q^3 = \epsilon_3\ddot{z} \tag{3.25}$$

where the new constants are defined below

$$\begin{aligned} \omega^2 &= \frac{\alpha_2}{\alpha_1}\beta^2, \;\; \epsilon_1 = \lambda^2\frac{\alpha_3}{\alpha_1} \\ \epsilon_2 &= 2\lambda^2\beta^2\frac{\alpha_4}{\alpha_1}, \;\; \epsilon_3 = \frac{\alpha_5}{\alpha_1} \\ \zeta_1 &= \frac{\beta^2\gamma_1}{\alpha_1}, \;\; \zeta_2 = \frac{\beta^2\gamma_4}{\alpha_1} \end{aligned} \tag{3.26}$$

Next, the case where the base motion, z, is harmonic with a frequency Ω, near the principal parametric resonant frequency is considered. Defining $\eta = \Omega q/L$ as the nondimensional displacement amplitude at the point of maximum deflection, one can assume that the beam-mass system is governed by the following mass normalized nondimensional second-order nonlinear ordinary differential equation

$$\ddot{\eta} + 2\widehat{\zeta_1}\dot{\eta} + 2\widehat{\zeta_2}\dot{\eta}\,|\dot{\eta}| + \omega^2\left[1 - f\cos(\widehat{\Omega}t)\right]\eta + +\widehat{\alpha}\eta^3 + \kappa_1\eta\dot{\eta}^2 + \kappa_2\eta^2\ddot{\eta} = 0 \tag{3.27}$$

where η is the temporal amplitude of the system's first mode, $\Omega = \widehat{\Omega}/\omega$ is the nondimensional frequency and $\widehat{\Omega}$ is the frequency of excitation. The term $\omega^2\eta$ is the linear restoring force, $2\widehat{\zeta_1}$ and $2\widehat{\zeta_2}$ are the linear and quadratic damping coefficients and they result in linear, $2\widehat{\zeta_1}\dot{\eta}$ and quadratic $2\widehat{\zeta_2}\dot{\eta}\,|\dot{\eta}|$ damping forces, respectively. The nonlinear damping terms model physical properties or phenomena including material damping (could be damage or crack related), structural properties and/or fluid drag. Cubic geometric and inertia restoring forces are modeled respectively by $\widehat{\alpha}\eta^3$ and $\kappa_1\eta\dot{\eta}^2$ where α is the cubic geometric stiffness nonlinearity and κ_1, κ_2 are the cubic inertia nonlinearities. These nonlinear restoring forces model the nonlinear beam curvature and distribution of the mass along the beam. The excitation is chosen to induce principal parametric resonance and hence produce large amplitude responses that allow quantification of the damping and nonlinear coefficients. As such, the excitation is expressed in the form $f\eta\cos(\widehat{\Omega}t)$ where the excitation frequency is chosen to be near twice the system's natural frequency ω.

3.3 Approximate Solution

In a nondimensional fashion with respect to the natural frequency ω, a new nondimensional time scale $\tau = \omega t$ is introduced and equation 3.27 is rewritten as

$$\ddot{\eta} + 2\epsilon\zeta_1\dot{\eta} + 2\epsilon\zeta_2\dot{\eta}\,|\dot{\eta}| + [1 - \epsilon f\cos(\Omega\tau)]\,\eta + \\ +\epsilon\alpha\eta^3 + \epsilon\kappa_1\eta\dot{\eta}^2 + \epsilon\kappa_2\eta^2\ddot{\eta} = 0 \tag{3.28}$$

where ϵ is a bookkeeping parameter used to indicate the relative contributions of the damping, nonlinear, and excitation parameters to the response. To perform identification of all parameters, we exploit the behavior of the beam-mass system by exciting it at a frequency $\Omega \approx 2$ close to twice the natural frequency of the beam-mass system. An approximate solution for the response of the system's governing equation, given by equation 4.1 is then obtained using the method of multiple scales (Nayfeh (1981)). The approximation is a first-order uniform expansion of the form

$$\eta = \eta_0(T_0, T_1) + \epsilon\eta_1(T_0, T_1) + \cdots \tag{3.29}$$

The parameter ϵ differentiates between slow and fast-varying effects of each term in the governing equation on the system. The time τ is also replaced with a new set of time scales T_n defined as

$$T_n = \epsilon^n\tau \tag{3.30}$$

Equation 3.30 suggests that $T_0 = \tau$ is a fast time scale and $T_1 = \epsilon\tau, T_2 = \epsilon^2\tau, T_3 = \epsilon^3\tau, ...$ are subsequent slower time scales. The governing ordinary differential equation 4.1 is then transformed to a partial differential equation where η is a function of the new time scales T_n given by equation 3.30. Denoting $\frac{\partial}{\partial T_n}$ by D_n, the time derivatives in terms of T_0, T_1, and T_2 are written as

$$\begin{aligned} \frac{d}{d\tau} &= \frac{dT_0}{d\tau}\frac{\partial}{\partial T_0} + \frac{dT_1}{d\tau}\frac{\partial}{\partial T_1} + \frac{dT_2}{d\tau}\frac{\partial}{\partial T_2} + \ldots = D_0 + \epsilon D_1 + \epsilon^2 D_2 + \ldots \\ \frac{d^2}{d\tau^2} &= \left(D_0 + \epsilon D_1 + \epsilon^2 D_2 + \ldots\right)^2 = {D_0}^2 + \epsilon^2 {D_1}^2 + 2\epsilon D_0 D_1 + 2\epsilon^2 D_0 D_2 + \ldots \end{aligned} \tag{3.31}$$

Moreover, the generalized coordinate and its first and second derivatives are written as follows

$$\begin{aligned}
\eta(\tau;\epsilon) &= \eta_0(T_0,T_1) + \epsilon\eta_1(T_0,T_1) && (3.32)\\
\dot{\eta}(\tau;\epsilon) &= (D_0+\epsilon D_1)(\eta_0(T_0,T_1)+\epsilon\eta_1(T_0,T_1)) && (3.33)\\
&= D_0\eta_0(T_0,T_1)+\epsilon D_1\eta_0(T_0,T_1)+\epsilon D_0\eta_1(T_0,T_1)+\epsilon^2 D_1\eta_1(T_0,T_1)\\
&= D_0\eta_0(T_0,T_1)+\epsilon^2 D_1\eta_1(T_0,T_1)+\epsilon(D_1\eta_0(T_0,T_1)+D_0\eta_1(T_0,T_1))\\
&= D_0\eta_0(T_0,T_1)+\epsilon(D_1\eta_0(T_0,T_1)+D_0\eta_1(T_0,T_1))\\
\ddot{\eta}(\tau;\epsilon) &= \left(D_0^2+2\epsilon D_0D_1\right)\eta && (3.34)\\
&= \left(D_0^2+2\epsilon D_0D_1\right)(\eta_0(T_0,T_1)+\epsilon\eta_1(T_0,T_1))\\
&= D_0^2\eta_0(T_0,T_1)+2\epsilon D_0D_1\eta_0(T_0,T_1)+\epsilon D_0^2\eta_1(T_0,T_1)+2\epsilon^2 D_0D_1\eta_1(T_0,T_1)\\
&= D_0\eta_0(T_0,T_1)+\epsilon(D_1\eta_0(T_0,T_1)+D_0\eta_1(T_0,T_1))\\
&= D_0^2\eta_0(T_0,T_1)+\epsilon\left(2D_0D_1\eta_0(T_0,T_1)+D_0^2\eta_1(T_0,T_1)\right)
\end{aligned}$$

Here, the solution of the nonlinear differential equation is assumed to be the sum of a general solution, η_0, associated with the time scale $T_0=\tau$ and has the largest influence on the response, and a particular solution, η_1, associated with the slower time scale $T_1=\epsilon\tau$ which has smaller influence and serves as a small adjustment to the response. T_0 quantitatively describes the nearness of $\widehat{\Omega}$ to 2ω, i.e. Ω to 2 and a detuning parameter σ is defined as $1=\left(\frac{1}{2}\Omega\right)^2+\epsilon\sigma$. Substituting equations 3.32 into equation 4.1 and equating coefficients of like powers of ϵ, one obtains

$$\begin{aligned}
O\left(\epsilon^0\right): D_0^2\eta_0+\frac{\Omega^2\eta_0}{4} &= 0 && (3.35)\\
O\left(\epsilon^1\right): D_0^2\eta_1+\frac{\Omega^2\eta_1}{4} &= -\sigma\eta_0+f\cos(\tau\Omega)\eta_0-2D_0D_1\eta_0-\alpha{\eta_0}^3+ && (3.36)\\
&- k_1\eta_0(D_0\eta_0)^2-k_2{\eta_0}^2\left(D_0{}^2\eta_0\right)-2D_0\eta_0\zeta_1+\\
&- 2\left|D_0\eta_0\right|D_0\eta_0\zeta_2
\end{aligned}$$

The approximate solution of the governing differential equation given by 4.1 is obtained from the system of equations 3.35 and 3.36. Equation 3.35 yields the general solution η_0. Plugging this solution in equation 3.36, yields the particluar solution η_1. Following this procedure the solution of equation 3.35 is written, in complex form, as

$$\eta_0 = A(T_0,T_1)\,e^{\frac{1}{2}i\Omega T_0}+\overline{A}(T_0,T_1)\,e^{-\frac{1}{2}i\Omega T_0} \qquad (3.37)$$

where $A = \frac{1}{2}ae^{i\beta}$ and $\overline{A}$ is its complex conjugate and where $A(T_0, T_1)$ is unknown at this level of approximation. Substituting the solution for η_0 from 3.37 into each term of equation 3.36, yields the following

$$
\begin{aligned}
D_0 D_1 \eta_0 &= \frac{1}{2} i\Omega A' e^{\frac{1}{2}i\Omega T_0} - \frac{1}{2} i\Omega \overline{A'} e^{-\frac{1}{2}i\Omega T_0} && (3.38)\\
D_0 \eta_0 &= \frac{1}{2} i\Omega A e^{\frac{1}{2}i\Omega T_0} - \frac{1}{2} i\Omega \overline{A} e^{-\frac{1}{2}i\Omega T_0} && (3.39)\\
\sigma \eta_0 &= \sigma \left(A e^{\frac{1}{2}i\Omega T_0} + \overline{A} e^{-\frac{1}{2}i\Omega T_0} \right) && (3.40)\\
\alpha {\eta_0}^3 &= \alpha \left(A e^{\frac{1}{2}i\Omega T_0} + \overline{A} e^{-\frac{1}{2}i\Omega T_0} \right)^3 && (3.41)\\
k_1 \eta_0 \left(D_0 \eta_0\right)^2 &= k_1 \left(A e^{\frac{1}{2}i\Omega T_0} + \overline{A} e^{-\frac{1}{2}i\Omega T_0} \right) \cdot && (3.42)\\
&\cdot \left(A \frac{1}{2} i\Omega e^{\frac{1}{2}i\Omega T_0} - \overline{A} \frac{1}{2} i\Omega e^{-\frac{1}{2}i\Omega T_0} \right)^2 \\
k_2 {\eta_0}^2 \left({D_0}^2 \eta_0\right) &= k_2 \left(A e^{\frac{1}{2}i\Omega T_0} + \overline{A} e^{-\frac{1}{2}i\Omega T_0} \right)^2 \cdot && (3.43)\\
&\cdot \left(-A \frac{1}{4} \Omega^2 e^{\frac{1}{2}i\Omega T_0} - \frac{1}{4} \overline{A} \Omega^2 e^{-\frac{1}{2}i\Omega T_0} \right) \\
f \cos(\tau\phi) \eta_0 &= -f \left(A e^{\frac{1}{2}i\Omega T_0} + \overline{A} e^{-\frac{1}{2}i\Omega T_0} \right) \left(\frac{1}{2} e^{i\Omega T_0} + \frac{1}{2} e^{-i\Omega T_0} \right) && (3.44)\\
& && (3.45)
\end{aligned}
$$

The computation of the term $D_0\eta_0 |D_0\eta_0|$ requires more attention. Since it is periodic with period $\frac{2\pi}{\Omega}$, it is expanded in Fourier series and set equal to:

$$
\begin{aligned}
D_0\eta_0 |D_0\eta_0| &= \int_0^{\frac{2\pi}{\Omega}} \sum_{n=-\infty}^{+\infty} g_1(T_1) e^{ni\Omega T_0} e^{-i\Omega T_0} dT_0 = && (3.46)\\
&= g_1 \int_0^{\frac{2\pi}{\Omega}} e^{ni\Omega T_0} e^{-i\Omega T_0} dT_0 = \begin{cases} 0 & \text{if } n \neq 1 \\ \frac{2\pi}{\Omega} & \text{if } n = 1 \end{cases}
\end{aligned}
$$

Consequently,

$$
\begin{aligned}
g_1 &= \frac{1}{2\pi} \int_0^{\frac{2\pi}{\Omega}} \left(ie^{iT_0} - ie^{-iT_0} \right) \left| ie^{iT_0} - ie^{-iT_0} \right| \cdot e^{-iT_0} d(T_0) && (3.47)\\
&= \frac{16i}{3\pi} \\
|D_0\eta_0| \, D_0\eta_0 &= g_1 A \frac{1}{2} \Omega e^{i\frac{1}{2}\Omega T_0} + g_1 \overline{A} \frac{1}{2} \Omega e^{-i\frac{1}{2}\phi T_0} && (3.48)
\end{aligned}
$$

Carrying out all the substitutions and collecting all the terms multiplying $e^{\frac{1}{2}i\Omega T_0}$, $e^{-\frac{1}{2}i\Omega T_0}$, $e^{\frac{3}{2}i\Omega T_0}$, $e^{-\frac{3}{2}i\Omega T_0}$, equation 3.36 yields

$$\begin{aligned} D_0^2\eta_1 + \frac{\Omega^2\eta_1}{4} = & - e^{\frac{3}{2}i\Omega T_0}\left(-\frac{Af}{2} + A^3\alpha - \frac{1}{4}A^3\Omega^2 k_1 - \frac{1}{4}A^3\Omega^2 k_2\right) + \\ & - e^{-\frac{3}{2}i\Omega T_0}\left(-\frac{\overline{A}f}{2} + \overline{A}^3\alpha - \frac{1}{4}\overline{A}^3\Omega^2 k_1 - \frac{1}{4}\overline{A}^3\Omega^2 k_2\right) + \\ & - e^{\frac{1}{2}i\Omega T_0}\Big(-\frac{\overline{A}f}{2} + 3A^2\overline{A}\alpha + A\sigma + \frac{1}{4}A^2\overline{A}\Omega^2 k_1 - \frac{3}{4}A^2\overline{A}\Omega^2 k_2 + \\ & - iA\Omega\zeta_1 - \frac{8iA\Omega^2|\overline{A}|\zeta_2}{3\pi} + i\Omega A'\Big) + \\ & + e^{-\frac{1}{2}i\Omega T_0}\Big(-\frac{Af}{2} + 3A\overline{A}^2\alpha + \overline{A}\sigma + \frac{1}{4}A\overline{A}^2\Omega^2 k_1 - \frac{3}{4}A\overline{A}^2\Omega^2 k_2 + \\ & + i\overline{A}\Omega\zeta_1 - \frac{8iA\Omega^2|\overline{A}|\zeta_2}{3\pi} - i\Omega\overline{A'}\Big) \end{aligned} \tag{3.49}$$

Any particular solution of equation 3.49 contains troublesome terms such as secular terms and small divisors. These terms are eliminated by setting

$$D_1 A = 0 \text{ or } A = A(T_1) \tag{3.50}$$

i.e.,

$$A' = \frac{-i\overline{A}f}{2\Omega} + \frac{3iA^2\overline{A}\alpha}{\Omega} + \frac{Ai\sigma}{\Omega} + \frac{1}{4}iA^2\overline{A}\Omega k_1 - \frac{3}{4}iA^2\overline{A}\Omega k_2 + A\zeta_1 + \frac{8A\Omega|\overline{A}|\zeta_2}{3\pi} \tag{3.51}$$

where the prime sign $'$ denotes the differentiation with respect to T_1. Letting

$$A = \frac{1}{2}ae^{i\beta}$$

and

$$\overline{A} = \frac{1}{2}ae^{-i\beta}$$

one obtains

$$A' = -\frac{iae^{-2i\beta}f}{4\Omega} + \frac{3ia^3\alpha}{8\Omega} + \frac{ia\sigma}{2\Omega} + \frac{1}{32}ia^3\Omega k_1 - \frac{3}{32}ia^3\Omega k_2 + \frac{a\zeta_1}{2} + \frac{2a^2\Omega\zeta_2}{3\pi} \tag{3.52}$$

Using

$$e^{-2i\beta} = \cos 2\beta - i\sin 2\beta \tag{3.53}$$

and defining the effective nonlinearity α_e as the parameter that combines the effects of all nonlinear terms

$$\alpha_e = \frac{1}{4}\left(3\alpha + \frac{1}{4}\Omega^2 k_1 - \frac{3}{4}\Omega^2 k_2\right) \tag{3.54}$$

equation 3.52 is re-written as

$$A' = \frac{3ia^3\alpha}{8\Omega} + \frac{ia\sigma}{2\Omega} - \frac{iaf\cos(2\beta)}{4\Omega} - \frac{af\sin(2\beta)}{4\Omega} + \frac{1}{32}ia^3\Omega k_1 - \frac{3}{32}ia^3\Omega k_2 + \frac{a\zeta_1}{2} + \frac{2a^2\phi\zeta_2}{3\pi} \tag{3.55}$$

Consequently, the solution of equation 3.49 becomes

$$\begin{aligned}\eta_1 &= \frac{1}{2\Omega^2}\left\{-\frac{1}{4}afe^{i\beta} + \frac{1}{8}a^3\alpha e^{3i\beta} - \frac{1}{32}a^3k_1\Omega^2e^{3i\beta} - \frac{1}{32}a^3k_1\Omega^2e^{3i\beta} - \frac{1}{32}ia^3\Omega^3\zeta_3e^{3i\beta}\right\}e^{\frac{3i\Omega T_0}{2}} + cc = \\ &= -\frac{af}{4\Omega^2}cos\left(\frac{3}{2}\Omega\tau + \beta\right) + \left(\frac{a^3\alpha}{8\Omega^2} - \frac{a^3k_1}{32} - \frac{a^3k_2}{32}\right)cos\left(\frac{3}{2}\Omega\tau + 3\beta\right)\end{aligned} \tag{3.56}$$

where *cc* stands for complex conjugate. By equating real and imaginary parts from both sides of equation 3.55, one obtains the modulation equations

$$\dot{a} = \epsilon\left(\zeta_1 + \frac{4a\Omega\zeta_2}{3\pi}\right)a - \frac{\epsilon fa}{2\Omega}\sin(2\beta) \tag{3.57}$$

$$a\dot{\beta} = \frac{\epsilon}{\Omega}\left(\sigma + \alpha_e a^2\right)a - \frac{\epsilon fa}{2\Omega}\cos(2\beta) \tag{3.58}$$

An approximate solution for equation 4.1 is then obtained by plugging equations 3.37, and 3.56 in equation 3.29 to yield

$$\begin{aligned}\eta(\tau) = \frac{1}{2}acos\left(\frac{1}{2}\Omega\tau + \beta\right) &+ \epsilon\Bigg\{-\frac{af}{4\Omega^2}cos\left(\frac{3}{2}\Omega\tau + \beta\right) + \\ &+ \left(\frac{a^3\alpha}{8\Omega^2} - \frac{a^3k_1}{32} - \frac{a^3k_2}{32}\right)cos\left(\frac{3}{2}\Omega\tau + 3\beta\right)\Bigg\} + ...\end{aligned} \tag{3.59}$$

where a and β are given by equations 4.3 and 4.4. Steady state responses of η are obtained by letting $\dot{a} = 0$ and $\dot{\beta} = 0$ in equations 4.3 and 4.4, thereby obtaining

$$\zeta_1\Omega + \frac{4a\Omega^2\zeta_2}{3\pi} = \frac{f}{2}\sin 2\beta \tag{3.60}$$

$$\sigma + \alpha_e a^2 = \frac{f}{2}\cos 2\beta \tag{3.61}$$

where $\Omega^2 = 4\left(1 - \epsilon\sigma\right)$. Equations 4.3 and 4.4 provide a relation between the spectral quantities and the damping and nonlinear parameters. Obviously, spectral estimates of the first harmonic amplitude, a and the phase relation 2β between excitation and response could be

substituted into equations 4.3 and 4.4 to determine the damping and effective nonlinearity parameters. Since the nonlinearity produces a third harmonic in the response, its amplitude, which is dependent on α, k_1, and k_2 can also be used to assess nonlinear effects. By squaring equations 4.6 and 4.7 and adding the resulted expressions, one obtains the frequency-response equation

$$\left(\sigma + \alpha_e a^2\right)^2 + \left(\zeta_1 \Omega + \frac{4a\Omega^2\zeta_2}{3\pi}\right)^2 = \frac{f^2}{4} \tag{3.62}$$

which can be manipulated to obtain

$$\alpha_e a^2 = -\sigma \pm \sqrt{\frac{f^2}{4} - \left(\zeta_1 \Omega + \frac{4a\Omega^2\zeta_2}{3\pi}\right)^2} \tag{3.63}$$

3.4 Experimental Setup

The experimental setup, shown in Figure 3.3, consists of a slender steel beam-mass system that is mounted onto a steel platform which, in turn, is positioned on a shaker. A photograph of the beam-mass system is presented in Figure 3.5. The width and thickness of the beam are *15.85 mm* and *0.559 mm*, respectively, and its length is *135 mm* measured from the clamped end. The length, width, and thickness of the steel lumped mass are respectively *30 mm*, *18 mm*, and *10 mm*, its weight is *42 g* and it is tightened *85 mm* away from the clamped end. The excitation acceleration is measured by a piezo-electric accelerometer attached to the shaker. The beam response is measured using a strain gage that was glued about *60 mm* above the mounting plate. Data, analyzed here, were sampled at a frequency of 500 Hz over 60-second periods. The resistance and the gage factor of the used strain gage are, respectively, 350 ± 0.3% *Ohm* at 24°C and 2.11 ± 0.5% at 24°C. The transverse sensitivity is +0.5 ± 0.2% at 24°C. These values of tolerance may affect the strain measurements. Moreover, the number of averages M used in the power spectrum and in the cross-bispectrum estimations are respectively, 8 and 50. These observations need to be made in order to point out that the first-mode amplitude and the phase estimations may be affected by uncertainties. The free response of the system before exciting the beam yielded a frequency for the first mode of 12.203 Hz.

A finite element model of the metallic beam carrying the lumped mass has been developed in order to check numerically the first mode natural frequency which was measured using the

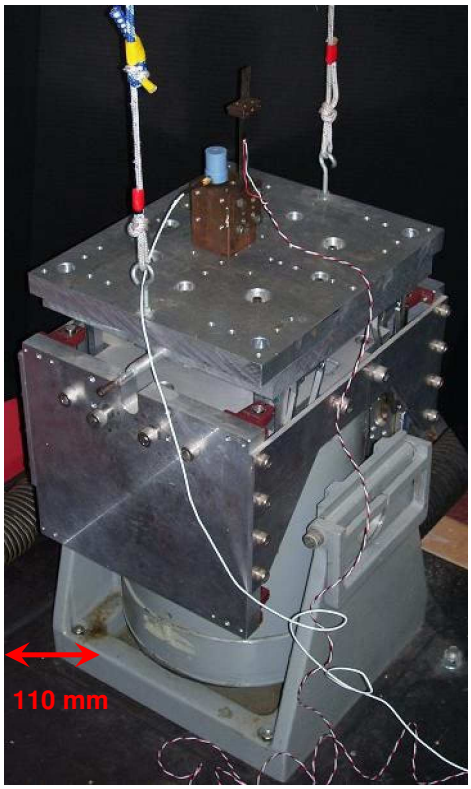

Figure 3.3: Experimental setup of the first metallic beam-mass system as mounted on a shaker. A piezo-electric accelerometer is used to measure the excitation and a strain gage is used to measure the beam's response.

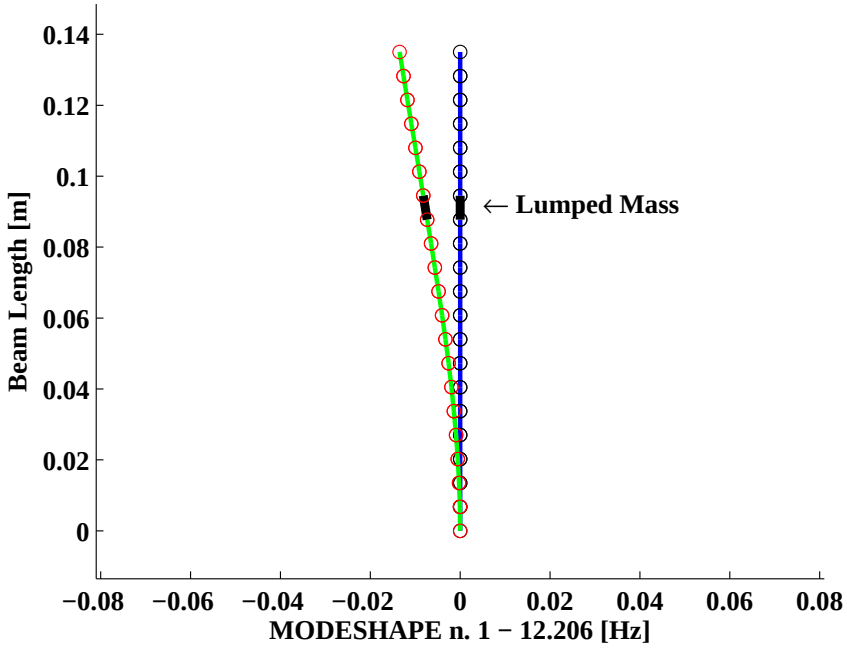

Figure 3.4: The first mode natural frequency is numerically checked using the finite element model of the steel beam carrying a lumped mass.

free response test. The beam was discretized in 20 elements and the lumped mass is considered as a concentrated mass in one element. The first mode natural frequency from the numerical model was found to be 12.206 Hz. This value is reasonably close to the one obtained from the experiments. The first modeshape is plotted and presented in Figure 3.4.

For the purpose of system identification, principal parametric excitation of the beam-mass system is exploited. This is done by performing frequency sweeps whereby the system was excited over a small range near twice its natural frequency. The excitation signal is generated by a two-channel, variable-phase wave synthesizer. During a frequency sweep over the excitation range, the excitation frequency $\widehat{\Omega}$ is decreased by a step size of 0.001 Hz while keeping its amplitude constant. Variations in the steady-state amplitude of the steel beam-mass system with the excitation frequency are presented in the frequency-response curves of Figure 3.6. As the excitation frequency $\widehat{\Omega}$ is decreased in increments of 0.001 Hz from 24.528 Hz to approach a value of 24.408 Hz which is very close to twice the system's natural frequency,

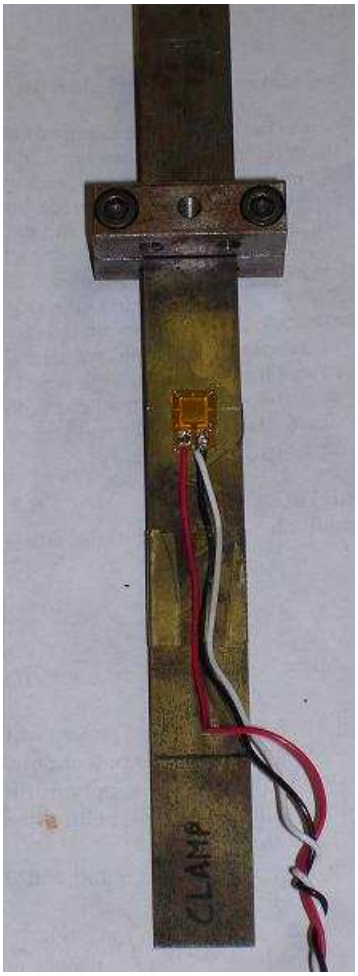

Figure 3.5: Photograph of the steel beam-mass system which has been used for the experiments.

ω, the steady-state amplitude of the response increases significantly. Of particuar interest is the time variation in the response shown in Figure 3.7 caused by an excitation having a frequency of 24.408 Hz. The response shows an increase from a steady-state amplitude of 316 $\mu\epsilon$ to about 1285 $\mu\epsilon$ which is followed by a drop to near 8 $\mu\epsilon$. This drop in the response is associated with a change in the natural frequency that is most likely due to damage caused by the large amplitude oscillations. As the excitation frequency is further decreased from 24.398 Hz to about 24.356 Hz, the amplitude of the steady-state response increases again. This increase was followed by a second drop. As shown in Figure 3.6, this behavior repeated itself five times as the excitation frequency was decreased. With further decrease in the excitation frequency, this repeated behavior changed significantly and the response of the beam was characterized by a quick and sudden jump from small to large amplitudes and vice-versa. A high resolution digital image of the beam, after removing it from its clamped support, showed a crack that was located al the location where the beam was clamped and that extended over 60% of its width. As such, it is fair to assume that the continuous variations in the frequency-response curves are associated with damage progression.

3.5 Spectral Analysis of Excitation and Response Data

Higher-order spectral analysis is performed on the measured data to determine the first harmonic amplitude a and the response phase 2β. The amplitude a of th response is determined from its power spectrum. The phase relation 2β between the input excitation and the response is determined from the phase of the cross-bispectrum. For a discrete, stationary, real-valued, zero-mean process, $x_T(nt_s)$ of length T, sampling time t_s and $n = 0, 1, 2, ..., N-1$, the power spectral density function $S_{xx}(l)$ for the k^{th} sample of a discrete, zero-mean, process $x(t_s)$ is estimated as

$$\begin{aligned} S_{xx}[l] &= \frac{2}{M}\sum_{k=1}^{M}\left|X_T^{(k)}[l]\right|^2 \quad l = 1, 2, ..., \frac{N}{2} - 1 \\ &= \frac{1}{M}\sum_{k=1}^{M}\left|X_T^{(k)}[l]\right|^2 \quad l = 0 \; or \; \frac{N}{2} \end{aligned} \tag{3.64}$$

where M is the number of samples.

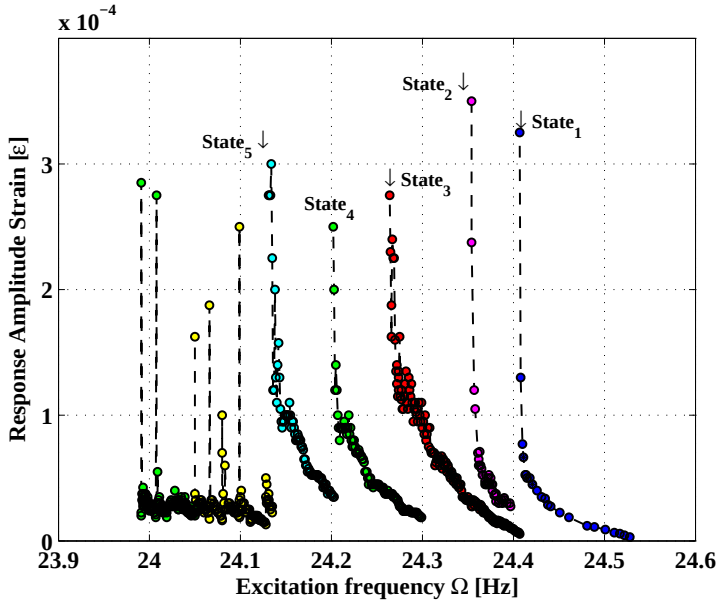

Figure 3.6: Variation of the steady-state response amplitude of the first metallic beam-mass system while the excitation frequency was swept near twice the natural frequency. The observed jumps in the amplitude of the response and its subsequent increase are indicative of damage initiation and progression in the beam. The system passed through five different states of damage during experimental tests. Each state was obtained by sweeping the excitation frequency $\widehat{\Omega}$ down by a step size of 0.001 Hz. Each point is obtained from the peak of the power spectrum of each steady state response. Each jump appeared every time the excitation frequency happened to be set to a value exactly twice the natural frequency and it was also associated with a slight change in the natural frequency. After $State_5$ this repeated behavior changed completely and this change was associated with the fact that the microcrack reached a size which did not allow further experimentation.

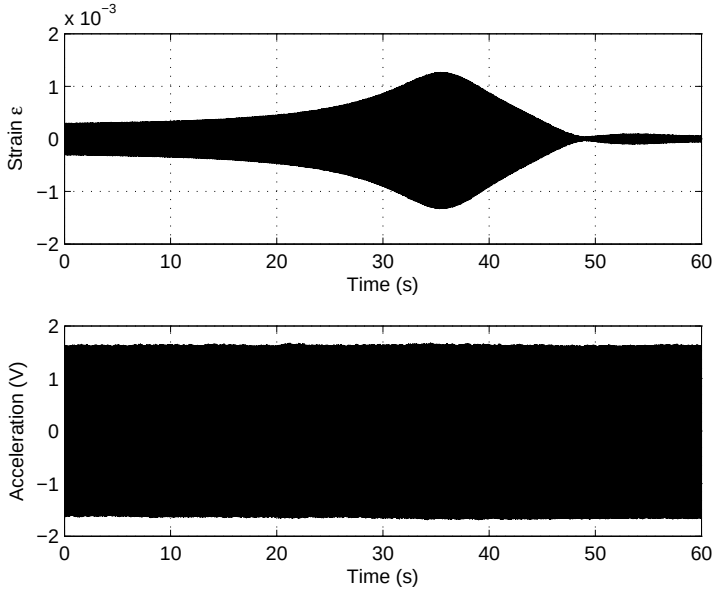

Figure 3.7: Time series of beam response (plot at the top, ϵ) and the corresponding excitation (plot at the bottom, $Volts$) over a 60-seconds time duration. Referring to Figure 3.6, these data were acquired when the excitation frequency was set near to 24.4069 Hz which is exactly twice the beam natural frequency at $State_1$. The amplitude increased significantly over a short period of time from a value near $316\mu\varepsilon$ to about $1285\mu\varepsilon$ and dropped again to a relatively small value near $8\mu\varepsilon$. During this period of time, the excitation amplitude and frequency were kept constant. This behavior is also associated to a slight change in the system's natural frequency. Similar responses were measured near the peaks of the other $States$.

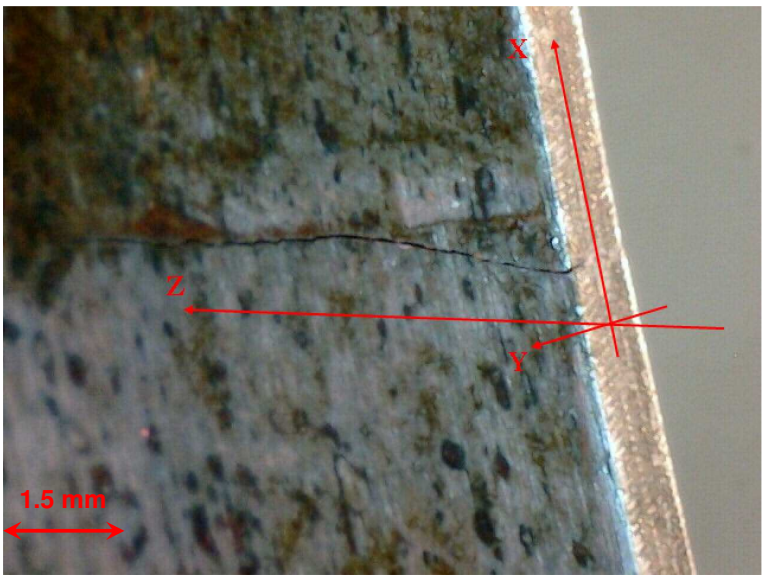

Figure 3.8: High resolution imaging of the beam after extended excitations showed a crack that has developed over more than 60% of the width of the beam (Z axis) and accross its thickness (Y axis).

The next higher-order spectrum is the cross-bispectrum, $B_{yxx}[l_1, l_2]$, is estimated as

$$B_{yxx}[l_1, l_2] = \frac{1}{M} \sum_{k=1}^{M} Y_T^{(k)}[l_1 + l_2] X_T^{*(k)}[l_1] X_T^{*(k)}[l_2] \tag{3.65}$$

where $X_T^{(k)}[l]$ and $Y_T^{(k)}[l]$ are the Discrete Fourier Transforms of the k^{th} ensemble of the time series $x(t)$ and $y(t)$, respectively and that are taken over a time duration T and the subscript * is used to denote the complex conjugate. The cross-bispectrum provides a measure of the nonlinear relation among frequency modes at l_1 and l_2 in $x(t)$ and their sum frequency component $l_1 + l_2$ in $y(t)$. If frequencies l_1, l_2, and $l_1 + l_2$ are coupled through a quadratically nonlinear interaction mechanism, phase coherence will exist among them. The cross-bispectrum of signals $x(t)$ and $y(t)$ is a two-dimensional function in frequency and is complex-valued. In averaging over many ensembles, the magnitude of the cross-bispectrum becomes a function of the phase relationship among sets of the frequency components at l_1, l_2, and $l_1 + l_2$. If there is a random phase relationship among the three components, the cross-bispectrum will average to a very small value. Should there be any phase relation-

ship among these frequency components, the corresponding cross-bispectral value will have a large magnitude. The cross-bispectrum is then able to detect nonlinear phase coupling among different frequency components in two signals because of its phase-preserving effect. The levels of nonlinear coupling and confidence in the estimated phase are determined from the normalized cross-bispectrum, called the cross-bicoherence, and is defined as

$$b^2_{yxx}[l_1,l_2]=\frac{\frac{1}{M}\sum_{k=1}^{M}\left|Y_T^{(k)}[l_1+l_2]X_T^{*(k)}[l_1]X_T^{*(k)}[l_2]\right|^2}{\frac{1}{M}\sum_{k=1}^{M}\left|X_T^{(k)}[l_1]X_T^{(k)}[l_2]\right|^2\frac{1}{M}\sum_{k=1}^{M}\left|Y_T^{(k)}[l_1+l_2]\right|^2} \tag{3.66}$$

Based on the Schwartz inequality, the auto-bicoherence will assume values between zero and one. The pair of frequency components at frequencies l_1, l_2 and their sum at l_1+l_2 are then quadratically coupled if $b^2(l_1,l_2)=1$, not quadratically coupled if $b^2(l_1,l_2)=0$, and partially coupled if $0<b^2(l_1,l_2)<1$. If there is no phase relationship among frequency components at l_1, l_2 in $x(t)$ and the frequency component at l_1+l_2 in $y(t)$, the value of the cross-bicoherence will be near zero. If there is a phase relationship among these frequency components, the value of the cross-bicoherence will be near unity. Values of cross-bicoherence between zero and one indicate partial quadratic coupling and variations in the phase relation. More details about these moments and their applications and a digital procedure for computing the auto and cross-bicoherence can be found in Kim and Powers (1979), Hajj, Miksad, and Hajj et al. (1993), Powers and Im (1995) and Hajj et al.. It is important to note here that the non-linearity produces a third harmonic in the response whose amplitude can also be used to assess damage. This is exemplified by the amplitude of the third harmonic in the approximate solution which is dependent on α, k_1 and k_2.

Examples of time histories acquired during the experiments are shown from Figure 3.9 to Figure 3.13. At each *State* three measurements of excitation and response are considered. Of particular interest is that the response amplitude increases only by decreasing the excitation frequency without varying its amplitude.

Power spectra of these measurements prove also this behavior and are shown from Figure 3.14 to Figure 3.18. The excitation shows two peaks corresponding respectively to the fundamental and the second harmonic. The response power spectrum shows three peaks corresponding respectively to the natural frequency, to the excitation frequency, and to a

third harmonic which is associated to the nonlinearities of the beam-mass system. As the excitation frequency is decreased, the response amplitude increases.

Cross-bicoherence contours of the same measurements are shown from Figure 3.19 to Figure 3.23. Quadratic phase coupling between excitation and response is then pointed out. The contour levels are set, indeed, between 0.98 and 0.99, indicating the expected high level of coupling and confidence in the estimated phase relation.

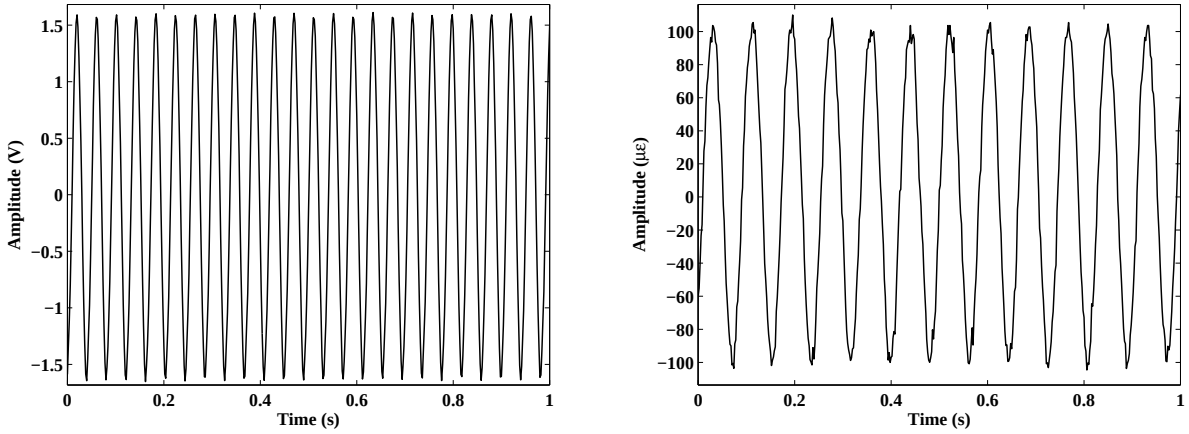

(a)

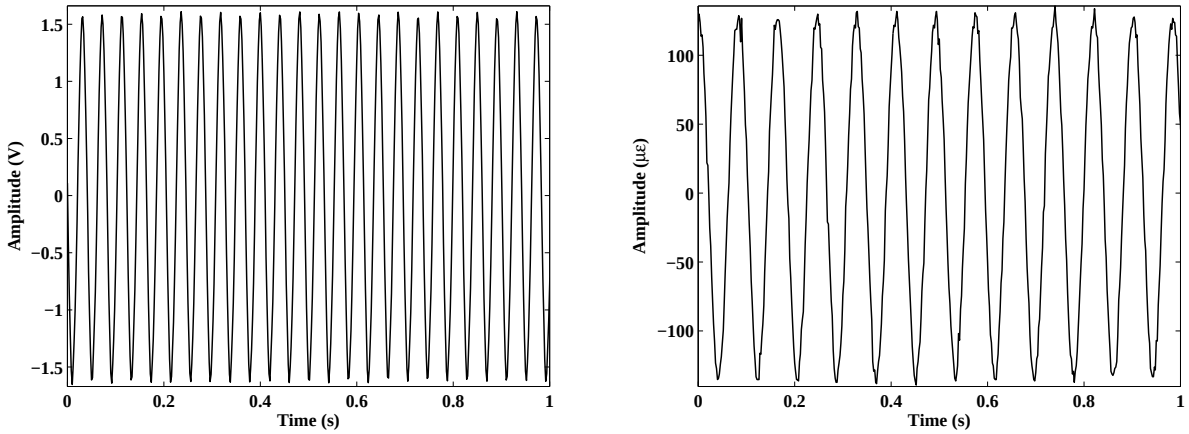

(b)

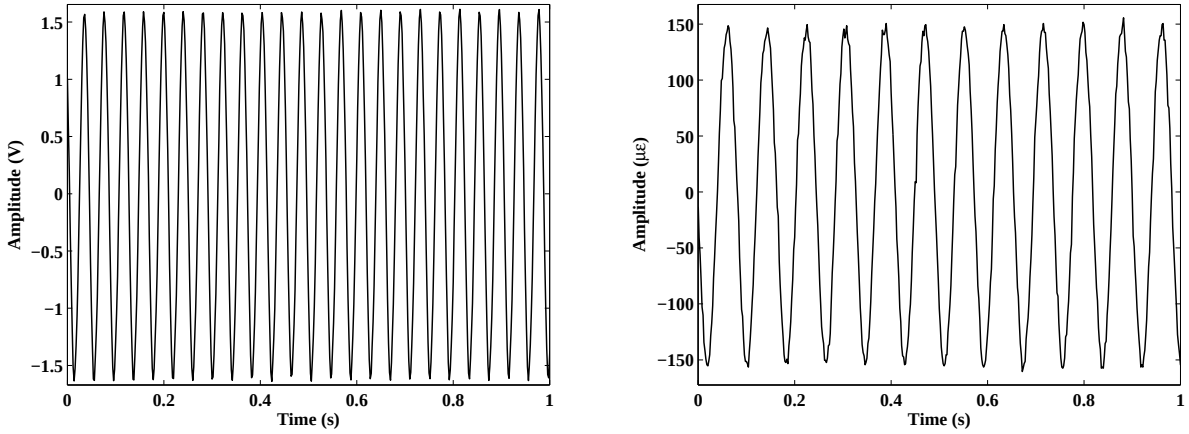

(c)

Figure 3.9: Time histories of excitation and response in $State_1$ for three different measurements when the excitation frequency is set equal to (a) $24.417Hz$, (b) $24.414Hz$, and (c) $24.411Hz$, respectively.

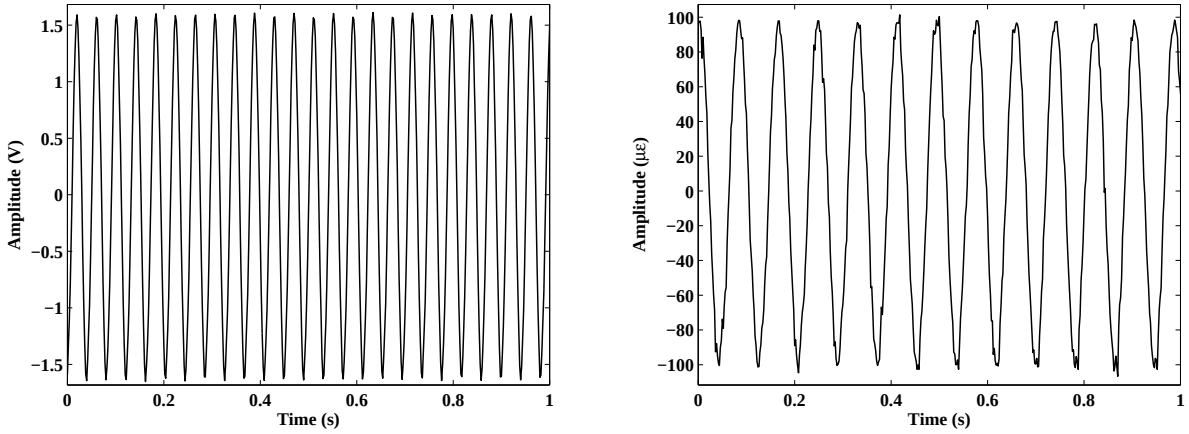

(a)

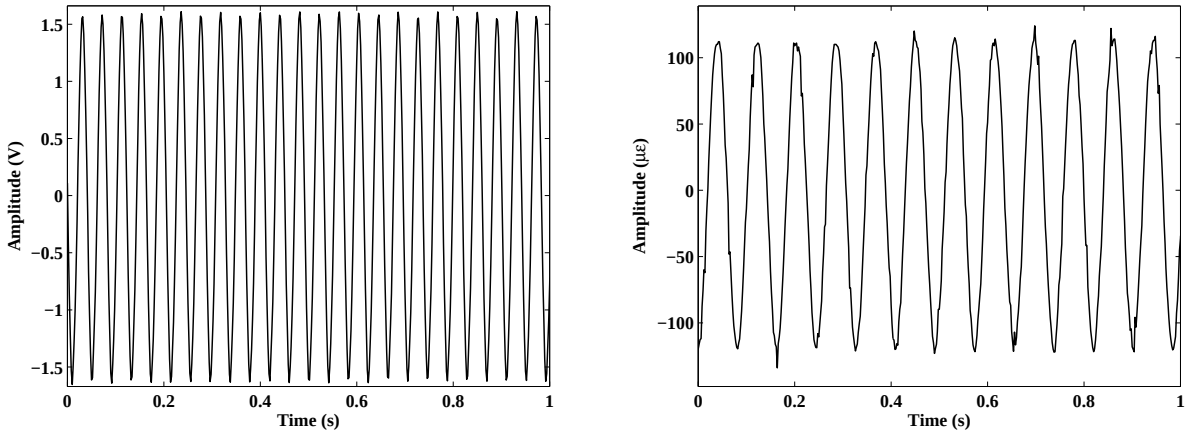

(b)

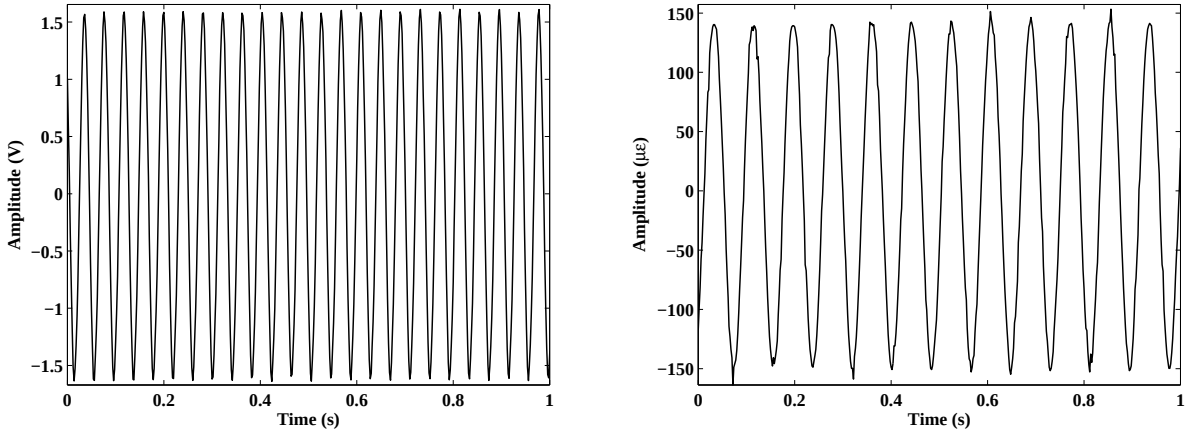

(c)

Figure 3.10: Time histories of excitation and response in $State_2$ for three different measurements when the excitation frequency is set equal to (a) $24.372Hz$, (b) $24.367Hz$, and (c) $24.362Hz$, respectively.

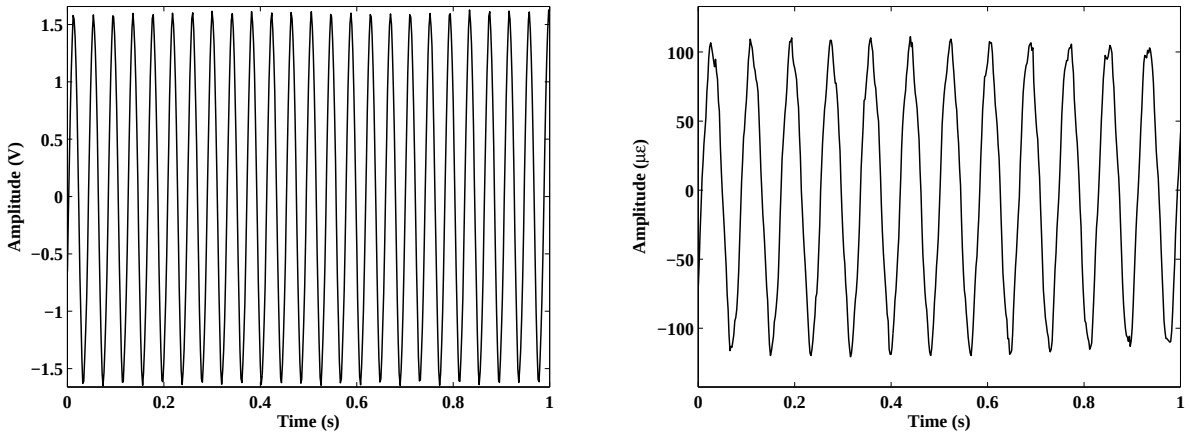

(a)

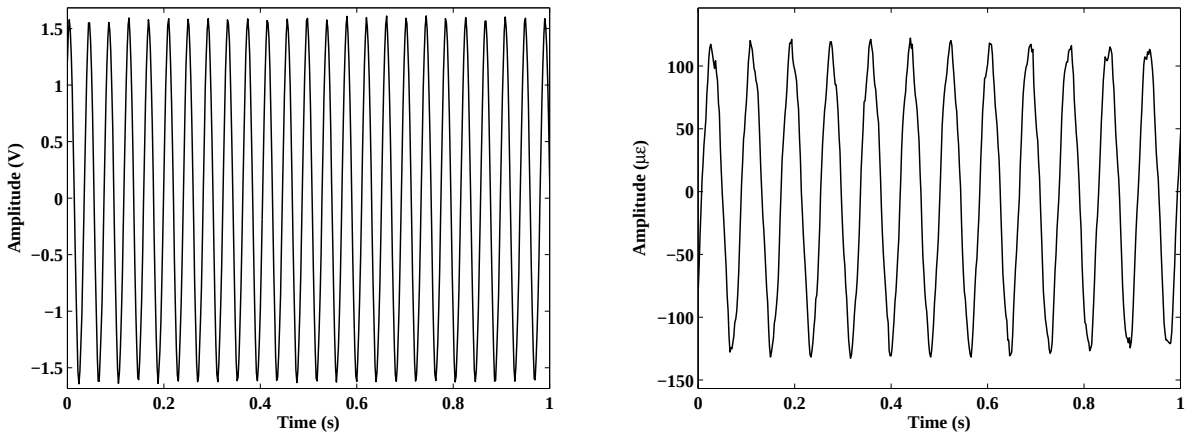

(b)

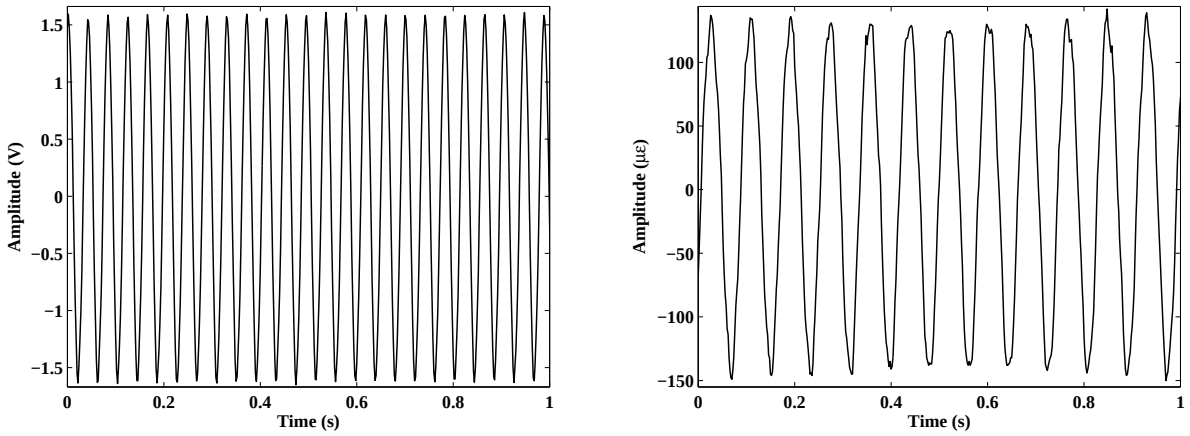

(c)

Figure 3.11: Time histories of excitation and response in $State_3$ for three different measurements when the excitation frequency is set equal to (a) $24.335Hz$, (b) $24.319Hz$, and (c) $24.316Hz$, respectively.

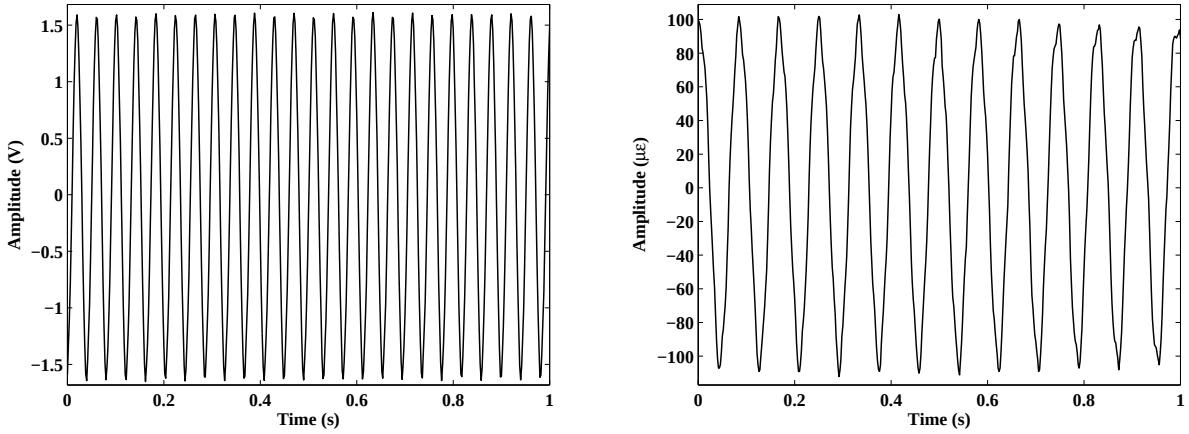

(a)

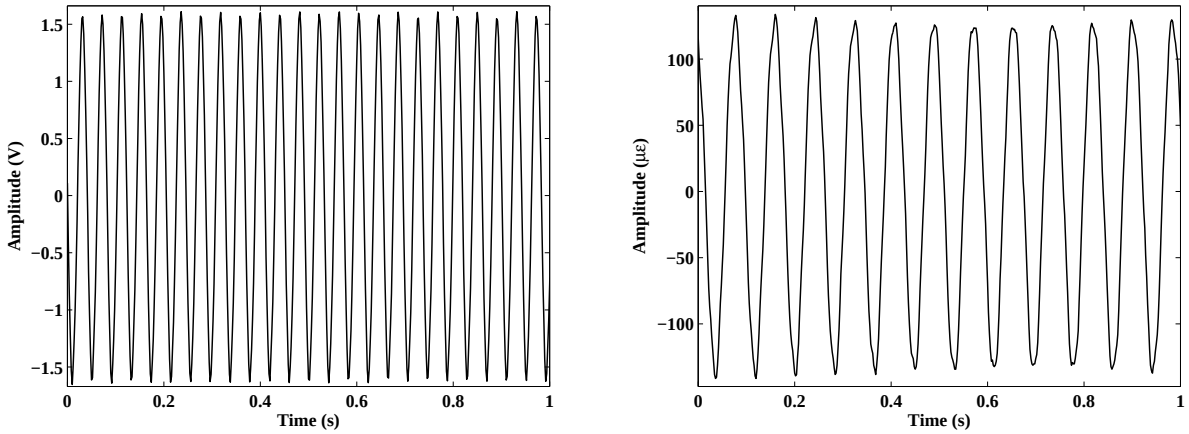

(b)

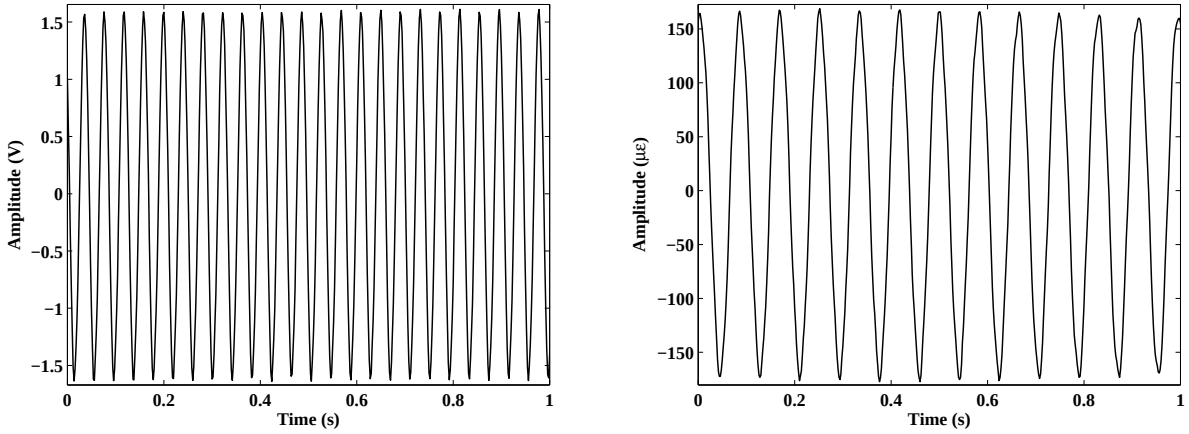

(c)

Figure 3.12: Time histories of excitation and response in $State_4$ for three different measurements when the excitation frequency is set equal to (a) $24.246Hz$, (b) $24.237Hz$, and (c) $24.226Hz$, respectively.

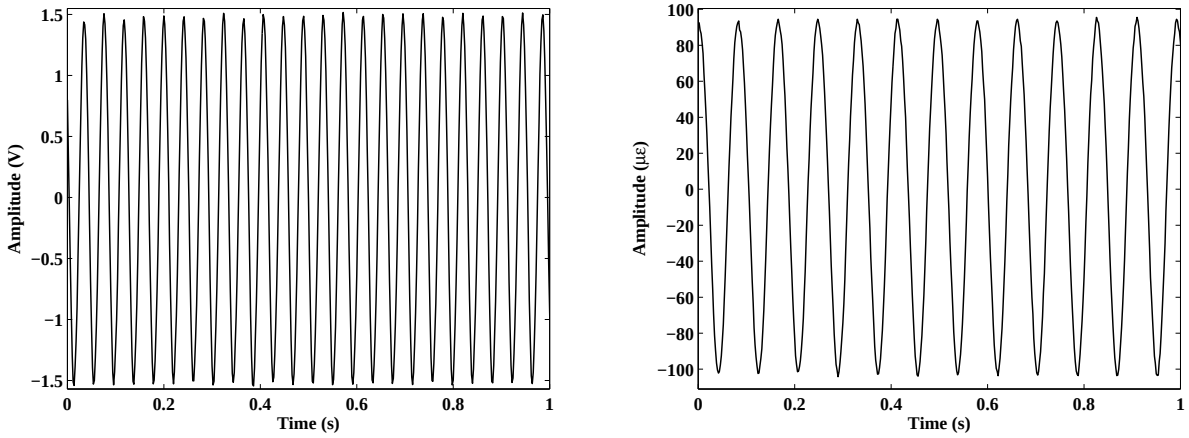

(a)

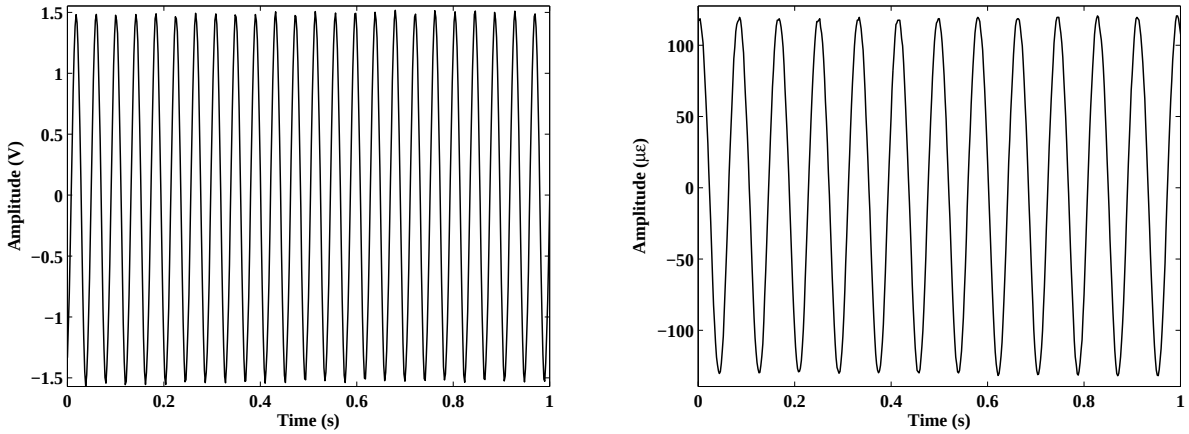

(b)

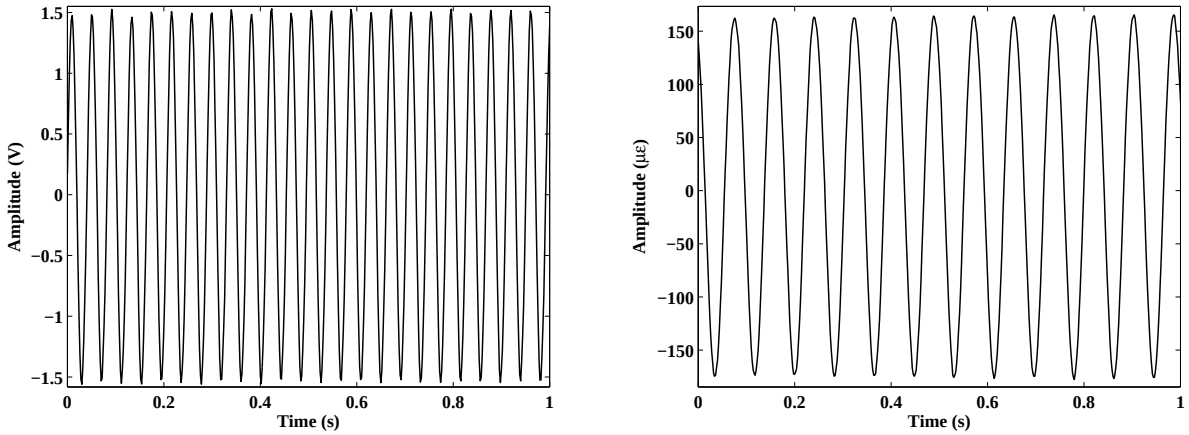

(c)

Figure 3.13: Time histories of excitation and response in $State_5$ for three different measurements when the excitation frequency is set equal to (a) $24.189Hz$, (b) $24.181Hz$, and (c) $24.172Hz$, respectively.

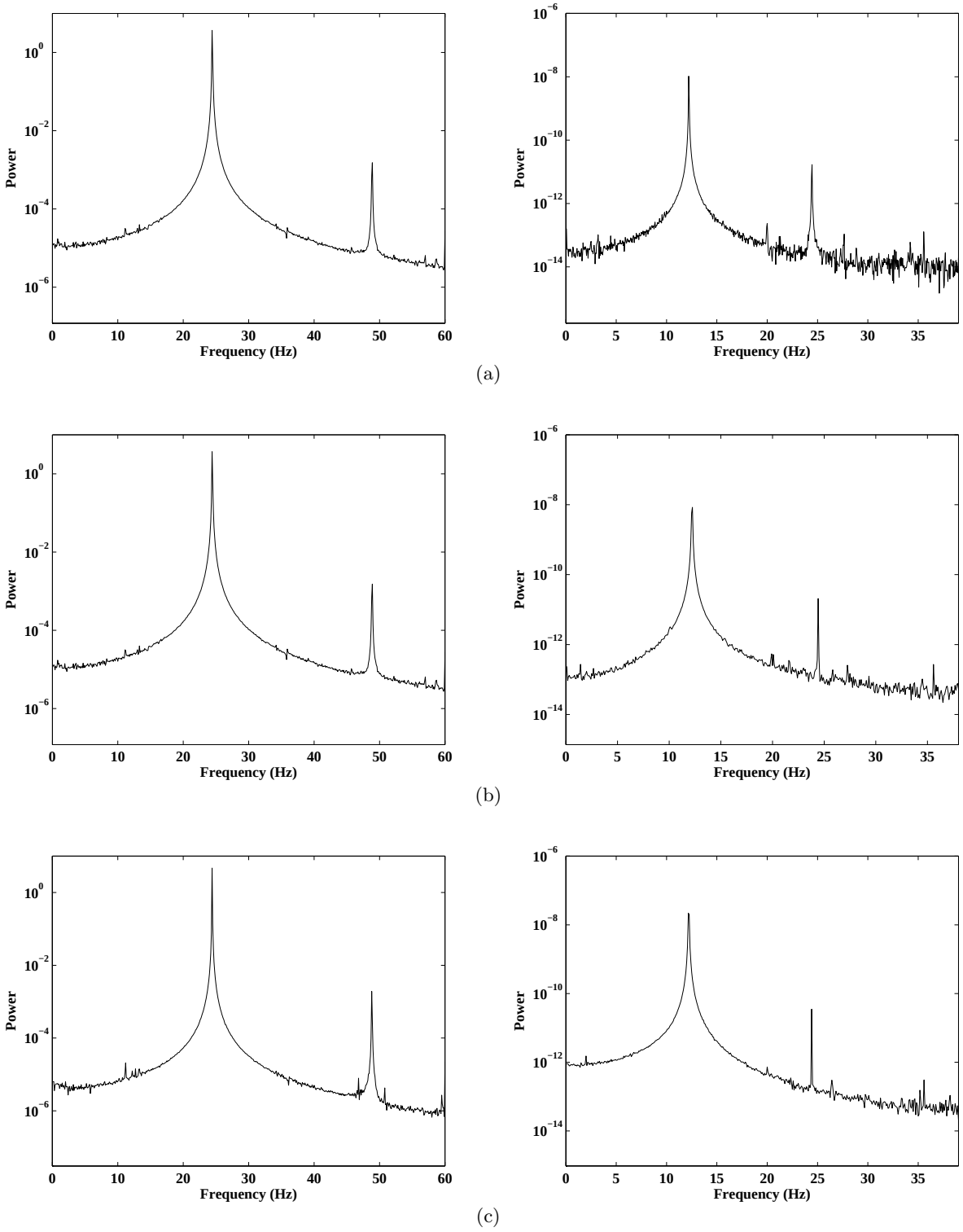

Figure 3.14: Power spectra of excitation and response in $State_1$ for three different measurements when the excitation frequency is set equal to (a) $24.417Hz$, (b) $24.414Hz$, and (c) $24.411Hz$, respectively.

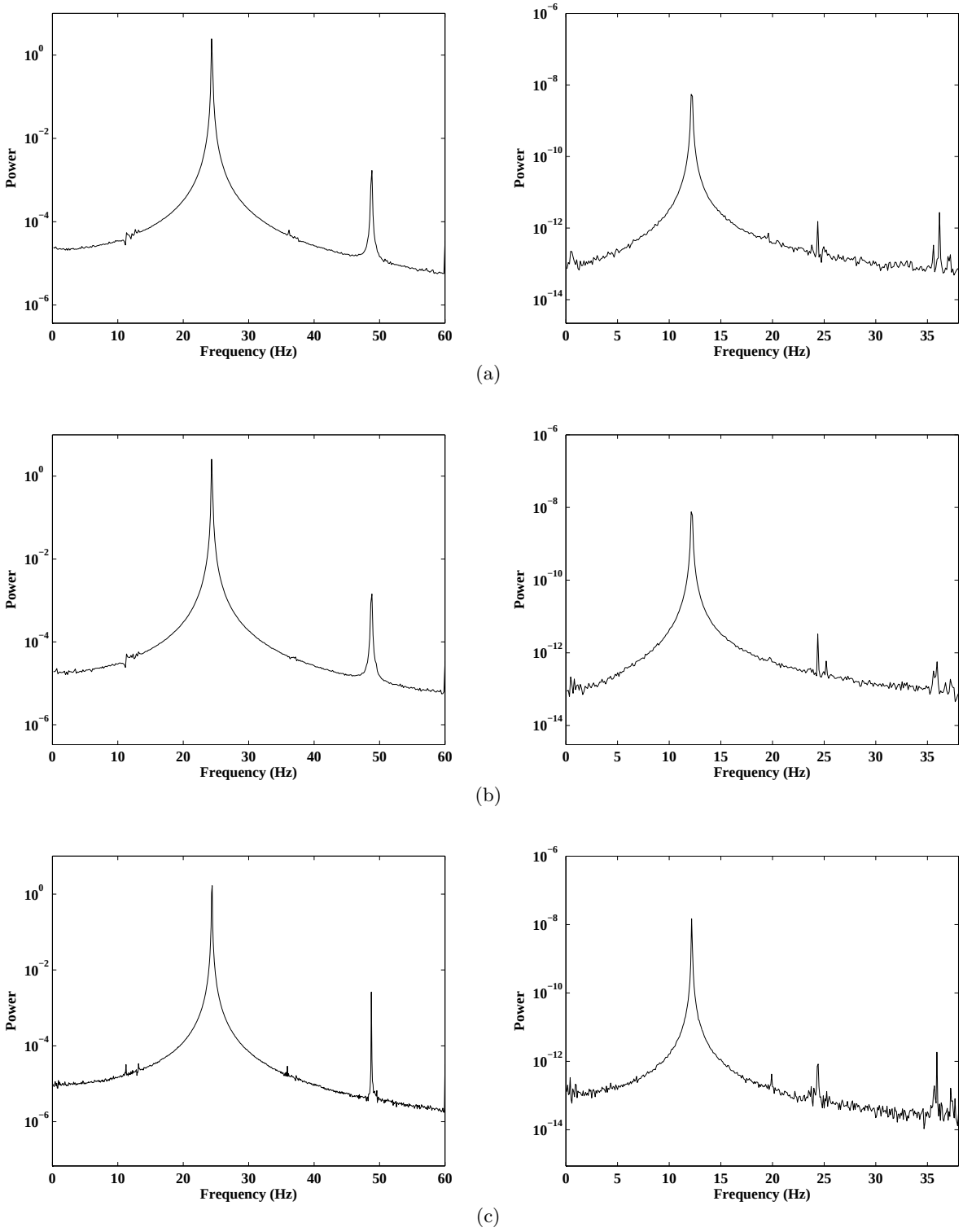

Figure 3.15: Power spectra of excitation and response in $State_2$ for three different measurements when the excitation frequency is set equal to (a) $24.372Hz$, (b) $24.367Hz$, and (c) $24.362Hz$, respectively.

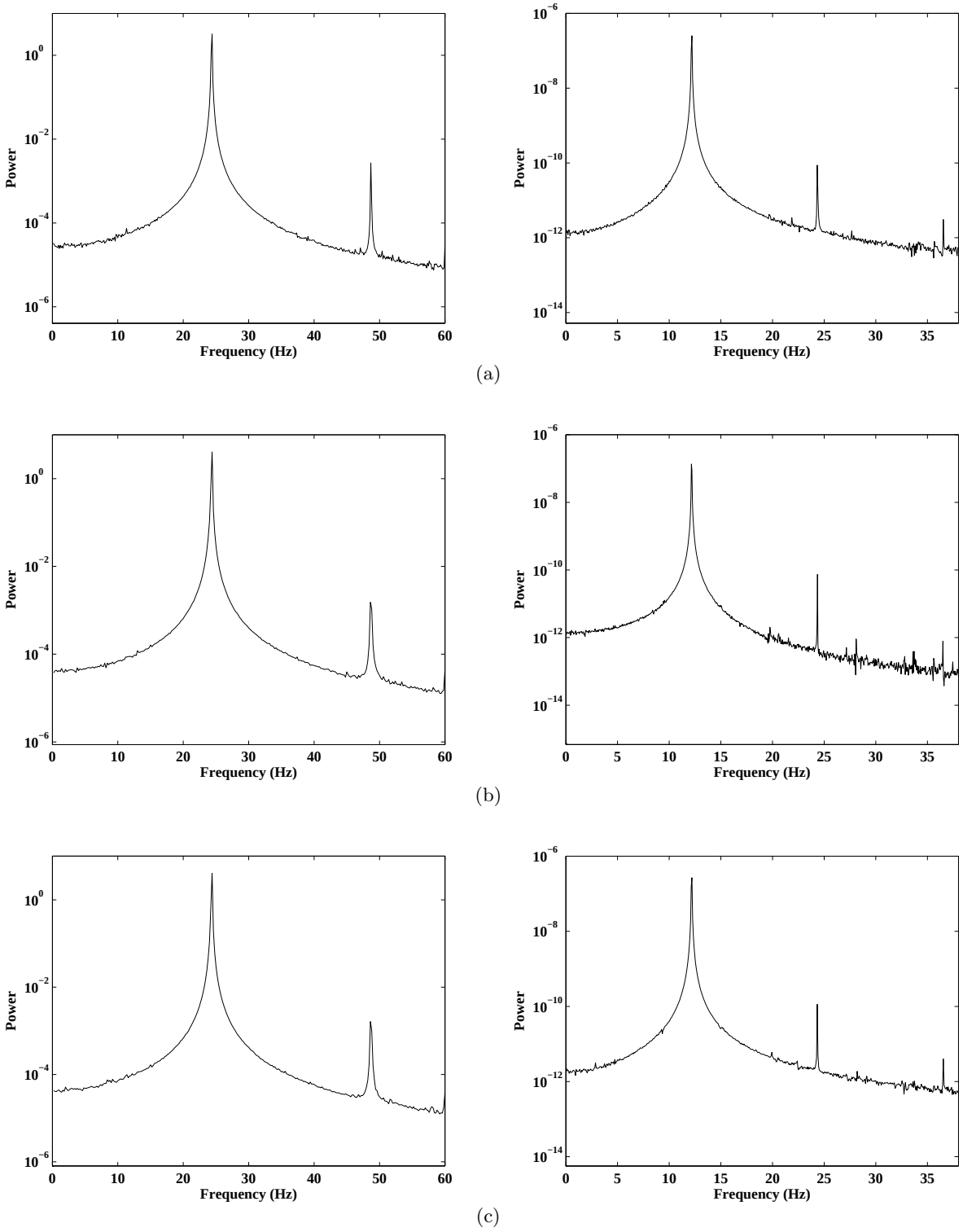

Figure 3.16: Power spectra of excitation and response in $State_3$ for three different measurements when the excitation frequency is set equal to (a) $24.335Hz$, (b) $24.319Hz$, and (c) $24.316Hz$, respectively.

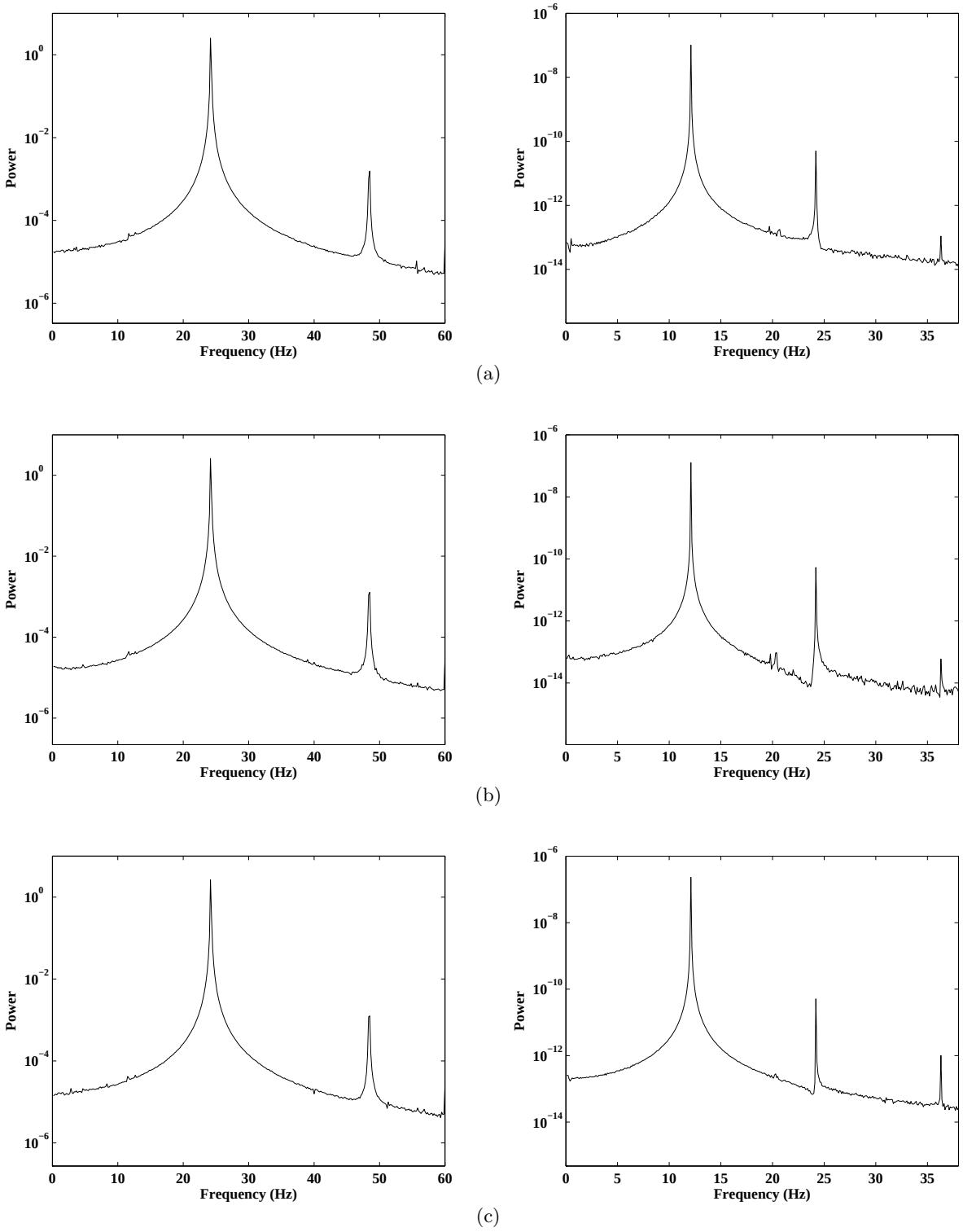

Figure 3.17: Power spectra of excitation and response in $State_4$ for three different measurements when the excitation frequency is set equal to (a) $24.246Hz$, (b) $24.237Hz$, and (c) $24.226Hz$, respectively.

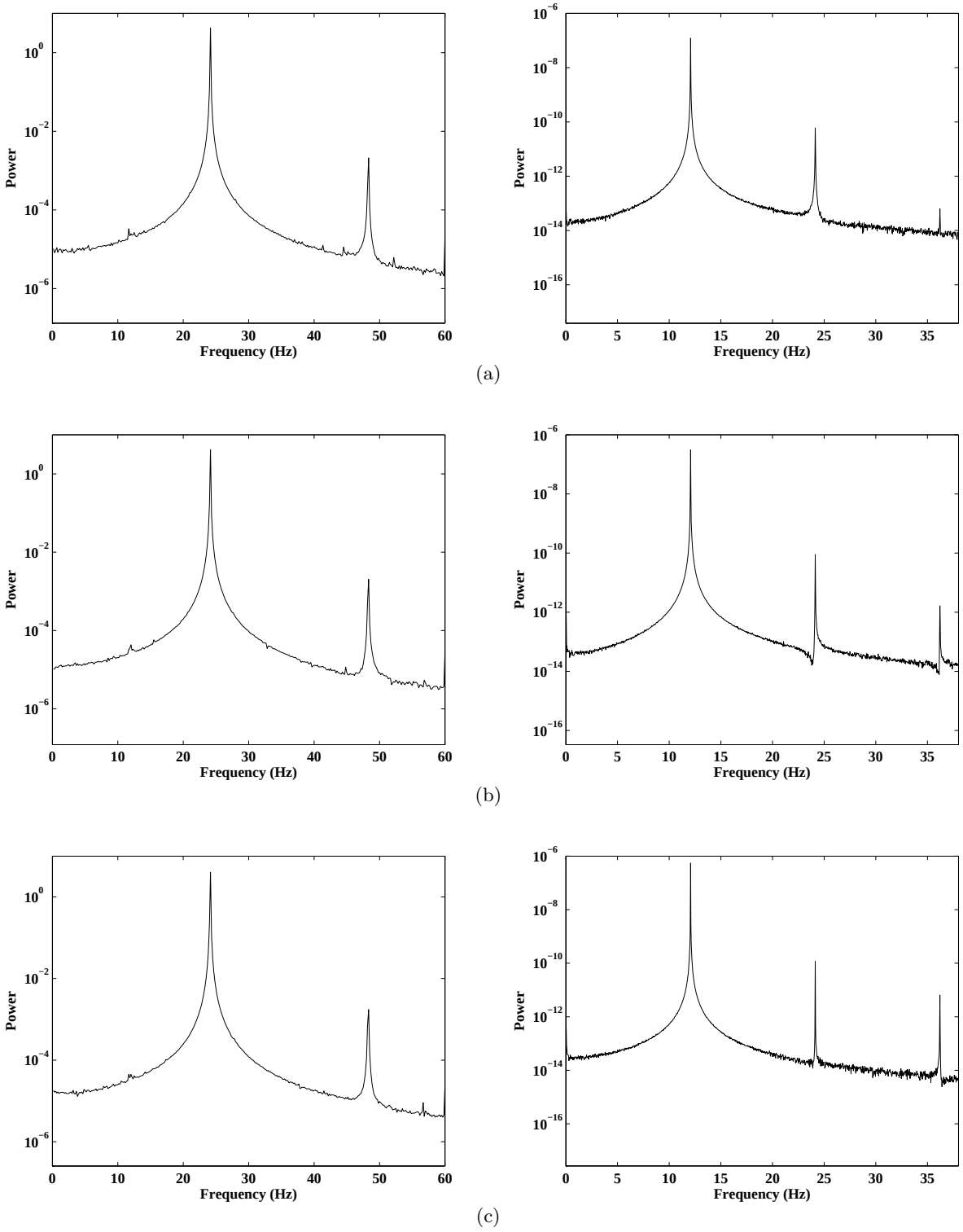

Figure 3.18: Power spectra of excitation and response in $State_5$ for three different measurements when the excitation frequency is set equal to (a) $24.189Hz$, (b) $24.181Hz$, and (c) $24.172Hz$, respectively.

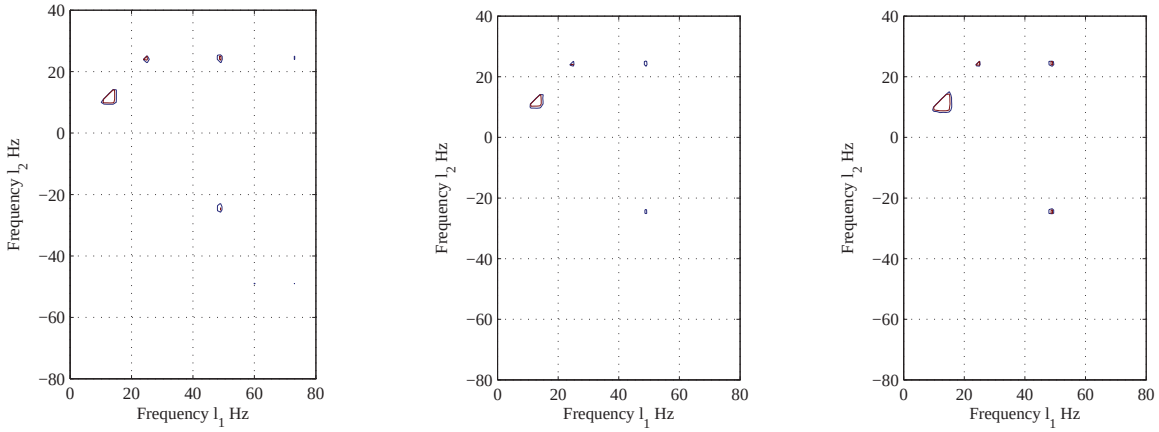

(a) (b) (c)

Figure 3.19: Cross-bicoherence $State_1$ for three different measurements when the excitation frequency is set equal to (a) $24.417Hz$, (b) $24.414Hz$, and (c) $24.411Hz$, respectively.

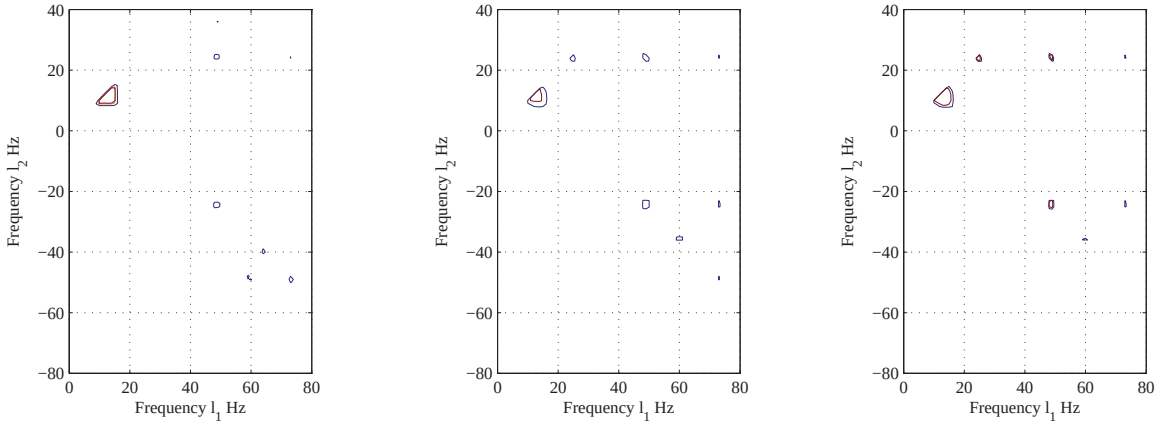

(a) (b) (c)

Figure 3.20: Cross-bicoherence $State_2$ for three different measurements when the excitation frequency is set equal to (a) $24.372Hz$, (b) $24.367Hz$, and (c) $24.362Hz$, respectively.

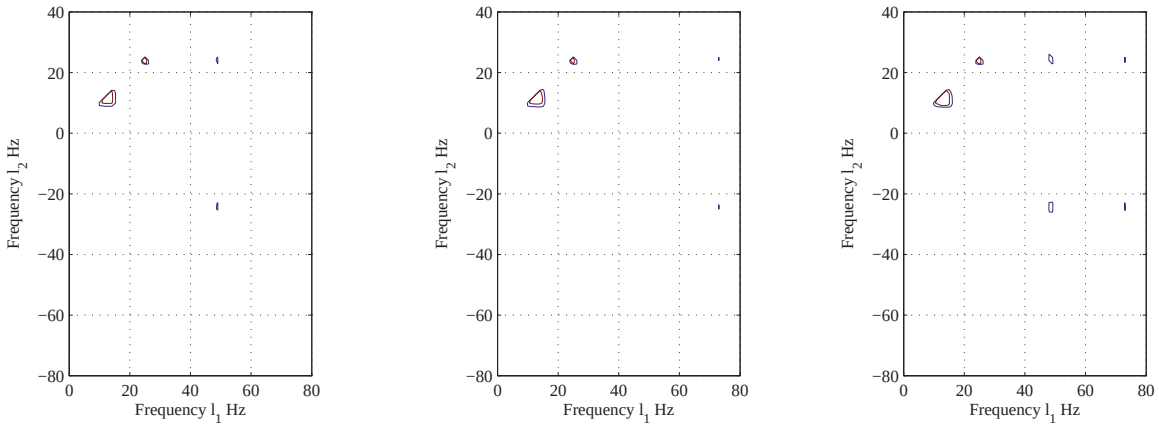

(a) (b) (c)

Figure 3.21: Cross-bicoherence $State_3$ for three different measurements when the excitation frequency is set equal to (a) $24.335Hz$, (b) $24.319Hz$, and (c) $24.316Hz$, respectively.

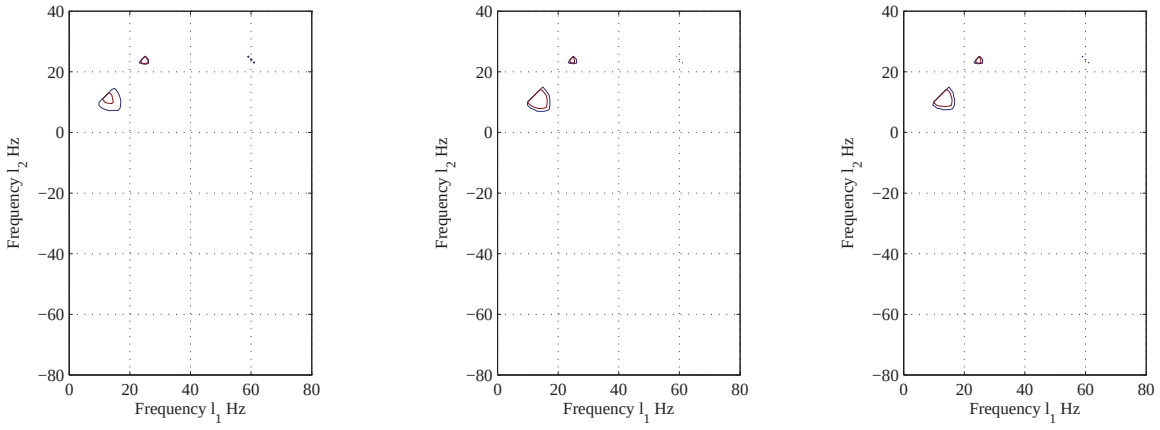

(a) (b) (c)

Figure 3.22: Cross-bicoherence $State_4$ for three different measurements when the excitation frequency is set equal to (a) $24.246Hz$, (b) $24.237Hz$, and (c) $24.226Hz$, respectively.

3.6 System Identification

Parameter identification was carried out through analysis of measured steady-state responses and corresponding excitations. The amplitude of the response, a, was determined from the power spectrum. The phase of the cross-bispectrum was used to determine the phase relation defined as 2β which was estimated to be between 130° and 140° for all data analyzed here. In all data, the cross-bicoherence between the excitation and response frequencies assumed values between 0.98 and 0.99; indicating the expected high level of coupling and confidence in the estimated phase relation. Table 3.1 shows the estimated value of the phase 2β, its corresponding cross-bicoherence, and the excitation frequency at which these values are identified for three measurements at each state. Variations in the natural frequency over the five states of Figure 3.6 are presented in Table 3.2. The results clearly show modest drop in the natural frequency with damage progression that would have been hard to evaluate without the slow sweep. Values of the excitation amplitude f along each state were approximated by $\frac{cos(2\beta)}{2\sigma}$ for the starting point along each state where the response amplitude was relatively small. Plotting $f\cos 2\beta$ vs. a^2, as presented in Figure 3.24, shows that the linear representation

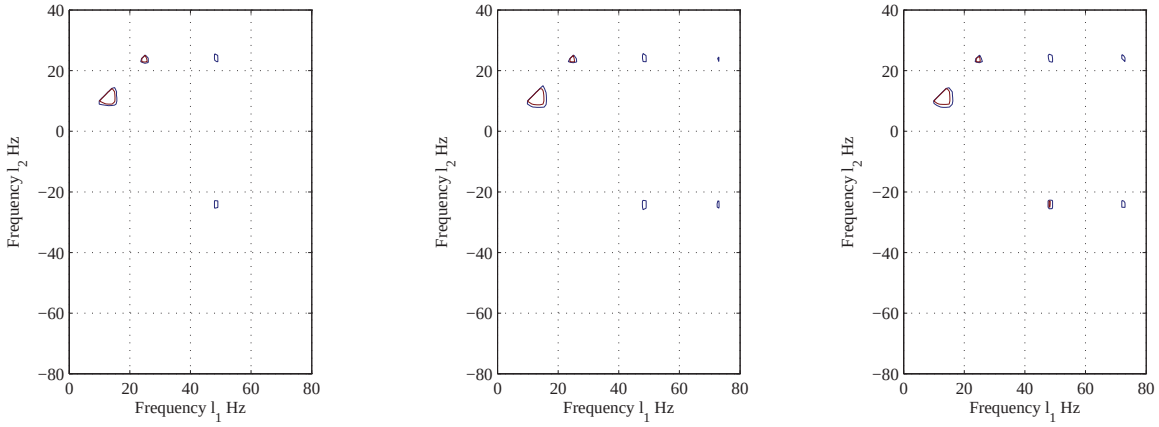

(a) (b) (c)

Figure 3.23: Cross-bicoherence $State_5$ for three different measurements when the excitation frequency is set equal to (a) $24.189Hz$, (b) $24.181Hz$, and (c) $24.172Hz$, respectively.

Table 3.1: Phase and bicoherence for the first metallic beam.

	2β	$b^2_{yxx}[l_1, l_2]$	$\widehat{\Omega}$ (Hz)
$State_1$	140.84	0.9869	24.417
(12.203 Hz)	140.99	0.9869	24.414
	141.04	0.9904	24.411
$State_2$	140.53	0.9949	24.372
(12.177 Hz)	140.64	0.9921	24.367
	140.78	0.9949	24.362
$State_3$	140.29	0.9965	24.335
(12.132 Hz)	140.47	0.9934	24.319
	140.41	0.9938	24.316
$State_4$	139.66	0.9983	24.246
(12.101 Hz)	140.06	0.9965	24.237
	140.14	0.9983	24.226
$State_5$	140.15	0.9951	24.189
(12.067 Hz)	140.24	0.9976	24.181
	140.65	0.9932	24.172

Table 3.2: Identified values of ω, f, α_e, ζ_1, and ζ_2.

	$\omega(Hz)$	$forcing$	α_e $(\mu\varepsilon^{-2})$	ζ_1	ζ_2 $(\mu\varepsilon^{-1})$
$State_1$	12.203	$4.173 \cdot 10^{-3}$	$7.26 \cdot 10^{-10}$	$6.42 \cdot 10^{-4}$	$1.44 \cdot 10^{-7}$
$State_2$	12.177	$4.415 \cdot 10^{-3}$	$8.21 \cdot 10^{-10}$	$6.84 \cdot 10^{-4}$	$1.61 \cdot 10^{-7}$
$State_3$	12.132	$4.657 \cdot 10^{-3}$	$1.02 \cdot 10^{-9}$	$7.26 \cdot 10^{-4}$	$1.71 \cdot 10^{-7}$
$State_4$	12.101	$5.112 \cdot 10^{-3}$	$1.18 \cdot 10^{-9}$	$8.01 \cdot 10^{-4}$	$2.09 \cdot 10^{-7}$
$State_5$	12.067	$6.014 \cdot 10^{-3}$	$1.51 \cdot 10^{-9}$	$9.45 \cdot 10^{-4}$	$2.78 \cdot 10^{-7}$

of this relation in equation 4.4 is correct. Furthermore, the slope of this linear fit yields the effective nonlinearity, α_e. Its variation over the different stages of damage progression is presented in Table 3.2. The results show that α_e increases with damage progression.

Plotting $f \sin 2\beta$ vs. a yields a linear relation which again shows the need to add the quadratic damping term in equation 4.1. Using equation 4.3, the intercept and slope of the linear fits yield, respectively, the values of the linear and quadratic damping coefficients. These values are presented in Table 3.2. Again the results show an increase in both damping coefficients. Validation of all values presented in Table 3.2 was performed by integrating equation 4.1 along all states. The coefficients α, k_1, and k_2 in this equation were evaluated from α_e and proportionally to the physically derived values of Zavodney and Nayfeh (1989).

Another measure of the effective nonlinearity can be determined from the amplitude of the third harmonic, a_3, as shown in equation 4.2. A plot of the variation of a_3 vs. a is presented in Figure 3.26. The results clearly show that the relative amplitude of $\frac{a_3}{a}$ increases with damage. This again shows that nonlinear effects become more relevant with damage progression. There are, however, two issues with using the amplitude ratio $\frac{a_3}{a}$. First, noise levels could impact these ratios. Second, this ratio depends on the amplitude of the response. As such, their values may not be clearly separated as is the case for $State_1$ and $State_2$ in Figure 3.26.

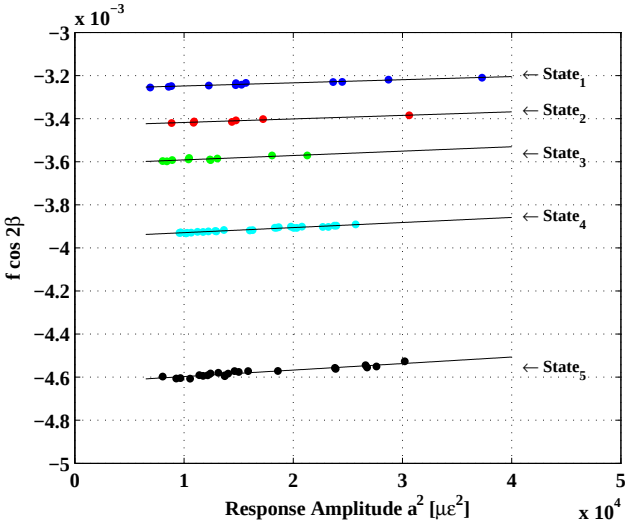

Figure 3.24: Variations of $f\cos 2\beta$ vs. a^2 used for identification of the effective nonlinearity coefficient α_e.

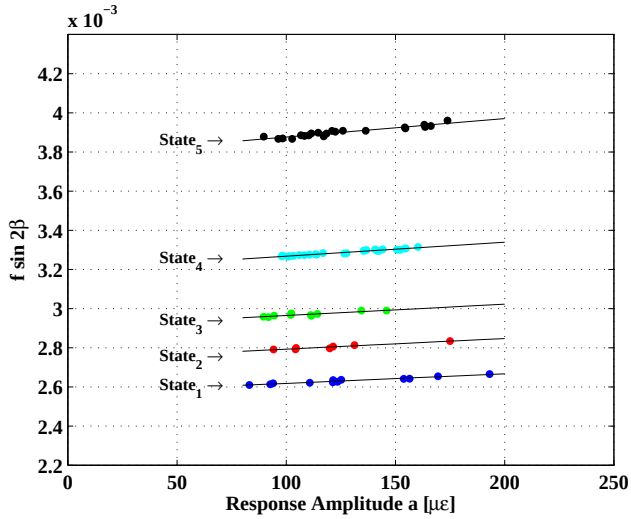

Figure 3.25: Variation of $f\sin 2\beta$ vs. a used for identification of linear and quadratic damping coefficients.

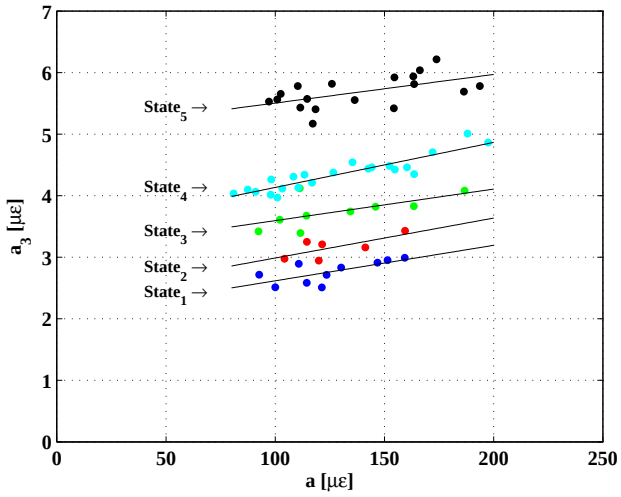

Figure 3.26: Variations of the third harmonic a_3 vs. the first harmonic a.

3.6.1 Sensitivity analysis

Percentage variations of natural frequency ω, linear and quadratic damping coefficients, and effective nonlinearity, over the different states of damage progression are presented in Table 3.3. The analysis shows that the reduction in the system's natural frequency is of the order of 1%. On the other hand, linear and quadratic damping parameters are characterized by remarkable increases of approximately 50% and 100%, respectively. The effective nonlinearity α_e shows also an increase of about 100%. Of particular interest is the trend of these variations where we observe that the percentage variation is continuously increasing between one state and next. As an example the variation between the first and second states of the nonlinear coeffient is about 13%. Between $State_4$ and $State_5$, this percentage is about 28%. This means that as $State_5$, where the crack has developed, was approached, the variations in all physical parameters were more pronounced.

3.6.2 Validation

Validation of the identified parameters was performed for three different measurements at each state. The results are shown from Figure 3.27 to Figure 3.31 and identified parameters

Table 3.3: Percentage variation of ω, α_e, ζ_1, and ζ_2.

	% ω	% α_e	% ζ_1	% ζ_2
$State_2$	-0.21	13.07	6.61	10.91
$State_3$	-0.58	40.26	13.15	17.78
$State_4$	-0.84	62.16	24.42	45.41
$State_5$	-1.12	108.27	47.17	93.32

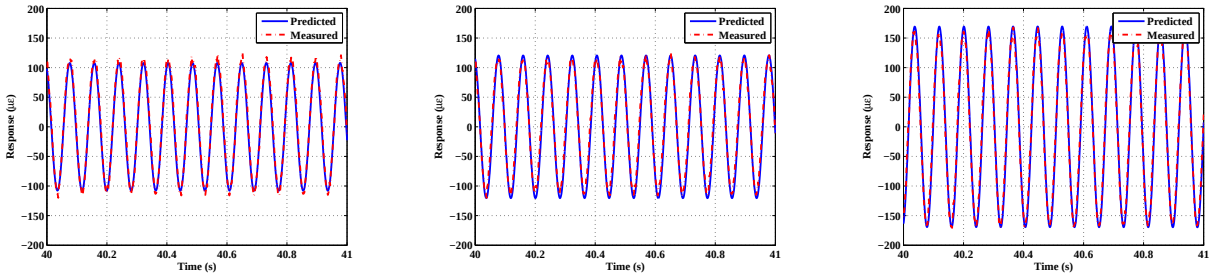

(a) (b) (c)

Figure 3.27: Validation of predicted response through comparison with the measured response for three different measurements of $State_1$ when the excitation frequency is set equal to (a) $24.417Hz$, (b) $24.414Hz$, and (c) $24.411Hz$, respectively.

yield correct prediction for the response.

3.7 Second Metallic Beam

A second set of experiments was designed in order to check the repeatability of the developed methodology for parametric identification and sensitivity analysis. Thus, a second metallic beam was machined with the same material and geometric characteristics as the first beam described above. Figure 3.32 shows the frequency response plot obtained from experiments. Each point was identified as the peak of the fundamental of the response power spectrum. The trend shown here resembles the one shown in Figure 3.6 for the first beam. The adopted experimental methodology is also the same. While keeping the excitation amplitude constant, its frequency was slowly descreased. When a value which is exactly twice the natural

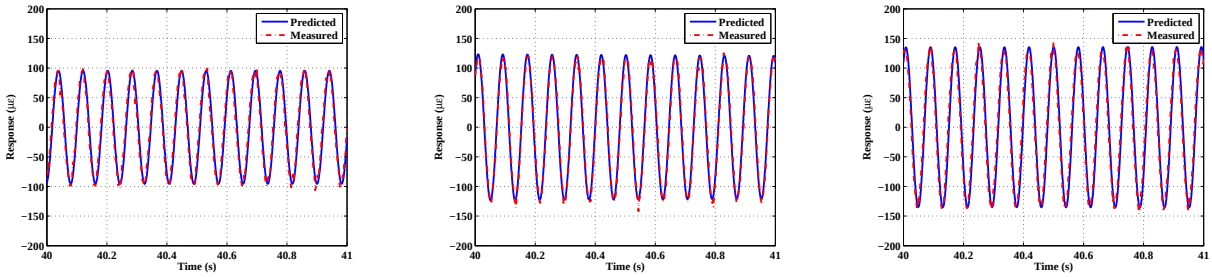

(a) (b) (c)

Figure 3.28: Validation of predicted response through comparison with the measured response for three different measurements of $State_2$ for three different measurements when the excitation frequency is set equal to (a) $24.372Hz$, (b) $24.367Hz$, and (c) $24.362Hz$, respectively.

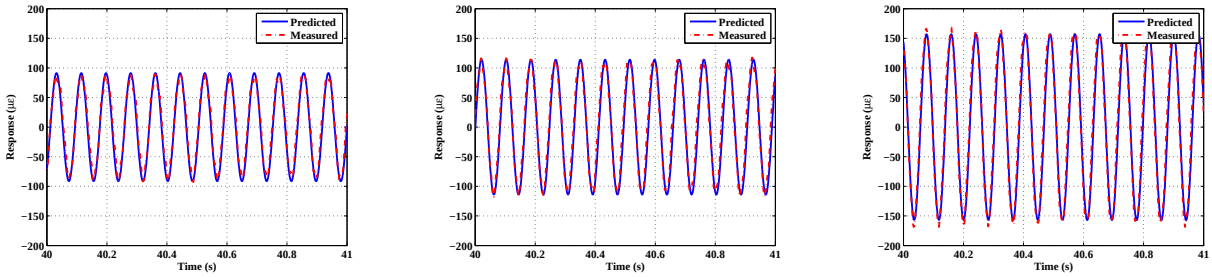

(a) (b) (c)

Figure 3.29: Validation of predicted response through comparison with the measured response for three different measurements of $State_3$ for three different measurements when the excitation frequency is set equal to (a) $24.335Hz$, (b) $24.319Hz$, and (c) $24.316Hz$, respectively.

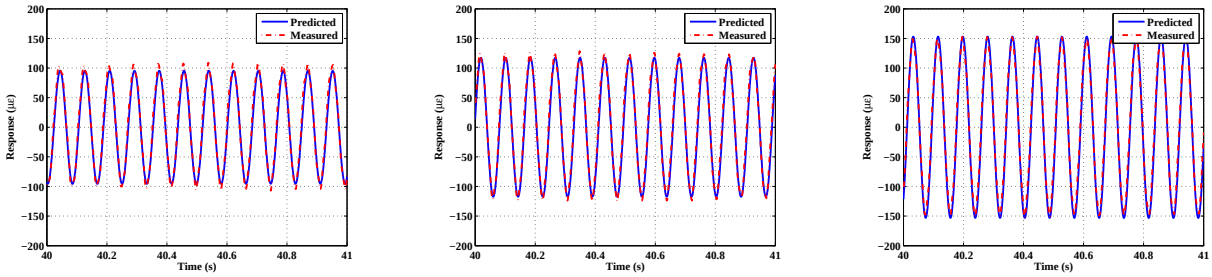

Figure 3.30: Validation of predicted response through comparison with the measured response for three different measurements of $State_4$ for three different measurements when the excitation frequency is set equal to (a) $24.246Hz$, (b) $24.237Hz$, and (c) $24.226Hz$, respectively.

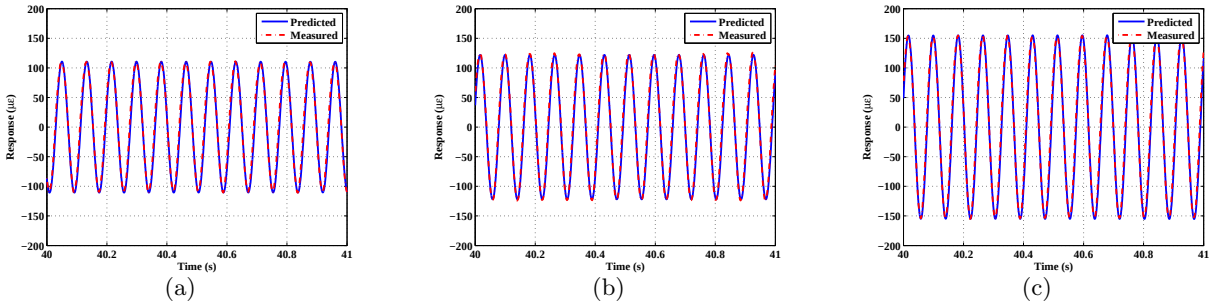

Figure 3.31: Validation of predicted response through comparison with the measured response for three different measurements of $State_5$ for three different measurements when the excitation frequency is set equal to (a) $24.189Hz$, (b) $24.181Hz$, and (c) $24.172Hz$, respectively.

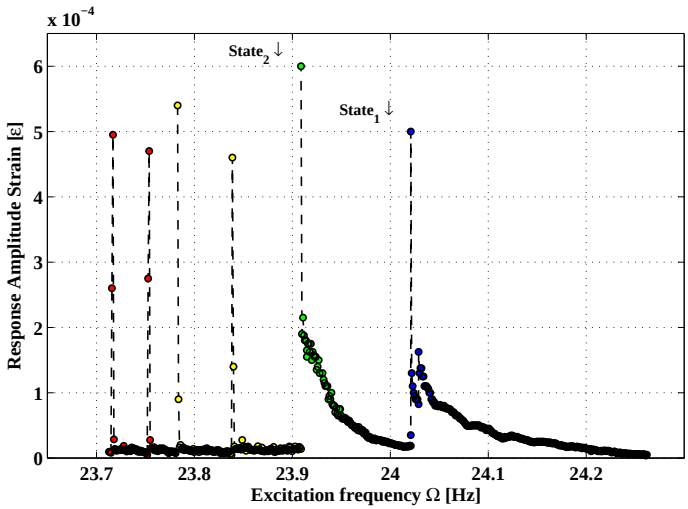

Figure 3.32: Frequency-response plot of the second metallic beam.

frequency was approched, the beam responded with large amplitude oscillation followed by a sudden drop. As the tests were further performed, this behavior repeated itself only a second time. The reason for this premature collapse is associated with the fact that the second beam amplitude response was much larger than the first beam and the cracks at each state propagated much quicker. Figure 3.33 is a photograph of the crack discovered in the second metallic beam at the end of the experiments.

3.7.1 Spectral Analysis of Excitation and Response

Examples of time histories acquired during the experiments are shown from Figure 3.34 to Figure 3.35. At each *State* three measurements of excitation and response are considered. Of particular interest is that the response amplitude increases only by decreasing the excitation frequency without varying its amplitude.

Power spectra of these measurements prove also this behavior and are shown from Figure 3.36 to Figure 3.37. The excitation shows two peaks corresponding respectively to the fundamental and the second harmonic. The response power spectrum shows three peaks corresponding respectively to the natural frequency, to the excitation frequency, and to a third harmonic which is associated to the nonlinearities of the beam-mass system. As the

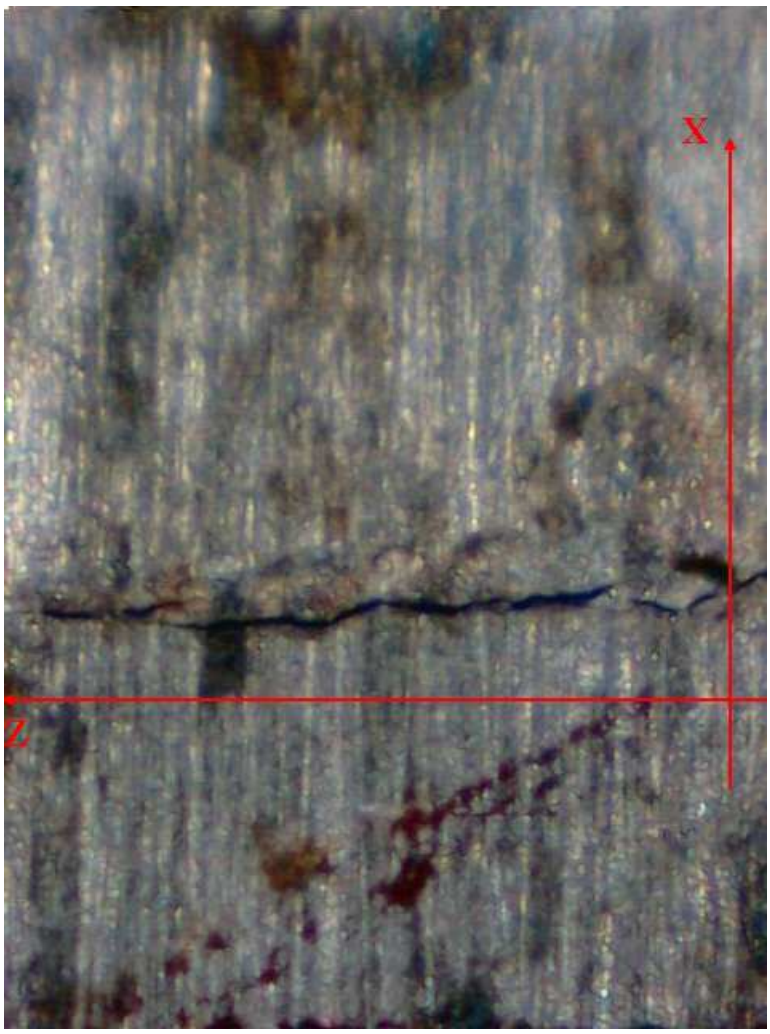

Figure 3.33: Photograph of the crack in the second metallic beam.

Table 3.4: Phase and bicoherence values for the second metallic beam.

	2β	$b^2_{yxx}[l_1, l_2]$	$\widehat{\Omega}$ (Hz)
$State_1$	155.88	0.9988	24.091
(12.0104 Hz)	155.67	0.9876	24.074
	154.48	0.9989	24.061
$State_2$	145.53	0.9908	23.961
(11.9544 Hz)	145.48	0.9933	23.955
	145.44	0.9864	23.949

excitation frequency is decreased, the response amplitude increases.

Cross-bicoherence contours of the same measurements are shown from Figure 3.38 to Figure 3.39. Quadratic phase coupling between excitation and response is then pointed out. The contour levels are set, indeed, between 0.98 and 0.99, indicating the expected high level of coupling and confidence in the estimated phase relation.

3.7.2 System Identification

Parameter identification adopted for the second metallic beam follows the same procedure described above for the first beam. Table 3.4 shows values of the identified phase 2β, its corresponding cross-bicoherence value, and the excitation frequency of the three measurements taken as example. Table 3.5 shows the identified natural frequency ω, the excitation forcing amplitude f, the effective nonlinearity α_e, the linear and quadratic damping coefficients ζ_1 and ζ_2, respectively. Figure 3.40 shows variations of $fcos2\beta$ vs. a^2 used for identification of the effective nonlinearity coefficient α_e and Figure 3.41 shows variations of $fsin2\beta$ vs. a used for identification of linear and quadratic damping coefficients. A plot of the variation of a_3 vs. a is presented in Figure 3.42. The results clearly show that the relative amplitude of $\frac{a_3}{a}$ increases with damage. The nonlinear effects become more relevant with damage progression.

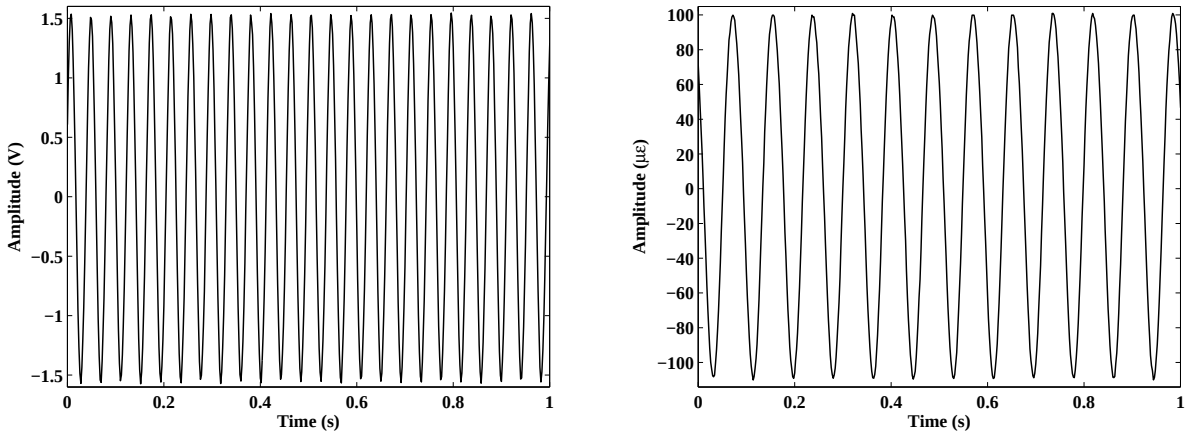

(a)

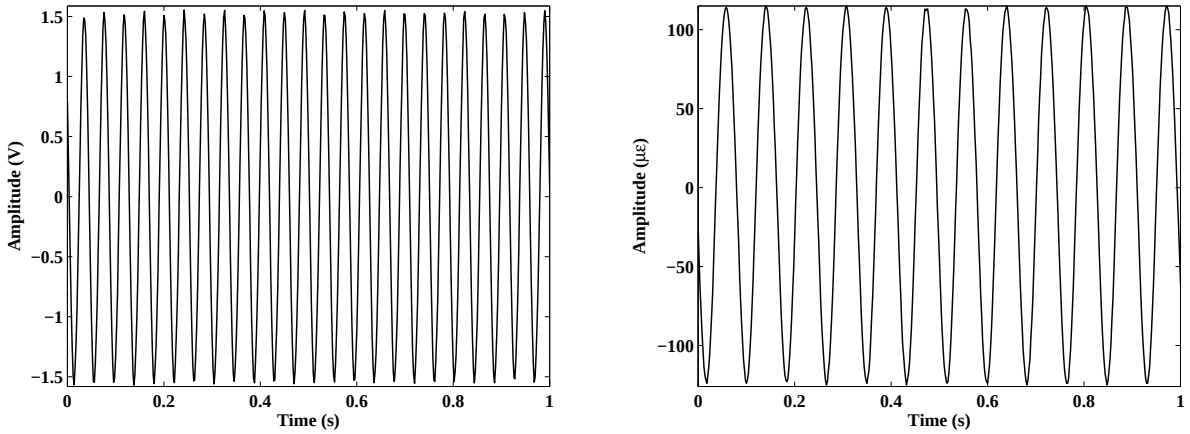

(b)

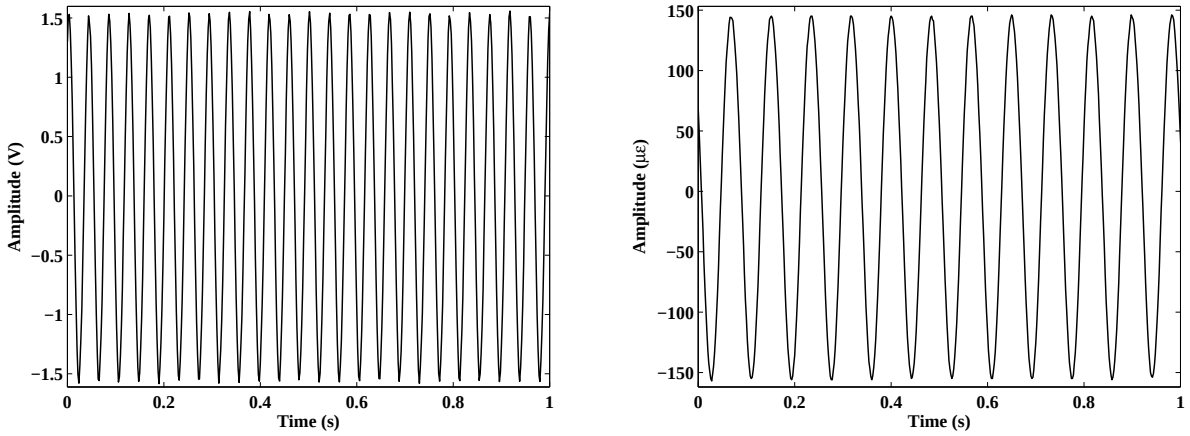

(c)

Figure 3.34: Time histories of excitation and response in $State_1$ for three different measurements when the excitation frequency is set equal to (a) $24.091Hz$, (b) $24.074Hz$, and (c) $24.061Hz$, respectively.

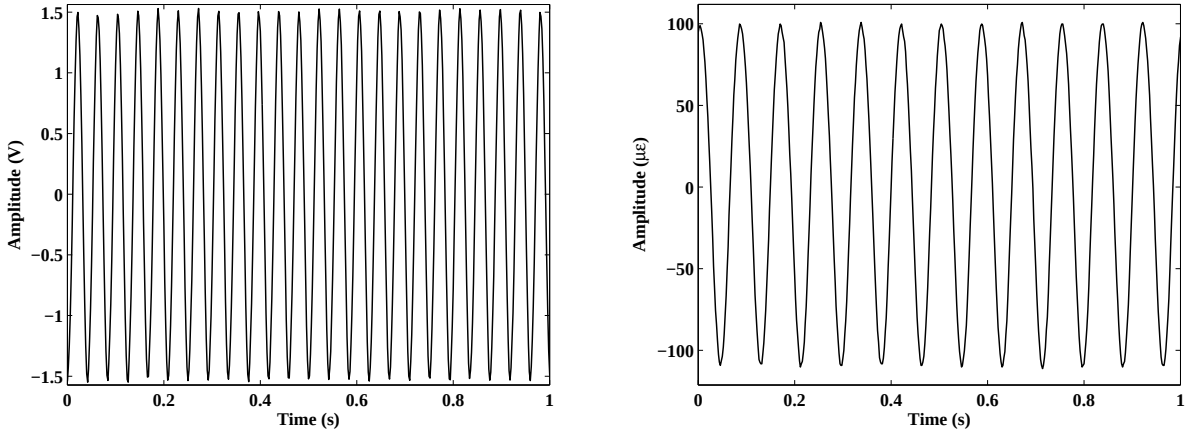

(a)

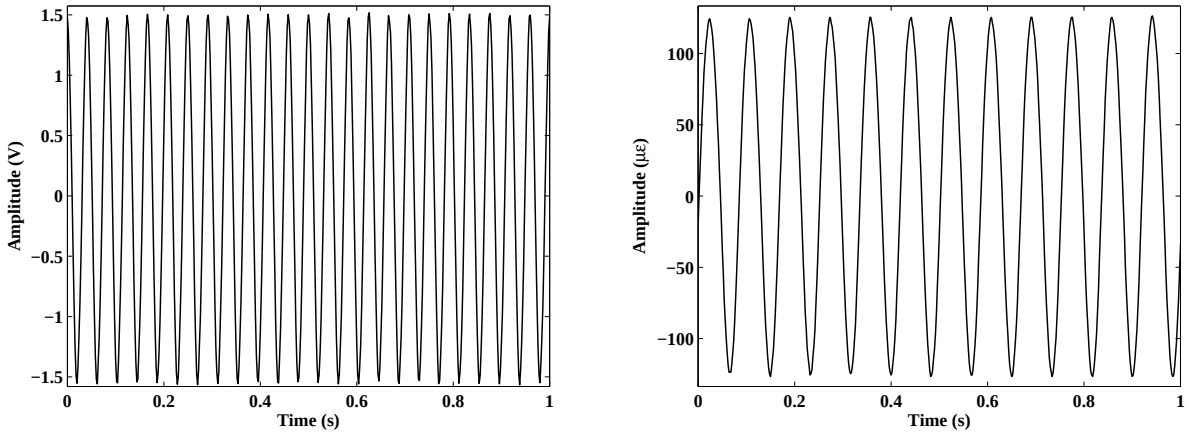

(b)

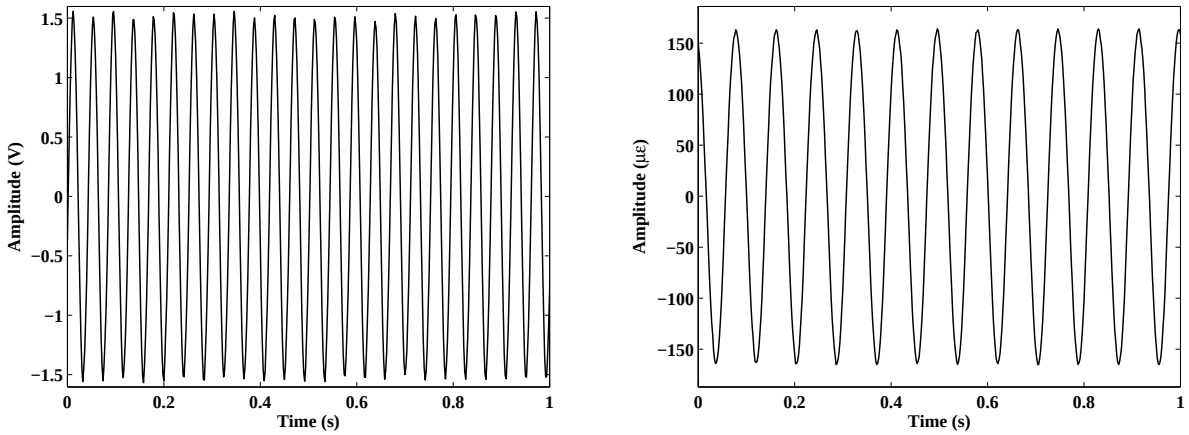

(c)

Figure 3.35: Time histories of excitation and response in $State_2$ for three different measurements when the excitation frequency is set equal to (a) $23.961Hz$, (b) $23.955Hz$, and (c) $23.949Hz$, respectively.

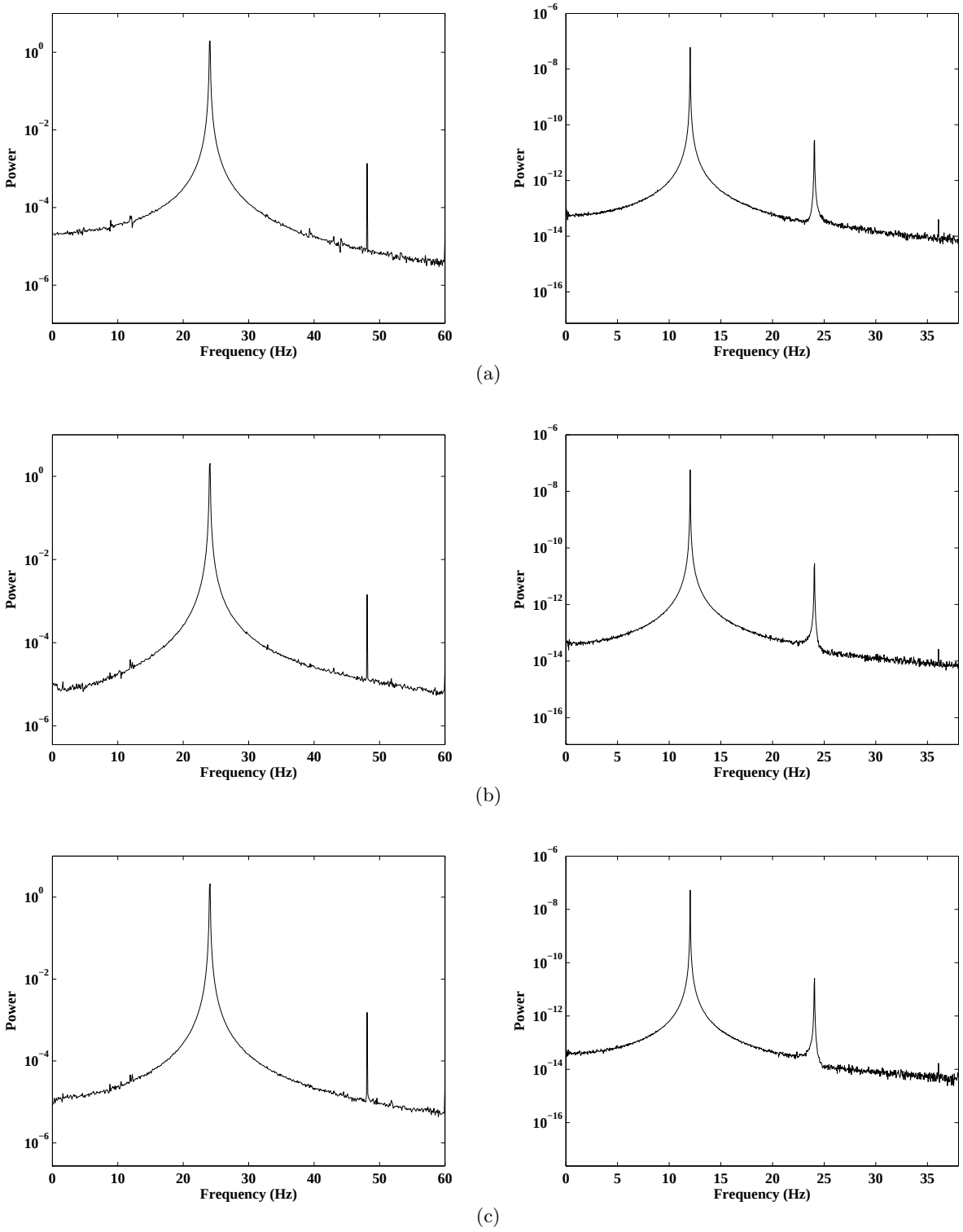

Figure 3.36: Power spectra of excitation and response in $State_1$ for three different measurements when the excitation frequency is set equal to (a) $24.091Hz$, (b) $24.074Hz$, and (c) $24.061Hz$, respectively.

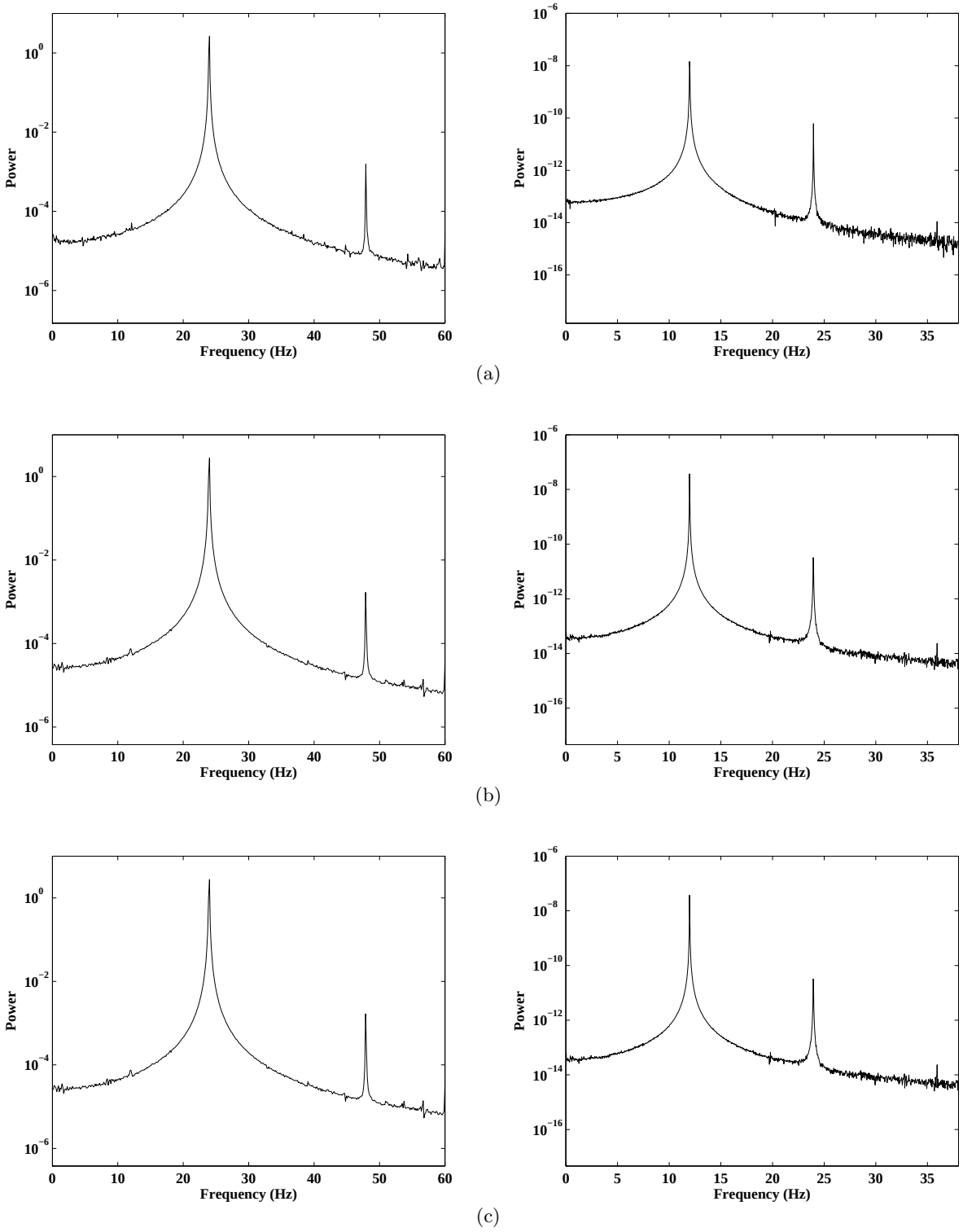

Figure 3.37: Power spectra of excitation and response in $State_2$ for three different measurements when the excitation frequency is set equal to (a) $23.961Hz$, (b) $23.955Hz$, and (c) $23.949Hz$, respectively.

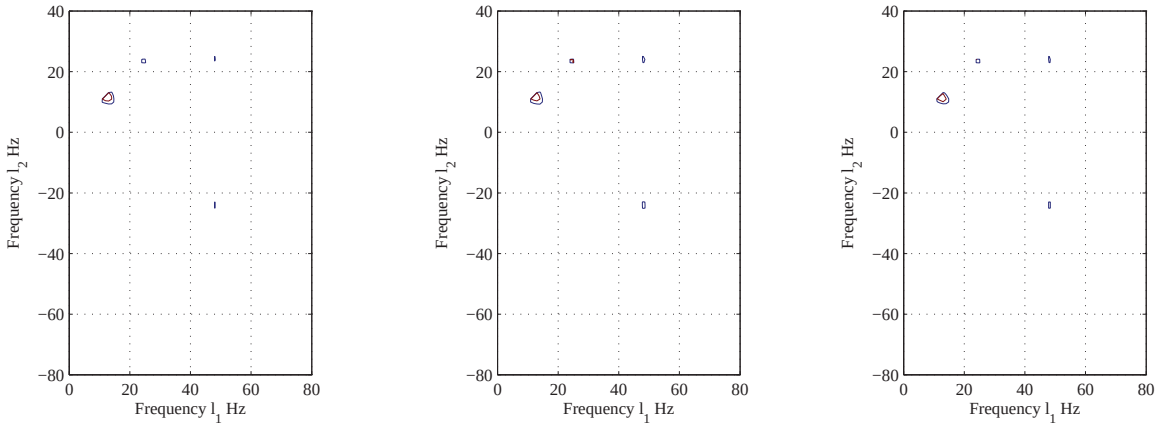

(a) (b) (c)

Figure 3.38: Cross-bicoherence $State_1$ for three different measurements when the excitation frequency is set equal to (a) $24.091Hz$, (b) $24.074Hz$, and (c) $24.061Hz$, respectively.

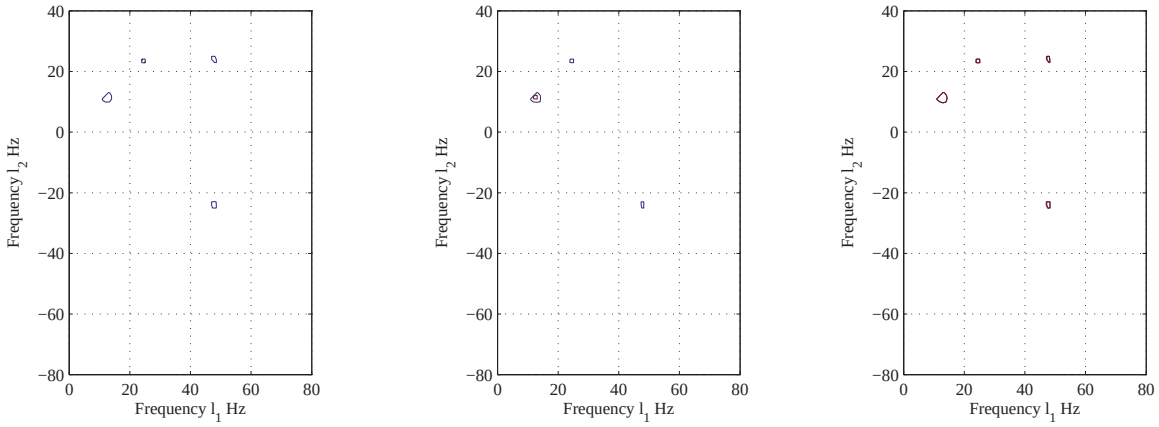

(a) (b) (c)

Figure 3.39: Cross-bicoherence $State_2$ for three different measurements when the excitation frequency is set equal to (a) $23.961Hz$, (b) $23.955Hz$, and (c) $23.949Hz$, respectively.

Table 3.5: Identified values of ω, f, α_e, ζ_1, and ζ_2 for the second metallic beam.

	$\omega(Hz)$	$forcing$	α_e $(\mu\varepsilon^{-2})$	ζ_1	ζ_2 $(\mu\varepsilon^{-1})$
$State_1$	12.010	0.01103	$4.37 \cdot 10^{-9}$	$9.88 \cdot 10^{-4}$	$1.53 \cdot 10^{-6}$
$State_2$	11.954	0.01304	$6.91 \cdot 10^{-9}$	$1.72 \cdot 10^{-3}$	$1.71 \cdot 10^{-6}$

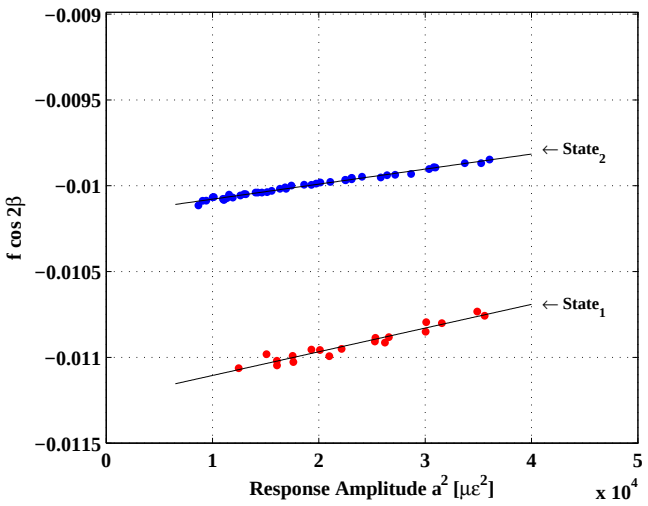

Figure 3.40: Variations of $fcos2\beta$ vs. a^2 used for identification of the effective nonlinearity coefficient α_e for the second metallic beam.

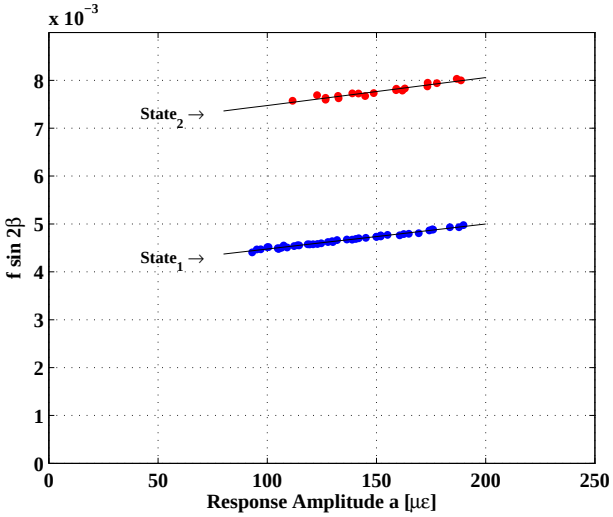

Figure 3.41: Variations of $f sin 2\beta$ vs. a used for identification of linear and quadratic damping coefficients for the second metallic beam.

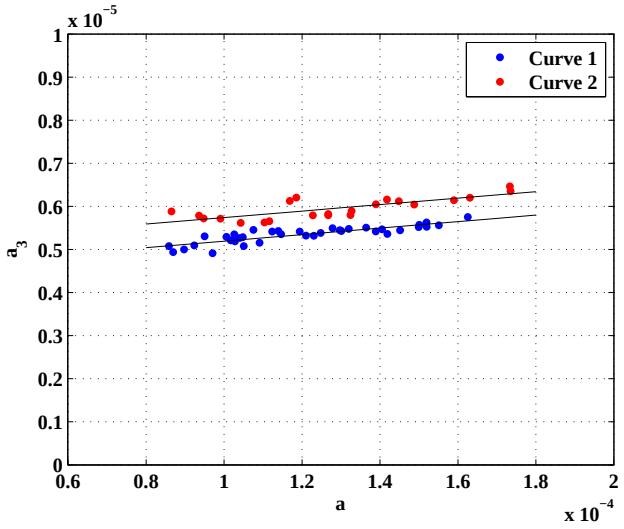

Figure 3.42: Variation of the third harmonic a_3 vs. first harmonic a for the second metallic beam.

3.7.3 Sensitivity Analysis

Percentage variations of the natural frequency ω, linear and quadratic damping coefficients, and effective nonlinearity, over the different states of damage progression are presented in Table 3.6. The analysis shows that the reduction in the system's natural frequency is of the order 0.5%. On the other hand, linear and quadratic damping parameters are characterized by remarkable increases of approximately 10% and 75%, respectively. The effetive nonlinearity α_e shows also an increase of about 60%. Of particular interest is the trend of these variations where we observe that the percentage variation is remarkably increasing from $State_1$ and $State_2$ which is an explanation of the sudden collapse of the second beam despite what happens to the first one.

Validation of the identified parameters was performed for three different measurements at each state. The results are shown from Figure 3.43 to Figure 3.44 and identified parameters yield correct prediction for the response.

Table 3.6: Percentage variation of ω, α_e, ζ_1, and ζ_2 for the second metallic beam.

	% ω	% α_e	% ζ_1	% ζ_2
$State_2$	-0.46	57.67	11.56	74.32

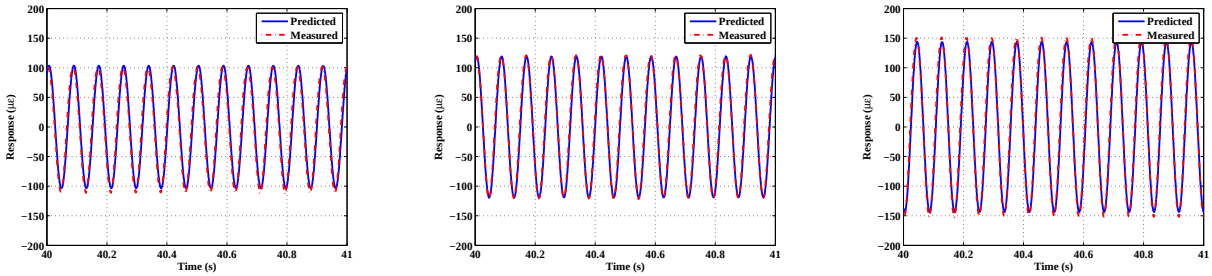

(a) (b) (c)

Figure 3.43: Validation of three measurements in $State_1$ for three different measurements when the excitation frequency is set equal to (a) $24.091Hz$, (b) $24.074Hz$, and (c) $24.061Hz$, respectively.

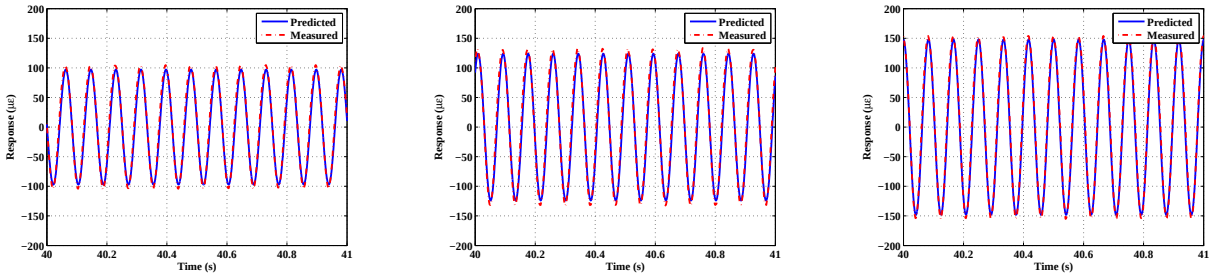

(a) (b) (c)

Figure 3.44: Validation of three measurements in $State_2$ for three different measurements when the excitation frequency is set equal to (a) $23.961Hz$, (b) $23.955Hz$, and (c) $23.949Hz$, respectively.

3.8 Third Metallic Beam

The experimental setup, described in the previous sections for the first and second metallic beam-mass systems, has been repeated for a third metallic beam-mass system. The objective of these new experiments resides in the question whether or not the beam-mass system starts its damaging process before encountering the first jump. Ahead of these tests, the beam was analyzed by means of an advanced technique called *Replica* (Struers Inc.), used for the inspection of critical surfaces and non-destructive testing. The surface of the beam was also visually inspected using a digital microscope. No microcracks were found before running the experiments.

The same experimental procedure, already described for the other two beams, was adopted again here to test the third beam. In particular, the experiment consists of three steps. The results are presented in Figure 3.45. In the first step, the excitation frequency was decreased by a step size of 0.001 Hz from a value near twice the system's first mode natural frequency to a value which did not yield a large amplitude oscillation response. At this point, the procedure was inversed, and the excitation frequency was, then, increased by a step size of 0.001 Hz. This is the second step of the experiment. As expected, a lower amplitude frequency response curve was obtained as the imposed initial conditions have changed. As a third step, the excitation frequency was again increased by the same step size. A third frequency response curve was, then, obtained and it is clearly superimposed to the first curve. These results show that, since the response behavior of the beam to the parametric excitation has not changed, damage did not developed during the tests along the curves representing the different states. Rather the damage progression and initiation can be associated with the observed jumps. Moreover, the beam was inspected again using the *Replica* technique and no microcrack presence was detected.

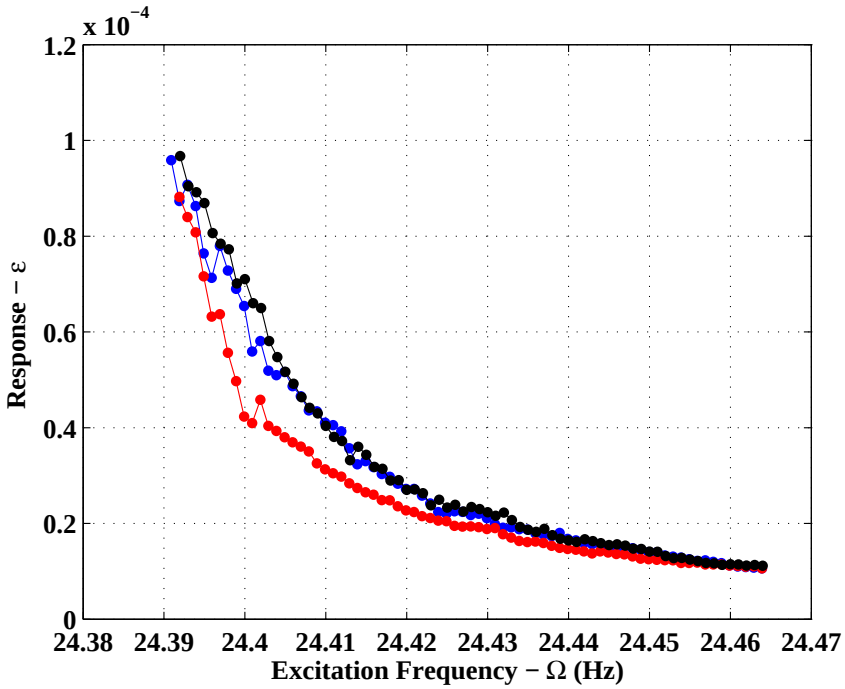

Figure 3.45: These frequency response curves were obtained in order to check whether or not the beam-mass system starts its damaging process before the very first jump occurs.

Chapter 4

Prognosis of a Composite Beam-Mass System

In this chapter, sensitivities of physical parameters including natural frequency, linear and nonlinear damping coefficients and effective nonlinearities to damage initiation and progression in a composite beam carrying a steel lumped mass are established. Through parametric excitation, the nonlinear behavior of the beam-mass system is exploited for the parametric identification. The procedure, as described in the previous chapter, is applied here for the composite beam-mass system. An approximate solution of the representative model is derived and matched with quantities obtained from spectral analysis of measured vibrations. Percentage variations of the identified parameters from the undamaged state through intermediate stages of damage progression are determined. Their sensitivities to the system's state of damage is also quantified. The results show a significant difference in the nonlinear response of the beam, in that its natural frequency continuously changed during the tests. Damping and effective nonlinearity parameters are found to be more sensitive to damage progression than variations in the natural frequency. Moreover, the sensitivity of nonlinear parameters to damage is better established using a physically-derived parameter rather than spectral parameters such as amplitudes, bispectra or bicoherence levels and/or amplitude ratios of harmonic components.

4.1 Experimental Setup

The symmetrical $0° - 90° - 90° - 0°$ 4-ply graphite-epoxy composite beam was cut from a *0.559 mm* thick plate. For nonlinear excitation, the beam was clamped onto a steel platform which is positioned on a shaker. The length of the beam from the clamped to the free end was *155 mm*. A steel mass, that weighs *42 g*, was positioned *110 mm* away from the clamped end. Its length, width, and thickness were respectively *30 mm*, *18 mm*, and *10 mm*. The excitation acceleration was measured by a piezo-electric accelerometer attached to the shaker. The beam response was measured using a strain gage that was glued *75 mm* away from the mounting plate. Data, analyzed here, were sampled at a frequency of 500 Hz over 60-second periods. The free response of the system before starting the nonlinear tests yielded a frequency for the first mode of 12.042 Hz. For the purpose of nonlinear system identification, principal parametric excitation of the beam-mass system is exploited. This is done by performing frequency sweeps whereby the system was excited over a small range near twice its natural frequency. The excitation signal was generated by a two-channel, variable-phase wave synthesizer. During the frequency sweep over the excitation range, the excitation frequency $\widehat{\Omega}$ was decreased by a step size of 0.001 Hz while keeping its amplitude constant. A photograph of the experimental setup representing the composite beam carrying a steel lumped mass as mounted on a shaker, the piezo-electric accelerometer used to measure the excitation, and the strain gage used to measure the beam's response, is shown in Figure 4.1.

4.2 Experimental Results on the Composite Beam-Mass System

4.2.1 Frequency-response

Variations in the steady-state amplitude of the composite beam carrying the lumped mass with the excitation frequency are presented in the frequency-response curves shown in Figure 4.2. As the excitation frequency $\widehat{\Omega}$ is decreased in increments of 0.001 Hz from 24.209 Hz to approach a value of 24.085 Hz which is very close to twice the system's natural frequency

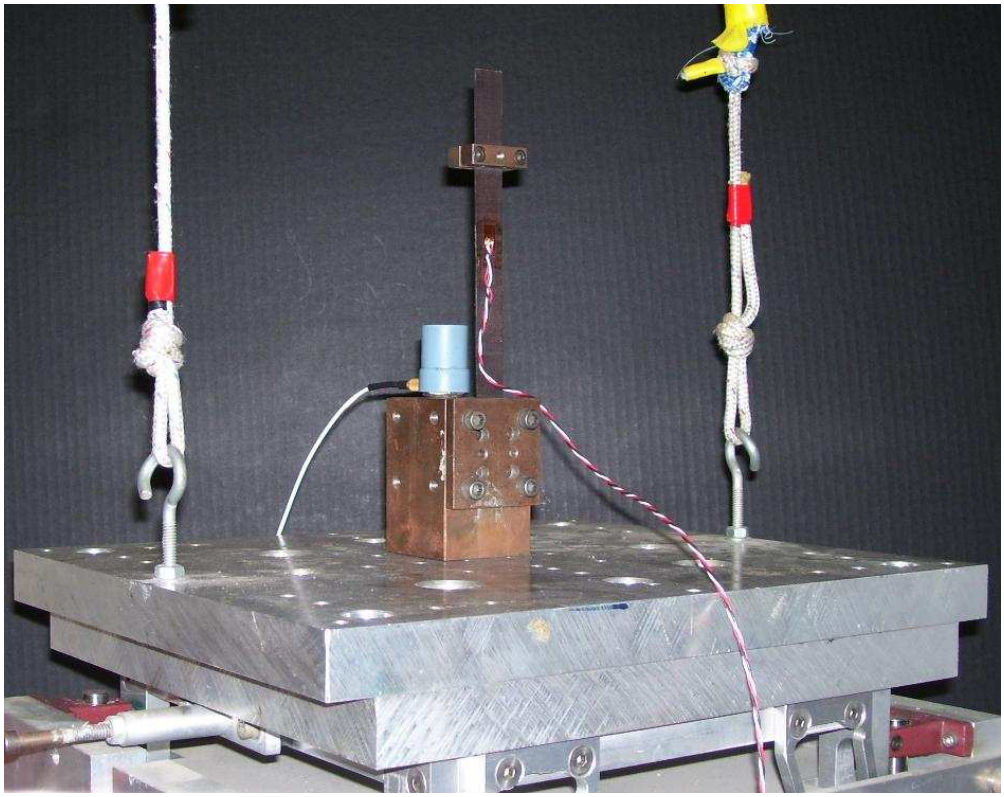

Figure 4.1: Photograph of the experimental setup representing the composite beam carrying a steel lumped mass as mounted on a shaker. A piezo-electric accelerometer is used to measure the excitation and a strain gage is used to measure the beam's response.

ω, the steady-state amplitude of the response increases sligthly. Of particular interest is the time variation in the response shown in Figure 4.3 caused by an excitation having a frequency of 23.994 Hz. Although the excitation amplitude is kept constant, the response shows a significant increase in amplitude from a steady-state value of $45\mu\epsilon$ to about $138\mu\epsilon$, the excitation amplitude is kept constant. After this sudden variation from small to large amplitude oscillation, the composite beam maintained a large-amplitude steady-state response, which slightly decreased as the frequency was further swept down. This shows that the natural frequency of the composite beam changed continuously as the excitation frequency is decreased. Stopping the experiments and repeating the excitation at a higher frequency yielded a small response. Decreasing the excitation frequency $\widehat{\Omega}$ yielded the second state in Figure 4.2. This behavior repeated itself over a third state. The differences in the responses along the three states shows that some physical parameters of the beam had changed. After removing the beam from its clamped support, a fatigue crack was found to have developed and propagated across the whole width of the beam which is a characteristic failure mode of composite beams. A high-resolution digital photograph of the beam, shown in Figure 4.4, shows the crack that was located at the root where the beam was clamped. Consequently, the variations in the frequency-response curves could be reasonably associated with damage progression.

4.2.2 Spectral Analysis of Excitation and Response Data

Examples of time series representing the three states of damage, characterized in Figure 4.2, are shown in Figures 4.5 to 4.7. Each figure consists of three parts denoted as (a), (b), and (c). Each part shows the excitation and corresponding response time series for specific excitations. Of particular interest is the observation that the response amplitude decreases slightly as the excitation frequency was decreased even though its amplitude was maintained constant.

Power spectra of these time series are presented in Figures 4.8 to 4.10. Each figure consists of three parts denoted as (a), (b), and (c). Each part shows the excitation and the corresponding response power spectra of the time series previously presented in Figures 4.5 to 4.7. Consistent characteristics are noticed. The power spectrum of the excitation shows mainly two large peaks. They correspond, respectively, to the first harmonic at which the

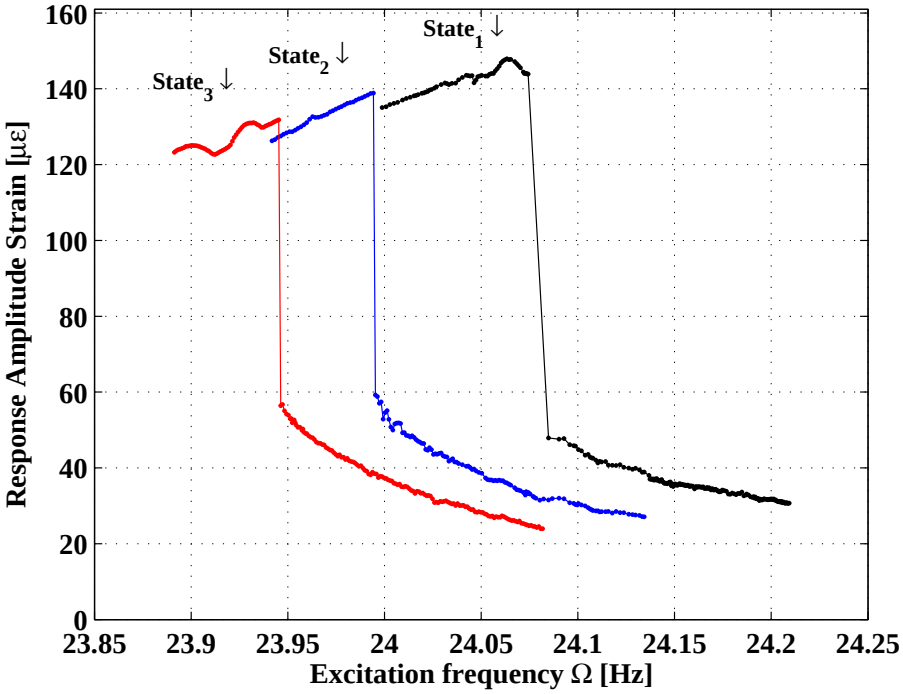

Figure 4.2: Frequency response curves quantify the change in the natural frequency due to damage initiation and further propagation. As the excitation frequency approached a value which is very close to twice that of the natural frequency, a jump was noted. After the jump, the composite beam maintained a large steady-state response amplitude which slightly decreased as the frequency was further swept down. This shows that the natural frequency of the composite beam was continuously changing. Stopping the experiment and repeating the excitation at a higher frequency yielded a small response. This behavior repeated itself over a second and a third curve. The differences in the response along the three frequency response curves shows that some physical parameters of the beam have changed. Each curve is then representative of a state of damage.

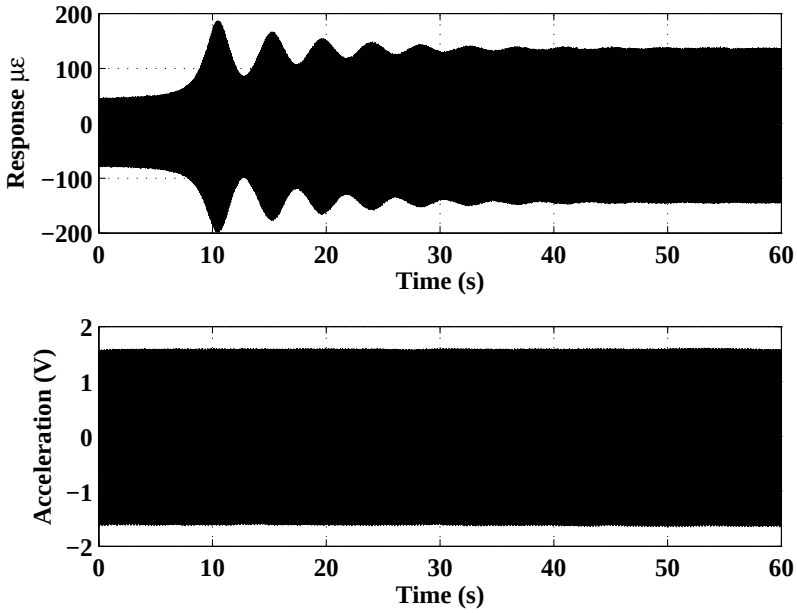

Figure 4.3: Top: Time series of the composite beam response variation when the excitation frequency Ω is set equal to 23.9943 Hz, exactly twice the system's natural frequency. Bottom: Time series of the constant amplitude excitation.

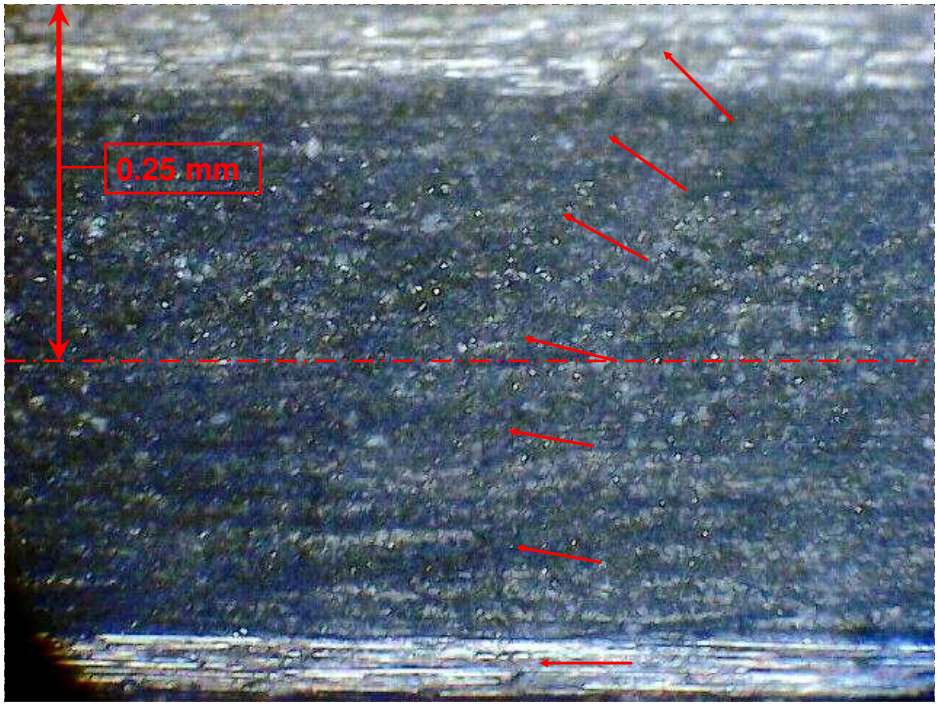

Figure 4.4: Photograph of the crack which has clearly propagated across the whole thickness and width, even without reaching the permanent failure of the structure.

excitation is driven, which is a value near twice the system's natural frequency, and a second harmonic, which is twice the value of the first peak. The response power spectrum shows, instead, three peaks. They correspond, respectively, to the first mode natural frequency, to the excitation frequency, and to the third harmonic. The peak of the first mode natural frequency is used both to generate the frequency response plot presented in Figure 4.2 and to perform the nonlinear parametric identification. The peak of the third harmonic is used, in turn, to establish whether the amplitude of additional spectral parameters is sensitive enough to successfully assess damage.

Cross-bicoherence contours of the same time series are shown in Figure 4.11 to 4.13. Each figure consists of three parts denoted as (a), (b), and (c). Each part shows the cross-bicoherence contours between the excitation and the response previously presented in parts (a), (b), and (c) of Figures 4.5 to 4.7. Strong quadratic phase coupling is clearly pointed out, for having set the contour levels to 0.98 and 0.99. This observation establishes also the extremely high level of confidence in the estimated phase relation between excitation and response as discussed below.

4.3 Representative Model

The nondimensional differential equation governing the temporal response of the first mode of the beam is derived from the Euler- Lagrange's equation and is given by (4.1)

$$\begin{aligned} \ddot{\eta} &+ 2\epsilon\zeta_1\dot{\eta} + 2\epsilon\zeta_2\dot{\eta}\,|\dot{\eta}| + \epsilon\alpha\eta^3 + \\ &+ \left[1 - \epsilon f\cos\left(\Omega\tau\right)\right]\eta + \epsilon\kappa_1\eta\dot{\eta}^2 + \epsilon\kappa_2\eta^2\ddot{\eta} = 0 \end{aligned} \tag{4.1}$$

where η is the temporal amplitude of the system's first mode, $\dot{\eta}$ is its first derivative with respect to the nondimensional time τ defined as $\tau = \omega t$, where ω is the natural frequency, and ϵ is a bookkeeping parameter used to indicate the relative contributions of the damping, nonlinear, and excitation parameters to the response. The parameters f and nondimensional frequency $\Omega = \frac{\widehat{\Omega}}{\omega}$ represent the excitation amplitude and frequency, respectively. The terms $2\zeta_1\dot{\eta}$ and $2\zeta_2\dot{\eta}\,|\dot{\eta}|$ represent the linear and quadratic damping forces, respectively. The nonlinear damping terms model physical properties or phenomena, including material damping

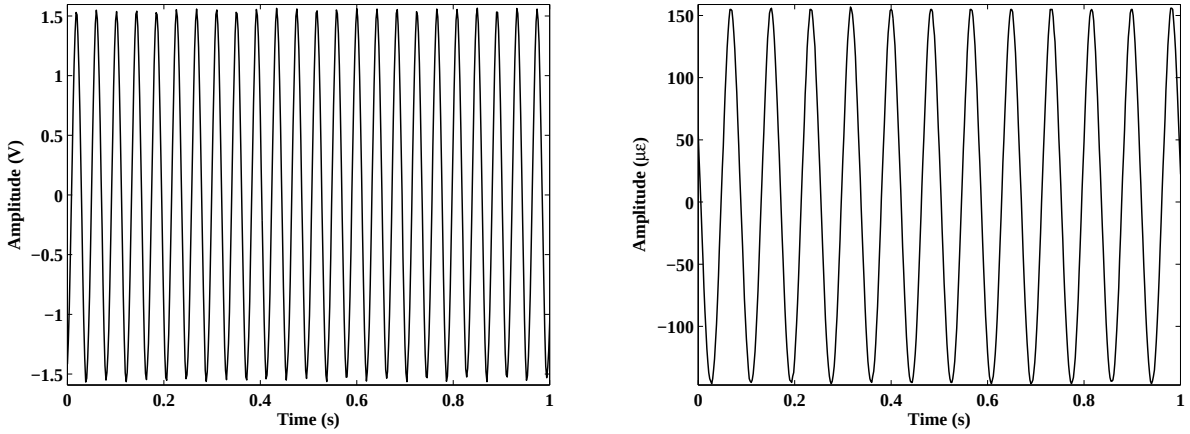

(a)

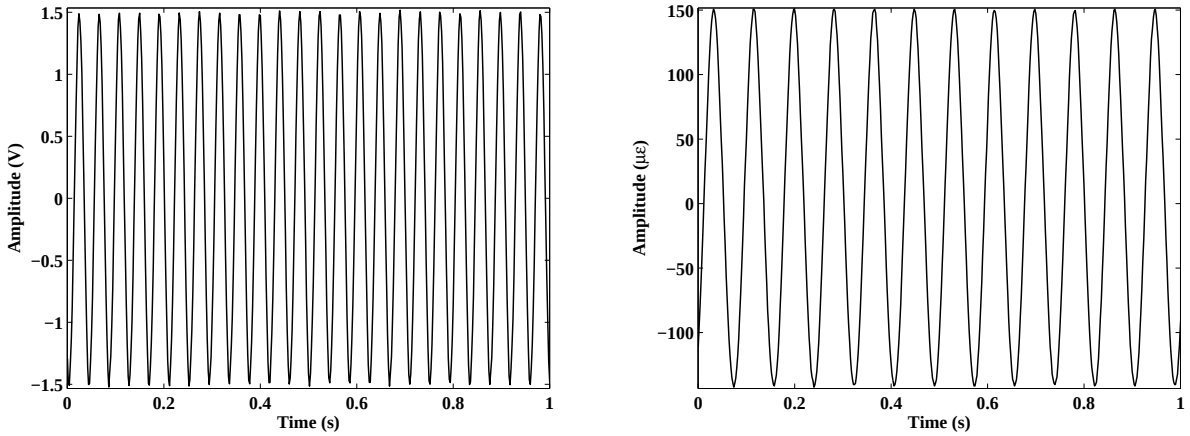

(b)

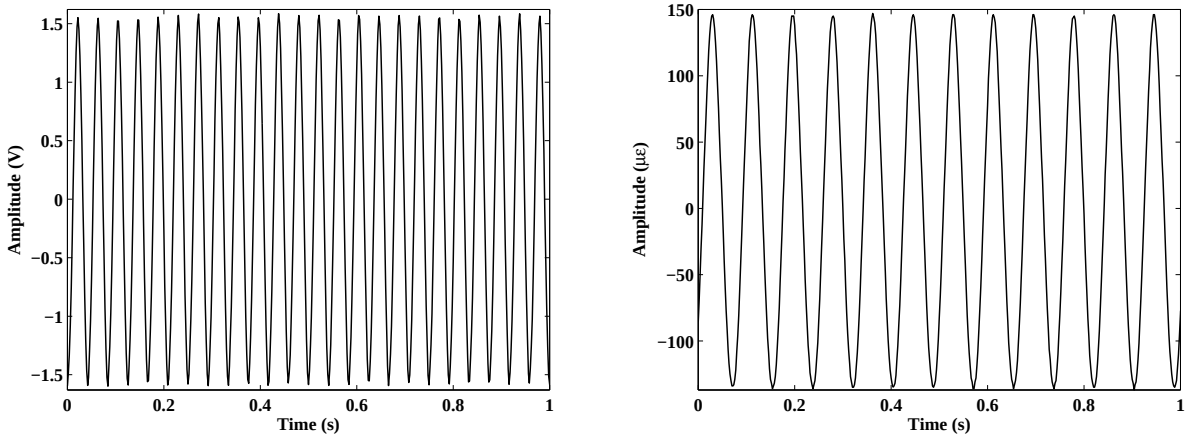

(c)

Figure 4.5: Time histories of excitation and response in $State_1$ for three different measurements when the excitation frequency is set equal to (a) $24.069Hz$, (b) $24.047Hz$, and (c) $24.017Hz$, respectively.

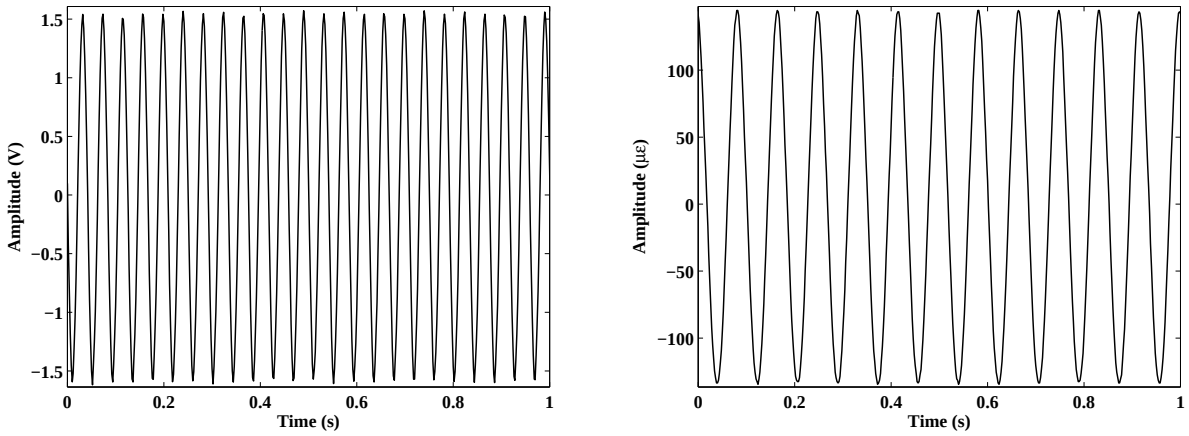

(a)

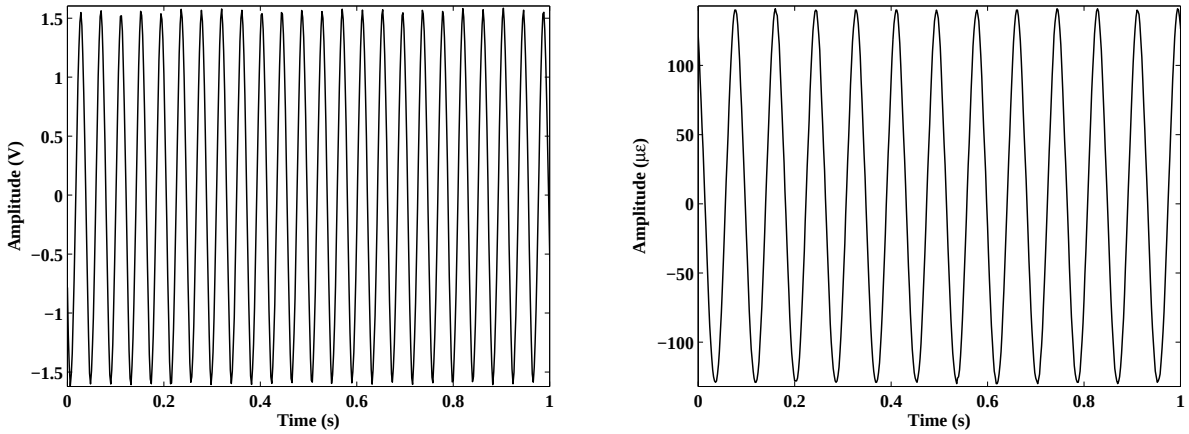

(b)

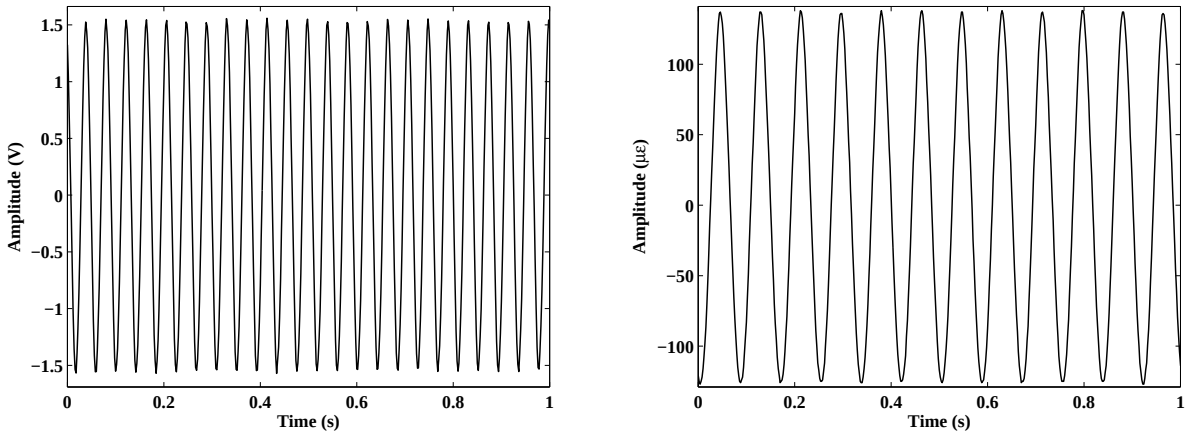

(c)

Figure 4.6: Time histories of excitation and response in $State_2$ for three different measurements when the excitation frequency is set equal to (a) $23.985Hz$, (b) $23.967Hz$, and (c) $23.952Hz$, respectively.

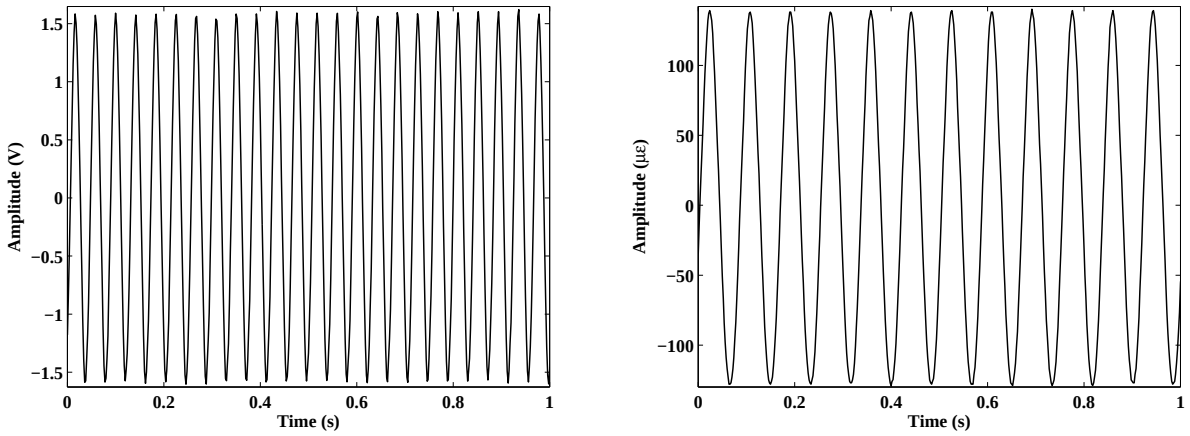

(a)

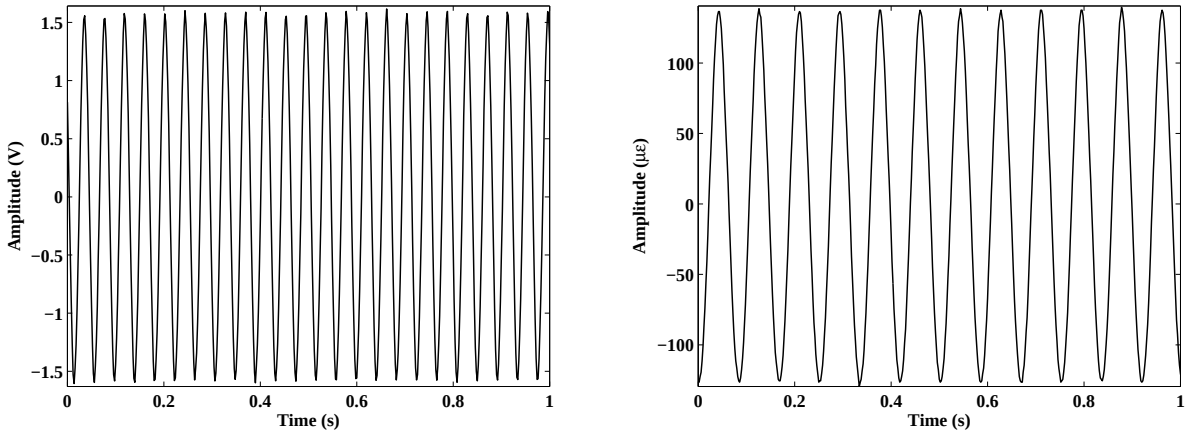

(b)

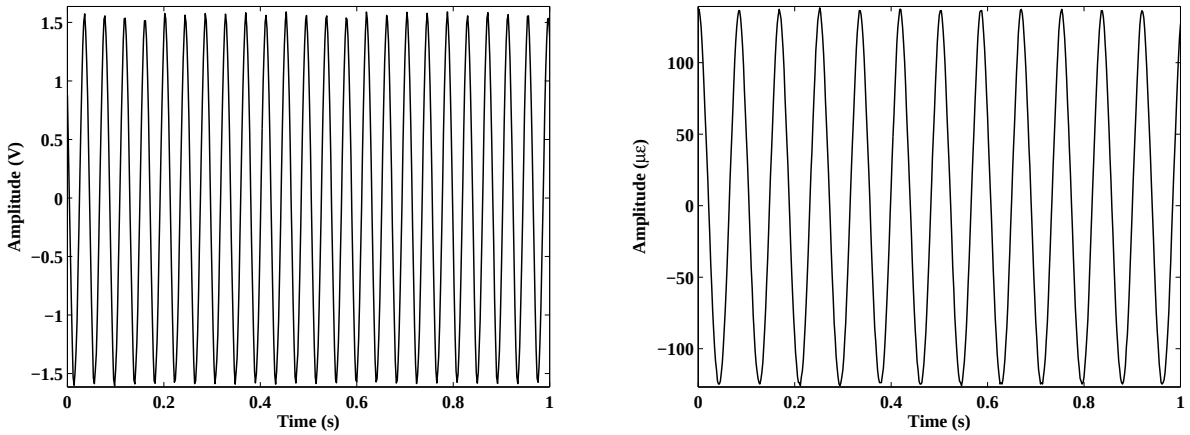

(c)

Figure 4.7: Time histories of excitation and response in $State_3$ for three different measurements when the excitation frequency is set equal to (a) $23.935Hz$, (b) $23.924Hz$, and (c) $23.918Hz$, respectively.

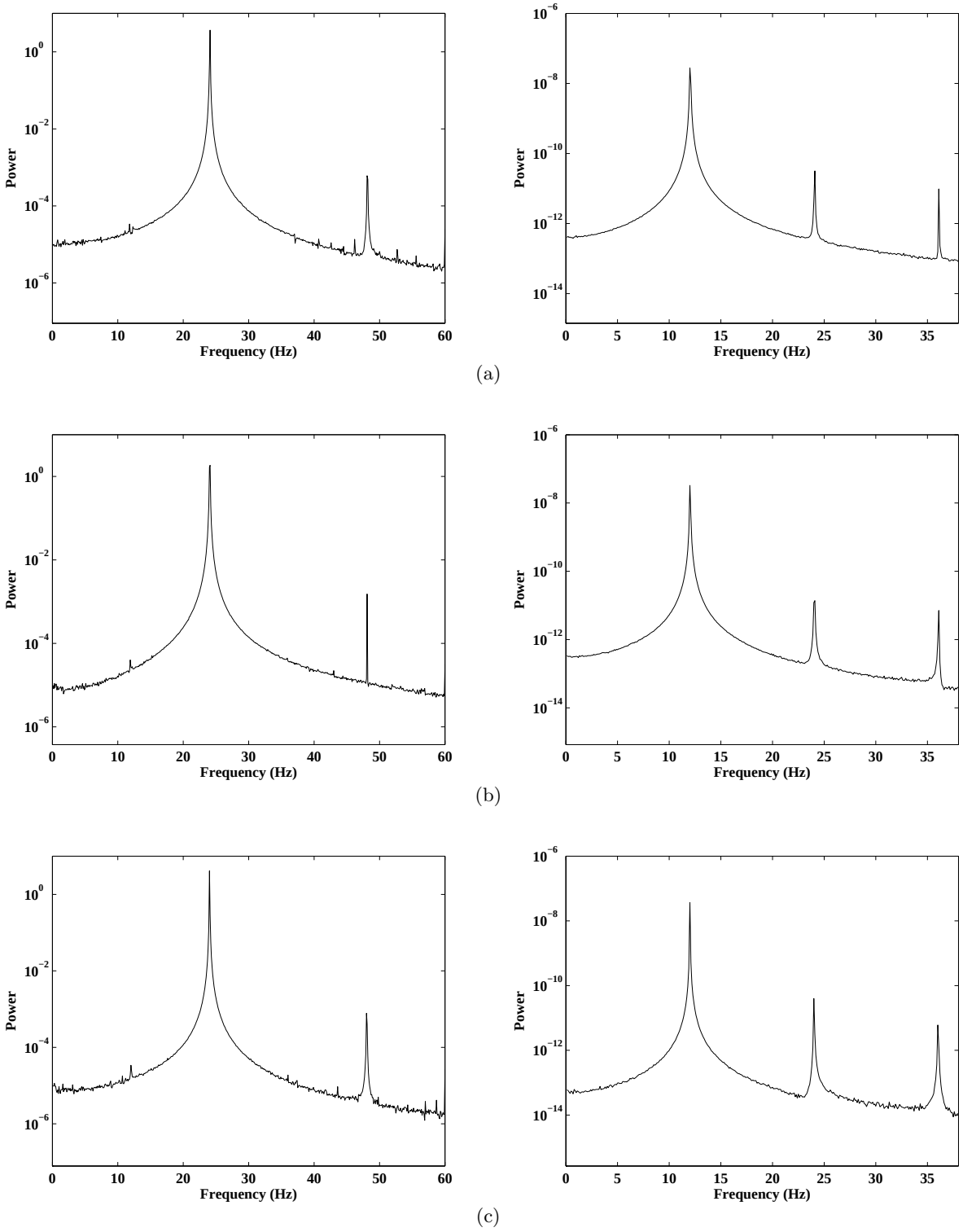

Figure 4.8: Power spectrum of excitation and response in $State_1$ for three different measurements when the excitation frequency is set equal to (a) $24.069Hz$, (b) $24.047Hz$, and (c) $24.017Hz$, respectively.

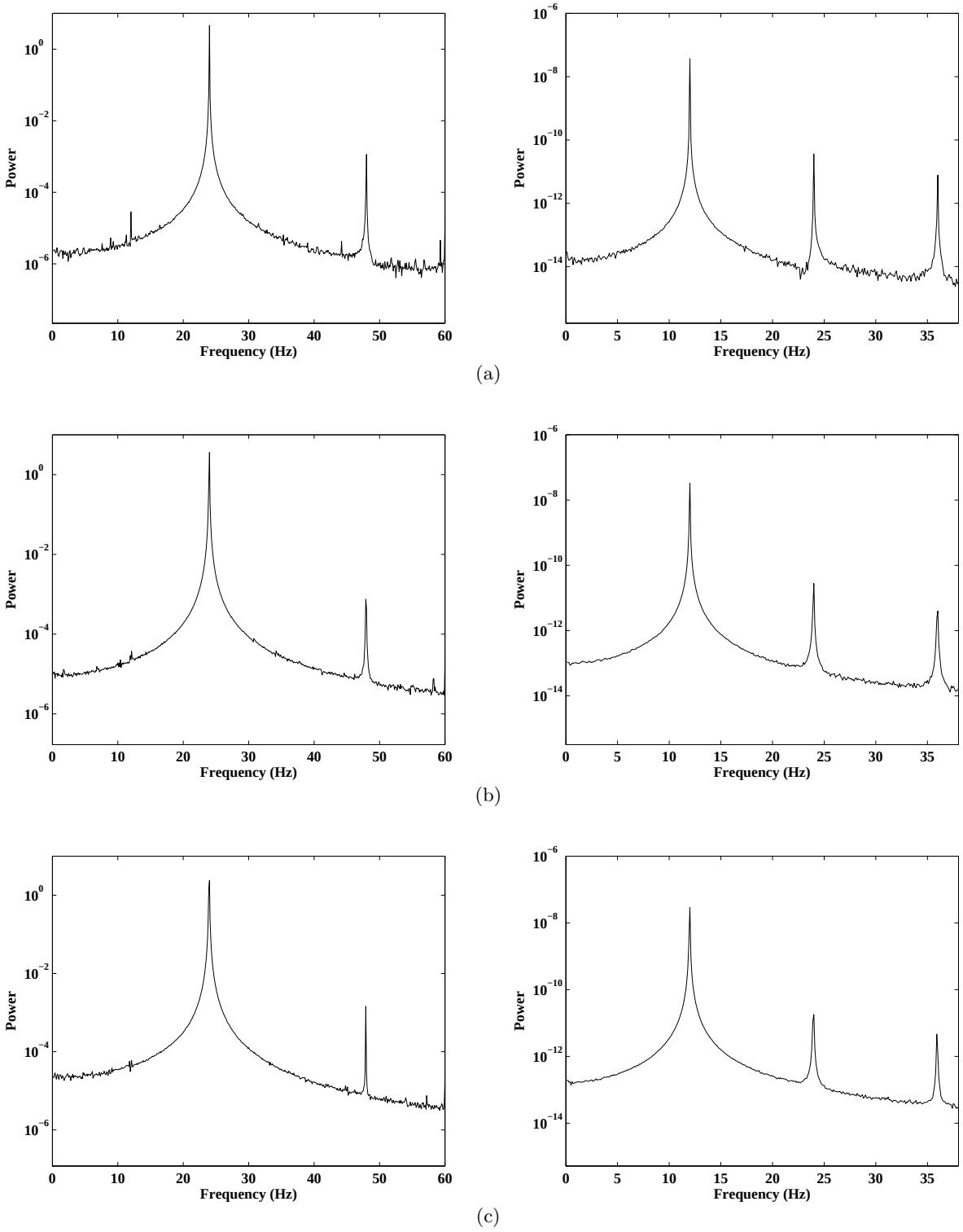

Figure 4.9: Power spectrum of excitation and response in $State_2$ for three different measurements when the excitation frequency is set equal to (a) $23.985Hz$, (b) $23.967Hz$, and (c) $23.952Hz$, respectively.

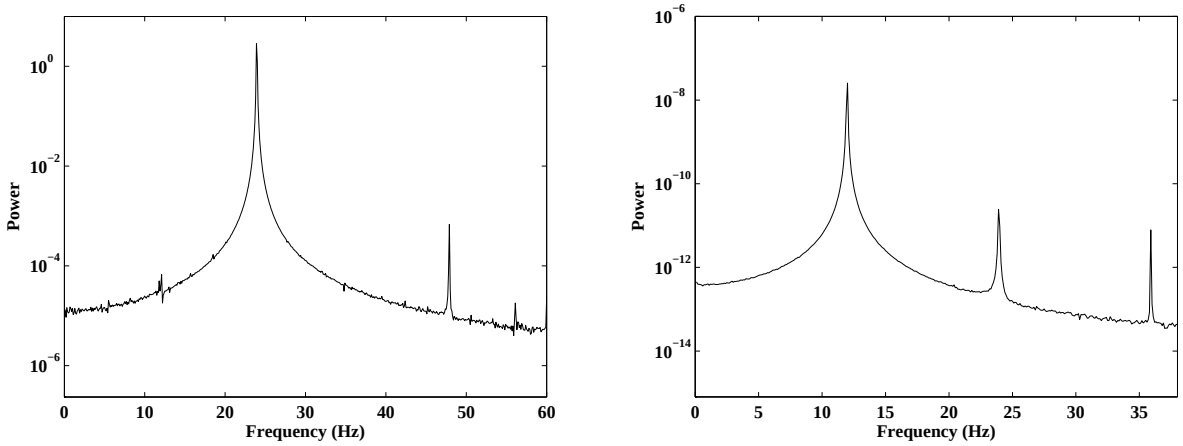

(a)

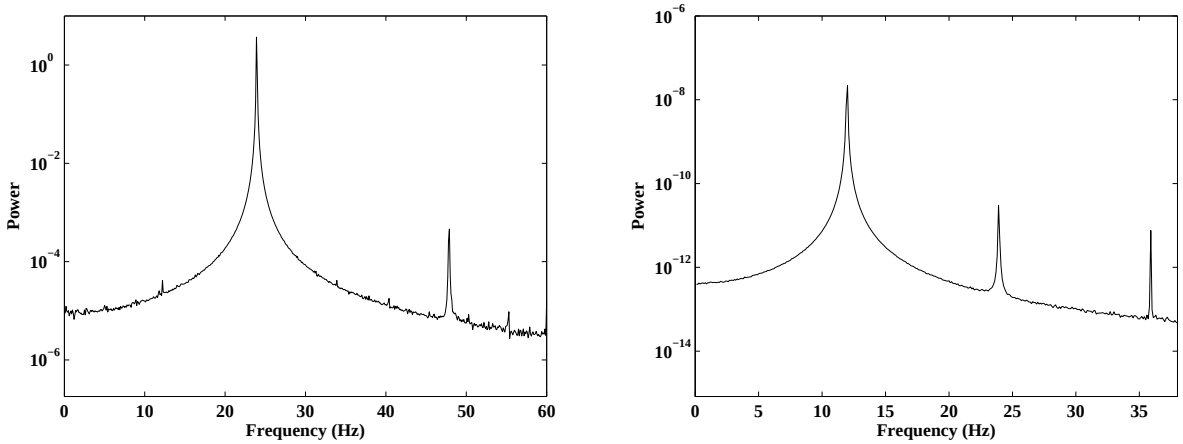

(b)

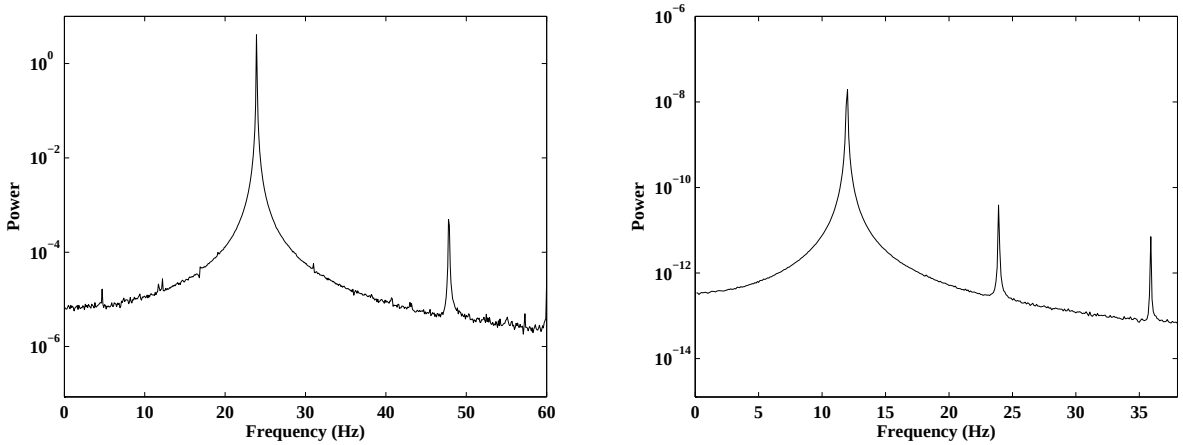

(c)

Figure 4.10: Power spectrum of excitation and response in $State_3$ for three different measurements when the excitation frequency is set equal to (a) $23.935Hz$, (b) $23.924Hz$, and (c) $23.918Hz$, respectively.

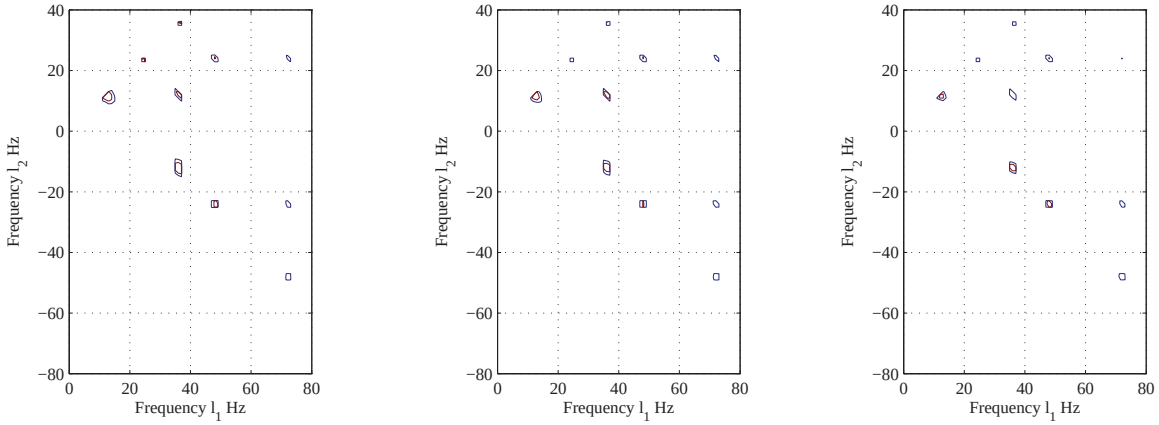

(a) (b) (c)

Figure 4.11: Cross-bicoherence $State_1$ for three different measurements when the excitation frequency is set equal to (a) $24.069Hz$, (b) $24.047Hz$, and (c) $24.017Hz$, respectively. Contour levels are set to [0.98 0.99].

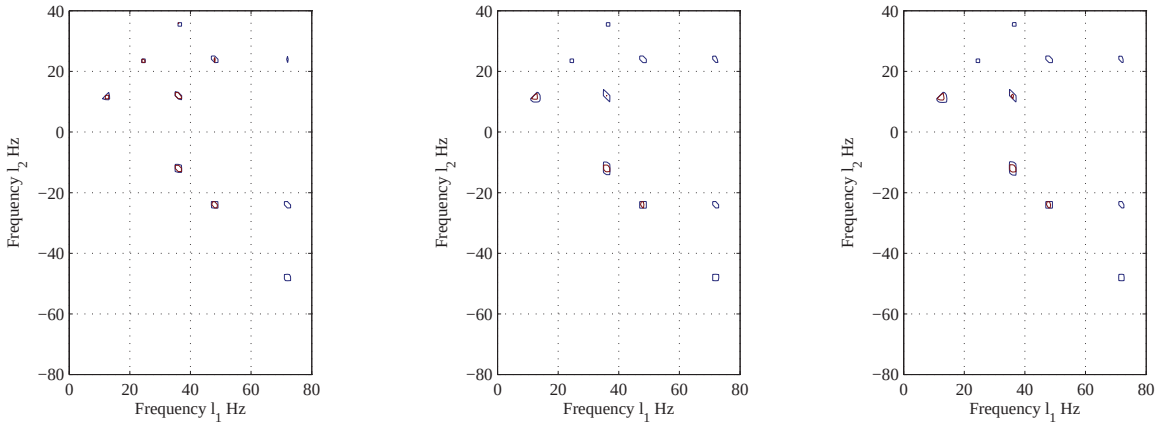

(a) (b) (c)

Figure 4.12: Cross-bicoherence $State_2$ for three different measurements when the excitation frequency is set equal to (a) $23.985Hz$, (b) $23.967Hz$, and (c) $23.952Hz$, respectively. Contour levels are set to [0.98 0.99].

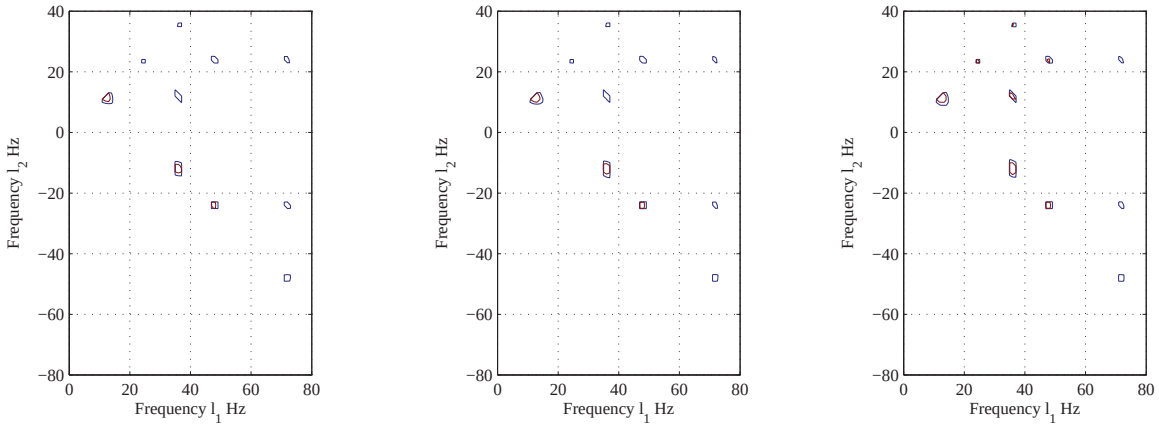

(a) (b) (c)

Figure 4.13: Cross-bicoherence $State_3$ for three different measurements when the excitation frequency is set equal to (a) $23.935Hz$, (b) $23.924Hz$, and (c) $23.918Hz$, respectively. Contour levels are set to [0.98 0.99].

(could be damage or crack related), structural properties, and/or fluid drag. These terms were added to match the analysis of the experimental results as explained by Hajj et al. (2000) and as will be explicitly shown later. Cubic geometric and inertia restoring forces are modeled respectively by $\alpha\eta^3$, $\kappa_1\eta\dot{\eta}^2$, and $\kappa_2\eta^2\ddot{\eta}$ where α is the cubic geometric stiffness nonlinearity and κ_1 and κ_2 are the cubic inertia nonlinearities. These nonlinear restoring forces model the nonlinear beam curvature and distribution of the mass along the beam. The excitation was chosen to induce principal parametric resonance and hence produce large-amplitude responses that allow quantification of the damping and nonlinear coefficients (Nayfeh (1985)). As such, the excitation is expressed in the form $f\eta\cos(\Omega\tau)$, where the dimensionless excitation frequency Ω is chosen to be near 2. An approximate solution for the response of the system, modeled by equation (4.1), is obtained using the method of multiple scales (Nayfeh (1981)). This solution is written as

$$\begin{aligned}\eta(\tau) &= \frac{1}{2}a\cos\left(\frac{1}{2}\Omega\tau+\beta\right)+\epsilon\Bigg\{-\frac{af}{4\Omega^2}\cos\left(\frac{3}{2}\Omega\tau+\beta\right)+ \\ &+ \left(\frac{a^3\alpha}{8\Omega^2}-\frac{a^3k_1}{32}-\frac{a^3k_2}{32}\right)\cos\left[3\left(\frac{\Omega}{2}\tau+\beta\right)\right]\Bigg\}+\ldots\end{aligned} \tag{4.2}$$

where the time variation of the response amplitude a and phase β are governed by the modulation equations

$$\dot{a} = \epsilon\left(\zeta_1 + \frac{4a\Omega\zeta_2}{3\pi}\right)a - \frac{\epsilon f a}{2\Omega}\sin(2\beta) \tag{4.3}$$

$$a\dot{\beta} = \frac{\epsilon}{\Omega}\left(\sigma + \alpha_e a^2\right)a - \frac{\epsilon f a}{2\Omega}\cos(2\beta) \tag{4.4}$$

Here, σ is a detuning parameter that is given by $1 = \left(\frac{1}{2}\Omega\right)^2 + \epsilon\sigma$ and, thus, quantifies the nearness of Ω to 2, and

$$\alpha_e = \frac{1}{4}\left(3\alpha + \frac{1}{4}\Omega^2\kappa_1 - \frac{3}{4}\Omega^2\kappa_2\right) \tag{4.5}$$

is an effective nonlinearity parameter that combines the effects of all nonlinear terms. The steady-state response of η is obtained by letting $\dot{a} = 0$ and $\dot{\beta} = 0$ in equations (4.3) and (4.4), respectively, thereby obtaining

$$\Omega\zeta_1 + \frac{4a\Omega^2\zeta_2}{3\pi} = \frac{f}{2}\sin 2\beta \tag{4.6}$$

$$\sigma + \alpha_e a^2 = \frac{f}{2}\cos 2\beta \tag{4.7}$$

The above equations provide a relation between the spectral quantities and the damping and nonlinear parameters. Obviously, spectral estimates of the first harmonic amplitude a and the phase relation 2β between the excitation and the response could be substituted into equations (4.3) and (4.4) to determine the damping and effective nonlinearity parameters as discussed below. Since the nonlinearity produces a third harmonic in the response, its amplitude can also be used to assess damage. This is exemplified by the amplitude of the third harmonic in the approximate solution which is dependent on f, α, k_1, and k_2.

4.4 System Identification

Parameter identification was carried out through analysis of measured steady-state responses and corresponding excitations. The amplitude of the response, a, was determined from the power spectrum. The phase of the cross-bispectrum was used to determine the phase relation defined as 2β which was estimated to be between 64° and 67° for all data analyzed here. In all data, the cross-bicoherence between the excitation and response frequencies assumed values

Table 4.1: Phase and bicoherence values for the composite beam.

	2β	$b^2_{yxx}[l_1, l_2]$	$\widehat{\Omega}\ Hz$
$State_1$	66.74	0.99	24.069
$(\omega = 12.042\ Hz)$	67.16	0.99	24.047
	66.51	0.99	24.017
$State_2$	66.07	0.99	23.985
$(\omega = 11.995\ Hz)$	65.89	0.99	23.967
	65.87	0.99	24.952
$State_3$	65.24	0.99	23.935
$(\omega = 11.973\ Hz)$	65.23	0.99	23.924
	65.18	0.99	23.918

Table 4.2: Identified values of ω, f, α_e, ζ_1, and ζ_2 for the composite beam.

	$\omega\ (Hz)$	f	$\alpha_e\ (\mu\varepsilon^{-2})$	ζ_1	$\zeta_2\ (\mu\varepsilon^{-1})$
$State_1$	12.042	0.0214	$1.45 \cdot 10^{-8}$	$7.07 \cdot 10^{-3}$	$1.08 \cdot 10^{-6}$
$State_2$	11.995	0.0235	$1.93 \cdot 10^{-8}$	$7.46 \cdot 10^{-3}$	$1.68 \cdot 10^{-6}$
$State_3$	11.973	0.0245	$2.80 \cdot 10^{-8}$	$7.58 \cdot 10^{-3}$	$2.30 \cdot 10^{-6}$

between 0.98 and 0.99; indicating the expected high level of coupling and confidence in the estimated phase relation.

Table 4.1 shows the estimated value of the phase 2β, its corresponding cross-bicoherence, and the excitation frequency at which these values are identified for three measurements at each state. Variations in the natural frequency over the three states of Figure 4.2 are presented in Table 4.2. The results clearly show modest drop in the natural frequency with damage progression that would have been hard to evaluate without the slow sweep. Values of the excitation amplitude f along each state were approximated by $\frac{cos(2\beta)}{2\sigma}$ for the starting point along each state where the response amplitude was relatively small.

Plotting $fcos2\beta$ vs. a^2, as presented in Figure 4.14, shows that the linear representation of this relation in the representative model is correct. Furthermore, the slope of this linear fit yields the effective nonlinearity, α_e. Its variation over the different stages of damage progression is presented in Table 4.2. The results show that the nonlinear parameter α_e increases with damage progression.

Plotting $fsin2\beta$ vs. a yields a linear relation which again shows the need to add the quadratic damping term in the representative model. The intercept and slope of the linear fits yield, respectively, the values of the linear and quadratic damping coefficients. These values are presented in Table 4.2. Again the results show an increase in both damping coefficients.

Another measure of the effective nonlinearity can be determined from the amplitude of the third harmonic, a_3. A plot of the variation of a_3 vs. a is presented in Figure 4.16. The results clearly show that the relative amplitude of $\frac{a_3}{a}$ increases with damage. This again shows that nonlinear effects become more relevant with damage progression. There are, however, two issues with using the amplitude ratio $\frac{a_3}{a}$. First, noise levels could impact these ratios. Second, this ratio depends on the amplitude of the response. As such, their values may not be clearly separated among $State_1$, $State_2$, and $State_3$ as shown in Figure 4.16.

4.4.1 Sensitivity Analysis

Percentage variations of natural frequency ω, linear and quadratic damping coefficients, and effective nonlinearity, over the different states of damage progression are presented in Ta-

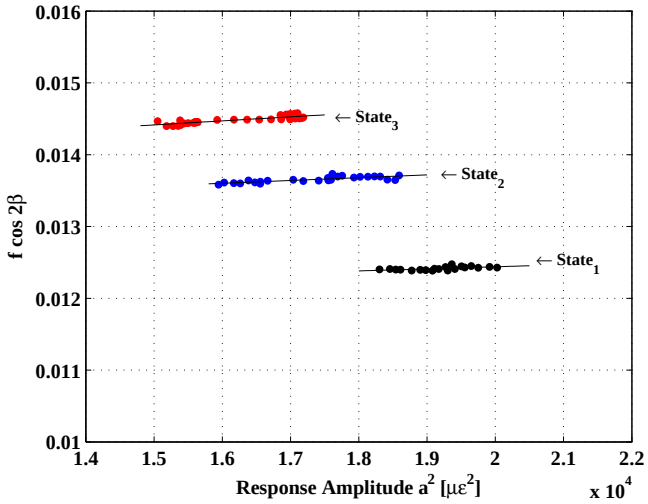

Figure 4.14: Variation of $fcos2\beta$ vs. a^2 used for identification of the effective nonlinearity coefficient α_e.

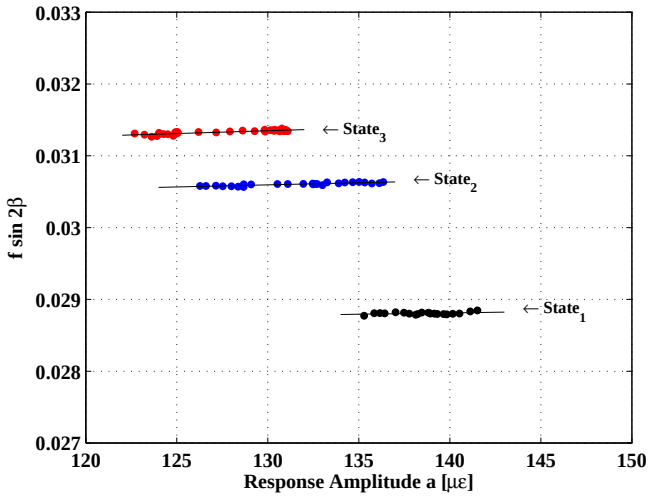

Figure 4.15: Variation of $fsin2\beta$ vs. a used for identification of linear and quadratic damping coefficients, ζ_1 and ζ_2.

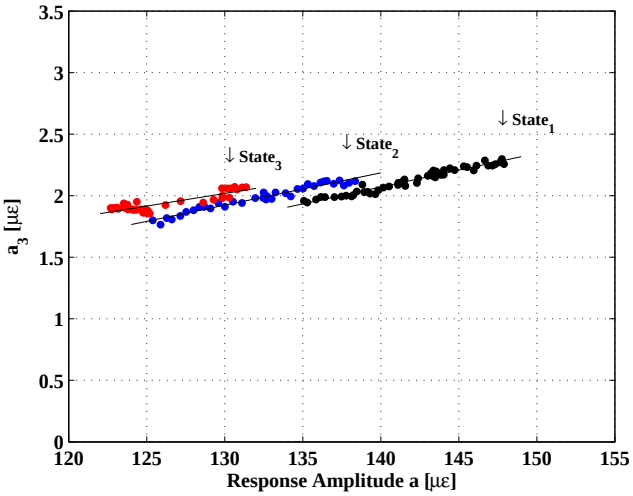

Figure 4.16: Variations of third harmonic a_3 vs. first harmonic a.

Table 4.3: Percentage variation of ω, α_e, ζ_1, and ζ_2.

	% ω	% α_e	% ζ_1	% ζ_2
$State_2$	-0.39	33.01	5.49	55.49
$State_3$	-0.57	92.19	7.20	112.15

ble 4.3. The analysis shows that the reduction in the system's natural frequency is less than 1%. On the other hand, linear and quadratic damping parameters are characterized by increases of approximately 10% and 100%, respectively. The effective nonlinearity α_e shows also an increase of about 90%. Of particular interest is the trend of these variations where it is observed that the percentages are remarkably increasing between $State_2$ and $State_3$. This means that as $State_3$, where the crack has developed, was approached, the variations in all physical parameters were more pronounced.

Chapter 5

Cracks Localization by Fiber Optics Sensors

In this chapter, the possibility of using fiber optics technology (Hill and Meltz (1997)) for crack localization is assessed. A composite beam-mass system, similiar to the one used in the previous chapter, is used for this assessment. Again, the nonlinear response of this system to a principal parametric excitation is exploited. The beam responses under undamaged and damaged conditions, where cracks are externally produced through a tensile force, are compared. Spectral moments and quantities obtained from fiber optic strain measurements are evaluated near and away from cracks to assess the relation between these moments and cracks. The spectral moments include power spectrum, linear coherence, and cross-bicoherence. The results show that noise levels in fiber optic signals are high in comparison to strain gage signals. Of particular interest, however, is the observation that the nonlinear response is more pronounced near the cracks than away from them.

5.1 Experimental Setup

A symmetrical 0° - 90° - 90° - 0° 4-ply graphite-epoxy composite plate that is *0.559 mm* thick was fabricated and cut into strips that are *15 mm* wide and *300 mm* long. In the experimental setup, the beam-mass system is clamped onto a steel platform which is positioned on a shaker, as schematically shown in Figure 5.1. The length of the beam from the clamped end to the

free end is *225 mm*. A steel mass (*42 g*) is positioned *145 mm* away from the clamped end. The length, width, and thickness of the lumped steel mass are, respectively, *30 mm*, *18 mm*, and *10 mm*.

The excitation acceleration is measured using a piezo-electric accelerometer attached to the shaker. The beam response is measured using a strain gage that is glued *70 mm* above the mounting plate. Both strain gage and accelerometer data were collected at a sampling rate of 166 Hz for 24-second periods. Moreover, as shown in Figure 5.2, an optical fiber that is *121.3 mm* long with a diameter of *125* μm is glued along the beam on the side opposite to that of the strain gage. The Time-Division Multiplexing principle (Kersey et al. (1997)) is adopted to transfer signals in the fiber with a *1550 nm* wavelengths range in the infrared region. This wavelength range defines which spectrum of light is transmitted through the optical fiber in order to avoid the attenuation of the glass fiber. This attenuation is caused by absorption and scattering. Absorption is due to water vapor in the glass and is present within wavelength regions called water bands. Scattering occurs when the light bounces off the atoms in the glass. The wavelengths range of *1550 nm* is high enough to avoid these disadvantages (Valente et al. (2003)). An M-Bond AE-15 epoxy adhesive is used as glue and cured in the oven for 2 hours at 150 °F as recommended by the Vishay Instruction Bulletin B-137 (Micro-Measurements (11137)). Eleven active gratings that are *9.95 mm*, center to center, are present along the fiber optic. The first active grating is located *18.3 mm* above the mounting plate. Each fiber grating returns *69* measurements that are spread evenly through a usable length of *3.3 mm*. The sixth grating, counted from the clamped support, is co-located with the strain gage on the opposite side of the beam. Data from all gratings were collected at a sampling frequency of 166 Hz for 24-second periods. The first and eleventh gratings are disregarded for the analysis because of their low accuracy. A photograph of the experimental setup representing the beam-mass system clamped on the shaker and the optical fiber glued on the beam is shown in Figure 5.1.

Two states of the beam-mass system are considered. The first is denoted as *Undamaged* and consists of the undamaged composite beam carrying the steel lumped mass. Free response tests of this beam-mass system yielded a first-mode natural frequency of 8.273 Hz. The second state is denoted as *Damaged*. In this state, the composite beam, used in the first state, was

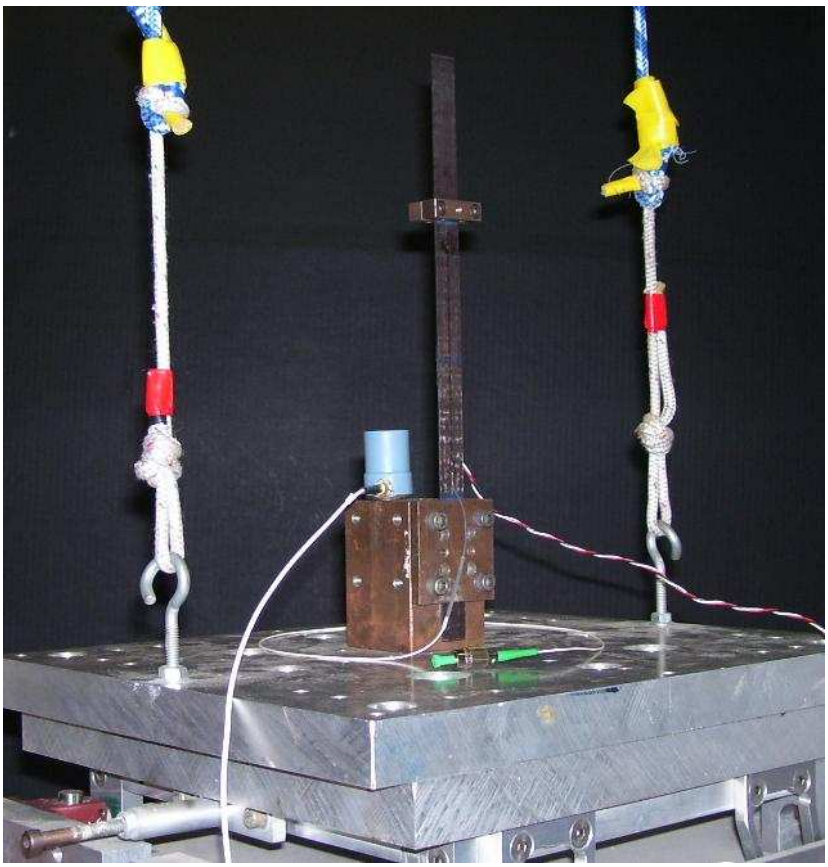

Figure 5.1: Photograph of the experimental setup representing the beam-mass system as mounted on a shaker. A piezo-electric accelerometer is used to measure the excitation and a Bragg Grating optical fiber is used to measure the beam's response.

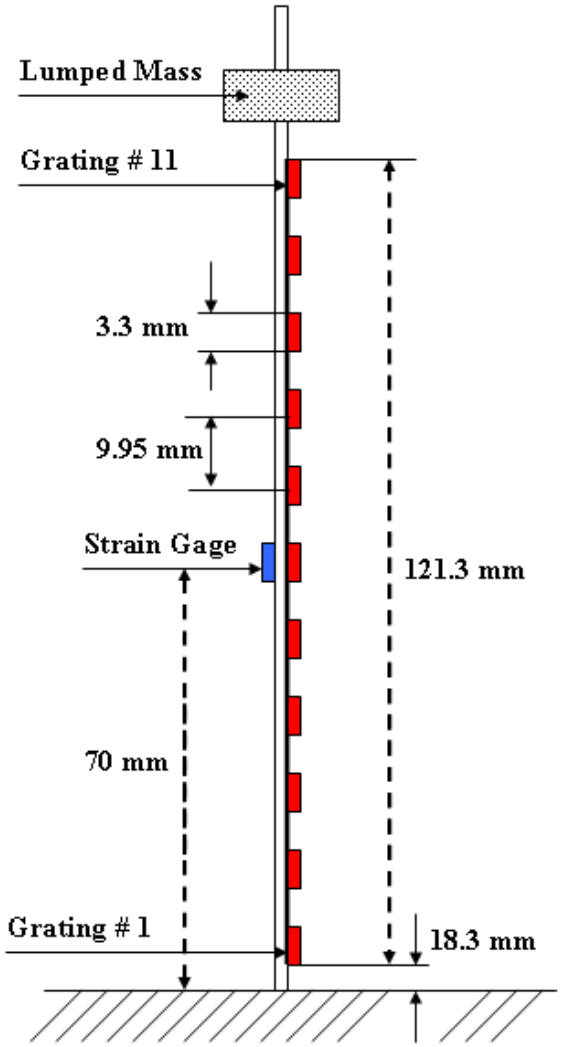

Figure 5.2: Schematic of the experimental setup, including composite beam geometry and locations of the strain gage and gratings of the fiber optic. The sixth grating is co-located with the strain gage on the opposite side of the beam and *70 mm* away from the mounting plate.

stretched using a tensile force to produce damage. The beam was then visually inspected using a digital microscope. Seven cracks were detected at *1.912 mm*, *12.235 mm*, *16.900 mm*, *22.537 mm*, *42.746 mm*, *60.664 mm*, and *130.002 mm* away from the mounting plate as shown in Figure 5.3. These cracks extended accross the whole width of the beam. A photograph of the crack located *42.746 mm* from the mounting plate is shown Figure 5.4. Free response tests performed on the damaged beam-mass system yielded a first-mode natural frequency of 7.974 Hz.

For the localization of the cracks through nonlinear system identification, principal parametric excitation of the beam-mass system is exploited. This is done by performing frequency sweeps whereby the system was excited over a small range near twice its natural frequency. The excitation signal is generated by a two-channel, variable-phase wave synthesizer. During the frequency sweep, the excitation frequency is decreased by a step size of 0.001 Hz while keeping its amplitude constant. This experimental procedure is performed on both the *Undamaged* and *Damaged* states. As expected, when the excitation frequency nears twice the first-mode natural frequency, the response of the beam-mass system shows a sudden increase in amplitude. Figure 5.5 shows sudden increase in the amplitude of the response, as measured by the strain gage, of the undamaged beam even though the amplitude and frequency of the excitation were maintained constant. It is noted that the excitation frequency of the case presented in this figure is set to 16.545 Hz, which is extremely close to twice the frequency of the first-mode natural frequency of 8.273 Hz. Time series showing the jump from small to large amplitude oscillations and variations in the response of the damaged beam, as measured by the strain gage, is presented in Figure 5.6. The excitation amplitude and frequency were, again, kept constant as shown by the time series of the excitation presented in the same figure. Also, in this case, the excitation frequency was set to 15.949 Hz which is almost exactly twice the natural frequency estimated from the free response test.

Variations in the steady-state amplitude of the composite beam-mass system with the excitation frequency are collected to produce the frequency-response curves shown in Figure 5.7. The jumps from small to large amplitude oscillations are clearly shown in this figure. After a value equal to twice the natural frequency is reached, the beam-mass system keeps responding with large amplitude oscillations. While the excitation frequency is slowly de-

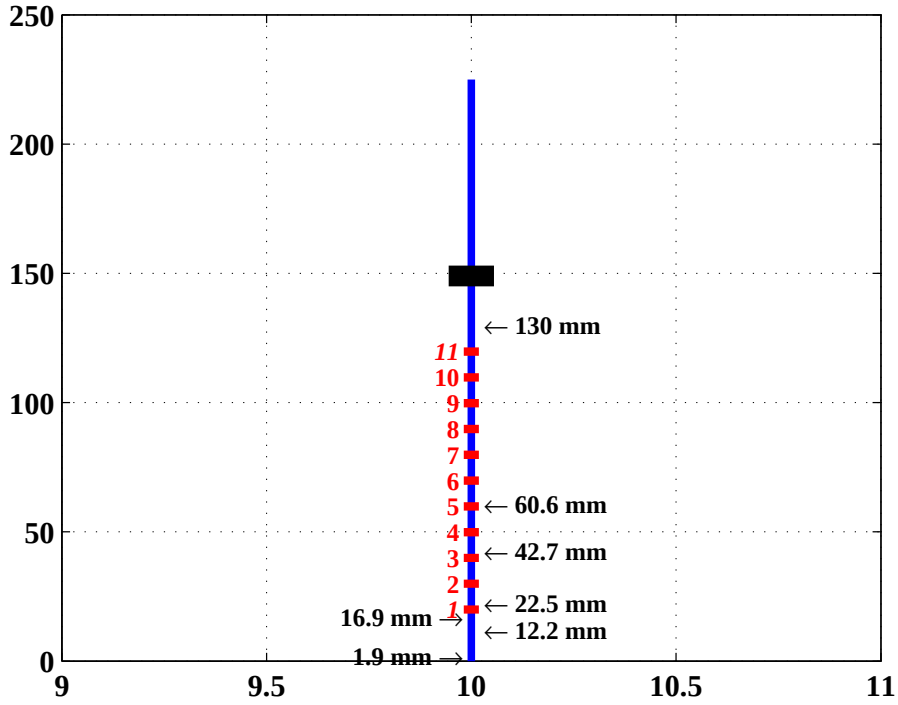

Figure 5.3: Locations, away from the mounting plate, of the seven cracks produced through the tensile force. All, but one, of the cracks, are located within *61 mm* from the mounting plate and are covered by the first five gratings of the fiber optic.

creased by a step size of 0.001 Hz, the beam mass-system response amplitude decreases. This behavior denotes that the system's natural frequency is continuously changing as the excitation frequency is decreased. This type of behavior is observed both for *Undamaged* and *Damaged* states.

5.2 Damage Effects on Beam's Response

In the following sections, results from spectral analysis of data from all gratings are presented. Differences in response amplitudes and linear and nonlinear coherence functions near and away from the cracks are detailed. The response amplitudes are determined from estimates

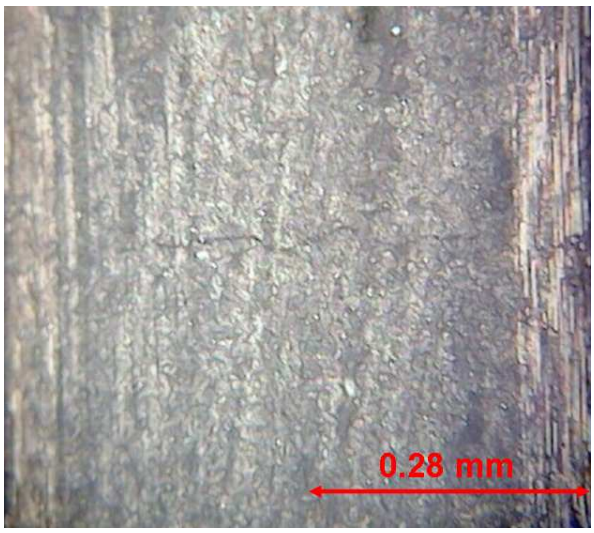

Figure 5.4: Photograph of the crack located *42.746 mm* away from the mounting plate.

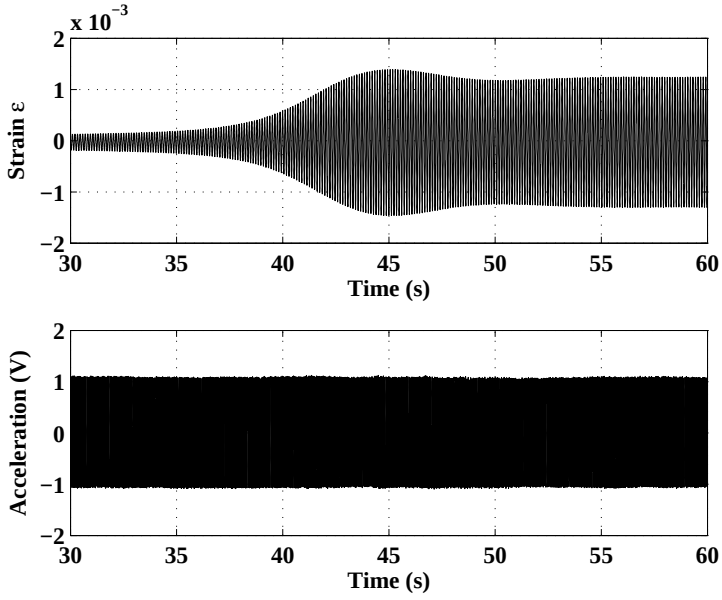

Figure 5.5: Time series showing the jump in the response of the undamaged composite beam when the excitation frequency is set to 16.545 Hz, which is near twice the natural frequency, 8.273 Hz.

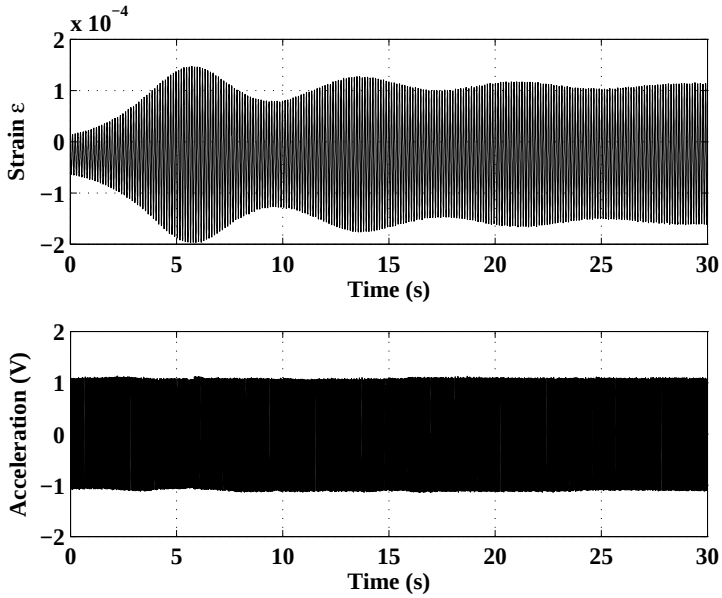

Figure 5.6: Time series showing jump and variations in the response of the damaged composite beam when the excitation frequency is set to 15.945 Hz, which is twice the natural frequency of the first-mode, 7.974 Hz.

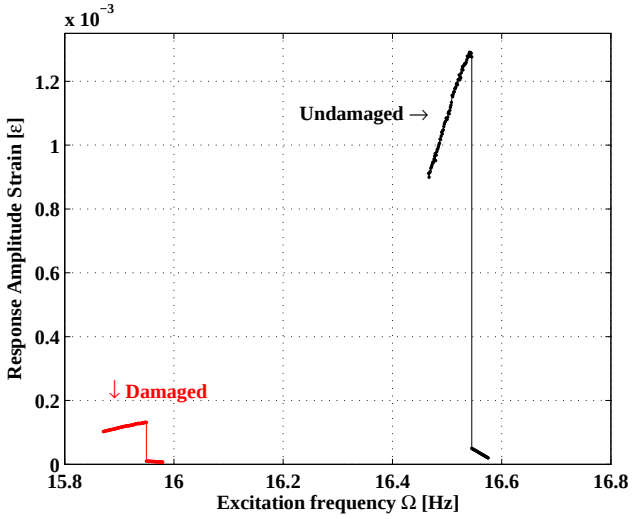

Figure 5.7: Frequency response curves for the *Undamaged* and *Damaged* beam-mass systems. The damaged beam response amplitude is one order of magnitude smaller than that of the undamaged beam. The frequency of the damaged beam is about 3.6% lower than that of the undamaged beam.

of the power spectrum. Because the beam-mass system is forced parametrically, the linear coherence between frequency components of the excitation and responses is expected to be low. Yet, analysis results are presented to complete the discussions. The nonlinear coherence between different frequency components in the excitation and response are determined from the cross-bicoherence functions (Kim and Powers (1979)).

5.2.1 Power Spectra of the Undamaged Beam Response

Differences in the frequency content of the strain at different locations along the undamaged beam are determined from power spectra at the center and end locations of each fiber grating. These spectra are presented in Figures 5.8 - 5.16. Parts (a), (b), and (c) of these figures show, respectively, the spectra of the strain as measured at the lowest end, centerline, and the highest end of each grating. It is observed that, in several gratings, the noise level in the measurements at the ends is much higher than those at the centerline. Consequently, the peaks of the response frequency are better defined from measurements at the centerline of each fiber grating. The same observations can be made about the peaks of the second (excitation) and third harmonics. These peaks are, in some of the spectra of the ends measurements, within the noise level. As such, in the following discussion, we will use the centerline measurements to assess nonlinear effects. This also shows that averaging the time series from all gratings might not be appropriate as signals with different noise levels will be mixed.

The power spectrum of the strain measurements captured by the strain gage is shown in Figure 5.17. Its content resembles the spectrum shown in Figure 5.12(b) which is derived from measurements at the centerline of the sixth fiber grating and co-located accross from the strain gage. Because its noise level is much lower than that of the fiber grating, the peaks of fundamental and higher harmonics are more clearly pointed out. It is also observed that the noise level up to about 15 Hz is the same as that of the centerline of the sixth fiber grating. On the other hand, it is significantly lower in the frequency range above 20 Hz.

5.2.2 Power Spectra of the Damaged Beam Response

Power spectra of the strain measurements for the damaged beam are produced again for both ends and centerline of each fiber grating. These spectra are presented in Figures 5.18

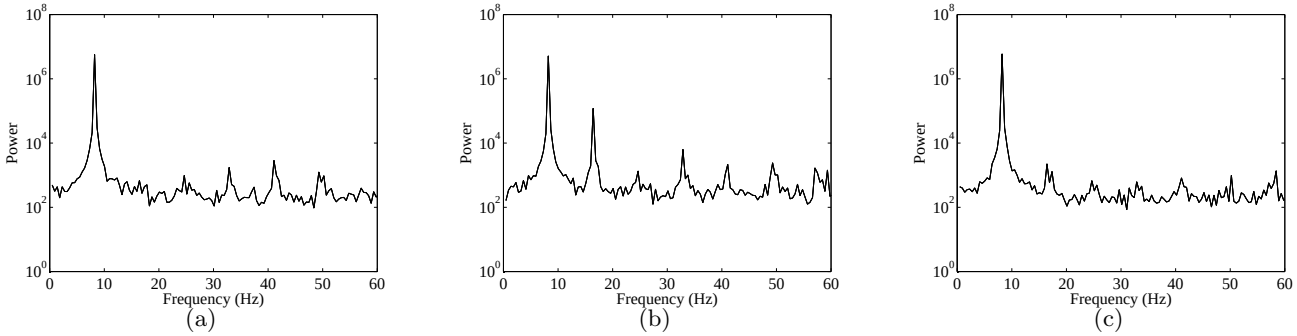

Figure 5.8: Power spectra of the strain measurements before damage as captured by (a) the lowest end, (b) the centerline, and (c) the highest end of fiber grating 2.

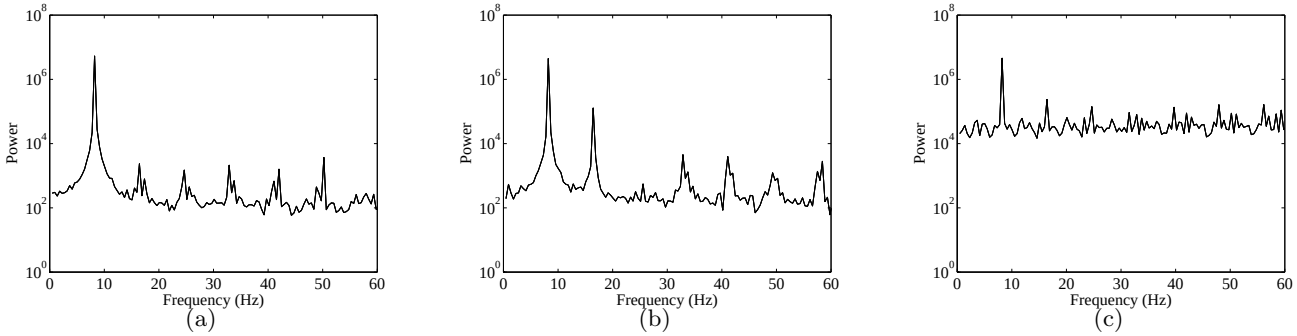

Figure 5.9: Power spectra of the strain measurements before damage as captured by (a) the lowest end, (b) the centerline, and (c) the highest end of fiber grating 3.

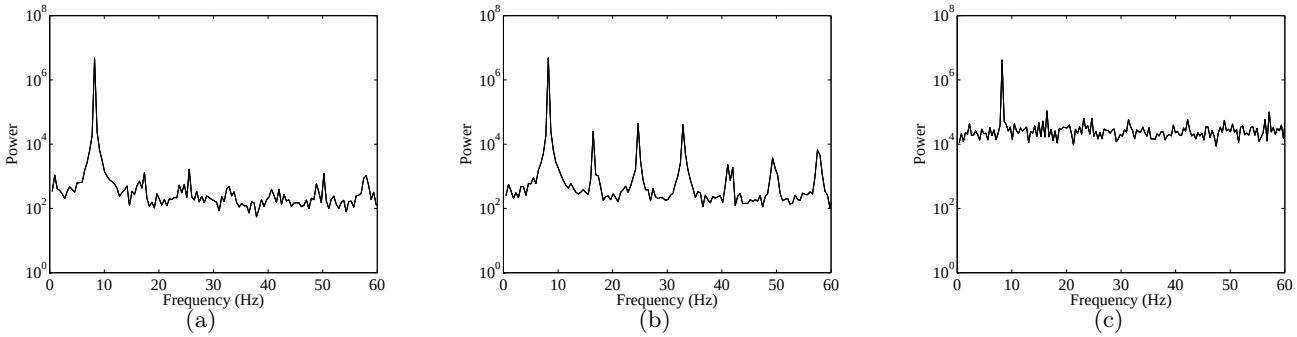

Figure 5.10: Power spectra of the strain measurements before damage as captured by (a) the lowest end, (b) the centerline, and (c) the highest end of fiber grating 4.

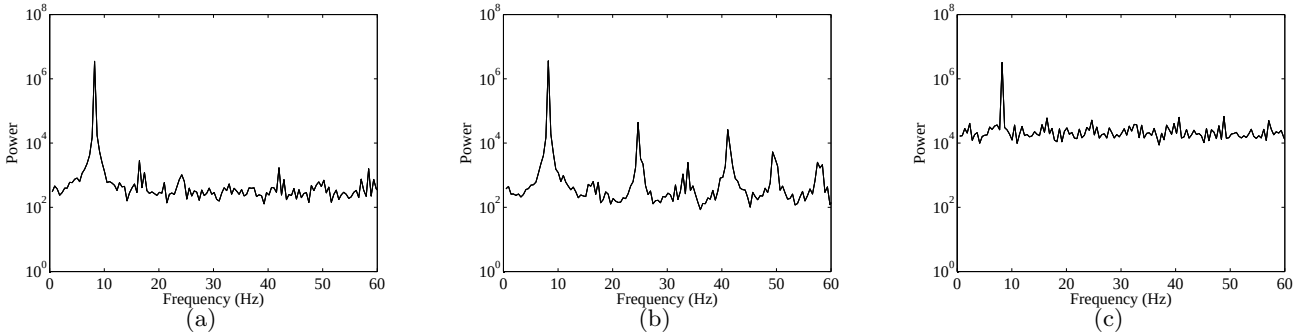

Figure 5.11: Power spectra of the strain measurements before damage as captured by (a) the lowest end, (b) the centerline, and (c) the highest end of fiber grating 5.

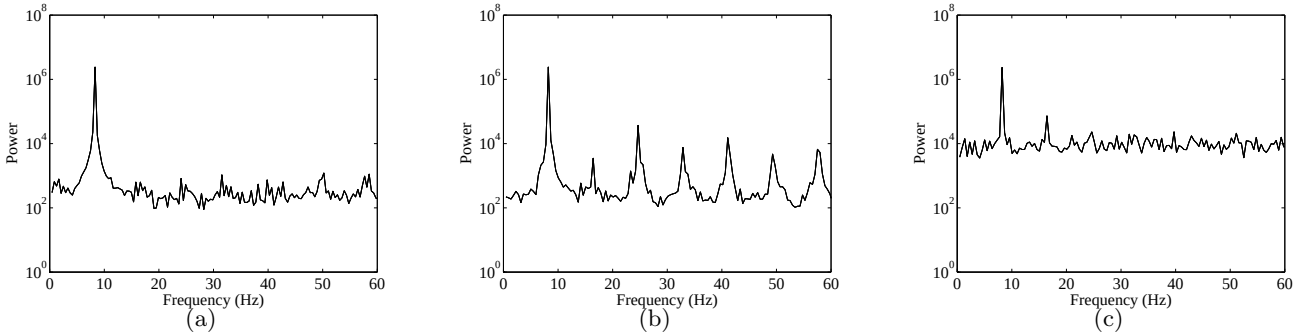

Figure 5.12: Power spectra of the strain measurements before damage as captured by (a) the lowest end, (b) the centerline, and (c) the highest end of fiber grating 6.

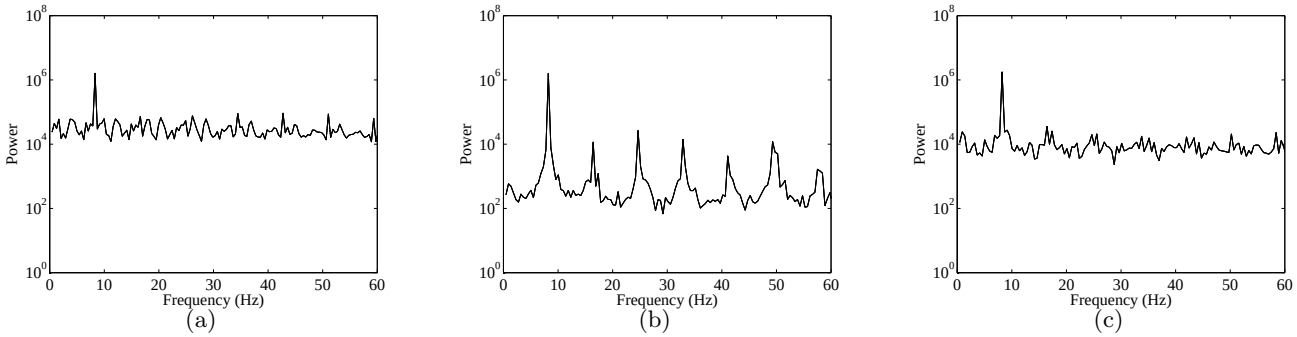

Figure 5.13: Power spectra of the strain measurements before damage as captured by (a) the lowest end, (b) the centerline, and (c) the highest end of fiber grating 7.

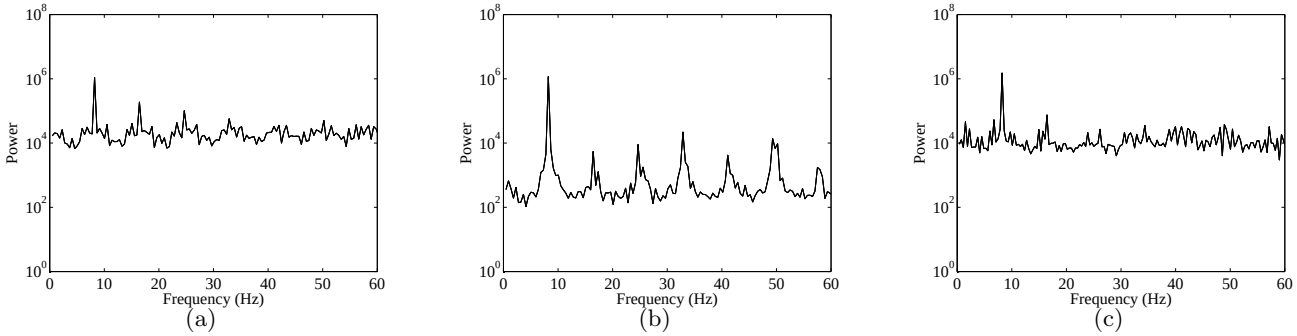

Figure 5.14: Power spectra of the strain measurements before damage as captured by (a) the lowest end, (b) the centerline, and (c) the highest end of fiber grating 8.

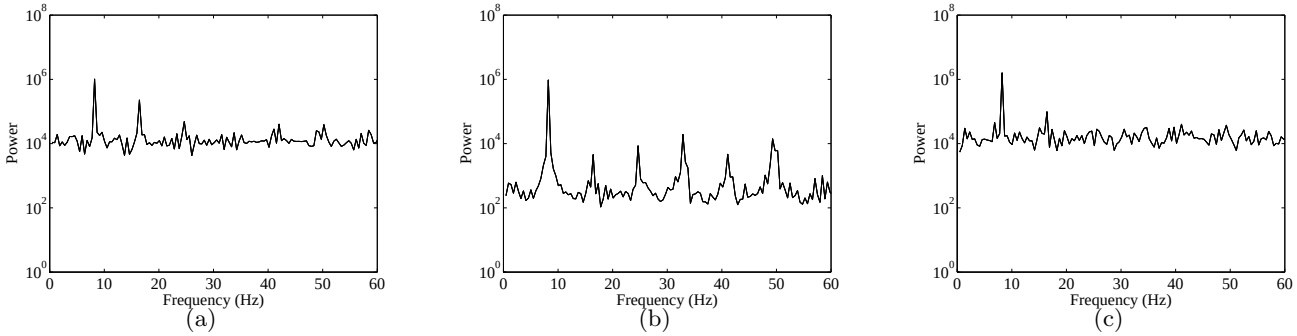

Figure 5.15: Power spectra of the strain measurements before damage as captured by (a) the lowest end, (b) the centerline, and (c) the highest end of fiber grating 9.

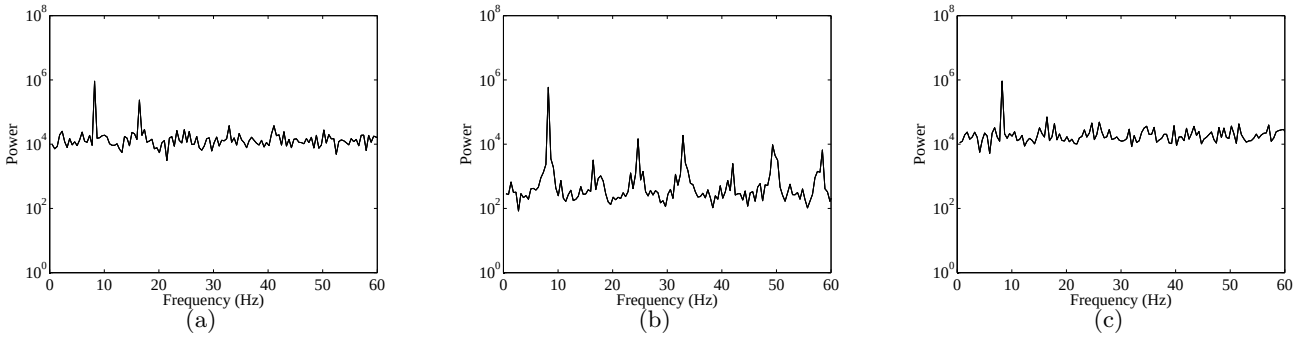

Figure 5.16: Power spectra of the strain measurements before damage as captured by (a) the lowest end, (b) the centerline, and (c) the highest end of fiber grating 10.

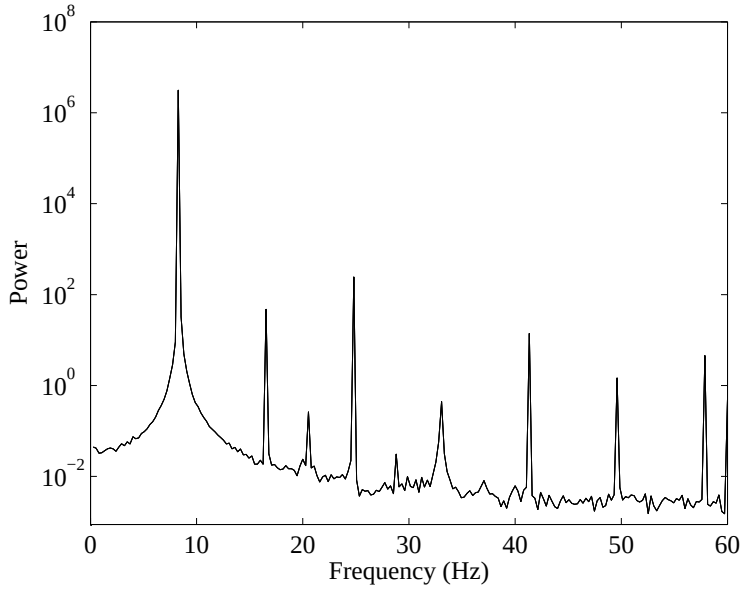

Figure 5.17: Power spectrum of the strain measurements captured before damage by the strain gage which is co-located on the opposite side of the beam with the sixth grating. Because its noise level is much lower than that of the fiber grating, the peaks of response frequency and higher harmonics are more clearly pointed out. It is also observed that the noise level up to about *15 Hz* is the same as that of the centerline of the sixth fiber grating. On the other hand, it is significantly lower in the frequency range above *20 Hz*.

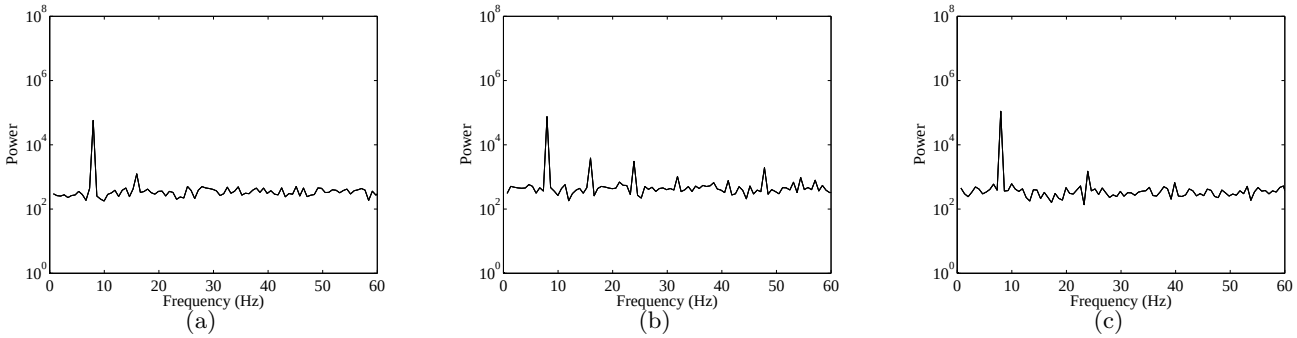

Figure 5.18: Power spectra of the strain measurements after damage as captured by (a) the lowest end, (b) the centerline, and (c) the highest end of fiber grating 2.

- 5.26. Parts (a), (b), and (c) of these figures show, respectively, the spectra of the lowest end, centerline, and the highest end of each grating. Clearly, the level of noise in the strain measurements for the damaged beam is about the same at the ends and centerlines of the different gratings. Additionaly, this level is lower than the levels measured in the undamaged beam. As such, the higher harmonics are better identified in signals from all gratings.

The power spectrum of the strain gage measurement positioned *70 mm* away from the clamped support is shown in Figure 5.27. Its content resembles the one shown in Figure 5.22(b) which is derived from the centerline measurements of the sixth fiber grating that is co-located in front of the strain gage. The presence of damage causes the peaks of both the fundamental and higher harmonics to be much lower than the undamaged state. For this reason, the peaks of the response power spectrum measured by the fiber grating are not clearly exhibited. On the contrary, the noise level of the strain gage measurement is much lower than the fiber gratings' noise level. Consequently, the peaks of fundamental and higher harmonics are clearly pointed out. It is observed, though, that the strain gage measurements after damage have a higher noise level than strain gage measurements of the undamaged beam presented in Figure 5.7.

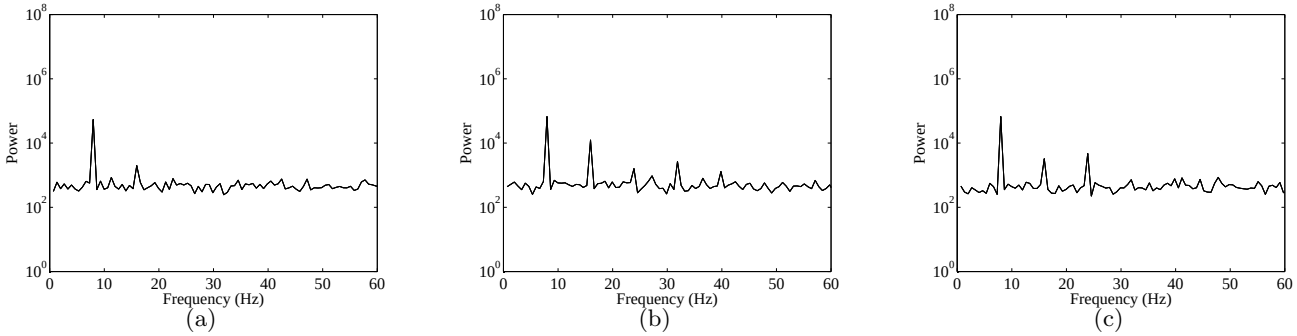

Figure 5.19: Power spectra of the strain measurements after damage as captured by (a) the lowest end, (b) the centerline, and (c) the highest end of fiber grating 3.

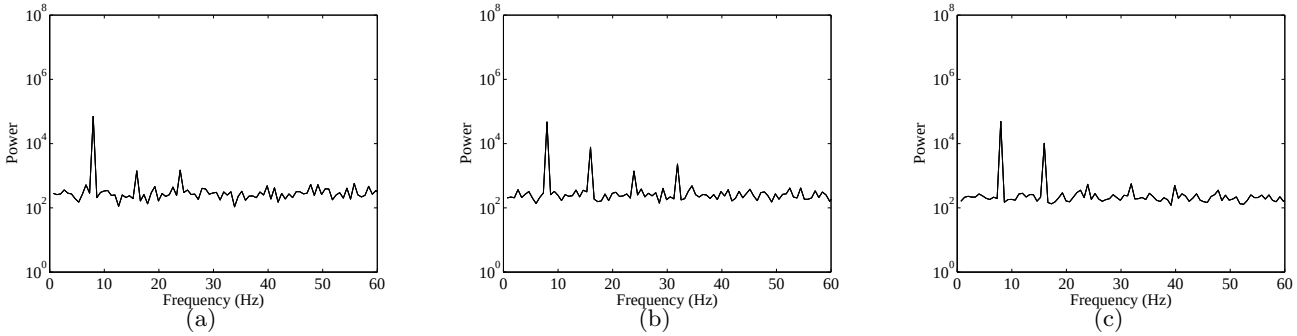

Figure 5.20: Power spectra of the strain measurements after damage as captured by (a) the lowest end, (b) the centerline, and (c) the highest end of fiber grating 4.

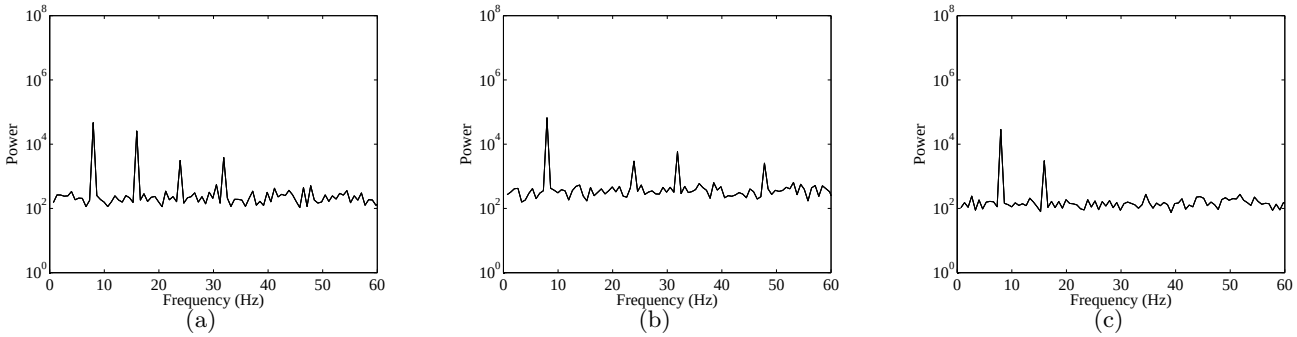

Figure 5.21: Power spectra of the strain measurements after damage as captured by (a) the lowest end, (b) the centerline, and (c) the highest end of fiber grating 5.

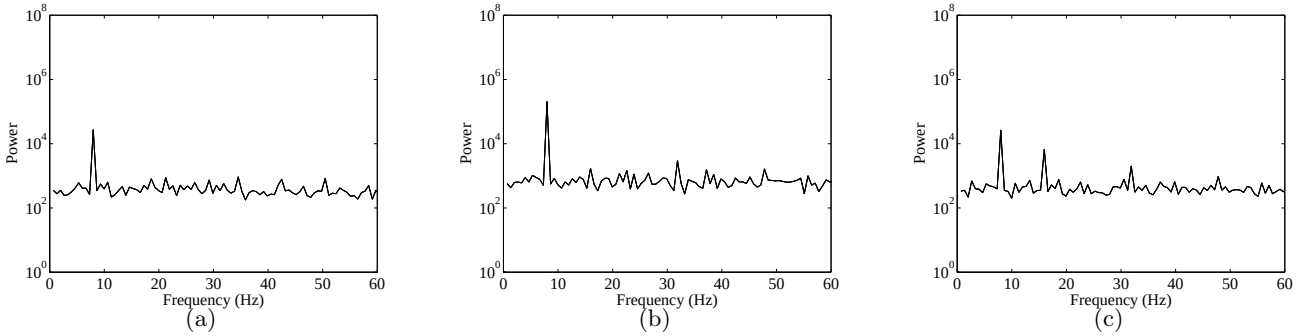

Figure 5.22: Power spectra of the strain measurements after damage as captured by (a) the lowest end, (b) the centerline, and (c) the highest end of fiber grating 6.

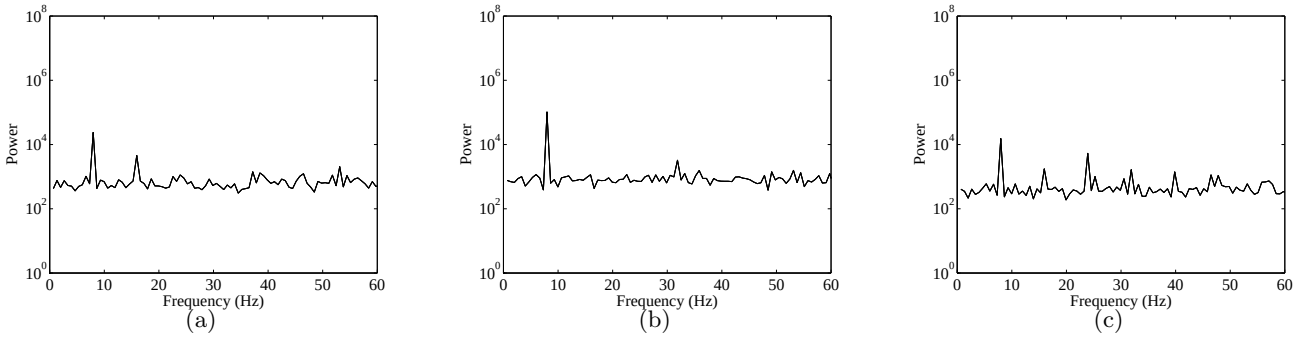

Figure 5.23: Power spectra of the strain measurements after damage as captured by (a) the lowest end, (b) the centerline, and (c) the highest end of fiber grating 7.

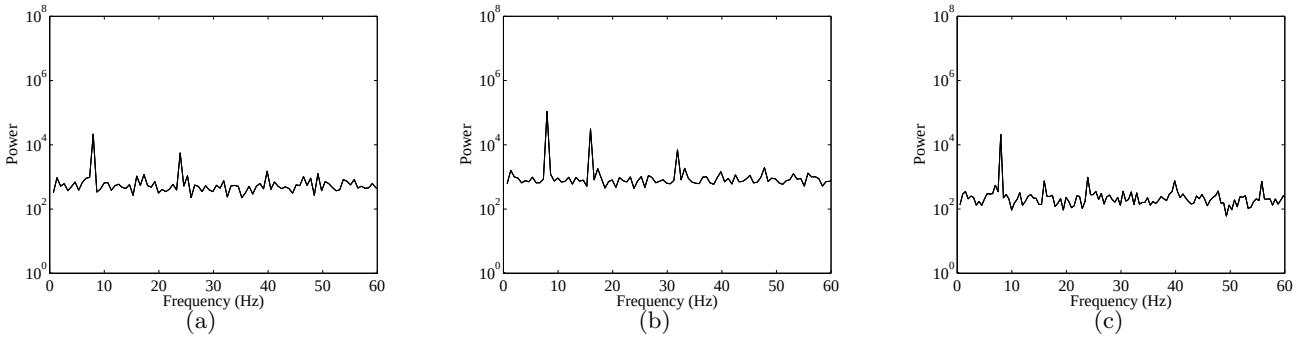

Figure 5.24: Power spectra of the strain measurements after damage as captured by (a) the lowest end, (b) the centerline, and (c) the highest end of fiber grating 8.

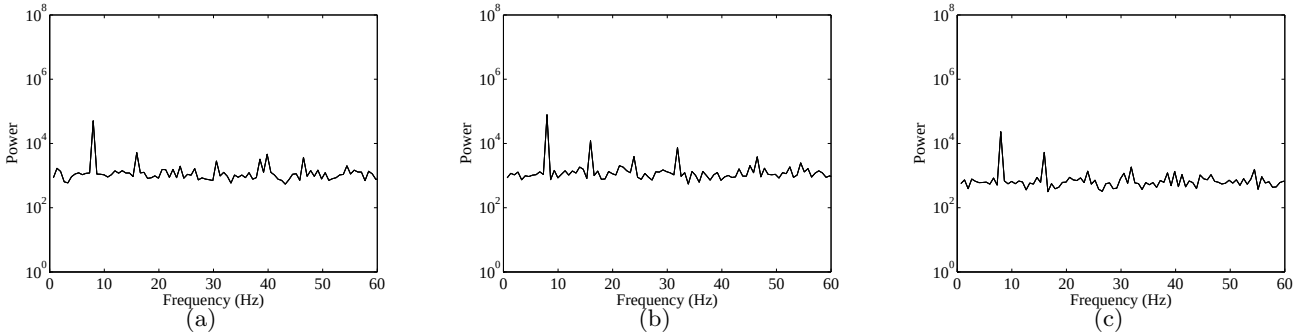

Figure 5.25: Power spectra of the strain measurements after damage as captured by (a) the lowest end, (b) the centerline, and (c) the highest end of fiber grating 9.

5.2.3 Excitation-Response Linear Coherence of the Undamaged Beam

Linear coherence of the strain measurements are determined at different locations along the undamaged beam in each fiber grating and are presented in Figures 5.28 - 5.36. Parts (a), (b), and (c) of these figures show, respectively, the linear coherence at the lowest end, centerline, and the highest end of each grating. As expected, the linear coherence at the response frequency is very low (< 0.1) in all gratings. On the contrary the linear coherence at the excitation frequency is largely affected by the noise level. Linear coherence at the ends, indeed, varies between 0.2 and 0.8. This variation is highly related to the noise levels as observed in the power spectra of Figure 5.20(b). The centerline measurements are, instead,

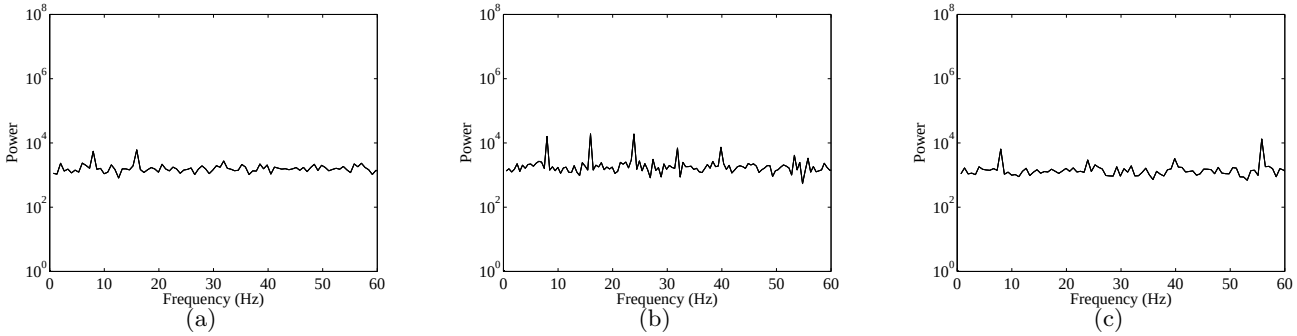

Figure 5.26: Power spectra of the strain measurements after damage as captured by (a) the lowest end, (b) the centerline, and (c) the highest end of fiber grating 10.

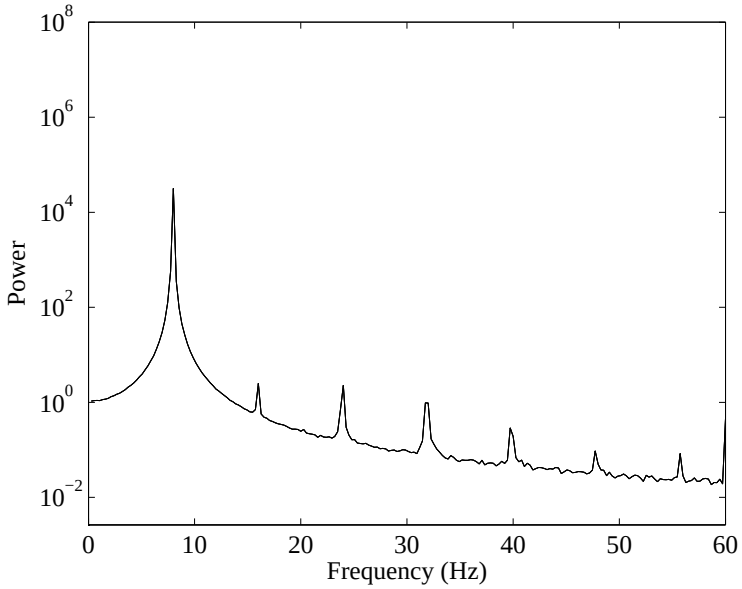

Figure 5.27: Power spectrum of the strain measurements captured after damage by the strain gage which is co-located on the opposite side of the beam with the sixth grating. It is observed that the strain gage measurement after damage is affected by a noise level which is higher than that measured by the strain gage of the undamaged beam.

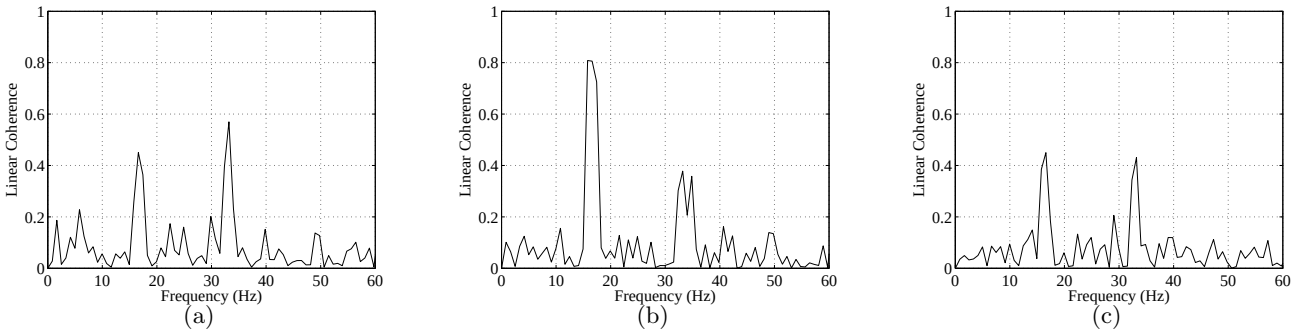

Figure 5.28: Linear coherence of the strain measurements before damage as captured by (a) the lowest end, (b) the centerline, and (c) the highest end of fiber grating 2.

more dependable because of their low noise level. The linear coherence at the centerline is, indeed, about 0.8 for all gratings' measurements except for the fifth where its value is about 0.3. Looking at the corresponding spectrum, in Figure 5.20(b), it is noted that this low coherence level can actually be associated with high noise level.

The linear coherence of the strain gage measurement positioned *70 mm* away from the mounting plate is presented in Figure 5.37. Its content resembles the one shown in Figure 5.32(b) which is the sixth fiber grating co-located in front of the strain gage. The level of linear phase coupling, at the response frequency, is about 0.1. This level increases to about 0.8 at the excitation frequency. These values are consistent with the coherence levels obtained from the strain gage and shown in Figure 5.37. It is observed that a high level of linear coherence is also present at *50 Hz*. This high value is not obtained, instead, by the optical fiber. The reason for this discrepancy may be due to the high noise level of the optical fiber which is much higher than that of the strain gage above *20 Hz*.

5.2.4 Excitation-Response Linear Coherence of the Damaged Beam

Linear coherence of the strain measurements in the damaged beam are again determined at different locations along the damaged beam in each fiber grating and are presented in Figures 5.38 - 5.46. Parts (a), (b), and (c) of these figures show, respectively, the linear coherence of the lowest end, centerline, and the highest end in each grating. It is observed

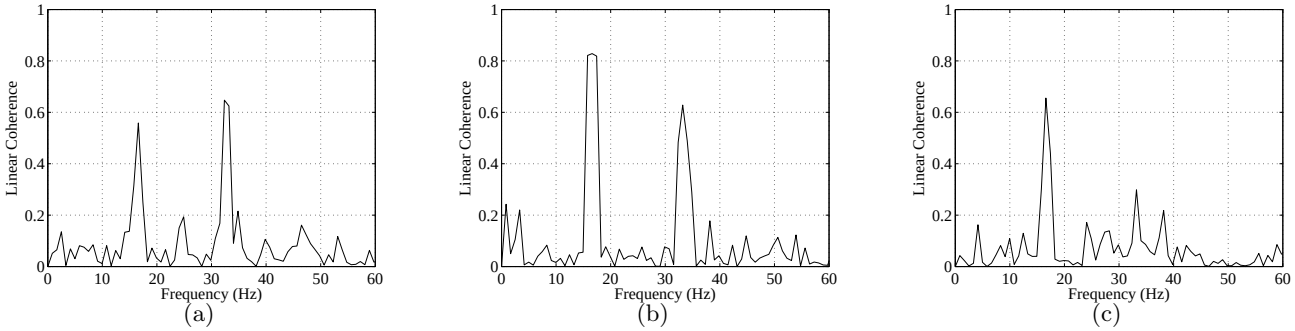

Figure 5.29: Linear coherence of the strain measurements before damage as captured by (a) the lowest end, (b) the centerline, and (c) the highest end of fiber grating 3.

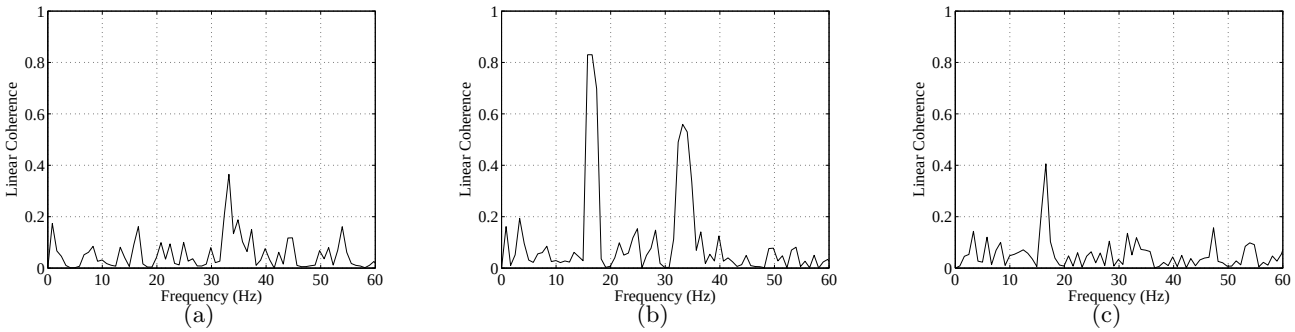

Figure 5.30: Linear coherence of the strain measurements before damage as captured by (a) the lowest end, (b) the centerline, and (c) the highest end of fiber grating 4.

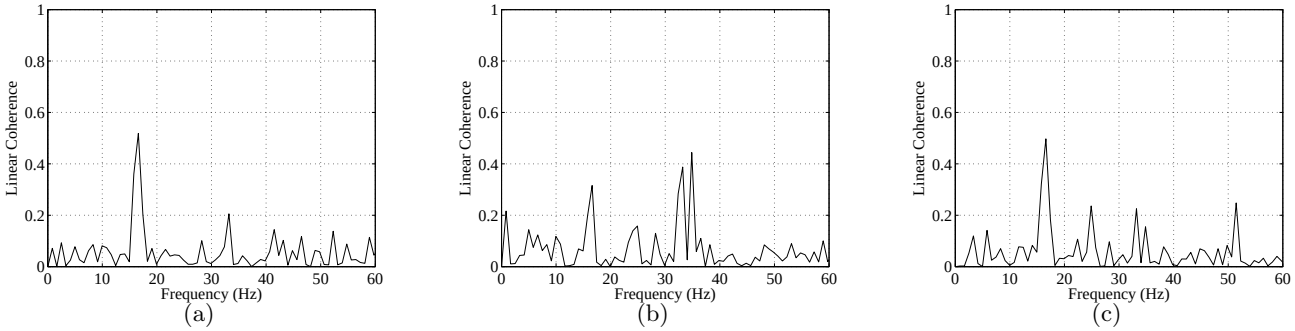

Figure 5.31: Linear coherence of the strain measurements before damage as captured by (a) the lowest end, (b) the centerline, and (c) the highest end of fiber grating 5.

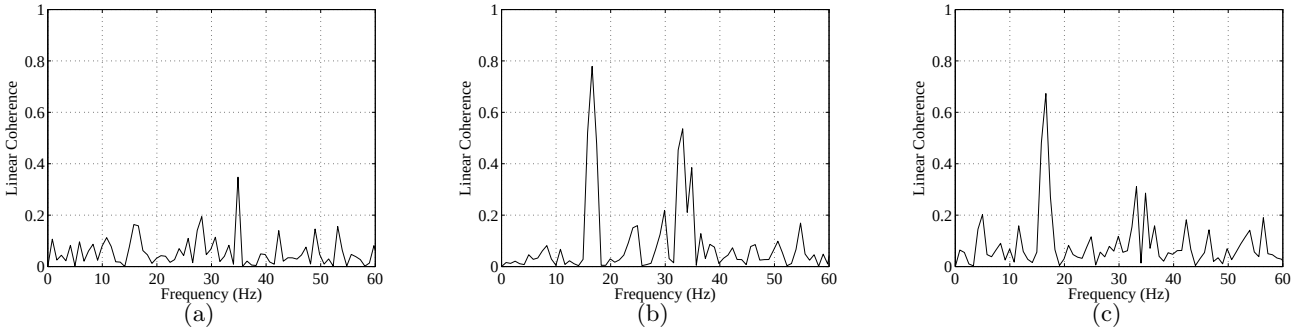

Figure 5.32: Linear coherence of the strain measurements before damage as captured by (a) the lowest end, (b) the centerline, and (c) the highest end of fiber grating 6.

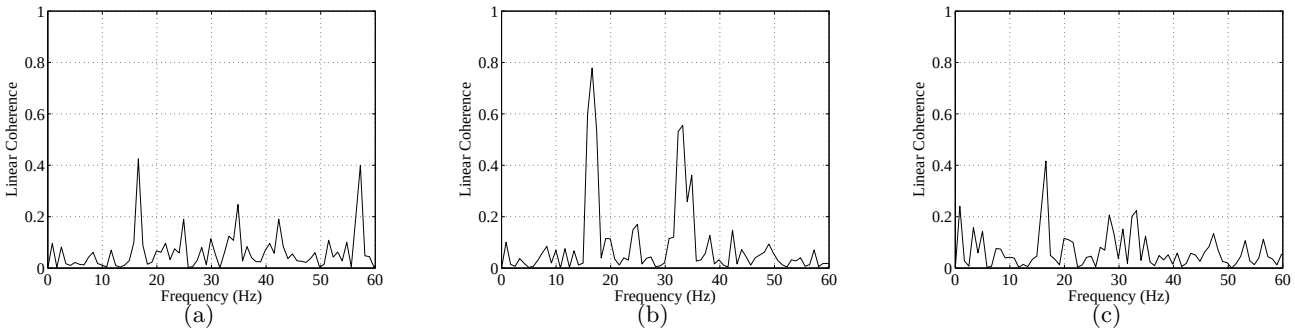

Figure 5.33: Linear coherence of the strain measurements before damage as captured by (a) the lowest end, (b) the centerline, and (c) the highest end of fiber grating 7.

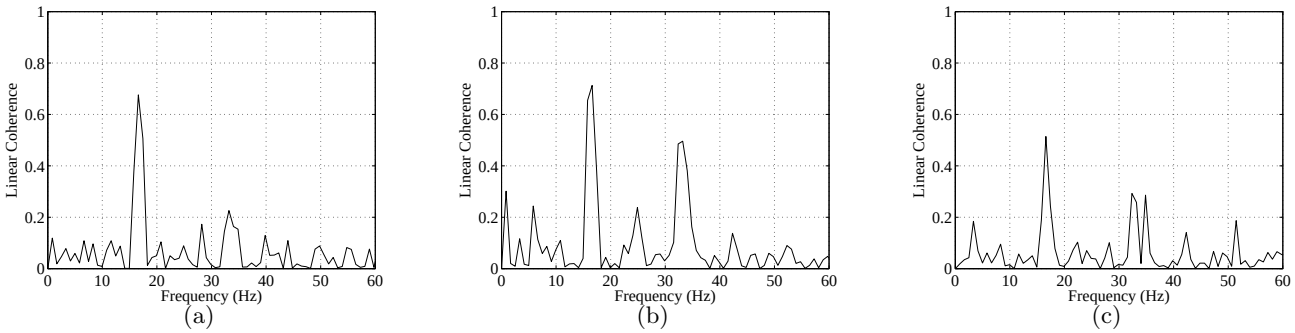

Figure 5.34: Linear coherence of the strain measurements before damage as captured by (a) the lowest end, (b) the centerline, and (c) the highest end of fiber grating 8.

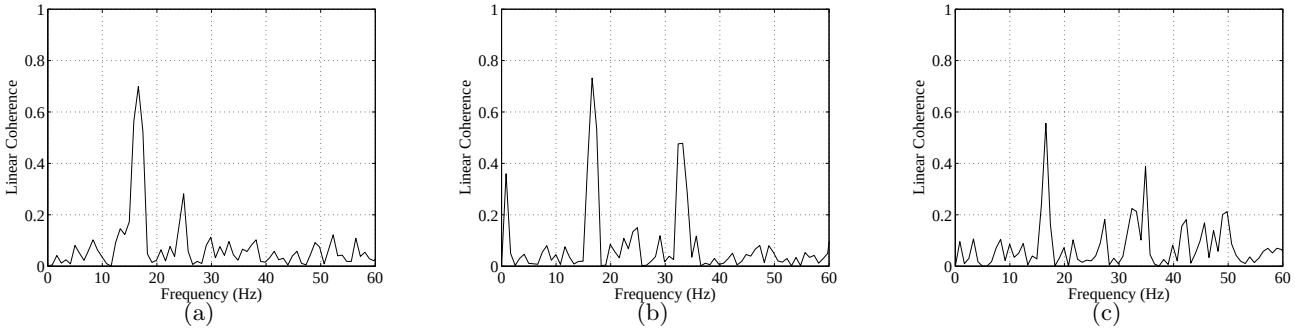

Figure 5.35: Linear coherence of the strain measurements before damage as captured by (a) the lowest end, (b) the centerline, and (c) the highest end of fiber grating 9.

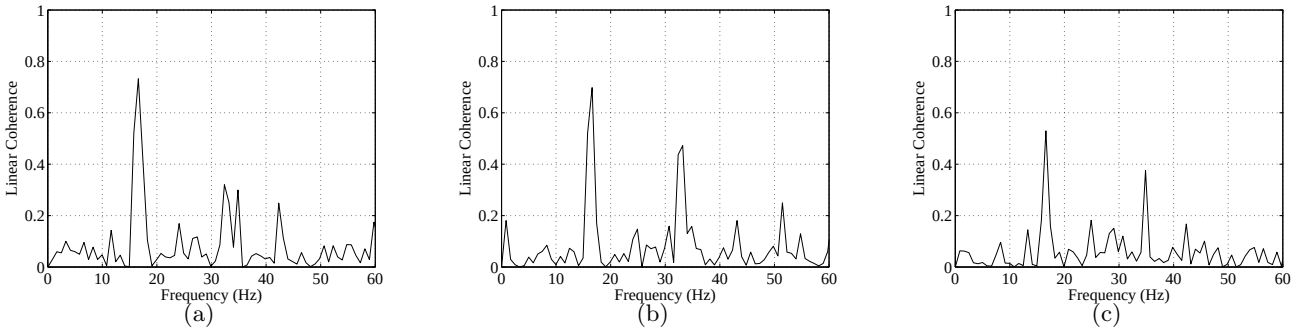

Figure 5.36: Linear coherence of the strain measurements before damage as captured by (a) the lowest end, (b) the centerline, and (c) the highest end of fiber grating 10.

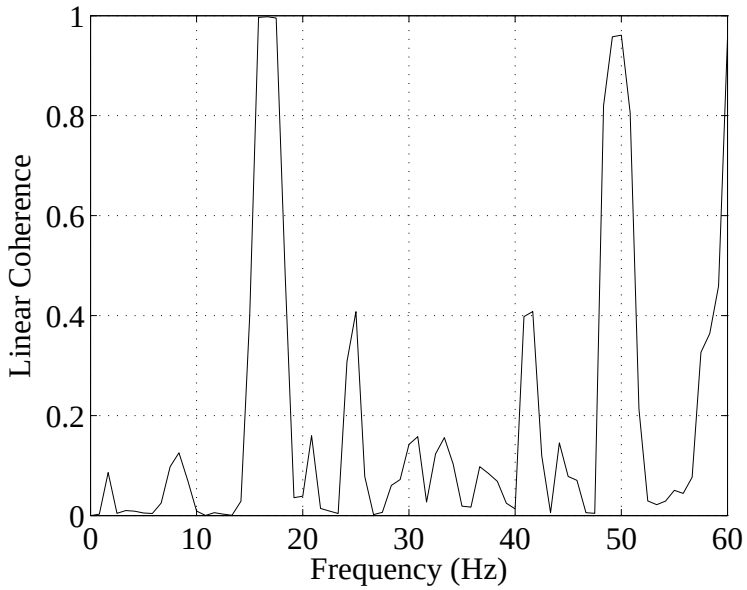

Figure 5.37: Linear coherence of the strain measurements captured before damage by the strain gage which is co-located on the opposite side of the beam with the sixth grating.

that the linear phase coupling at the response frequency has dramatically decreased with respect to the undamaged beam. Its level is constant and less than 0.01 for all gratings' measurements taken at the ends and centerline. The linear coherence at the excitation frequency is again largely affected by the noise level. At the ends it ranges between 0.1 and 0.7, but, in general, its levels have decreased in comparison with the undamaged beam. The linear coherence as measured by the strain gage are close to those estimated from the optical fiber measurements. The linear phase coupling has decreased with respect to the undamaged beam, as shown in Figure 5.47. Its level at the response frequency is equal to 0.01. At the excitation frequency, this level is, instead, equal to 0.9.

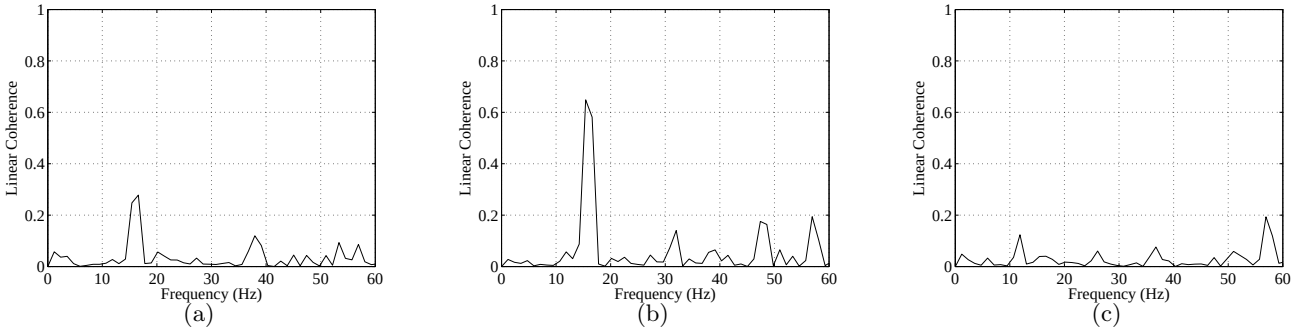

Figure 5.38: Linear coherence of the strain measurements after damage as captured by (a) the lowest end, (b) the centerline, and (c) the highest end of fiber grating 2.

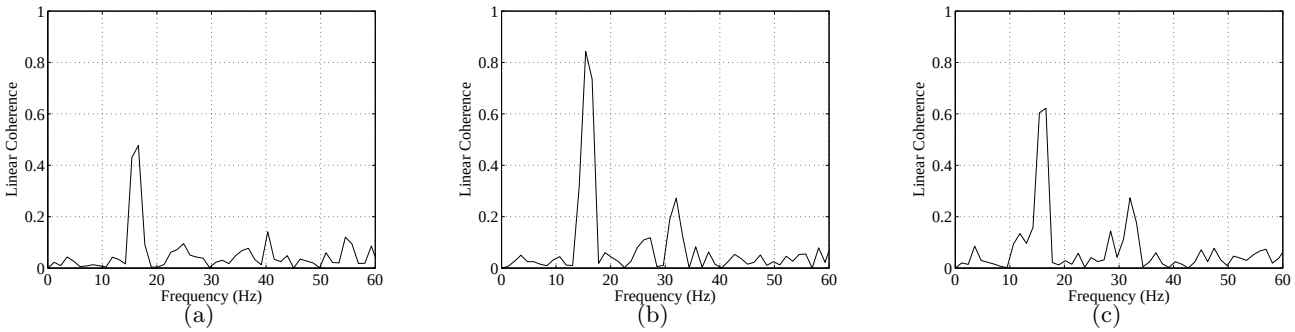

Figure 5.39: Linear coherence of the strain measurements after damage as captured by (a) the lowest end, (b) the centerline, and (c) the highest end of fiber grating 3.

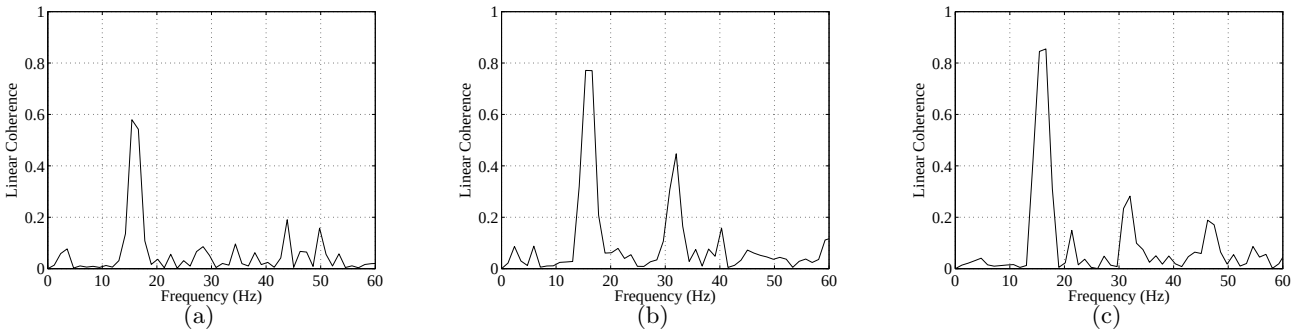

Figure 5.40: Linear coherence of the strain measurements after damage as captured by (a) the lowest end, (b) the centerline, and (c) the highest end of fiber grating 4.

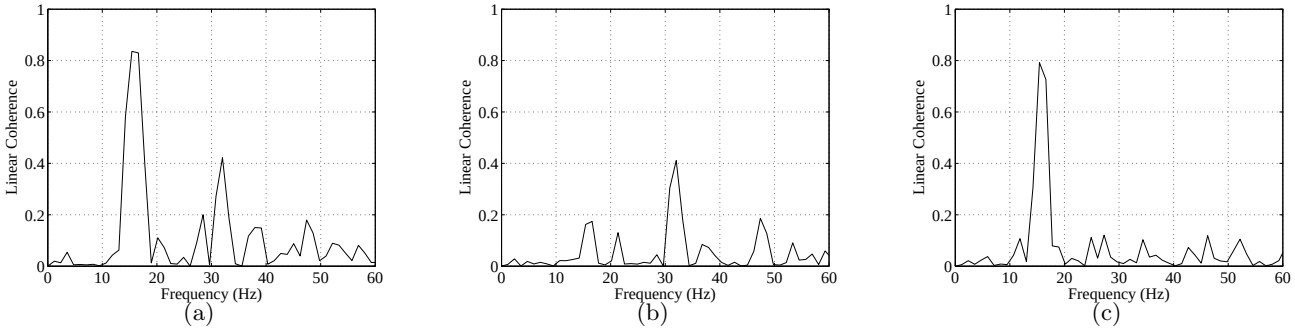

Figure 5.41: Linear coherence of the strain measurements after damage as captured by (a) the lowest end, (b) the centerline, and (c) the highest end of fiber grating 5.

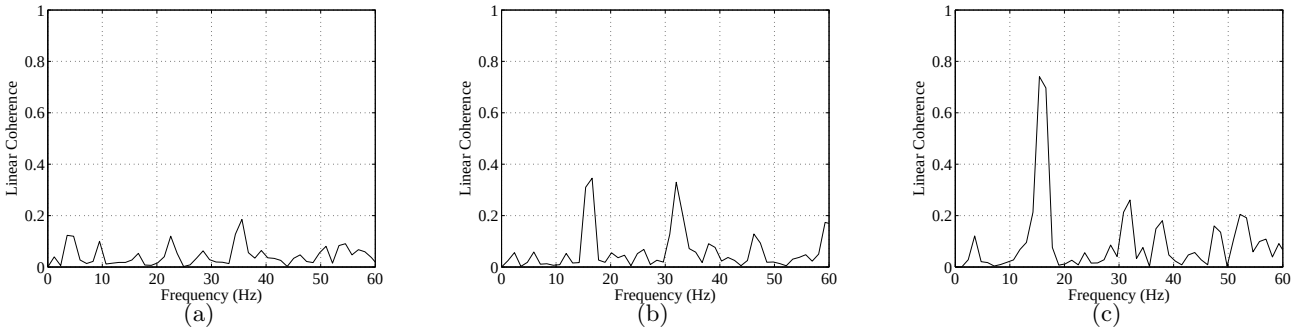

Figure 5.42: Linear coherence of the strain measurements after damage as captured by (a) the lowest end, (b) the centerline, and (c) the highest end of fiber grating 6.

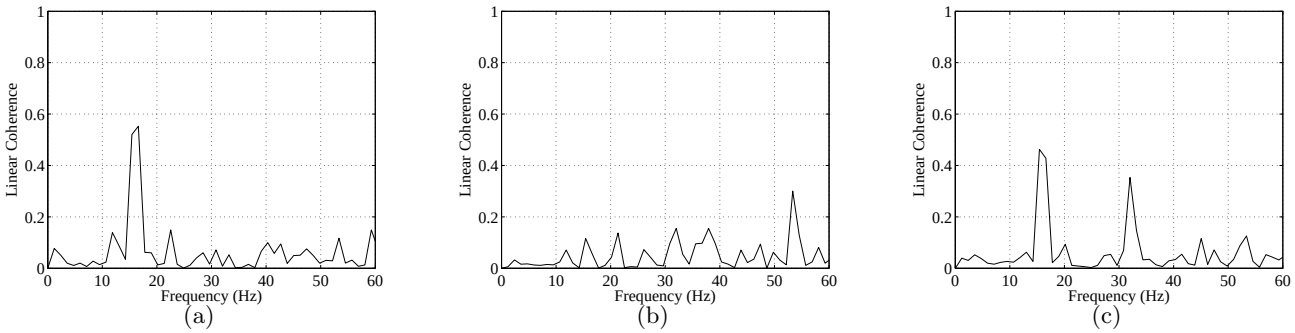

Figure 5.43: Linear coherence of the strain measurements after damage as captured by (a) the lowest end, (b) the centerline, and (c) the highest end of fiber grating 7.

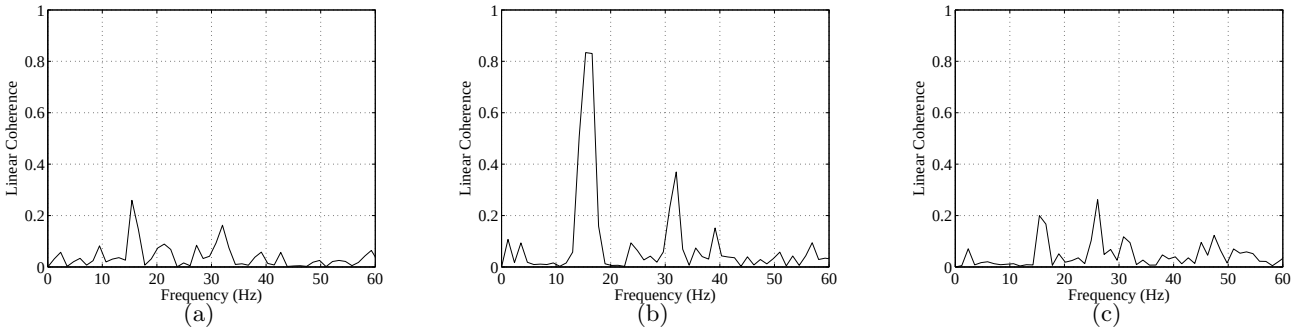

Figure 5.44: Linear coherence of the strain measurements after damage as captured by (a) the lowest end, (b) the centerline, and (c) the highest end of fiber grating 8.

5.2.5 Identification of Nonlinear Response-Excitation Dynamics of the Undamaged Beam

Local nonlinear response identification is determined from cross-bicoherence levels between the excitation and response frequencies. The cross-bicoherence of Gaussian noise is zero. As such, it yields a highly reliable quantification of nonlinear effects. Similarly to the power spectra estimates, the cross-bicoherence is obtained for specific data points of each fiber grating, namely, the lowest end, centerline, and highest end of each grating. Cross-bicoherence contour levels among frequency components in the excitation and response time series of the undamaged case at fiber gratings 2 to 10 are presented in Figures 5.48 - 5.56.

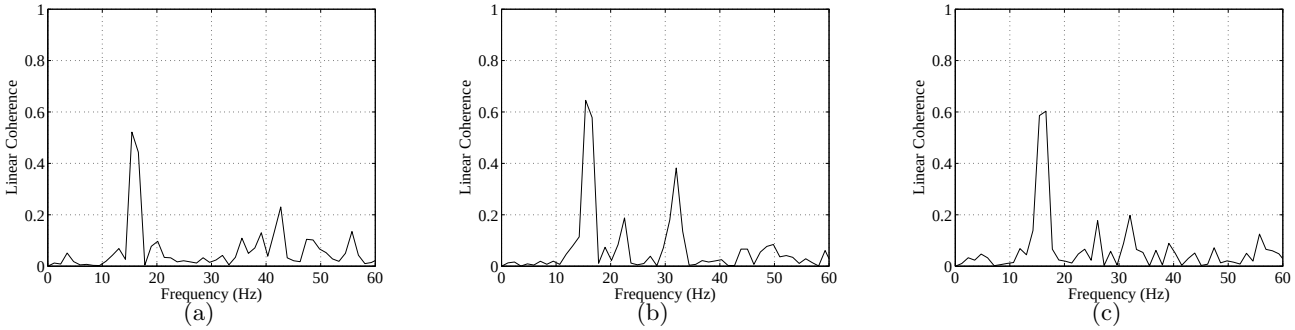

Figure 5.45: Linear coherence of the strain measurements after damage as captured by (a) the lowest end, (b) the centerline, and (c) the highest end of fiber grating 9.

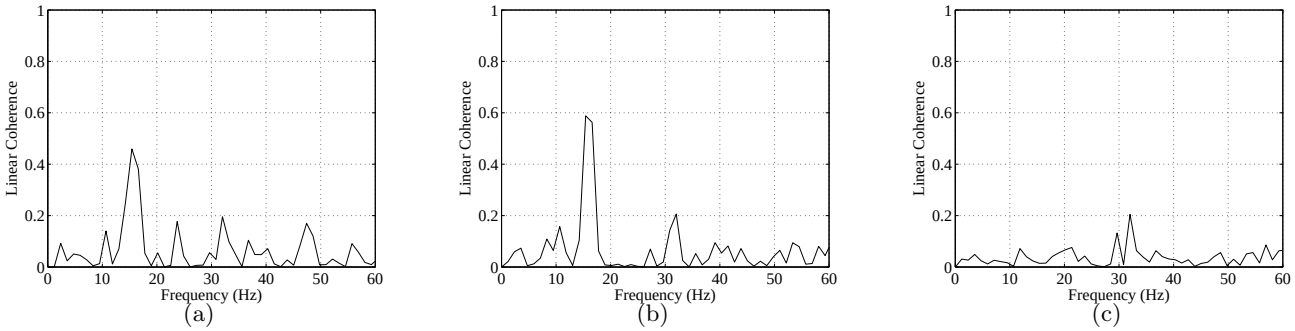

Figure 5.46: Linear coherence of the strain measurements after damage as captured by (a) the lowest end, (b) the centerline, and (c) the highest end of fiber grating 10.

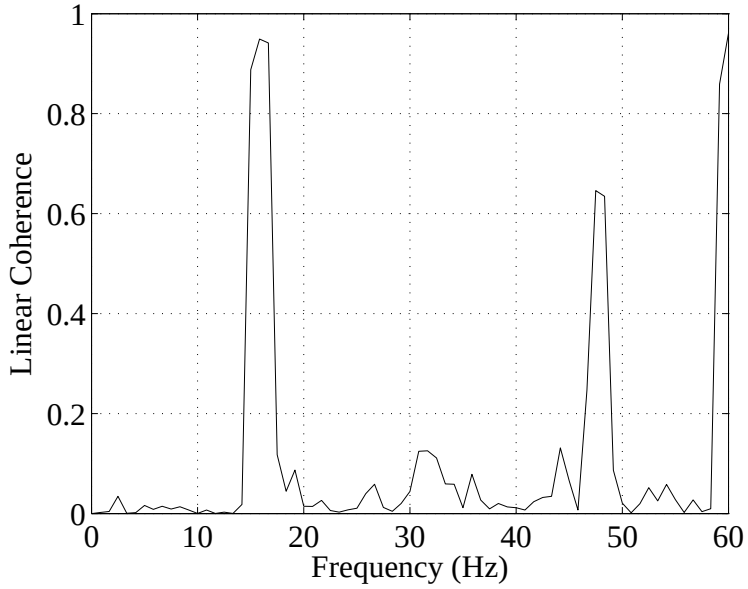

Figure 5.47: Linear coherence of the strain measurements captured after damage by the strain gage which is co-located on the opposite side of the beam with the sixth grating.

Three triples of frequencies are analyzed, namely $(f_{resp}, f_{resp}, f_{exc})$, $(3f_{resp}, f_{resp}, f_{exc})$, and $(4f_{resp}, f_{exc}, f_{exc})$. It is observed that the highest level of coupling is for the first triple, $(f_{resp}, f_{resp}, f_{exc})$, which ranges between 0.7 and 0.8. Cross-bicoherence levels for the triple of frequencies $(3f_{resp}, f_{resp}, f_{exc})$ range, between 0.4 and 0.6. Moreover, cross-bicoherence levels for the triples $(4f_{resp}, f_{exc}, f_{exc})$ are, instead, below 0.4. It is observed that the highest level of coupling is for the triple of frequencies $(f_{resp}, f_{resp}, f_{exc})$. Nevertheless, it has to be noted that, the estimated level of confidence from the cross-bicoherence varies from the ends to the centerline of each fiber grating. At the ends lower levels of confidence are, indeed, consistently estimated in comparison to the centerline. Moreover, at the ends these estimates are affected by large fluctuactions. On the contrary, the centerline shows more steady estimates of the level of coupling than at the ends. This observation makes the centerline measurements more dependable than the ones at the ends of each fiber grating.

The cross-bicoherence of the strain gage measurement is shown in Figure 5.57. Its contour levels are set to 0.9 and 0.99. Contour levels higher than the fiber optics measurements are

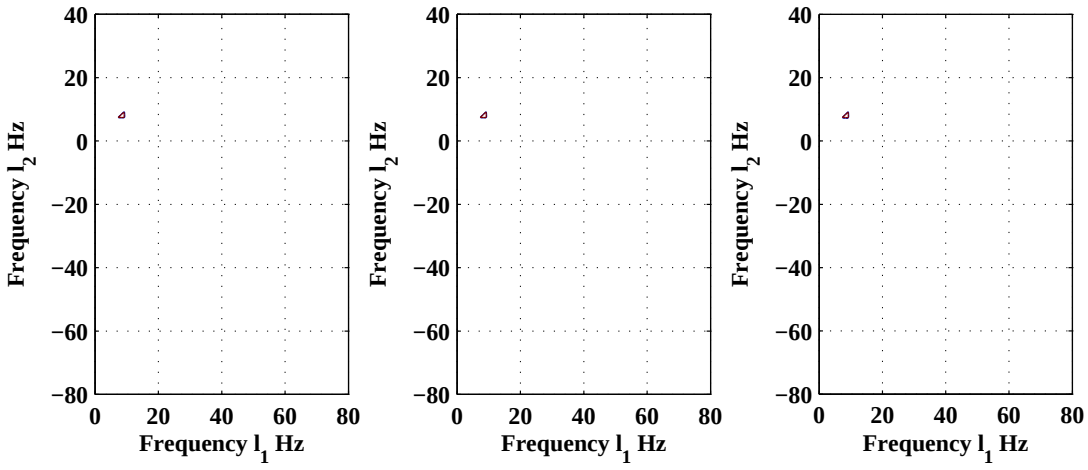

Figure 5.48: Cross-bicoherence between excitation and response at (a) the lowest end, (b) the centerline, and (c) the highest end of the fiber grating 2 before damage. Contour levels [0.7, 0.8].

present here because of its low noise level. Moreover, the presence of higher harmonics has to be noticed for the strain gage, which resembles the grating measurement at the centerline. This is due to the low level of noise at the center than at the ends.

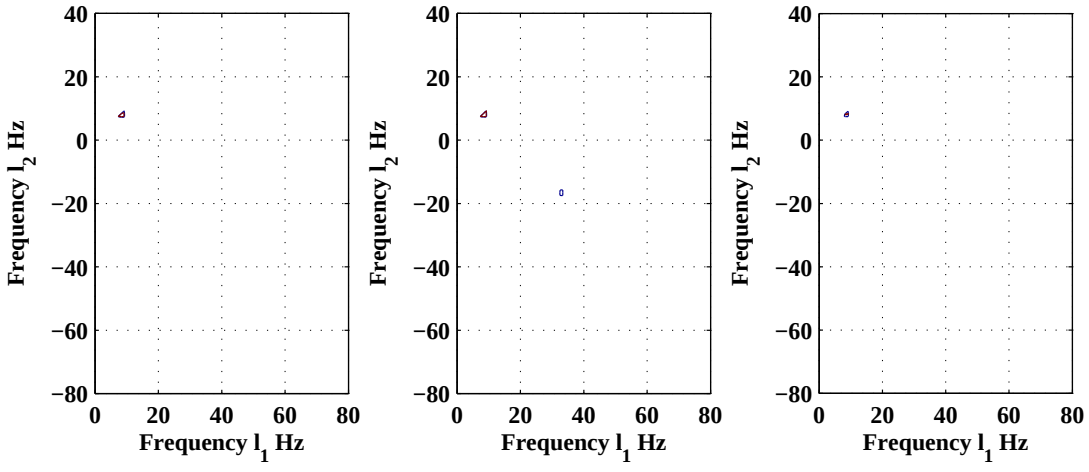

Figure 5.49: Cross-bicoherence between excitation and response at (a) the lowest end, (b) the centerline, and (c) the highest end of the fiber grating 3 before damage. Contour levels [0.7, 0.8].

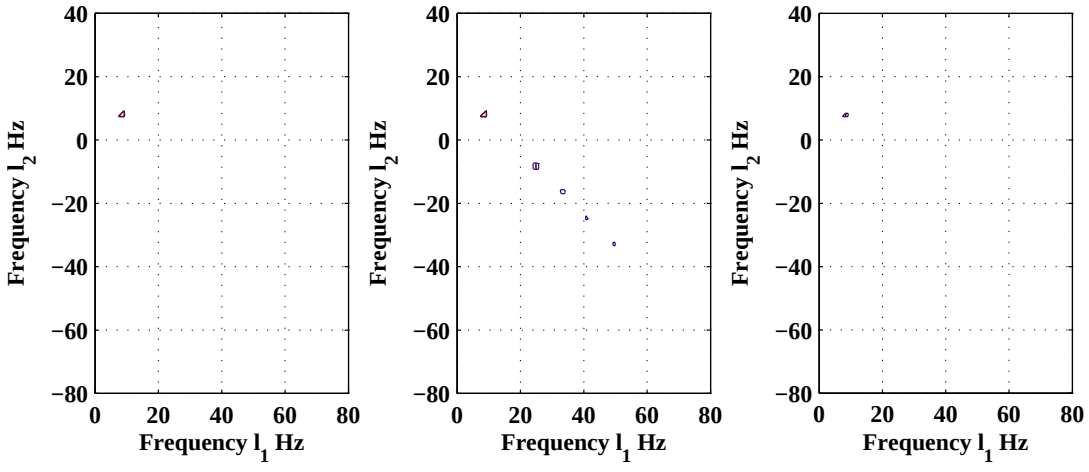

Figure 5.50: Cross-bicoherence between excitation and response at (a) the lowest end, (b) the centerline, and (c) the highest end of the fiber grating 4 before damage. Contour levels [0.7, 0.8].

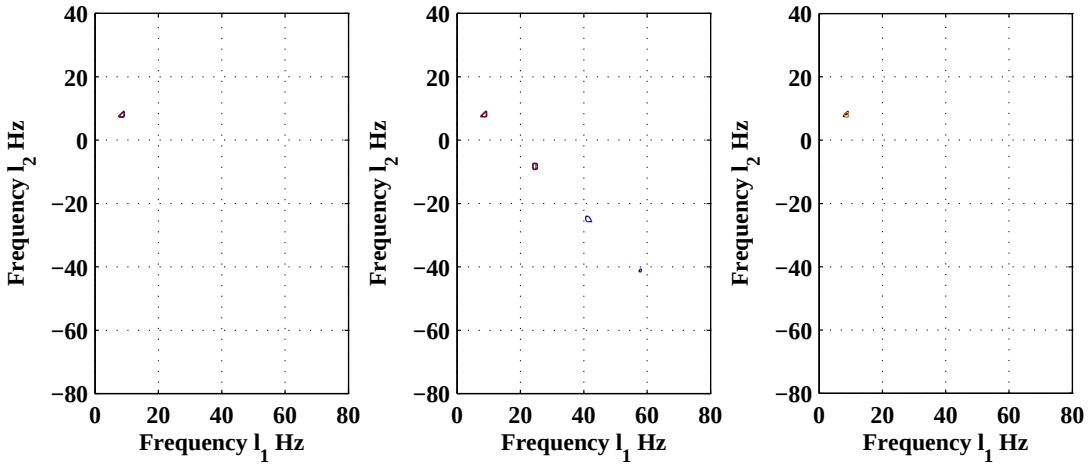

Figure 5.51: Cross-bicoherence between excitation and response at (a) the lowest end, (b) the centerline, and (c) the highest end of the fiber grating 5 before damage. Contour levels [0.7, 0.8].

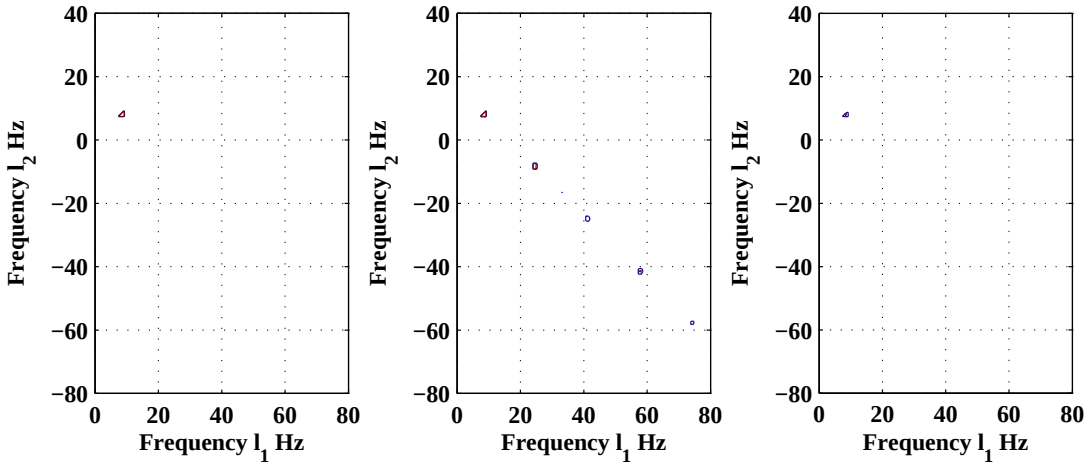

Figure 5.52: Cross-bicoherence between excitation and response at (a) the lowest end, (b) the centerline, and (c) the highest end of the fiber grating 6 before damage. Contour levels [0.7, 0.8].

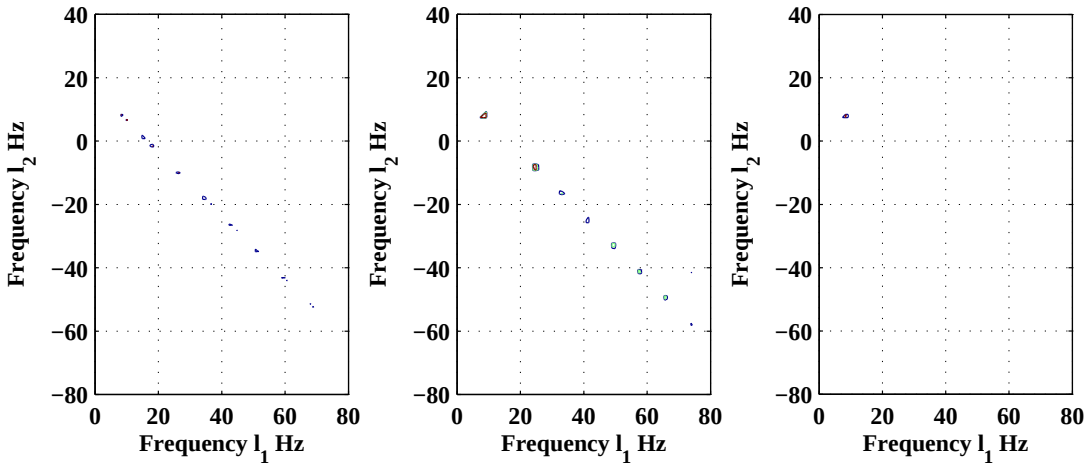

Figure 5.53: Cross-bicoherence between excitation and response at (a) the lowest end, (b) the centerline, and (c) the highest end of the fiber grating 7 before damage. Contour levels [0.7, 0.8].

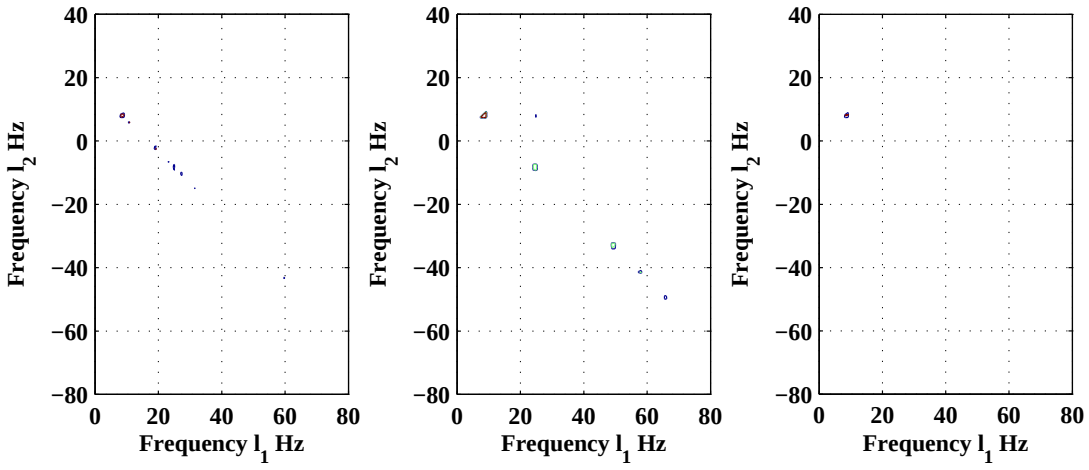

Figure 5.54: Cross-bicoherence between excitation and response at (a) the lowest end, (b) the centerline, and (c) the highest end of the fiber grating 8 before damage. Contour levels [0.7, 0.8].

5.2.6 Identification of Nonlinear Response-Excitation Dynamics of the Damaged Beam

Cross-bicoherence contour levels among frequency components in the excitation and response time series of the damaged case at fiber gratings 2 to 10 are presented in Figures 5.58 to 5.66. Similarly to the previous section, the cross-bicoherence is obtained for specific data points of each fiber grating, namely, the lowest end, centerline, and highest end of each grating. Three triples of frequencies are, again, analyzed here, namely $(f_{resp}, f_{resp}, f_{exc})$, $(3f_{resp}, f_{resp}, f_{exc})$, and $(4f_{resp}, f_{exc}, f_{exc})$. It is observed that the highest level of coupling is again present for the triple of frequencies $(f_{resp}, f_{resp}, f_{exc})$. It is also noted that these levels vary with the presence and nearness of cracks. Contour levels range, indeed, between 0.8 and 0.9 for the fiber gratings located near cracks (between *20 mm* and *60 mm*), and drop to 0.6 and 0.7 in the region far away from cracks location (between *60 mm* and *100 mm*). The fiber grating number 10, which is the farest from the cracks locations, shows contour levels between 0.2 and 0.3. It is also affected by the highest level of noise. This local variation allows the

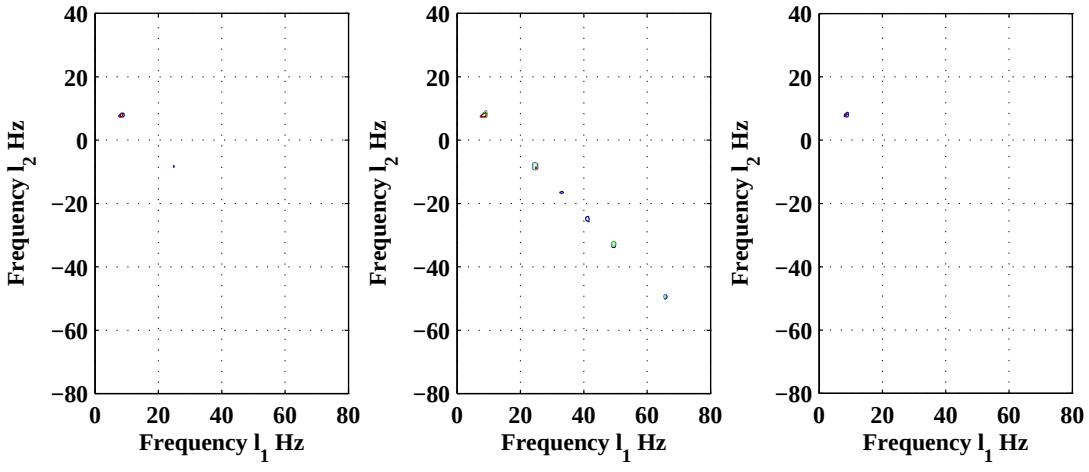

Figure 5.55: Cross-bicoherence between excitation and response at (a) the lowest end, (b) the centerline, and (c) the highest end of the fiber grating 9 before damage. Contour levels [0.7, 0.8].

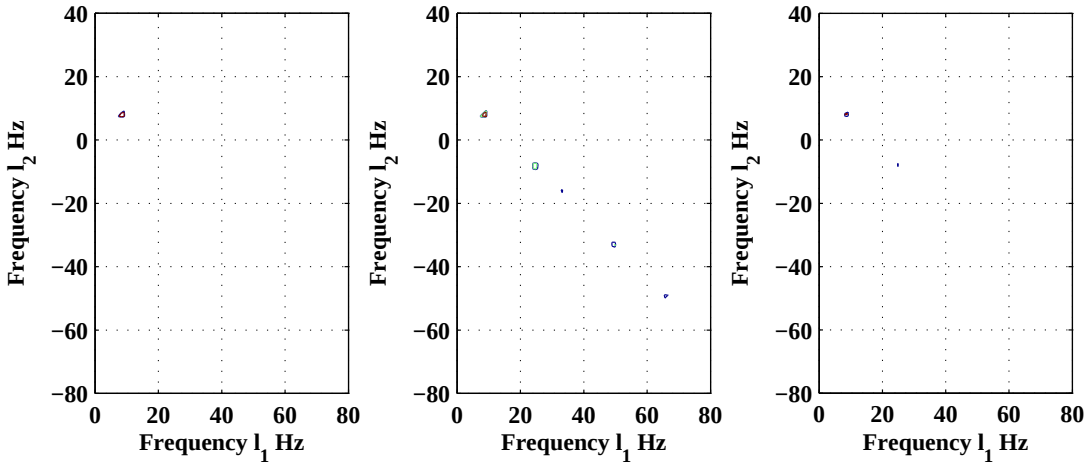

Figure 5.56: Cross-bicoherence between excitation and response at (a) the lowest end, (b) the centerline, and (c) the highest end of the fiber grating 10 before damage. Contour levels [0.7, 0.8].

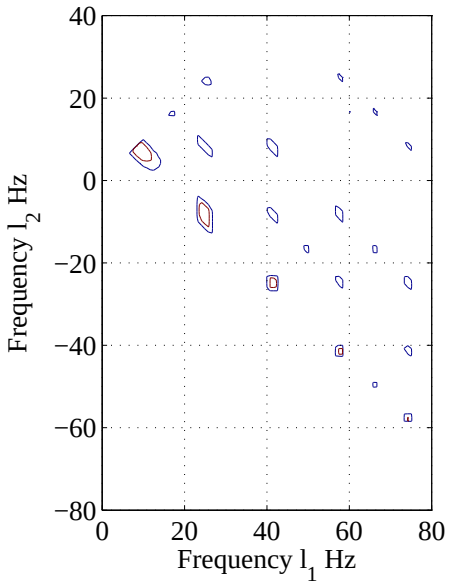

Figure 5.57: Cross-bicoherence between excitation and response from strain gage measurement before damage. Contour levels [0.9, 0.99].

localization of cracks. Contour levels of the damaged beam are higher in the damaged region and lower in the undamaged region of the beam in comparison to the undamaged case, for which contour levels are constant.

Contour levels for the other triples $(3f_{resp}, f_{resp}, f_{exc})$ and $(4f_{resp}, f_{exc}, f_{exc})$ are instead largely decreased for the damaged beam. The first triple has dropped from 0.4 - 0.6 to 0.3 - 0.4. The second triple has dropped from 0.3 to 0.2. Again, measurements at the centerline are more dependable than those at the ends because they are affected by a lower noise level.

The cross-bicoherence of the strain gage measurement is shown in Figure 5.57 for the damaged beam. Its contour levels are set again to 0.9 and 0.99. The presence of less harmonics suggests a lower level of coupling amongst frequecies triples due to damage. However, contour levels are still higher than the fiber optics ones because of the low noise level which affects the strain gage sensor. This cross-bicoherence plot, again, resembles the grating measurement at the centerline.

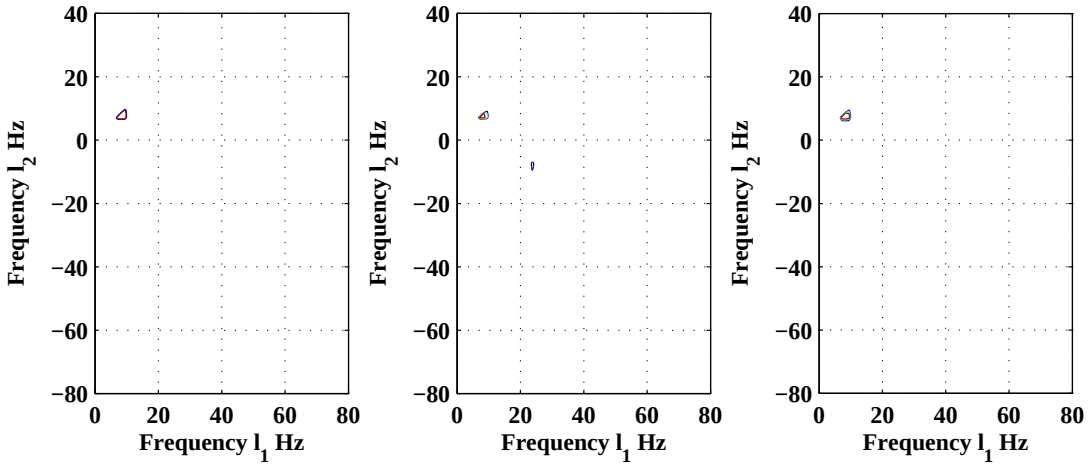

Figure 5.58: Cross-bicoherence between excitation and response at (a) the lowest end, (b) the centerline, and (c) the highest end of the fiber grating 2 after damage. Contour levels [0.8, 0.9].

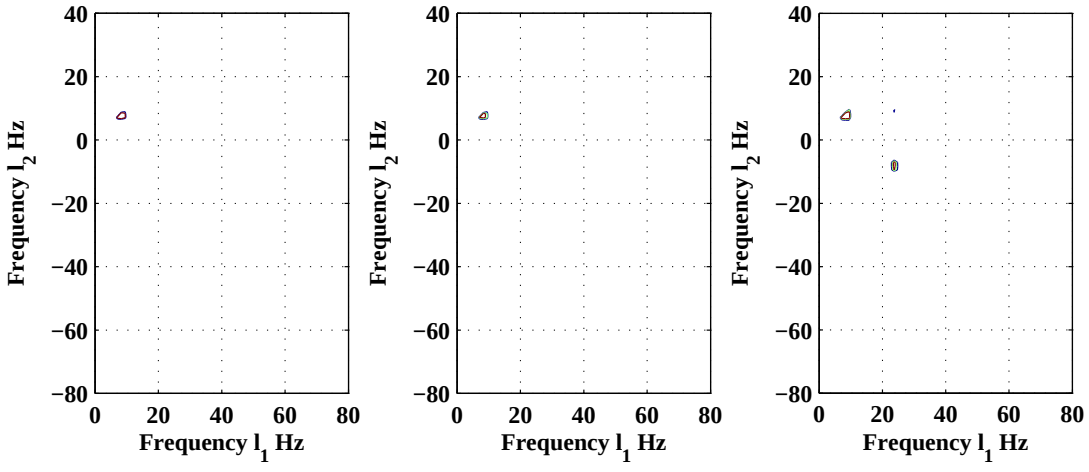

Figure 5.59: Cross-bicoherence between excitation and response at (a) the lowest end, (b) the centerline, and (c) the highest end of the fiber grating 3 after damage. Contour levels [0.8, 0.9].

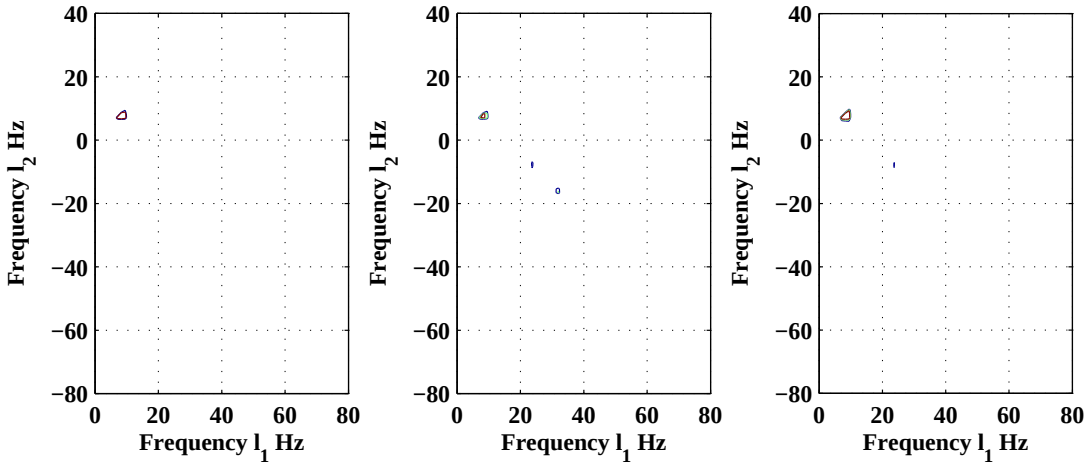

Figure 5.60: Cross-bicoherence between excitation and response at (a) the lowest end, (b) the centerline, and (c) the highest end of the fiber grating 4 after damage. Contour levels [0.8, 0.9].

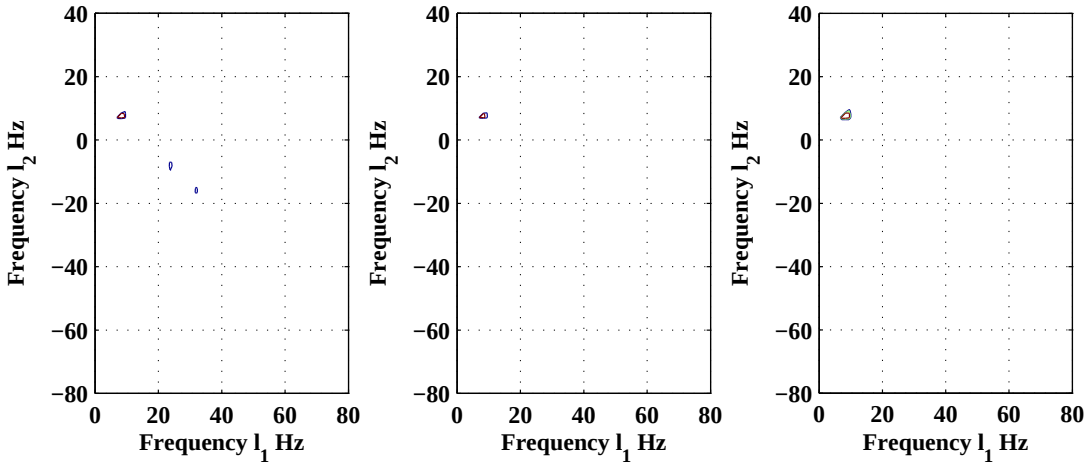

Figure 5.61: Cross-bicoherence between excitation and response at (a) the lowest end, (b) the centerline, and (c) the highest end of the fiber grating 5 after damage. Contour levels [0.8, 0.9].

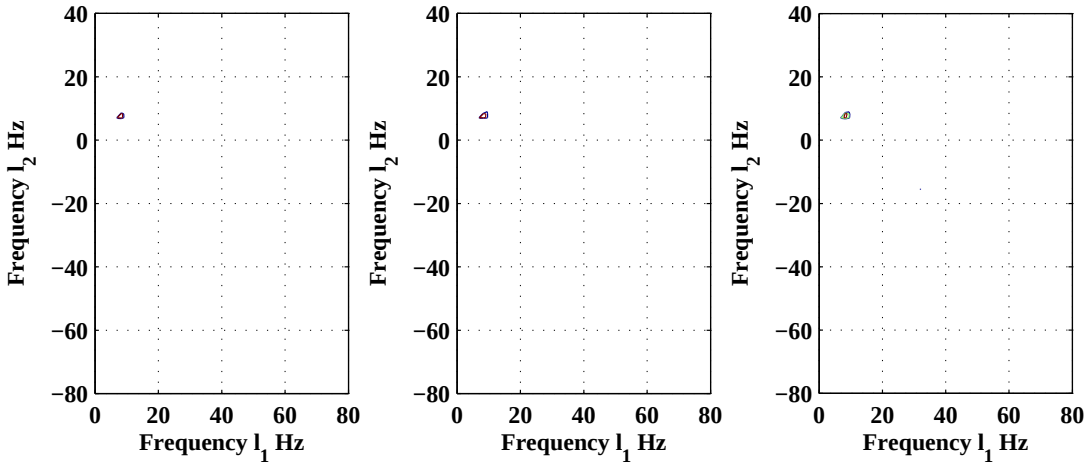

Figure 5.62: Cross-bicoherence between excitation and response at (a) the lowest end, (b) the centerline, and (c) the highest end of the fiber grating 6 after damage. Contour levels [0.7, 0.8].

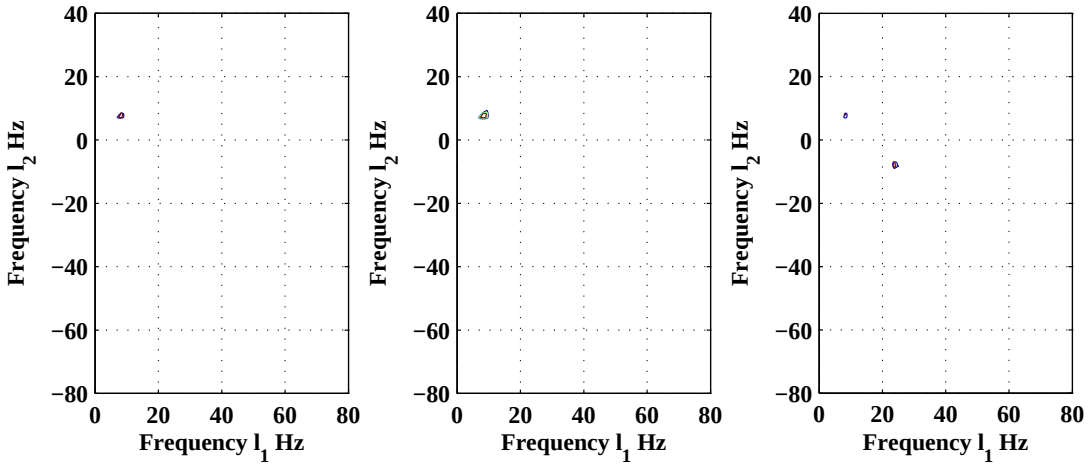

Figure 5.63: Cross-bicoherence between excitation and response at (a) the lowest end, (b) the centerline, and (c) the highest end of the fiber grating 7 after damage. Contour levels [0.6, 0.7].

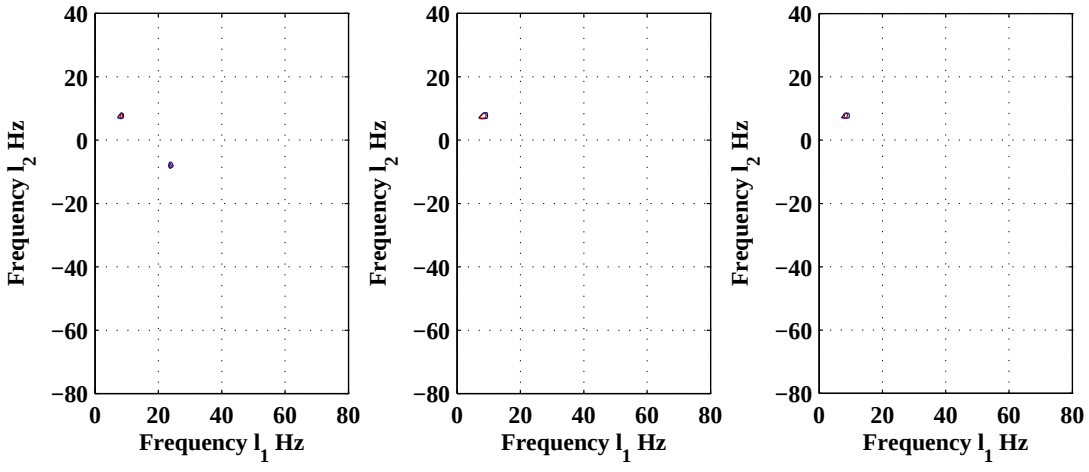

Figure 5.64: Cross-bicoherence between excitation and response at (a) the lowest end, (b) the centerline, and (c) the highest end of the fiber grating 8 after damage. Contour levels [0.7, 0.8].

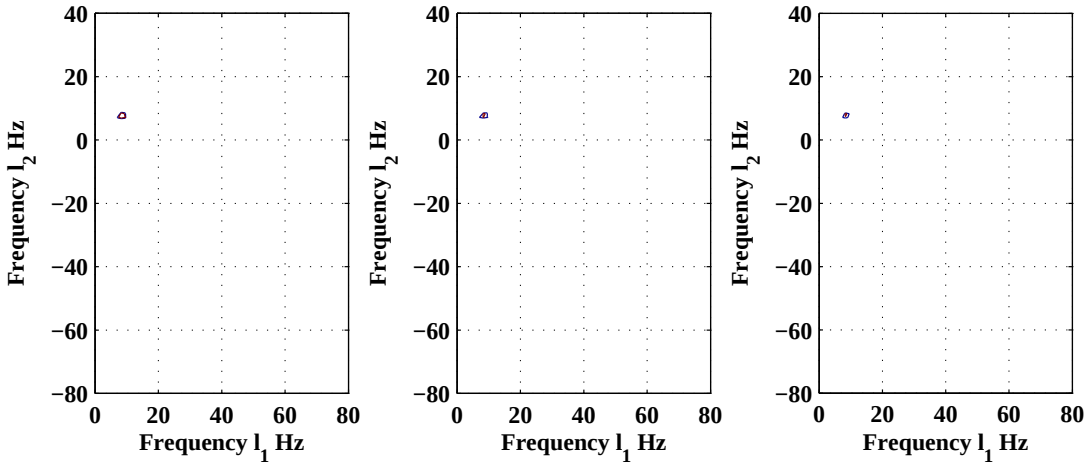

Figure 5.65: Cross-bicoherence between excitation and response at (a) the lowest end, (b) the centerline, and (c) the highest end of the fiber grating 9 after damage. Contour levels [0.6, 0.7].

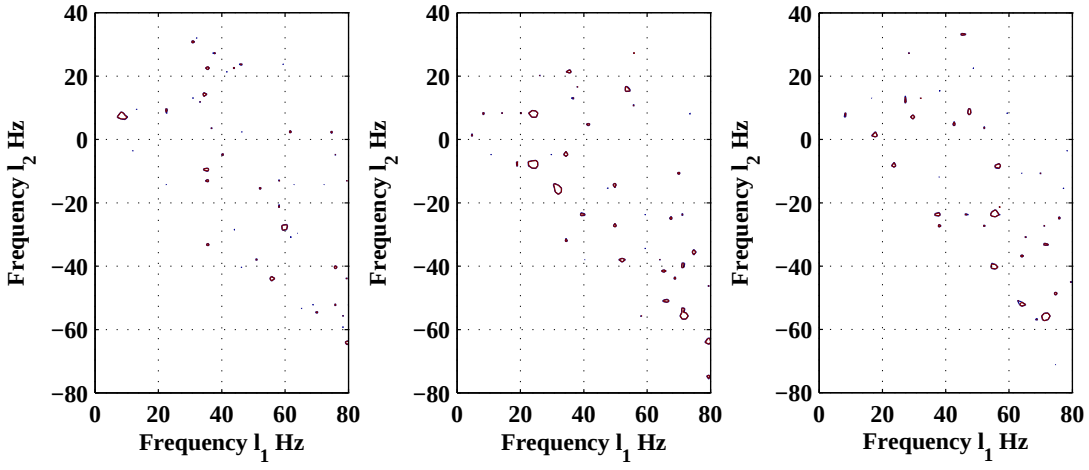

Figure 5.66: Cross-bicoherence between excitation and response at (a) the lowest end, (b) the centerline, and (c) the highest end of the fiber grating 10 after damage. Contour levels [0.2, 0.3].

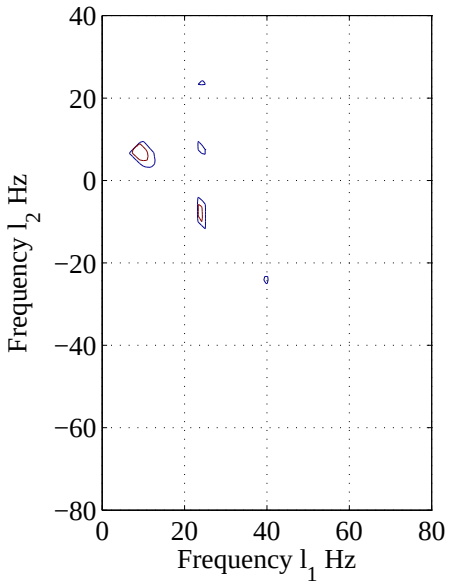

Figure 5.67: Cross-bicoherence between excitation and response from strain gage measurement after damage. Contour levels [0.9, 0.99].

5.3 Crack Localization

Crack localization is performed by computing linear and higher-order spectral moments on experimental data captured by the fiber optic gratings located along the beam. Physical quantities are then estimated from the data acquired before and after introducing cracks. Particular interest is focused on the ends and the centerline of each grating in order to describe their local overall performance. Comparisons of these experimentally derived paramaters are carried out for both undamaged and damaged beam. Magnitudes of the response and excitation frequency, and third harmonic are computed from the response power spectra, linear coherence, and higher-order moments. These spectral quantities are evaluated in order to assess their variations for the undamaged and damaged beam. The comparison of the amplitude of the first mode response between undamaged and damaged beam for the lowest edge of each grating is shown in Figure 5.68(a). The same plots are shown in Figures 5.68(b) and 5.68(c), respectively, for the lowest end, centerline, and the highest end of each grating, respectively. A large reduction of the response amplitude caused by the cracks presence is easily noticed, but it is not possible to make an easy assessment on the exact location of cracks. In order to overcome this limit, the ratio of the response amplitude before and after cracks is computed and results are presented in Figures 5.69(a), 5.69(b), 5.69(c). Because measurements obtained from the ends are largely affected by noise levels, average parameters are computed from these plots. Figure 5.70 shows that this ratio is sensitive to the cracks location. Two cracks are located between *20 mm* and *60 mm* and a third crack is located at *130 mm*. The ratio is, indeed, small in the region near the cracks and becomes large where there is no crack.

Another parameter chosen to assess crack localization is the linear coherence computed between excitation and response and evaluated at the response frequency. A consistent drop of this parameter is noticed for the damaged beam. This trend compared between undamaged and damaged beam is shown in Figures 5.71(a), 5.71(b), and 5.71(c), for the the lowest end, centerline, and the highest end of each grating, respectively. In addition, the linear coherence evaluated at the excitation frequency before and after cracks is also estimated, but it is, instead, largely affected by the level of noise. Its overall level is, however, smaller after crack

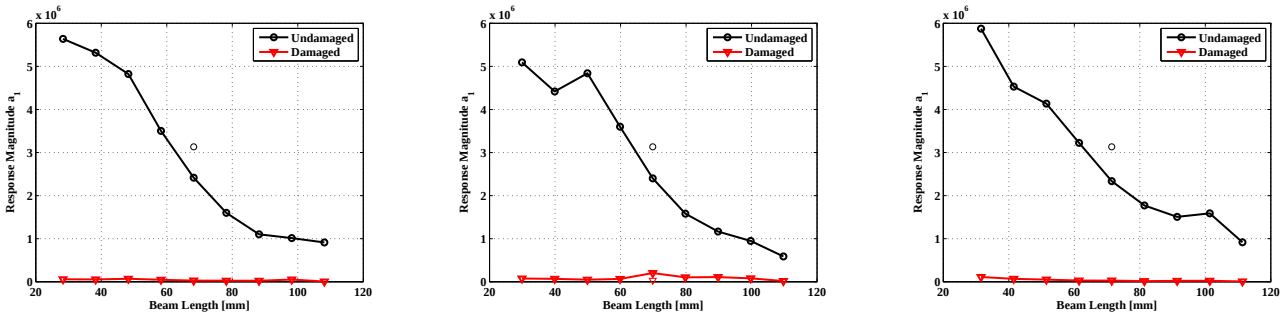

(a) (b) (c)

Figure 5.68: Comparison between undamaged and damaged beam of the peaks of the power spectrum at the fundamental frequency for (a) the lowest end, (b) the centerline, and (c) the highest end of each grating. The strain gage measurement is also shown here for the undamaged beam, which is reasonably close to the optical fiber estimations, and damaged beam, which is covered by the optical fiber estimations.

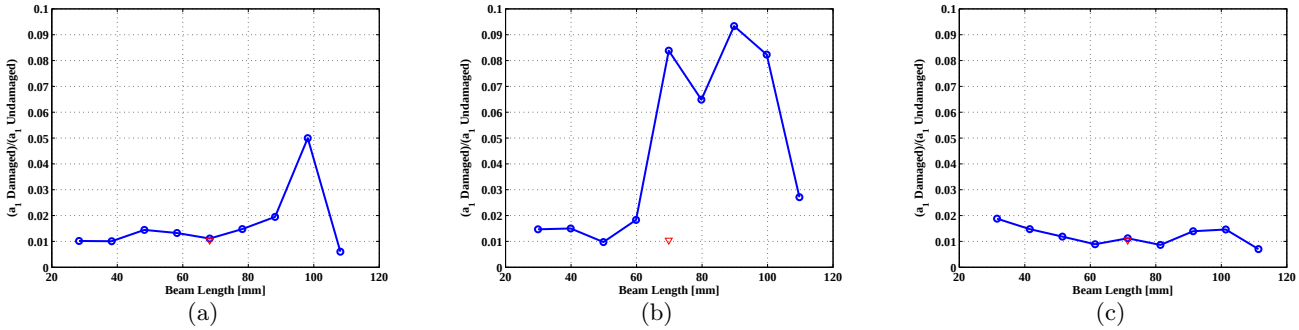

(a) (b) (c)

Figure 5.69: Ratio of the peak of the power spectrum at the fundamental frequency for (a) the lowest end, (b) the centerline, and (c) the highest end of each grating.

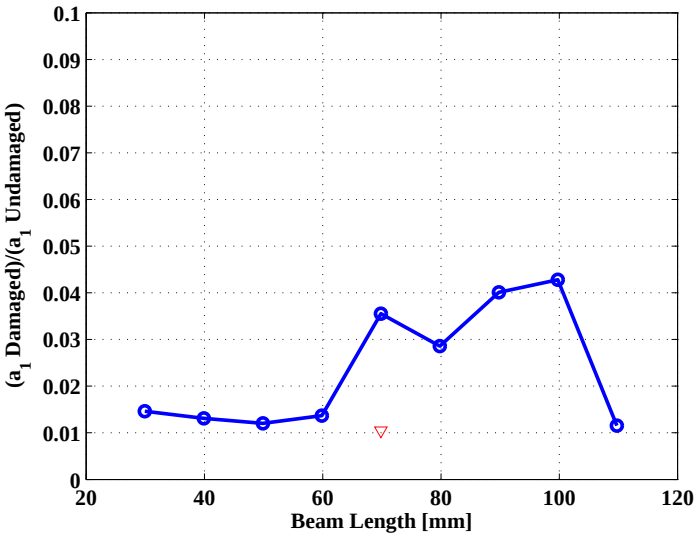

Figure 5.70: Ratio of the peak of the power spectrum at the fundamental frequency averaged over (a) the lowest end, (b) the centerline, and (c) the highest end of each grating. The strain gage ratio is also shown here and its overall estimation agrees with the pattern captured by the optical fiber.

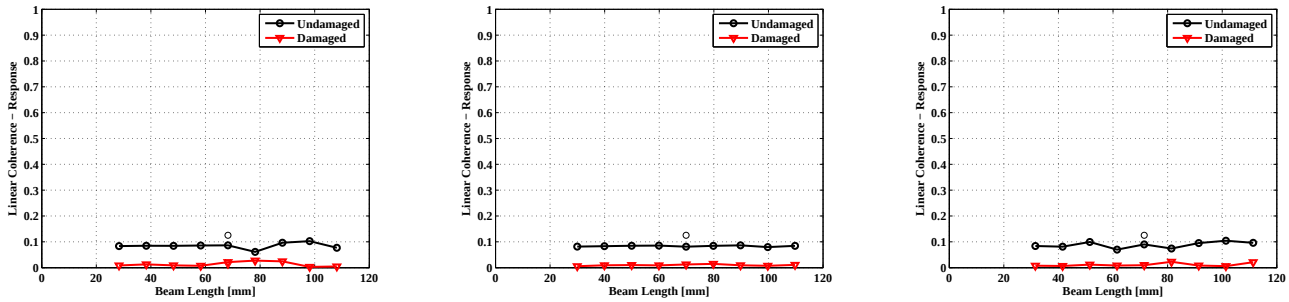

Figure 5.71: Comparison between undamaged and damaged beam of the linear coherence computed between excitation and response evaluated at the fundamental frequency for (a) the lowest end, (b) the centerline, and (c) the highest end of each grating.

as it is shown in Figures 5.71(a), 5.72(b), and 5.72(c) respectively, for the the lowest end, centerline, and the highest end of each grating.

Cross-bicoherence levels of quadratic phase coupling between frequencies at $(f_{resp}, f_{resp}, f_{exc})$ are computed before and after crack introduction at the ends and centerline of each fiber grating. The estimation of these parameters is not dependant on the noise level of the signals and nonlinearities involved in the system are better established. Cross-bicoherence levels computed for signals acquired respectively at the lowest, centerline, and the highest edge of each fiber grating are shown in Figures 5.73(a), 5.73(b), and 5.73(c). All these plots show the same pattern which is summarized in the average plot shown in Figure 5.74. Nonlinear response is more pronounced in the region that is close to cracks between *20 mm* and *60 mm* and less evident where the damage is not present between *60 mm* and *120 mm*. The level of this response decreases away from the cracks. Cross-bicoherence levels of quadratic phase coupling between frequencies at $(3f_{resp}, f_{resp}, f_{exc})$ are shown in Figures 5.75(a), 5.75(b), and 5.75(c) and summarized in the averaged plot shown in Figure 5.76. Nonlinear response is less pronounced after damage than before, resulting in a decrease of quadratic phase coupling among these frequencies.

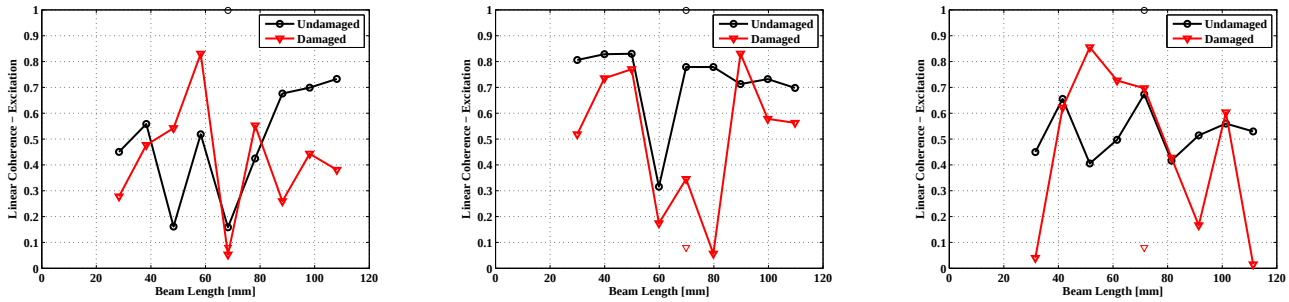

(a) (b) (c)

Figure 5.72: Comparison between undamaged and damaged beam of the linear coherence computed between excitation and response evaluated at the excitation frequency for (a) the lowest end, (b) the centerline, and (c) the highest end of each grating.

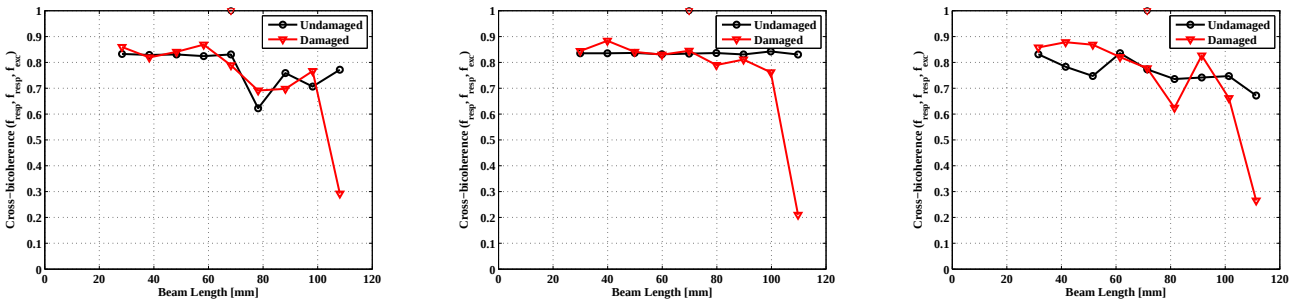

(a) (b) (c)

Figure 5.73: Comparison between undamaged and damaged beam of the cross-bicoherence levels at the frequencies triple $(f_{resp}, f_{resp}, f_{exc})$ of (a) the lowest end, (b) the centerline, and (c) the highest end.

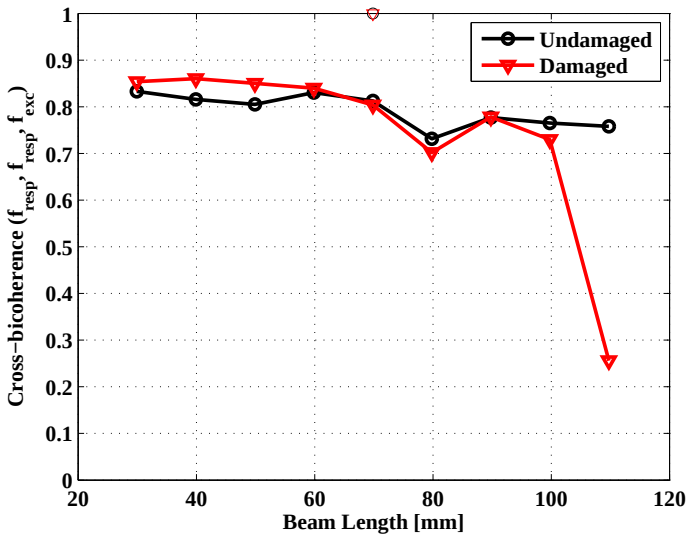

Figure 5.74: Comparison between undamaged and damaged beam of the cross-bicoherence levels at the frequencies triple $(f_{resp}, f_{resp}, f_{exc})$ averaged over (a) the lowest end, (b) the centerline, and (c) the highest end.

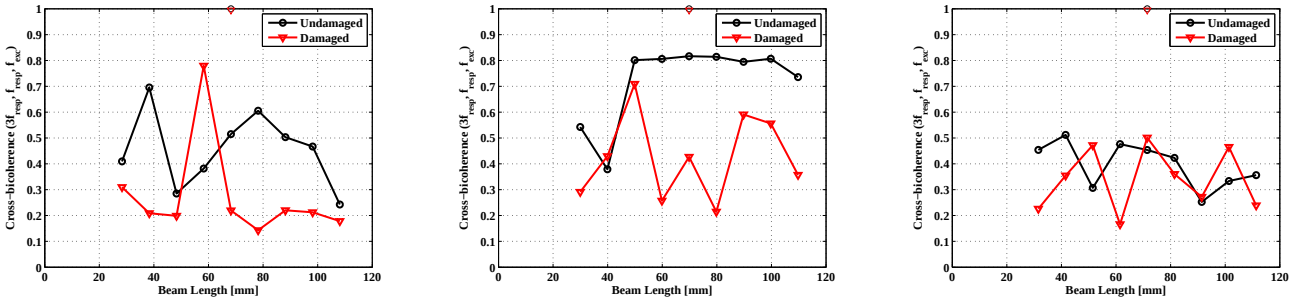

Figure 5.75: Comparison between undamaged and damaged beam of the cross-bicoherence levels at the frequencies triple $(3f_{resp}, f_{resp}, f_{exc})$ of (a) the lowest end, (b) the centerline, and (c) the highest end.

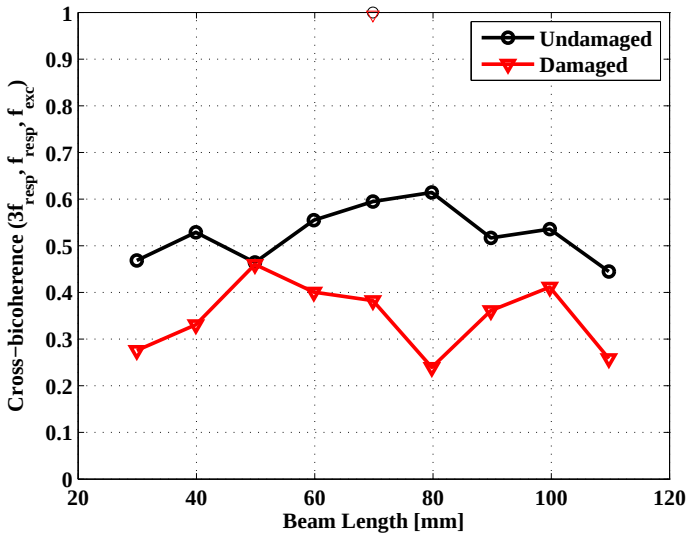

Figure 5.76: Comparison between undamaged and damaged beam of the cross-bicoherence levels at the frequencies triple $(3f_{resp}, f_{resp}, f_{exc})$ averaged over (a) the lowest end, (b) the centerline, and (c) the highest end.

Cross-bicoherence levels of quadratic phase coupling between frequencies at $(4f_{resp}, f_{exc}, f_{exc})$ are shown in Figures 5.75(a), 5.75(b), and 5.75(c) and summarized in the average plot shown in Figure 5.78. Again, nonlinear response is less pronounced after damage than before, resulting in a decrease of quadratic phase coupling among these frequencies. It has to be observed that the cross-bicoherence levels at the frequencies triples $(3f_{resp}, f_{resp}, f_{exc})$ and $(4f_{resp}, f_{exc}, f_{exc})$ shown in Figure 5.76, and Figure 5.78, respectively, do not yield a good assessment of damage location.

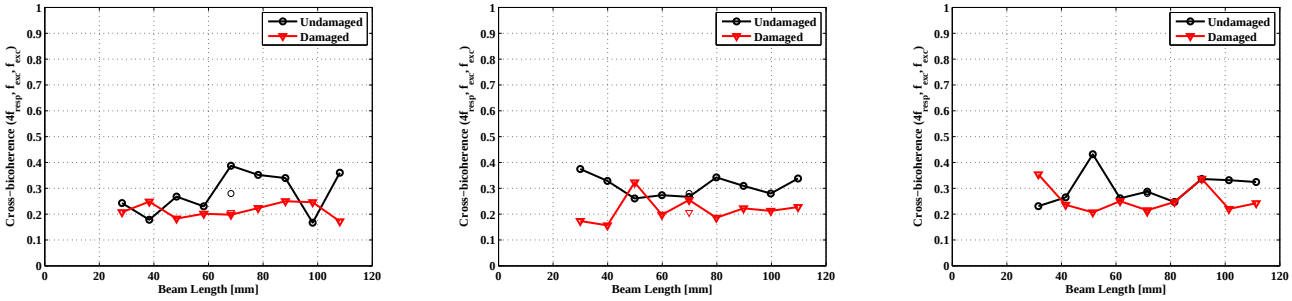

(a) (b) (c)

Figure 5.77: Comparison between undamaged and damaged beam of the cross-bicoherence levels at the frequencies triple $(4f_{resp}, f_{exc}, f_{exc})$ of (a) the lowest end, (b) the centerline, and (c) the highest end.

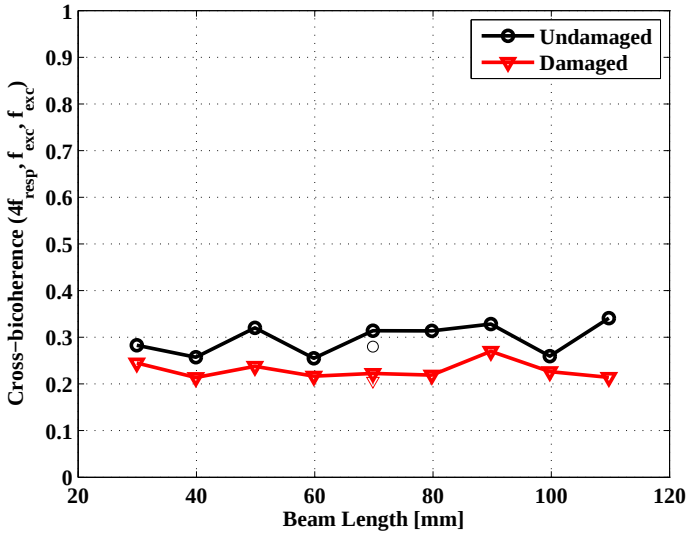

Figure 5.78: Comparison between undamaged and damaged beam of the cross-bicoherence levels at the frequencies triple $(4f_{resp}, f_{exc}, f_{exc})$ averaged over (a) the lowest end, (b) the centerline, and (c) the highest end.

Chapter 6

Conclusions

In the first part of this work, a novel damage prognosis technique is presented for two structural systems: a metallic beam-mass system and a composite beam carrying a steel lumped mass. Both structures are tested under cyclic fatigue loads starting from the undamaged state through intermediate damage stages up to failure. Variations in the parameters representing the natural frequency, damping, and effective nonlinearity to damage propagation in these structures are quantified. The identification procedure is performed by exploiting and modeling the nonlinear behavior of the system and matching an approximate solution of the representative model with quantities obtained from spectral analysis of measured vibrations. Sensitivity of the different parameters to the damage conditions of the beams is obtained by comparing the percentage variations in their values. The results show that the damping and effective nonlinearity coefficients are more sensitive to damage conditions than the natural frequency. Moreover, while the third harmonic results from the cubic nonlinearity, its amplitude ratio to that of the first mode does not vary significantly. As such, sensitivity of nonlinear parameters to damage conditions is better established using a physically derived parameter, such as the effective nonlinearity presented here rather than spectral amplitudes of harmonic components. The validation of the analytical model has been established through numerical integration of the governing differential equation using experimentally identified parameters. Repeatibility of the performed experiments and reliability of the obtained results have been successfully verified on a second metallic beam.

The above results, determined from experiments on simple structures, show advantages for associating damping and/or nonlinear parameters, rather than natural frequencies or spectral parameters, with damage initiation and progression in more complex or field structures. On the other hand, such structures may exhibit complex nonlinear responses from different sources. Furthermore, damping identification may not be straightforward. As such, reduced-order or parametric models for the response of such structures to excitation must be derived or established. This can be realized by developing abilities to identify and define the nonlinearity that will be exploited (Chabalko et al. (2008)), modeling the nonlinear responses (Nayfeh et al. (2008)), determining the form of parameters to be identified (Nayfeh et al. (2003)), and/or efficiently using and locating sensors. Furthermore, the higher sensitivity of damping than stiffness to damage, as shown in this study, may be beneficial in field measurements where noise effects could be relatively large.

In the second part of this work, the possibility of using fiber optics technology for crack localization is assessed in a composite beam-mass system. Again, the nonlinear response of this system to a principal parametric excitation is exploited. The beam responses under undamaged and damaged conditions, where cracks are externally produced through a tensile force, are compared. Spectral moments and quantities obtained from fiber optic strain measurements are evaluated near and away from cracks to assess the relation between these moments and cracks. The spectral moments include power spectrum, linear coherence, and cross-bicoherence. The results show that noise levels in fiber optic signals are high in comparison to strain gage signals. Of particular interest, however, is the observation that the nonlinear response is more pronounced near the cracks than away from them.

The reduced-order modeling and system identification tools as proposed in this work should advance SHM procedures in large engineered systems. Using these procedures, one could actually relate sensitive parameters to damage progression and localization.

Bibliography

Bahlous, S. E.-O., Abdelghani, M., Smaoui, H., and El-Borgi, S. A modal filtering and statistical approach for damage detection and diagnosis in structures using ambient vibrations measurements. *Journal of Vibration and Control*, 13:281–308, 2007.

Boller, C. and Buderath, M. Fatigue in aerostructures-where structural health monitoring can contribute to a complex subject. *Philosophical Transaction of Royal Society A*, 365: 561–587, 2007.

Bramban, D., Dupuis, J. P., and Jean, B. P. Impact detection and localization airborne system develepment for avionics applications. In *Structural Health Monitoring, 2005: Advancements and Challanges for Implementation By Ku-Fuo Chang*, pages 1235–1242, 2005.

Cawley, P. and Simonetti, F. Structural health monitoring using guided waves - potential and challenges. *Structural Health Monitoring, 2005: Advancements and Challanges for Implementation By Ku-Fuo Chang*, pages 503–510, 2005.

Chabalko, C., Hajj, M. R., and Silva, W. Interrogative testing for nonlinear identification of aeroelastic systems. *AIAA Journal*, 46(11):2657–2658, 2008.

Davidson, N. C. and Chase, S. B. Radar tomography of bridge decks. In *Structural Materials Technology III An NDT Conference, SPIE*, volume 3400, pages 250–256, 1998.

Fassois, S. D. and Sakellariou, J. S. Time-series methods for fault detection and identification in vibrating structures. *Philosophical Transaction of Royal Society A*, 365:411–448, 2007.

Friswell, M. I. Damage identification using inverse methods. *Philosophical Transaction of Royal Society A*, 365:393–410, 2007.

Gelman, L., White, P., and Hammond, J. Fatigue crack diagnostics: A comparison of the use of the complex bicoherence and its magnitude. *Mechanical Systems and Signal Processing*, 19:913–918, 2005.

George, D., Hunter, N., Farrar, C., and Deen, R. Identifying damage sensitive features using nonlinear time series and bispectral analysis. In *IMAC-18*, 2000.

Hajj, M. R., Miksad, R. W., and Powers, E. J. Perspective: Measurements and analyses of nonlinear wave interactions with higher-order spectral moments. *Journal of Fluid Engineering*, 119.

Hajj, M. R., Miksad, R. W., and Powers, E. J. Fundamental-subharmonic interaction: Effect of phase relation. *Journal of Fluid Mechanics*, 256:403–426, 1993.

Hajj, M. R., Fung, J., Nayfeh, A. H., and Fahey, O. F. Damping identification using perturbation techniques and higher-order spectra. *Nonlinear Dynamics*, 23:189–203, 2000.

Hamdan, M. N. and Dado, M. H. F. Large amplitude free vibrations of a uniform cantilever beam carrying an intermediate lumped mass and rotary inertia. *Journal of Sound and Vibration*, 199:737–750, 1997.

Hill, K. O. and Meltz, G. Fiber bragg grating technology fundamentals and overview. *Journal of Lightwave Technology*, 15:1263–1276, 1997.

Jiang, D. S. and Liu, S. C. The application and research of fbg sensors based load cell to bowstring arch bridge health monitoring. *Structural Health Monitoring, 2005: Advancements and Challanges for Implementation By Ku-Fuo Chang*, pages 323–330, 2005.

Kersey, A. D., Davis, M. A., Patrick, H. J., LeBlanc, M., Koo, K. P., Askins, C. G., Putnam, M. A., and Friebele, E. J. Fiber grating sensors. *Journal of Lightwave Technology*, 15: 1442–1463, 1997.

Kim, Y. C. and Powers, E. J. Digital bispectral analysis and its applications to nonlinear wave interactions. *IEEE Trans. Plasma Sci.*, pages 120–131, 1979.

Leng, J. S., Du, S. Y., Winter, D., Barnes, R. A., Mays, G. C., and Fernando, G. F. Structural strain monitoring of smart civil structure using fiber optic sensors. *Structural Health Monitoring, 2005: Advancements and Challanges for Implementation By Ku-Fuo Chang*, pages 331–339, 2005.

Mal, A., Banerjee, S., and Ricci, F. An automated damage identification technique based on vibration and wave propagation data. *Philosophical Transaction of Royal Society A*, 365: 479–491, 2007.

Micro-Measurements, V. *Strain Gage Applications with M-Bond AE-10, AE-15 and GA-2 Adhesive System*. Vishay, Document No., 11137.

Nair, K. K. and Kiremidjian, A. S. Time-series based damage diagnosis algorithm using gaussian mixture models. In *Structural Health Monitoring, 2005: Advancements and Challanges for Implementation By Ku-Fuo Chang*, pages 929–936, 2005.

Nayfeh, A. H. Parametric identification of nonlinear dynamic systems. *Computer and Structures*, 20:487–493, 1985.

Nayfeh, A. H. *Introduction to Perturbation Techniques*. Wiley-Interscience, New York, 1981.

Nayfeh, A. H., Owis, F., and Hajj, M. R. A model for the coupled lift and drag on a circular cylinder. In *Proc. of ASME 19th Biennial Conference on Mechanical Vibrations and Noise, Sept. 2-6, 2003, Chicago, IL, USA, DETC2003/VIB-48455*, 2003.

Nayfeh, A. H., Hajj, M. R., Nayfeh, S. A., Chabalko, C., and Beran, P. A reduced-order model for lco dependence on mach number in f16 flight tests. In *49th AIAA/ASME/ASCE/AHS/ASC Structures, Structural Dynamics, and Materials Conference, Apr. 7-10, 2008, Schaumburg, IL, USA, AIAA-2008-1755*, 2008.

Park, G. and Inman, D. J. Structural health monitoring using piezoelectric impedance measurements. *Philosophical Transaction of Royal Society A*, 365:373–392, 2007.

Powers, E. J. and Im, S. *Introduction to Higher-Order Statistical Signal Processing and its Applications*. Boashash, Powers & Zoubir, Longman, Australia, 1995.

Rivola, A. and White, P. R. Bispectral analysis of the bilinear oscillator with application to the detection of fatigue cracks. *Journal of Sound and Vibration*, 216(2):889–910, 1998.

Salvino, L. W., Purekar, A. S., and Pines, D. J. Damage identification using time-frequency wave propagation data. In *Structural Health Monitoring, 2005: Advancements and Challanges for Implementation By Ku-Fuo Chang*, pages 582–589, 2005.

Silva, M. R. M. C. D. and Glynn, C. C. Nonlinear flexural-flexural-torsion dynamics of inextensional beam, i: Equation of motion. *Journal of Structural Mechanics*, 6:437–461, 1978.

Staszewski, W. J. and Robertson, A. N. Timefrequency and timescale analyses for structural health monitoring. *Philosophical Transaction of Royal Society A*, 365:449–477, 2005.

Todd, M. D., Nichols, J. M., Trickey, S. T., Seaver, M., Nichols, C. J., and Virgin, L. N. Bragg grating-based fibre optic sensors in structural health monitoring. *Philosophical Transaction of Royal Society A*, 365:317–343, 2007.

Valente, L. C. G., Braga, A. M. B., Riberio, A. S., Regazzi, R. D., Ecke, W., Chojetzki, C., and Willsch, R. Combined time and wavelength multiplexing technique of optical fiber grating sensor arrays using commercial otdr equipment. *IEEE Sensors Journal*, 3:31–35, 2003.

Wagner, H. The large-amplitude free vibrations of a beam. *Transaction of the ASME, Journal of Applied Mechanics*, 32:887–897, 1965.

Zavodney, L. D. and Nayfeh, A. H. The non-linear response of a slender beam carrying a lumped mass to a principal parametric excitation: Theory and experiment. *Int. J. Non-Linear Mechanics*, 24:105–125, 1989.